Spring 2019

Comparison of Support Methods for Static Aerodynamic Testing and Validation of a Magnetic Suspension and Balance System

Cameron K. Neill
Old Dominion University, cam.k.neill@gmail.com

COMPARISON OF SUPPORT METHODS FOR STATIC AERODYNAMIC TESTING AND VALIDATION OF A MAGNETIC SUSPENSION AND BALANCE SYSTEM

by

Cameron K. Neill
B.S. May 2016, Georgia Institute of Technology

A Thesis Submitted to the Faculty of
Old Dominion University in Partial Fulfillment of the
Requirements for the Degree of

MASTER OF SCIENCE

AEROSPACE ENGINEERING

OLD DOMINION UNIVERSITY
May 2019

Approved by:

Colin Britcher (Director)

Drew Landman (Member)

Brett Newman (Member)

Mark Schoenenberger (Member)

ABSTRACT

COMPARISON OF SUPPORT METHODS FOR STATIC AERODYNAMIC TESTING AND VALIDATION OF MAGNETIC SUSPENSION AND BALANCE SYSTEM

Cameron K. Neill
Old Dominion University, 2019
Director: Dr. Colin Britcher

Magnetic suspension wind tunnels offer an alternative to traditional physical support methods. They allow for the collection of support interference free data and broader dynamic test capabilities than existing methods. Determination of dynamic aerodynamic characteristics is a crucial portion of the design of new re-entry capsules. A NASA initiative restored the 6-inch Magnetic Suspension and Balance System to support the design of a new MSBS for a supersonic wind tunnel. Before a new MSBS can be constructed, the characteristics of the current MSBS must be examined.

This thesis discusses the calibration and validation of the 6-inch MSBS. After calibration, three aerodynamic tests were performed in order to characterize the data collected from the MSBS. They included a traditional sting supported test, a free-flying magnetically suspended test, and a magnetically suspended test with aerodynamic interference from a dummy sting. The ideology behind the chosen experimental design was to isolate the effect of support interference from any MSBS calibration errors. Any differences between the sting supported and the dummy sting tests would be caused by the MSBS. Any differences between the free-flying and the dummy sting tests would be due to support interference. Multiple components were designed and constructed, in order to support this effort.

The goals of this thesis were met. The MSBS data had high repeatability and accuracy, which validated the force recovery method. Aerodynamic testing showed in minimal variation

between support methods at low angles of attack. Discrepancies between support methods increased with models mounted at high angles of attack. Current references generally exhibit much higher Reynolds numbers than the MSBS and the wind tunnel can achieve. Support interference free reference data in an achievable Reynolds number was generated for future NASA testing. While the outcome was successful, multiple possible improvements or future projects were identified that can be completed prior to design and construction of the new MSBS.

This thesis is largely dedicated to my parents. I would not be the person I am today without you. Your support and encouragement are what allowed me to even contemplate obtaining a graduate degree. Thank you so much for your extreme tolerance and your unyielding efforts, which have prepared me for a bright future.

To my Grandparents – Your support has allowed me to reach these heights and pursue my interests to their fullest.

To Haley – It has been a long road so far, a fact that I have been reminded of only a couple of times. You have really been the driving force in my finally getting this thing onto paper and in wrapping up this chapter of my life. You have encouraged me whenever the tasks seemed too great to overcome. I am eager to begin our next chapter.

ACKNOWLEDGEMENTS

There are many people who have contributed to the successful completion of this thesis. My advisor, Dr. Colin Britcher, who has guided and supported my graduate studies and my thesis work, deserves special recognition, especially after his many hours reading and correcting several drafts of this thesis. I am very thankful for our meeting those years ago; this has provided me with one of the most gratifying experiences of my life. Mark Schoenenberger, Timothy Schott, and David Cox comprise the major NASA contributors to my research; this thesis would not exist in any form without their efforts. I especially thank Mark for his assistance with this thesis as a committee member. I extend many, many thanks to my other committee members, Dr. Brett Newman and Dr. Drew Landman, for their patience and hours of guidance and editing of this manuscript. Dr. Newman also helped to guide my graduate studies with many hours of instruction, both in and out of the classroom.

NOMENCLATURE

A	MS-100 balance axial component.
A_1	Area at static tap 1.
A_2	Area at static tap 2.
AoA	Angle of attack.
α	Angle of attack.
A_t	Area of the test section.
b_k	Systematic uncertainty, generally taken from sensor or fit uncertainties.
C_1	First order interaction coefficient matrix; 6x6.
C_2	Second order interaction coefficient matrix; 6x21.
CD	Coefficient of drag.
C_{dcav}	Coefficient of drag after cavity pressure correction.
C_{du}	Uncorrected drag coefficient.
CL	Coefficient of lift.
C_m	Coefficient of moment.
C_{pcav}	Coefficient of pressure for the model cavity.
$D_{current}$	Drag coil current.
dp/dl	Rate of change of test section static pressure over its length.
DOE	Design of Experiments
Drag	Drag force.
ΔE	Change in second order interaction correction matrix between iterations.

E_n	Second order interaction correction matrix of current iteration.
E_{n-1}	Second order interaction correction matrix of previous iteration.
E_{final}	Second order interaction correction matrix that satisfies the tolerance acceptance criteria. Subtracted from F_1 to calculate true balance loads.
ε_{solid}	Solid blockage effect.
ε_{wake}	Wake blockage effect.
f	Source function for which the combined uncertainty is being generated.
F	Force and moment matrix.
|F|	Magnitude of
F_1	Initial force and moment approximation.
F_A	Axial force.
F_{output}	True forces and moments from the strain gage balance.
F_N	Normal force.
F_n	Load matrix for a particular iteration.
F_u	Uncorrected load.
F_Y	Side force.
g	The standard acceleration due to gravity; 9.80665 m/s^2
γ	Loading misalignment angle.
K_1	Constant that captures pressure loss effects.
K_2	Constant relating the area ratio between static taps.
K_3	Constant relating the area ratio between static tap 2 and the test section.
κ	Sensitivity constant matrix.
k_d	Ratio between magnetically generated drag force and drag coil current.

k_l	Ratio between magnetically generated drag force and drag coil current.
k_s	Ratio between magnetically generated lift force and lift coil current.
λ	Body shape factor; equal to 1 for spheres.
$L_{current}$	Lift coil current.
Lift	Lift force.
L_{model}	Characteristic length of model; maximum diameter of model.
M	Moment after moment center transfer.
$M_{applied}$	Applied moment.
$M_{measured}$	Moment measured at balance moment center.
μ	Dynamic viscosity of dry air; taken to be 1.846×10^{-5} kg/(m*s).
M_X	Rolling moment.
M_Y	Pitching moment.
M_Z	Yawing moment.
N	MS-100 balance normal component.
ω	Force and moment product matrix.
ω_1	First force and moment product matrix approximation.
P	MS-100 balance pitch component.
p_1	Static pressure at tap 1.
p_2	Static pressure at tap 2.
P_3	Static pressure at tap 3.
p_a	Ambient atmospheric pressure.
p_{cav}	Cavity pressure.

p_∞	Test section static pressure.
Q	Dynamic pressure in the test section.
q_1	Dynamic pressure at tap 1.
q_2	Dynamic pressure at tap 2.
q_{cav}	Dynamic pressure in the test section after sensor and blockage corrections. Specifically corresponding to the cavity pressure measurement.
$q_{interpolated}$	Dynamic pressure in the test section after sensor correction.
q_{raw}	Uncorrected dynamic pressure measurement from sensor.
q_{test}	Dynamic pressure in the test section after sensor calibration and blockage corrections.
R	MS-100 balance roll component.
R_a	Specific gas constant of dry air; 287.05 J/(kg*K).
Re	Reynolds number.
ρ	Air density.
S	MS-100 side component.
$S_{current}$	Side coil current.
Side	Side force.
σ	Standard deviation.
S_{model}	Cross-sectional area of the model.
S_{sting}	Contact area between model and MS-100 force balance.
S_{tunnel}	Area of the test section.
s_x	Random error, generally taken as the standard deviation of the mean.
T_a	Ambient temperature.
τ	Test section shape factor; approximated as 0.8 for octagonal test sections.

θ	6x1 column matrix of the raw balance output.
u	Free stream velocity in the test section.
U_{95}	Combined uncertainty with a 95% level of confidence.
U_{cd}	Combined uncertainty for calculated drag coefficients.
U_D	Drag force uncertainty.
U_i	Expanded uncertainty for a single variable.
U_q	Dynamic pressure uncertainty.
U_{re}	Combined uncertainty for calculated Reynolds numbers.
U_{Ta}	Temperature uncertainty.
V_1	Free stream velocity at tap 1.
V_2	Free stream velocity at tap 2.
V_{model}	Volume of sphere with diameter equal to L_{model}.
V_t	Free stream velocity in the test section.
Y	MS-100 balance yaw component.

TABLE OF CONTENTS

Page

LIST OF TABLES

Page

LIST OF FIGURES

Page

CHAPTER 1.
INTRODUCTION

1.1. Background

Experimental dynamic stability data of blunt body re-entry capsules is vitally important to support both the design of new capsule geometries and the planning of trajectories for new missions. This data has traditionally relied heavily on ballistic range testing [1-3]. Such testing can be resource-intensive and can have a limited range of data. Free-oscillation tests can also be conducted in vertical wind tunnels, but such tests are limited in tunnel conditions because there is only one dynamic pressure where drag exactly offsets the weight of the test model. An initiative to produce a less costly and more flexible test method is underway as a joint project between NASA and ODU.

This initiative involves the reactivation of the 6-inch Magnetic Suspension and Balance System (MSBS) and the accompanying subsonic wind tunnel. The MSBS and tunnel were constructed in the 1960s as a joint project between the Massachusetts Institute of Technology and NASA [4,5]. The MSBS was operated at NASA Langley Research Center in the 1980s and 1990s. ODU acquired the MSBS and the wind tunnel after its retirement. The MSBS remained defunct, while the wind tunnel was used for various low-speed experiments. Around 2016, the MSBS and the wind tunnel were loaned back to NASA and underwent a revitalization process [6,7]. The MSBS utilizes multiple electromagnetic coils in conjunction with an electromagnetic position sensor system to suspend an iron or neodymium core. Figure 1 shows the MSBS as configured during this thesis. Various plastic shells can be attached to the model core to test different capsule geometries; such shells can be rapidly and inexpensively constructed via casting, machining, or 3D printing. The goals of the project are to explore free-oscillation

suspension, to locate areas where the MSBS may be improved or expanded in capability, and to eventually support the design and construction of a new MSBS for a supersonic wind tunnel.

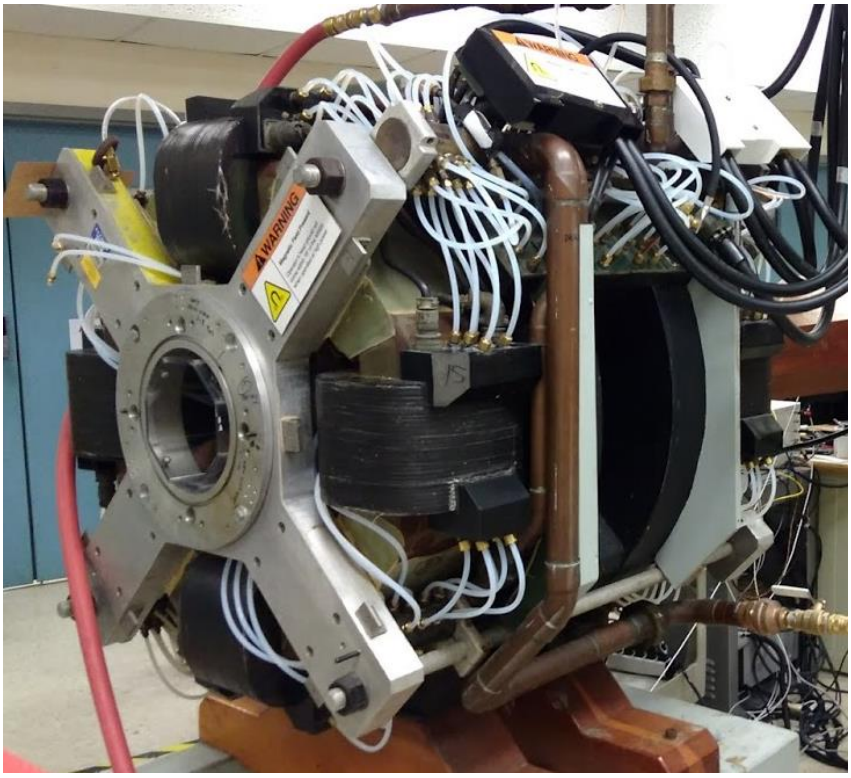

Figure 1: 6-Inch MSBS with inlet removed.

The purpose of this thesis is to examine the testing conditions of the MSBS and to validate data collection methods by conducting static wind tunnel tests using multiple suspension techniques. Before the MSBS may be utilized to support capsule design, the correctness of the MSBS data collection methods must be evaluated. Furthermore, it is important to understand how the MSBS data differs, if at all, from traditionally-gathered data. A secondary goal of this

thesis was to produce support interference free drag data that would be used in the larger NASA project.

Traditional wind tunnel tests involve some manner of physical support. The physical support, and sometimes the adaptation of a model to accept the support, interfere with the measured data. Therefore, traditional reference data could not be used to verify the data collected from the MSBS. Due to the large differences in Reynolds numbers, the reference data could not be used to determine the effect of support interference.

Three experiments were designed as a solution to the problem above. The first experiment was a traditional sting supported test performed in the MSBS wind tunnel (referred to as sting supported tests). This experiment would generate a set of reference data with the same test conditions and Reynolds number regime as the MSBS data. The second experiment used the MSBS to suspend a model with a magnetic core to determine aerodynamic data without support interferences (referred to as magnetically suspended or free flying tests). At this stage, it was unknown if discrepancies between MSBS and sting data were due to support interference or error in MSBS data collection. A third experiment was designed as a hybrid of the previous methodologies, in order to bridge the gap in the data. This experiment utilized a magnetically suspended model and a rod that served as a fake or dummy sting support (referred to as dummy sting tests). The model geometry was altered in such a manner that the dummy sting could aerodynamically interfere without physically contacting the model. In theory, the aerodynamic data collected from this test would be the same as the aerodynamic data collected by the sting supported test. Any discrepancy between the first and third experiments would, therefore, be due to MSBS data collection methodologies. Data discrepancy between the second and third experiments would be due to support interference. These three experiments would isolate

measurement discrepancy from sting interference, and therefore would satisfy the goals of MSBS verification and support interference quantification.

The model geometry used in this thesis was that of the Stardust Sample Return Capsule. Stardust was a space probe launched in 1999 designed to recover dust samples from the 81P/Wild comet. The sample return capsule and the dust samples were successfully recovered in 2006. The sample return capsule, henceforth referred to as Stardust, was selected as the tested geometry for this thesis because of the availability of reference data and the simplicity of design, and to provide reference data to other concurrent projects that were using the Stardust geometry. Figure 2 is an example render of the Stardust geometry with the forebody facing upwards. The tested models had a nominal maximum diameter of 44.45 mm (1.75 in); exact model diameters are shown in Appendix A.6.

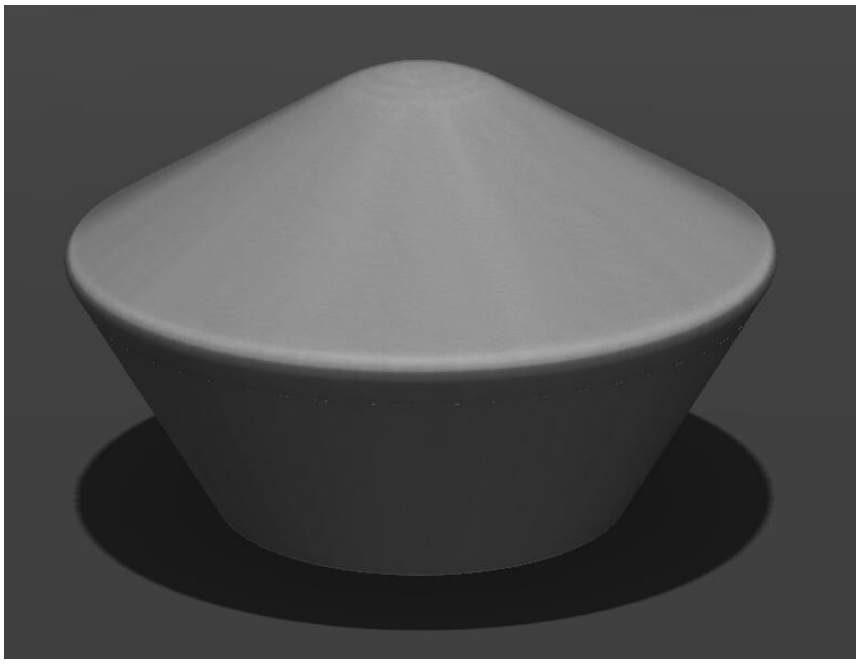

Figure 2: 3D render of Stardust capsule.

1.2. Literature Review

1.2.1. Strain Gauge Balance Reduction

A strain gauge is a thin resistive sensor that is attached to an object to measure deformation. As the object deforms, the gauge also deforms, which can increase or decrease the resistance of the sensor. The change in resistance results in a voltage differential in the measurement circuit. Wind tunnel strain gauge force balances combine multiple strain gauges in a known geometry to measure forces and moments in multiple axes [8]. For single axis applications involving a single strain gauge, such as testing the tensile properties of materials or weighing oneself with a bathroom scale, this voltage can generally be converted directly to a strain value.

The same direct conversion cannot be applied to wind tunnel force balances because of significant interactions between axes. The lift channel might be affected by the drag force, and the pitching moment channel might be affected by the side force times the rolling moment. The first is an example of a linear interaction, where the effect is caused by a single component; the second is an example of a nonlinear interaction, where the effect is caused by a specific combination of components or power of a single component [8,9]. Linear effects arise from build and material errors, while nonlinear effects are thought to be caused by off-axis deformation under load. In practice, a single component of a monolithic 6-component force balance will rely on 27 variables and interactions [8,9]. This encompasses all of the linear and second order interactions; higher order terms and interactions are neglected.

The equations governing the interactions are solved through the use of an algorithm. Multiple algorithms, with varying levels of precision and computing cost, have been developed. This thesis uses a matrix-based algorithm that was developed in 1972 at NASA LARC [9].

Equations (1) through (10) comprise the algorithm. The force matrix is defined in Equation (1). Equation (2) is the force and moment product matrix.

$$F = [F_N, F_A, M_Y, M_X, M_z, F_Y]^T \tag{1}$$

$$\begin{aligned}\omega = [&{F_N}^2, F_N F_A, F_N M_Y, F_N M_X, F_N M_z, F_N F_Y, {F_A}^2, F_A M_Y, F_A M_X, F_A M_z, F_A F_Y,\\ &{M_Y}^2, M_Y M_X, M_Y M_z,\ M_Y F_Y, {M_X}^2, M_Y M_X, M_X M_z, M_X F_Y, {M_Z}^2,\ M_Z F_Y, {F_y}^2]^T\end{aligned} \tag{2}$$

Equation (3) establishes the relationship between the balance output and the components affecting the output. The balance output, scaled by the sensitivity constants, is equal to the sum of first order and second order interactions. Equation (4) isolates the load matrix as the desired result. Equation (5) is a redefinition of Equation (4) by the insertion of a combined interaction matrix, C_3, and the uncorrected load, F_u.

$$\kappa\theta = C_1 F + C_2 \omega \tag{3}$$

$$F = {C_1}^{-1}\kappa\theta - {C_1}^{-1} C_2 \omega \tag{4}$$

$$C_3 = {C_1}^{-1} C_2; F_u = \kappa\theta$$

$$F = {C_1}^{-1} F_u - C_3 \omega \tag{5}$$

Then, the iteration begins. Equation (6) is the initial guess value that begins the iteration. The loads in F_1 are used to generate the first force and moment product matrix, ω_1. As shown in Equation (7), the term $C_3\ \omega_n$ becomes the second-order interaction correction matrix, E_n. E_n is used to generate the next load matrix in Equation (8). F_{n+1} is used to generate ω_{n+1}, which generates E_{n+1}, and the cycle repeats. Eventually, the algorithm converges toward a specific numerical approximation. Convergence criteria is met when ΔE in Equation (9) is within some desired tolerance. Once the desired ΔE is met, the current E_n becomes E_{final} and is used to

calculate the final load matrix, as shown in Equation (10). The outputs of this equation are considered to be the true forces and moments that are acting on the balance.

$$F_1 = {C_1}^{-1} F_u \tag{6}$$

$$E_n = C_3 \omega_n \tag{7}$$

$$F_{n+1} = F_1 - E_n \tag{8}$$

$$\Delta E = |E_n - E_{n-1}| \tag{9}$$

$$F_{output} = F_1 - E_{final} \tag{10}$$

1.2.2. Sting Interference

In general, traditional aerodynamic testing of 3D models requires the addition of some sort of support system. Magnetic suspension, vertical tunnels, and ballistic testing were discussed in the background as three major exceptions. Any mechanical support will influence the measured forces, and a significant effort has been made to quantify these effects. Barlow establishes three categories to describe the support influences: the added aerodynamic forces acting on the support, the flow changes around the model caused by the support, and the flow changes around the support caused by the model [8]. The latter categories make isolated measurement of the first impossible. Classical interference tests involve various configurations of dummy and true supports, such that the support interference can be isolated from the multiple force measurements.

Sting supports, which support the model at the end of a long rod, are often used as a method of minimizing support interference on the greater portion of the model. In supersonic wind tunnels, sting supports are nearly exclusively used, because other support methods can cause extreme flow blockages due to shock interference [8, pp. 285]. Sting supports can increase

or decrease drag, depending on model and support configuration [10]. Formulae exist to estimate the effect of sting interference on axisymmetric models or to design a sting support that will minimize interference. Models that have aerodynamically significant, or models that do not have axisymmetric, aft sections, such as submarines and aircraft, will often require specific investigation into sting interference [11, 12]. Under some circumstances, support interference can change, measured drag, by more than 100%; in other circumstances support interference is extremely small [12, 13].

A benefit of a magnetic suspension wind tunnel is the complete removal of support interference. This saves significant time and effort and allows for rapid changes in model geometries and configurations without necessitating a reevaluation of support effects. However, it is important to understand support interference effects in order to accurately categorize magnetic suspension data within the realm of traditionally collected reference data.

1.2.3. Magnetic Balance

Electromagnets are utilized pervasively in the modern world. The speakers in a car, the junkyard scrap-metal crane, MRIs, VCRs, and so on all utilize electromagnets. With proper control, electromagnets can be used to suspend or to levitate an object without any physical contact. Applications include Maglev systems and magnetic bearings [14]. Aerodynamic models may be magnetically suspended in wind tunnels in a conceptually similar manner.

The core component of a magnetic suspension wind tunnel is the Magnetic Suspension and Balance System (MSBS). The MSBS is a combination of electromagnets that work in concert to overcome gravity and that counteract the aerodynamic forces acting on a model during testing. The MSBS consists of a number of electromagnets in a variety of geometric configurations. Some systems completely decouple control of each aerodynamic force, while

others may use the same electromagnets for multiple axes [15]. No matter the configuration, all MSBS require a method of position sensing and control. Position sensors can be optical or electromagnetic, with various advantages and disadvantages to each. Optical position sensors may rely on specific lighting conditions that may preclude certain forms of flow visualization. Electromagnetic position sensors can be difficult to isolate from electromagnetic interference. Figure 3 shows the electromagnetic coil and position sensor configuration for the 6-inch MSBS.

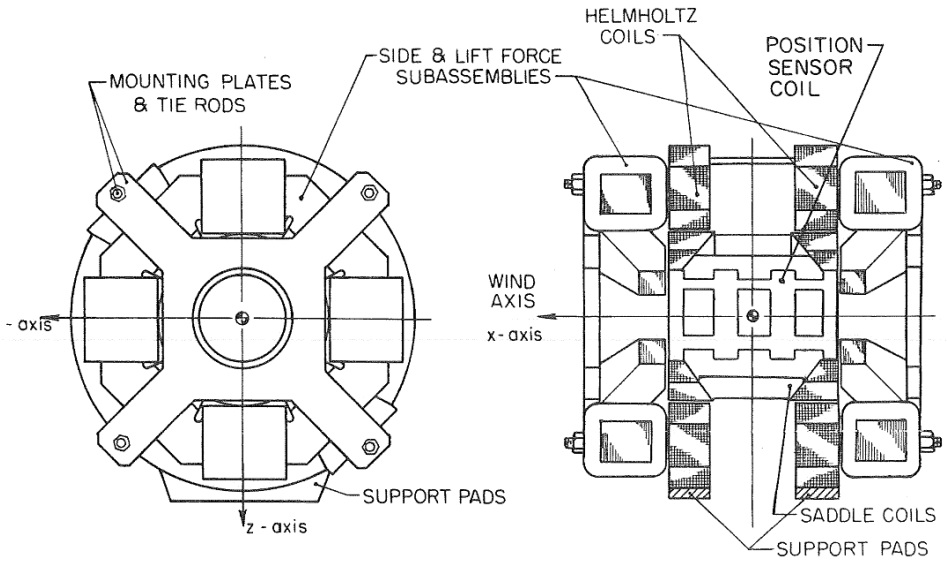

Figure 3: Electromagnetic coil and position sensor configuration for the 6-inch MSBS [4].

The recovery of aerodynamic forces during suspension is another problem with many solutions. During testing, the aerodynamic forces acting on a model are balanced with the electromagnetic forces produced by the MSBS coils. If the model is in equilibrium, and the electromagnetic forces are known, the aerodynamic forces can be determined [15]. The force

produced by an electromagnet is largely linearly related to coil current via a simple scaling constant. Traditionally, this constant is determined by suspending a model that is attached via string to a pulley and a weight hanger, as shown in Figure 4, and then successively adding more mass to the hanger. The pulley uses dual precision ball bearings and has an approximate moment of inertia of $1.86*10^{-6}$ kg*m^2. Figure 5 shows the assumed free-body diagram during calibration; tension is assumed to be equal to the weight of the string, hanger, and added masses. When applied forces and coil currents are known, a relationship may be determined, and the MSBS may be used in the same manner as a traditional force balance [15-17]. Larger models may facilitate the inclusion of an internal force balance between a suspended magnetic element and the surrounding aerodynamic shell. This force balance is powered by a battery and can either transmit the recovered signals or store data locally for later retrieval [13,18].

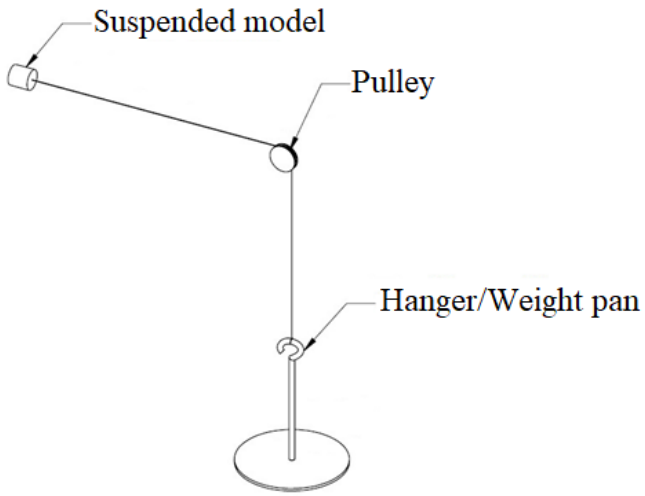

Figure 4: Electromagnetic drag force calibration via pulley and weights.

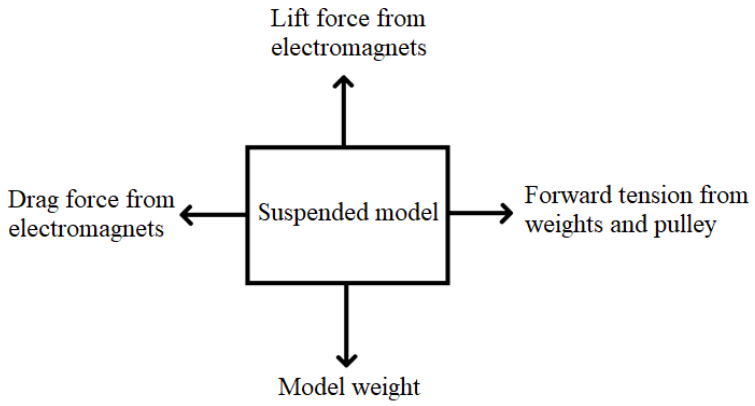

Figure 5: Basic 2D free-body diagram representative of drag force calibration.

There are several benefits to magnetic suspension wind tunnels, the primary of which is the complete removal of all physical supports and accompanying interference. Dynamic testing can be performed with larger ranges of motion than with a traditional dynamic test. Disadvantages can include limited access to the test section, facility cost, and a reduced dynamic pressure compared to a traditional support system.

1.2.4. Pressure Measurement and Corrections

Historical Dynamic Pressure Determination

Use of a pitot probe to determine test section dynamic pressure is usually not possible during model testing. The probe would interfere with the model and position sensor, and the model's wake would influence the pressure reading. To solve this problem, the following methodology was used by MIT to determine the dynamic pressure in the test section [19]. The flow is assumed to be steady, incompressible, and inviscid. Figure 6 represents the inlet of the wind tunnel. Location 1 represents a static tap in the settling chamber, location 2 represents a

static tap where the area is approximately one tenth of the area at location 1, and location T represents the test section.

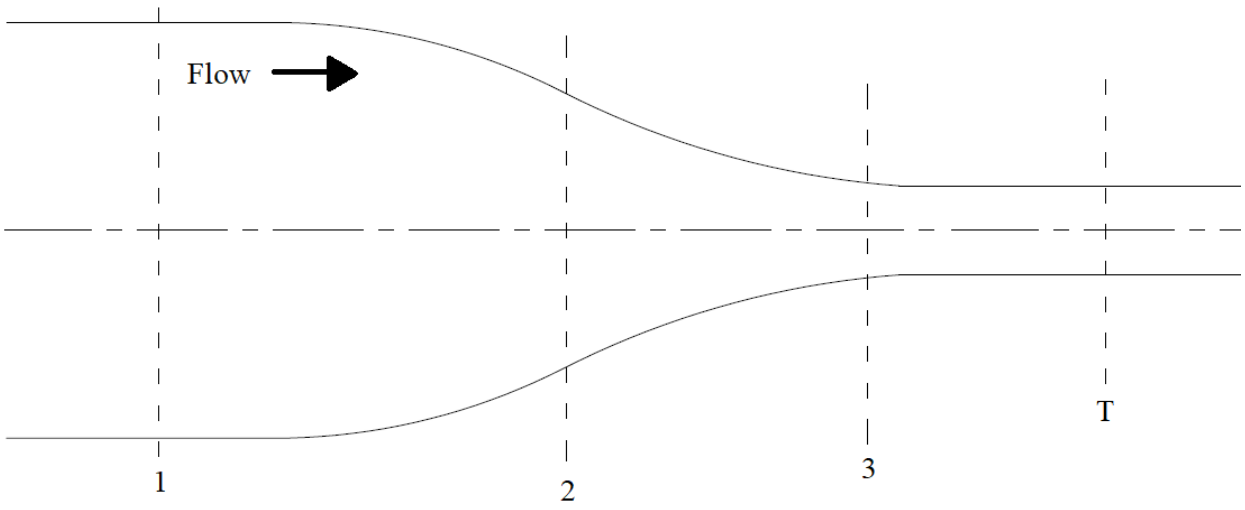

Figure 6: Representation of inlet static pressure locations.

Equation (11) begins with an application of a simplified form of the Bernoulli equation with an added error term. Equation (12) isolates the two measurements, P_1 and P_2.

$$P_1 + q_1 = P_2 - K_1 q_2 + q_2 \tag{11}$$

$$P_1 - P_2 = -K_1 q_2 + q_2 - q_1 \tag{12}$$

Equation (13) is a simplified form of the continuity equation for incompressible flow.

$$A_1 V_1 = A_2 V_2 \tag{13}$$

Square Equation (13) and multiply by one half of the air density to return Equation (14):

$$\frac{\rho}{2}{A_1}^2{V_1}^2 = \frac{\rho}{2}{A_2}^2{V_2}^2 \tag{14}$$

Substituting the definition of dynamic pressure, Equation (15), and a new constant ratio, Equation (16), into Equation (14) produces Equation (17), which relates the dynamic pressures at the two static tap locations.

$$q = \frac{\rho}{2}V^2 \tag{15}$$

$$K_2 = \frac{{A_2}^2}{{A_1}^2} \tag{16}$$

$$q_1 = K_2 q_2 \tag{17}$$

Equations (18) and (19) are produced by substituting Equation (17) into Equation (12) and simplifying. Now, q_2 must be related to q_T.

$$P_1 - P_2 = -K_1 q_2 + q_2 - K_2 q_2 \tag{18}$$

$$P_1 - P_2 = (1 - K_1 - K_2)\, q_2 \tag{19}$$

Following the same steps as before, a third constant is defined in Equation (22), and q_2 is related to q_T in Equation (23).

$$A_T V_T = A_2 V_2 \tag{20}$$

$$\frac{\rho}{2}{A_T}^2{V_T}^2 = \frac{\rho}{2}{A_2}^2{V_2}^2 \tag{21}$$

$$K_3 = \frac{{A_T}^2}{{A_2}^2} \tag{22}$$

$$q_2 = K_3 q_T \tag{23}$$

With a final substitution of Equation (23) into Equation (19), the test section dynamic pressure is related to the two static tap measurements in Equation (24). The three constants are combined

into a single linear regression variable and the value is determined experimentally, as shown in Equation (25) [19].

$$P_1 - P_2 = (1 - K_1 - K_2)\, K_3 q_T \tag{24}$$

$$\frac{q_T}{P_1 - P_2} = 7.93 \tag{25}$$

In the time between the original calibration and the experiments in this thesis, a third static pressure tap was added immediately before the test section at a location with approximately the same area as the test section. In this thesis, the differential pressure between pressure tap 1 and 3 was used to determine test section dynamic pressure and the above methodology was used to calibrate measurements. As described in Section 1.2.4, the addition of a constant bias term was necessary, in order to provide the best fit over the desired dynamic pressure range. Equation (26) is the determined linear regression that was used to determine $q_{interpolated}$ in this thesis.

$$q_{interpolated} = 0.9970(P_1 - P_3) + 7.0697 \tag{26}$$

Blockage Corrections

The cross-sectional area ratio between the models and the test section used in this thesis was approximately 0.074, which is near the maximum suggested value [8]. This means that, while there were significant boundary effects, they were within the range of correctability using standard formulae. In this thesis, solid blockage and wake blockage corrections were applied. Other corrections exist, such as for horizontal buoyancy, downwash, streamline curvature, and flow angularity, but these were disregarded as negligible.

Solid blockage is the result of a physical obstruction in the test section. A larger obstruction creates a larger blockage effect. The effect of a solid blockage is functionally similar

to fluid flow through a venturi. The blockage causes the air velocity, and thus dynamic pressure, to increase locally as flow passes around a test model. This results in under-reporting dynamic pressure and thus over-reporting coefficients that are normalized by dynamic pressure [8].

Wake blockage also causes flow to accelerate around a model and can result in an increase in measured drag. It is similar in effect to the displacement thickness of the test section boundary layer and functions as a displacement area. It is often modeled as a physical object equal in size to the wake. The effect depends on the size of the wake produced; this generally depends on model size and shape. Different shapes require different considerations; for example, appropriate corrections for an airfoil may involve induced drag and flap area, while a body of revolution may rely solely on area ratio and on measured drag.

Horizontal buoyancy is a result of a change in static pressure along the length of a wind tunnel due to thickening of the boundary layer. The effect is smaller on shorter bodies and when the test section has a downstream divergence [8]. Axial dynamic pressure variation was measured with nine static taps evenly spaced along the test section and was found to be approximately -22 Pa/m for the dynamic pressure range considered in this thesis [5]. Equation (27) is the approximate buoyancy correction for a spherical model [8]. For the models used in this thesis, the change in drag was approximately 0.0015 N (0.24% of the average drag forces experienced during testing) and was neglected.

$$\Delta Drag = -\frac{\pi}{4} {L_{model}}^3 \frac{dp}{dl} \tag{27}$$

Downwash corrections and other similar effects result in a change in effective angle of attack due to changes in flow direction around a lifting body. These corrections generally apply to lifting bodies and were disregarded as negligible for an axisymmetric blunt body, even while at an angle of attack, because the lift force was small.

A significant number of methodologies have arisen to correct for these effects, with ongoing research from the early 20th century to the present. In this thesis, the corrections for solid and wake blockages were taken from reference [8]. These equations were chosen due to applicability, availability of input data, and prior MSBS laboratory convention. Equations (28-31) describe the correction methodology. The solid blockage correction in Equation (28) is solely based on the geometric properties of the model and tunnel. The uncorrected drag coefficient is determined in Equation (29). The wake blockage correction in Equation (30) depends upon the area ratio and on the uncorrected coefficient of drag. Equation (31) is the correction from measured to true dynamic pressure. Equation (32) is a recalculation of the drag coefficient with the corrected dynamic pressure.

$$\varepsilon_{solid} = \lambda\tau \frac{V_{model}}{S_{tunnel}^{\frac{3}{2}}} \tag{28}$$

$$C_{du} = \frac{Drag}{q_{interpolated} S_{model}} \tag{29}$$

$$\varepsilon_{wake} = \frac{C_{du} S_{model}}{4 S_{tunnel}} \tag{30}$$

$$q_{test} = q_{interpolated}(1 + \varepsilon_{solid} + \varepsilon_{wake})^2 \tag{31}$$

$$C_d = \frac{Drag}{q_{test} S_{model}} \tag{32}$$

CHAPTER 2.
FACILITIES AND EQUIPMENT

2.1. Wind Tunnel

Figure 7 is an overall diagram of the wind tunnel used in this thesis [4]. The test section and the MSBS roughly encompass the area bounded by the dashed box.

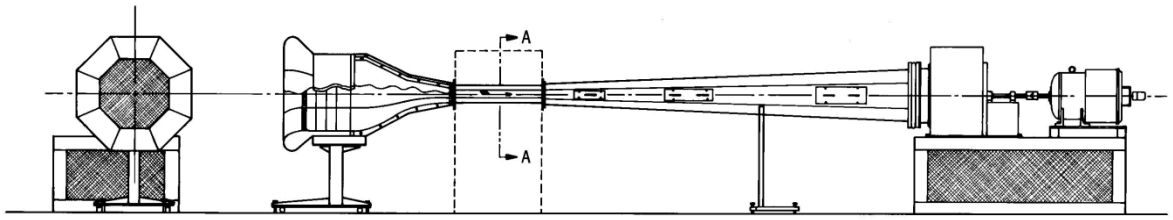

Figure 7: Wind tunnel configuration.

2.1.5. Inlet

The inlet is composed of a settling chamber and contraction cone. The contraction ratio of the cone is 20:1 and there are three screens in the settling chamber to reduce turbulence. The inlet is mounted on guiderails and slides forward to permit access to the test section. A foam-rubber gasket prevents leakage between the inlet and the test section. The inlet is clamped to the test section prior to testing to ensure a consistent seal. Three static pressure taps are installed along the side of the inlet. The first tap is in the settling chamber, the second is located where the cone area to test section area ratio is 2:1, and the third tap is near the end of the cone where the

area ratio is approximately 1:1. The pressure taps in the settling chamber and at the end of the inlet were used to determine the dynamic pressure in the test section.

2.1.6. Pressure Transducer

A Mensor CPT 6100 high precision pressure transducer was used to measure the differential pressure between static taps 1 and 2 on the inlet. Pressure was recorded at a rate of 2 Hz by vendor-supplied LabVIEW virtual instruments (VIs) which were embedded in the "Wind Tunnel Controller" VI. The pressure range of the sensor was 0 to 6900 Pa with a full-scale error limit of 0.010%. The pressure transducer was mounted vertically on the inlet to ensure that the tubing would not interfere with the opening of the test section.

A Scanivalve DSA3017 16-channel pressure scanner was used to correlate the dynamic pressure calculated using static taps 1 and 2 on the inlet, and the dynamic pressure determined via a traditional pitot probe. Both measurements were recorded simultaneously, with the same sensor, in order to isolate the effect of the tunnel geometry. The Scanivalve was also used to record the cavity pressure during the second set of dummy sting tests. The DSA 3017 recorded a differential pressure of up to +/- 2490 Pa (+/- 10" water) with a full-scale error of +/- 0.2%.

2.1.7. Test Section

A new test section was fabricated with 12.7 mm (1/4 in) thick clear acrylic sheets. It was approximately 914 mm (36 in) long and was octagonal in cross-section. It had an entrance width of 161.9 mm (6 3/8 in) between the flats, and there was a designed divergence of 3.2 mm (1/8 in) fore to aft. This divergence was included in the original wind tunnel design to account for boundary layer growth and to maintain a constant velocity over the entire length of the test section [5]. The aft end of the test section fit into an octagonal seat in the diffuser flange plate; a

foam-rubber gasket ensured that there would be no leakage between the test section and diffuser. The forward end was secured with friction created by tightening four lateral “stops.”

2.1.8. Diffuser

The diffuser was 3.785 m (149 in) long with a 5° wall-to-wall divergence. It had three access panels along its length so that lost models might be retrieved. The diffuser consisted of two pieces that could be separated in order to remove the diffuser without shifting the MSBS.

2.1.9. Fan

A Chicago Blower Corporation airfoil centrifugal fan with a diameter of 50.8 cm (20 in) provided the required pressure differential. The fan, fan motor, and motor drive were mounted on a steel platform. A steel wire mesh screen with an open area of 79% was secured immediately forward of the fan in order to protect both the fan and any lost models from damage. A flexible coupling directly connected the fan shaft to motor shaft.

2.1.10. Motor

The fan was driven by a Century E-plus 3 14.9 kW (20 HP) AC motor. This motor replaced the original DC motor. It had a maximum operating speed of 3535 RPM.

2.1.11. Controller

The AC motor was powered by a Cerus Industrial Titan S Series CL-020-S4 variable frequency motor drive. Fan speed was commanded via a remote voltage signal sent from a MCCDAQ USB-231 data acquisition device. The DAQ was controlled by a PC running the “Wind Tunnel Controller” LabVIEW VI.

2.1.12. Exit Duct

A square duct with multiple turning vanes routed air from the blower exit. The duct was designed to minimize pressure loss and to prevent the surging experienced in the original MIT installation, where air exhausted downwards.

2.1.13. Thermocouple

An Omega type J thermocouple and a UTC-USB thermocouple connector were used to measure ambient temperature. The thermocouple had a stated error of +/- 2.2 degrees Celsius. In addition, only whole numbers were reported by the thermocouple; with the inclusion of rounding error, total uncertainty was taken to be +/- 2.7 degrees Celsius. When this temperature range was propagated through to a final velocity or Reynolds number value, it created an uncertainty range of +/-0.51% for either value.

2.1.14. Pitot Probe

A United Sensor pitot-static probe, serial number USNH-a-157 9738, was used for recording dynamic pressure in the test section. It was 6.35 mm (0.25 in) in diameter and 254 mm (10 in) long (excluding the protruding tubes). The static tap was approximately 101.6 mm (4 in) from the tip of the probe. Brass tubes were fixed to the existing pressure tubes to extend the total length of the probe by 76.2 mm (3 in).

2.1.15. Camera

An Edgertronic SC1 high speed camera was used to capture images and video of aerodynamic tests. It was fixed to an external aluminum frame and was triggered remotely via ethernet. The camera could be configured to record only a subset of pixels, in order to reduce file

size, and it was configured to record only via the test section side window. It was also used in real time to monitor the test section during the dummy sting aerodynamic tests.

2.2. Magnetic Suspension and Balance System

2.2.1. Coil Configuration

The MSBS is an extensively decoupled system of magnetic coils, as previously shown in Figure 3. Each aerodynamic axis is controlled by a separate group of coils. The drag axis is controlled by a Helmholtz coil pair, shown in Figure 8, where two identical magnetic coils (referred to as drag coils) are used to produce a quasi-uniform magnetic field. The lift axis is controlled by four electromagnets (referred to as lift coils). The side axis is also controlled by four electromagnets (referred to as side coils). The lift and side coils, shown in Figure 9, work in concert to produce somewhat uniform magnetic fields over the length of the test section. The magnetization coils are co-wound with the drag coils and serve two purposes, depending on the type of core to be suspended. When suspending a ferrous element, these coils serve to magnetize it so that the forcing coils may more easily interact with it. When suspending a permanent magnet, these coils serve to orient the magnet, similarly to the way in which a compass orients to Earth's magnetic field. The magnetization coils are shown in Figure 8. Finally, the MSBS is equipped with saddle coils to control model attitude, but these coils were not operative during the tests presented in this thesis.

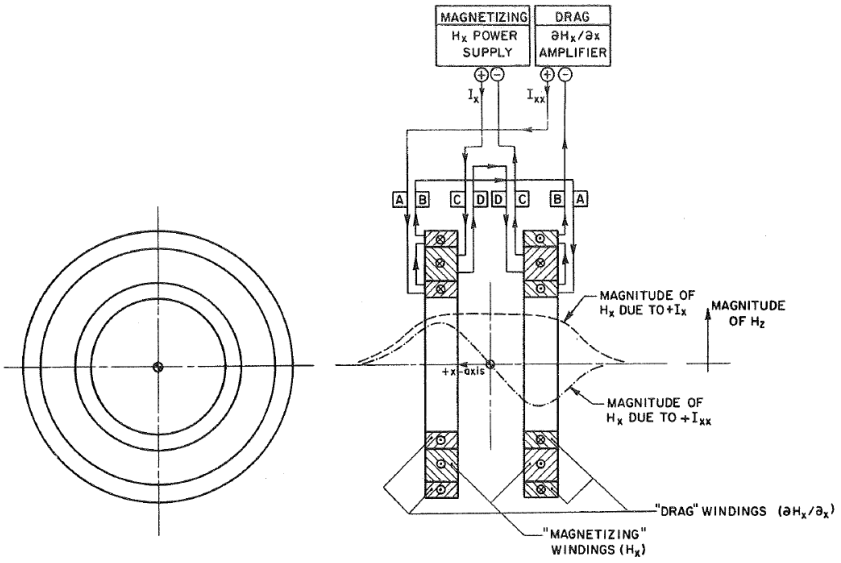

Figure 8: Drag and magnetization coil configuration [4].

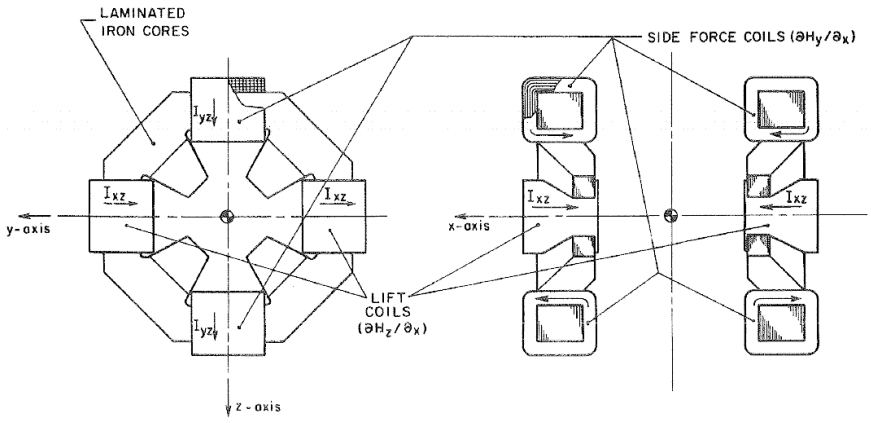

Figure 9: Lift and side coil configuration [4].

2.2.2. Electromagnetic Position Sensor System

The Electromagnetic Position Sensor System (EPS) is a set of copper windings that just surround the test section. Their inner diameter limits the test section size. The measured signal differential between the coils determines where the ferrous or permanent magnet core is located

in three-dimensional space. The analog voltages were demodulated and filtered before being digitized. Before they could be used as a state for the controller, the voltages must be correlated to a physical distance. This was done by traversing a core through a known distance and comparing the signal change in each axis. The system was zeroed by placing a core at the desired zero location and adjusting potentiometers so that the measured signal would reach a minimum point.

2.2.3. Cooling System

All of the magnetic coils on the MSBS use hollow square tube windings to allow for adequate cooling and are serviced by the primary cooling loop. Distilled water is circulated through the windings by an external heat exchanger. From the intake, water branches six ways. The two primary branches service the drag and the magnetization coils. The four secondary branches each cool two lift or side coils in series. Each winding layer receives cooling in parallel.

A secondary cooling loop was attached to the heat exchanger as a heatsink. A submerged pump circulated tap water from a 400 liter reservoir through a filter into the heat exchanger.

The coils are theoretically operable until 100 degrees Celsius, where boiling would cause inconsistent cooling and hot spots. Operation is typically ceased at 50 degrees Celsius to prevent any possible insulation degradation.

2.2.4. Power Amplifiers

Primary power was provided by a Magna-Power MS Series DC power supply. This power supply powered four Performance Controls Inc. GA 301 single axis precision gradient amplifiers. Each amplifier was capable of producing 300 volts with a continuous current of 60 amps. The drag coil was powered by two amplifiers in a parallel configuration. The lift and side coils were powered by a single amplifier each.

Secondary power was provided by two TDK-Lambda Genesys 250-60 DC power supplies in a master/slave (parallel) configuration. Each TDK was rated to 15 kW with an output of up to 250 V or 60 A. The TDKs powered the magnetization coil.

2.2.5. Data Acquisition

The primary data collected from the MSBS were the currents running through the four coils. Each of the four output cables from the power amplifiers ran through a separate DaniSense DS200ID 200-amp high precision current transducer. The transducers were flux gate sensors. From DC-10Hz, they exhibited a total accuracy of 22 PPM. They exhibited an error of +/- 0.01% from 10Hz-5kHz, +/- 1.00% from 5kHz-100kHz, and +/- 20% from 100kHz-1000kHz.

2.2.6. Controller

A Speedgoat 109100 performance real-time target machine ran a PID controller in a Simulink instance. The Simulink controller received state information from the EPS, current information from the DaniSense, one coil temperature from a type J thermocouple, and dynamic pressure from the “Wind Tunnel Controller” VI. The Speedgoat recorded this data at a rate of 1kHz. The controller also estimated the current states, based on past inputs, in order to increase responsiveness. A separate controller mode and gain table were used for each core material, which could then be switched between different stiffnesses. In this context, stiffness refers to the relative cost weighting given to control response and model position, and generally results in changes in proportional gain. A stiffer controller would use larger control inputs in order to minimize model motion (a higher ‘spring stiffness’). All levitated tests in this thesis were completed with the stiffest controller mode for magnetic cores, in order to best replicate a static test condition.

The Speedgoat was interfaced via a physical switchboard and through MATLAB commands from a host PC over ethernet. The front switch panel initialized the amplifiers, set the controller mode, started and stopped levitation, applied offsets to the EPS signals to allow for manual model positioning, and commanded data collection. The MATLAB functions were required to pull data from the Speedgoat logs and could also be used to command data collection and to control the wind tunnel speed. Figure 10 is a schematic of the various pieces of equipment used in operation of the MSBS.

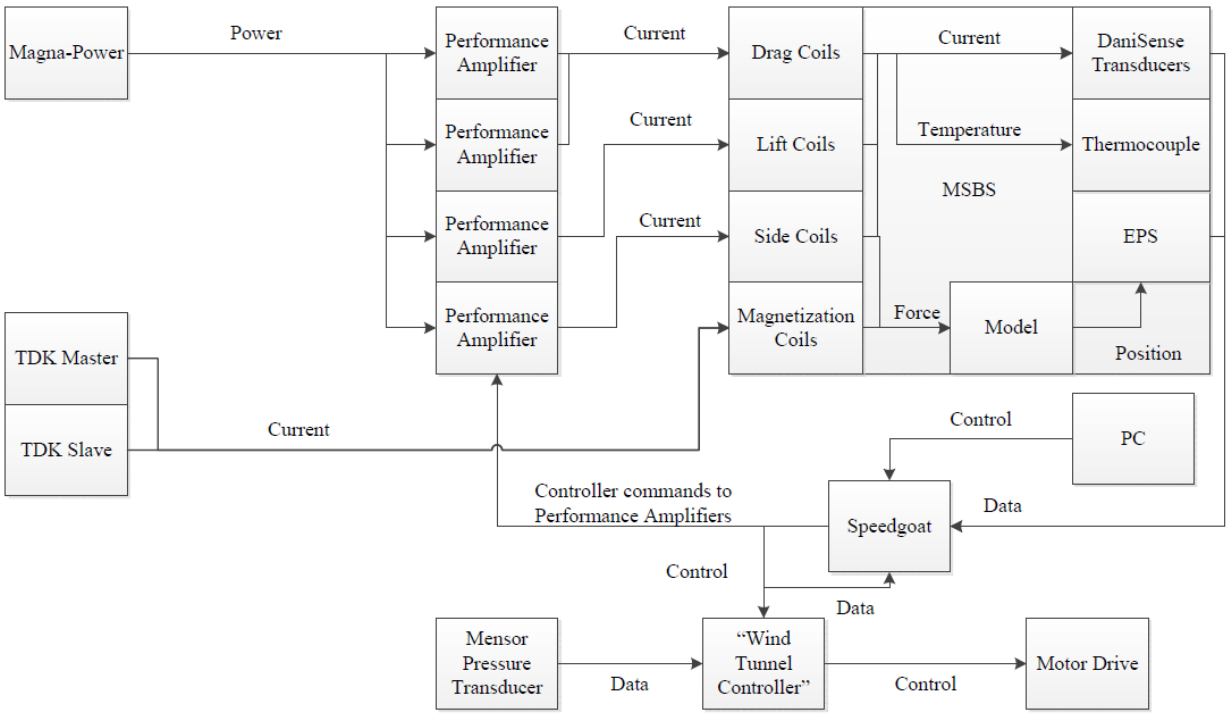

Figure 10: Schematic of MSBS configuration.

2.3. MS - 100 6-Component Strain-Gage balance

The MS-100 is an aluminum 6-component strain-gage force balance that was constructed in the mid-1980s. The balance uses 5000 ohm strain gage bridges. It was initially calibrated in 1985 and was last inspected in 2016 [20]. The balance was recalibrated for this project, as described in Section 3.2.2. An outline drawing of the MS-100 is included in Appendix A.2.

2.3.1. Data Acquisition

A NI cDAQ-9172 was used, in concert with two NI 9211 I/O modules, to record the output signal from each strain gauge and the supply voltage. The NI 9211s have a measurement range of +/- 80mV with a resolution of 24 bits. The NI 9211 is designed for use with thermocouples, but it has the required range and the sensitivity to capture the strain gauge outputs. The documentation for these devices list temperature error referenced to the type of thermocouple attached. As such, it was appropriate to determine the total error of the balance and DAQ through experimental measurements of known loads. This is discussed in Section 3.2.

2.3.2. Power Supply

A Datel Systems UMC-5/250 single output power supply provided continuous 5V source voltage to power to the balance. To account for any drift, the source voltage was measured by the NI-DAQ through a voltage divider where the recorded voltage was 0.010175914 multiplied by the true voltage. This ratio was determined by comparing the recorded source voltage and the true source voltage as measured by a digital multi-meter. The error inherent in this value was captured in the total error term developed in Section 3.2.

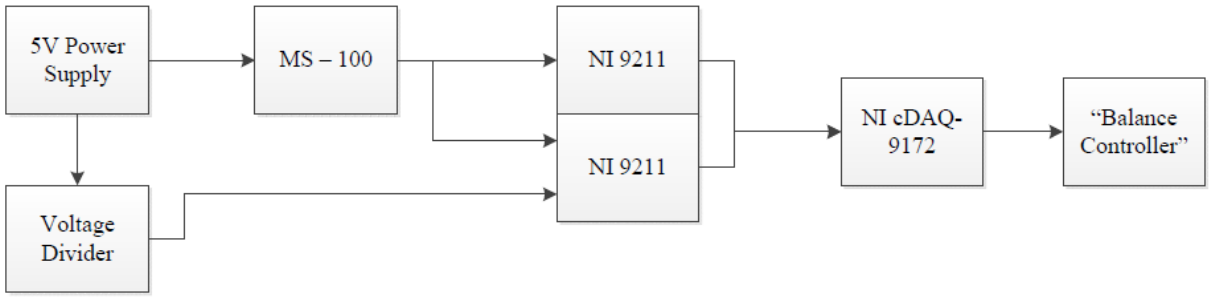

Figure 11: Schematic of MS-100 operation.

2.4. Sting

It was necessary to fabricate a nonmagnetic sting to support the balance. The balance drawings and an existing steel sting were referenced to design the new sting. To facilitate ease of construction, the traditional key and keyway alignment mechanism was replaced. Instead, a pair of set screws were machined to size in order to slot into the keyseat on the MS-100. The sting was machined out of aluminum. The sting was hollow, and a threaded rod was inserted into the aft end. This rod attached to a support strut. A brass tube was slid over the sting and MS-100 to shield it from accidental contact. Aluminum standoffs were used to vary the axial position of the model in the test section. Drawings of components are included in Appendix A. Figure 12 shows the sting as configured during testing.

Figure 12: Sting with MS-100, brass sleeve, threaded rod, and standoff installed.

2.5. Dummy Sting

The second phase of testing involved magnetically suspending models with sting interference. The newly manufactured sting and MS-100 could not be used in this test. It was highly likely that the sting and the balance would be impacted by the models through incidental contact during alignment or by loss of control during the tests. In addition, the EPS reports the centroid location of all metallic mass in the test section; a large aluminum rod in the test section would render levitation impossible with the available controllers.

Instead, two dummy stings were fabricated out of nonmetallic materials. The first dummy sting was turned down from a single phenolic resin rod to match the outer dimensions of the full sting and MS-100 assembly. It had an overall length of 438 mm (17.25 in) and the tip sat just aft of the test section center. As with the aluminum sting, a threaded rod was inserted into the aft end of the dummy sting to attach to a support strut.

With experience from the first dummy sting, a second composite dummy sting was designed and fabricated. This dummy sting was constructed with a fiberglass rod and a phenolic resin sleeve. A pressure tap was installed in the tip of the dummy sting to measure cavity pressure. Drawings of both dummy stings are in Appendix A. Figure 13 shows the forward end of the composite dummy sting and the cavity pressure tap.

Figure 13: Second dummy sting with cavity pressure tap.

2.6. Wind Tunnel Extension

The MSBS was not designed to support conventional wind tunnel tests; therefore, there was no location available to install a mount for the sting. A 63.5 mm (3.5 in) long octagonal test section extension was designed to support a vertical strut that the sting would screw into. The extension had a guideway for the vertical strut. The component parts were machined out of aluminum. The extension was then assembled and installed between the MSBS and the diffuser. Drawings of the components and the assembly are in Appendix A.4.

2.7. Vertical Support Strut

The vertical support strut was a compromise between flow interference, structural strength, and machinability. The most important consideration was minimizing flexure of the support, so it was designed to be thicker than would be necessary to support the expected static loads. A traditional airfoil shape was rejected, in favor of simple shapes and flat faces to facilitate ease of machining. The support is an irregular hexagonal prism with a width of 12.7 mm (0.5 in), a length of 76.2 mm (3 in), and a height of 168.275 mm (6.625 in) was machined out of aluminum. When the strut is installed, a 6.35 mm (0.25 in) hole runs axially along the centerline of the wind tunnel. The threaded rod at the end of each sting slid into this hole and was secured with a nut. The support structure is aft of the test section in order to minimize its impact on the flow characteristics of the test section. The extension and the strut were in place for all tests to ensure that all tests would be consistently influenced by any downstream obstruction. The drawing of the support is in Appendix A.4. Figure 14 shows the support strut and wind tunnel extension as installed during testing. Figure 15 is an example assembly of the tunnel extension, sting, balance, and model, as configured during sting supported testing.

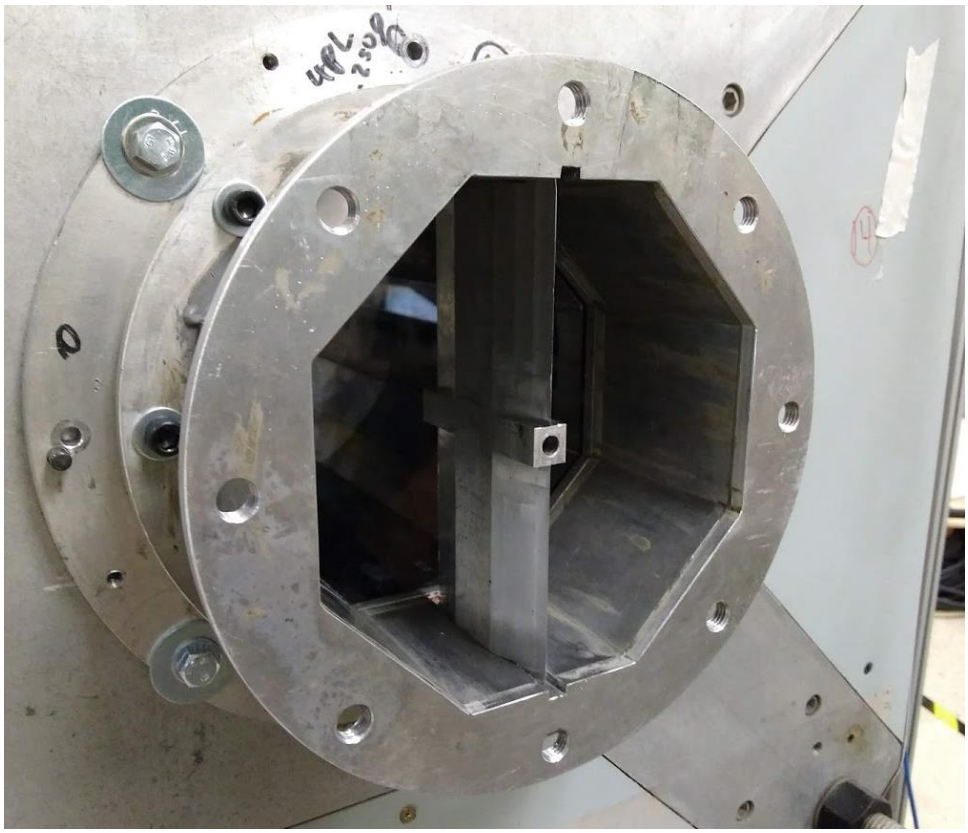

Figure 14: Wind tunnel extension and vertical support strut affixed to the aft-end of the MSBS.

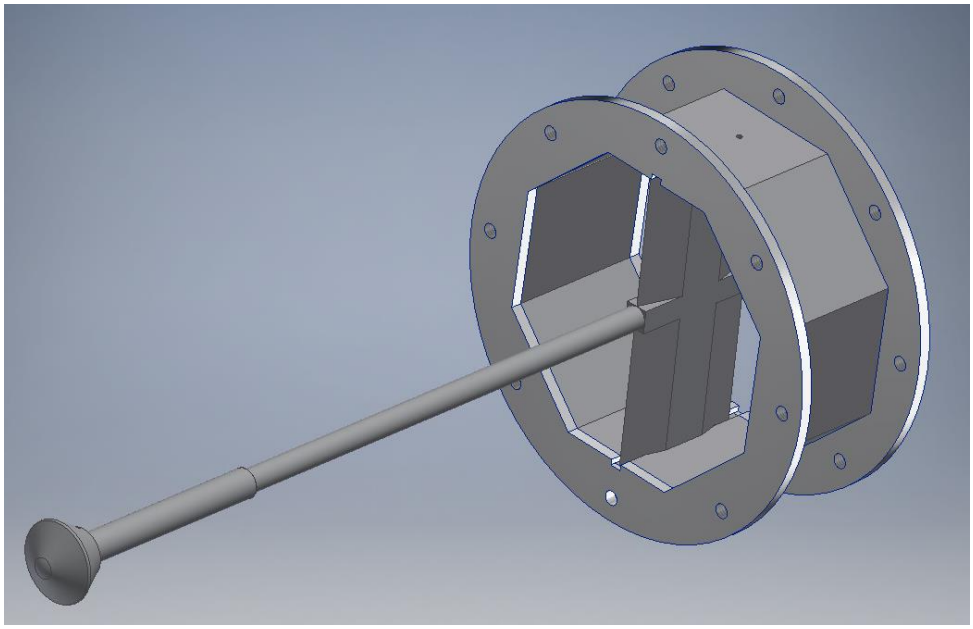

Figure 15: Assembly of extension, strut, sting, MS-100, sleeve, and model.

2.8. Magnetic Element

A permanent magnet core, rather than an iron core, was chosen for use in this thesis, for two reasons. The use of a pre-magnetized core significantly reduced the required axial current. This significantly reduced heat generation and increased total allowable suspension time. The pre-magnetized core also exhibited extremely strong pitch and yaw stiffness. This allowed the core to be oriented inside of a model, so that the model could be suspended at a consistent angle of attack.

A cylindrical 19.05 mm by 19.05 mm (0.75 in by 0.75 in) Neodymium-Iron-Boron magnet was inserted into the dummy sting and magnetically suspended models. The mass of the magnet was 40.85 g. The same magnet was used in all tests, including force calibration. This was to ensure that the magnetic moment of the core would remain constant throughout all of the tests.

2.9. Models

As previously mentioned, the models tested were of the same geometry as the Stardust sample return capsule. They were 3D printed with a nominal maximum diameter of 44.45 mm (1.75 in) and a nominal height of 28.37 mm (1.117 in). Exact model diameters are shown in Appendix A.6. In this thesis, the models are referred to by their angle of attack and support method.

2.9.1. Sting Supported

The sting supported models were single piece 3D prints. They were designed with a cavity to match the end of the MS-100. They were secured to the MS-100 via a dowel pin. The models were rotated about their centroid in order to mount them at the desired angle of attack. The models are shown in Figure 16. Drawings of the models are in Appendix A.7.

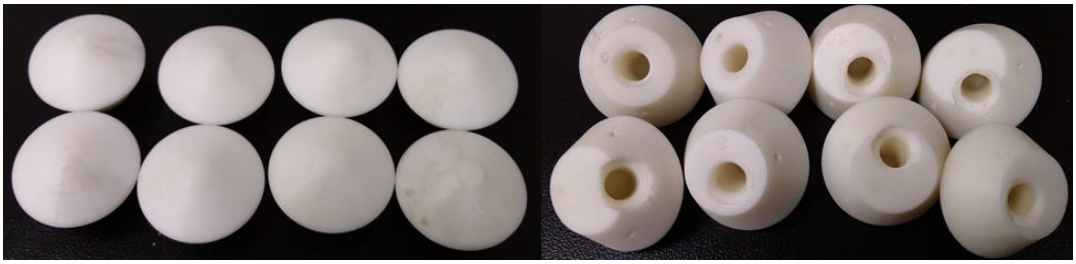

Figure 16: Fore and aft views of the sting supported models.

2.9.2. Models for use with the Dummy Stings

The models for testing with the dummy sting were also single-piece. They were designed to accept the 19.05 mm x 19.05 mm (0.75 in x 0.75 in) cylindrical magnetic core. The model has a single open cavity that extends from the back face into the model, approximately 19.05 mm in diameter and 23.7 mm in depth. The core was inserted into the cavity, and the remaining space was used to dock the model on the dummy sting. The cavity was rotated about the centroid of the model to reach the desired angle of attack. The models are shown in Figure 17. Drawings of each model are in Appendix A.8.

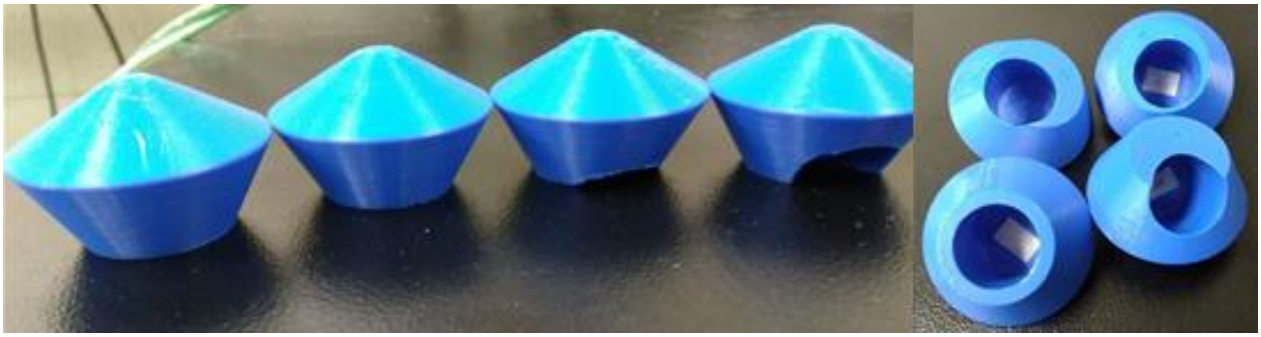

Figure 17: Fore and aft views of dummy sting models.

2.9.3. Magnetically Suspended

The magnetically suspended models were designed and printed in two pieces. The geometry was divided at the centroid, orthogonally to the model centerline. The magnetic core was inserted into the hollow center of the front piece, and the back piece was pressed onto the protruding core. The halves were secured together with double-sided tape. The models are shown in Figure 18. Drawings of all pieces are in Appendix A.9.

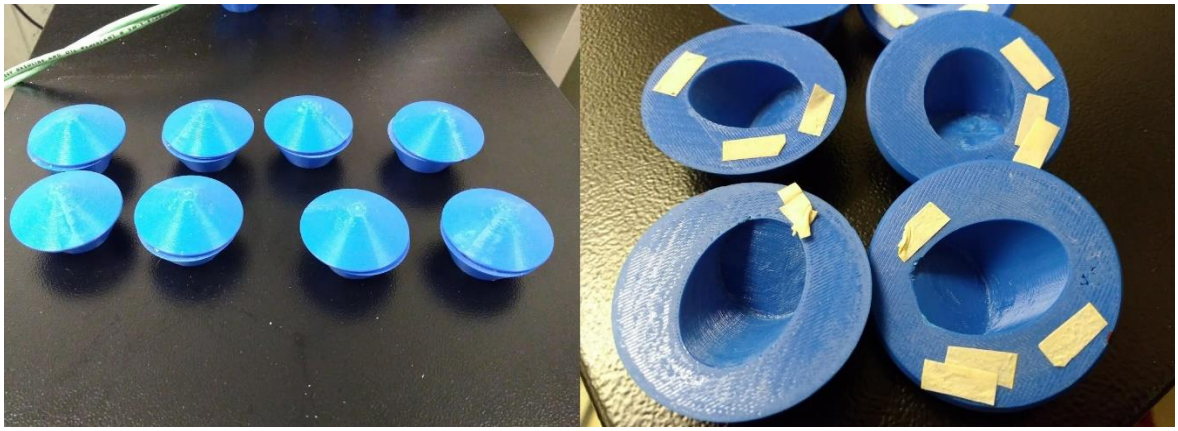

Figure 18: External and internal views of the magnetically suspended models.

2.9.4. Print Defects and Surface Discrepancies

After printing, the models had lines of extra material running axially along the outer and inner surfaces. It was determined that these lines were the locations of the transitions between print layers. A file was used to remove these lines from the models. Care was taken to ensure that only the excess material was removed, and that the surface finish of the model was not substantially altered.

The surface finish was not the same on all models. The sting supported models were printed with a layer height of 0.127 mm, and the models with magnetic cores were printed with a layer height of 0.178 mm. The models with magnetic cores could not be printed at the smaller layer height because they were damaging the print bed. Due to constraints on time and cost, the sting supported tests were not repeated with new models. Instead, two additional sting supported tests were completed for zero angle of attack orientation. One model was printed by an external service with a layer height of 0.200 mm; the other model was printed by NASA with an approximate layer height of 0.033 mm as a calibration print for a new selective laser sintering (SLS) 3D printer. The effects of layer height on aerodynamic data are examined in Section 2.9.4.

CHAPTER 3.
CALIBRATION

A comprehensive characterization of the MSBS and of accompanying instruments was not attempted in this thesis for two reasons. The basic functionality of the wind tunnel had not yet been verified, and so the level of examination presented in this thesis was sufficient to identify hardware, software, or experimental methods that were in need of improvement. Furthermore, the final configuration of the MSBS was not fixed. After the necessary data was collected for this thesis, the coil configuration was altered to explore further avenues of model alignment. This involved alternate configurations such as producing lift force with the drag coils, which would invalidate the characterization of the lift coils producing lift force, and so forth. After a final configuration is chosen, a complete characterization of the tunnel and MSBS will be performed.

3.1. Dynamic Pressure Calibration

3.1.1. Methodology

A pitot-static probe was inserted into the vertical support strut where it was secured in place. Due to the mounting constraints and probe length, the tip was approximately 15 cm behind the center of the test section and the static tap was approximately 30 cm behind the center of the test section. This was considered an acceptable location because the test section was designed to maintain a constant dynamic pressure throughout its length. For the pressure ranges considered in this thesis, the dynamic pressure variation between the entrance and the exit of the test section was less than 1% [5].

This test required simultaneous measurement of four pressures. The Mensor CPT 6100 transducer was not used because it was only equipped with two pressure ports. Instead, the

Scanivalve DSA 3017, with 16 pressure ports, was used to simultaneously measure the pressures from the pitot probe and inlet static taps. The only variable was the aerodynamic source of the dynamic pressure measurements.

Prior to the test, the Scanivalve was powered and left to reach a steady-state operational temperature, and the inlet was clamped to the MSBS to ensure that the seal, and any tunnel leakage, would remain constant between calibration and model testing.

Vendor-supplied LabVIEW VIs were used to control the Scanivalve, and the "Wind Tunnel Controller" VI was used to control fan speed. The Scanivalve was zeroed, and a data set was collected at zero velocity. The tunnel was stepped through seven fan speeds, and a data set was collected at each speed once the dynamic pressure reached a steady value. After the tunnel was powered down, a second zero point was collected. Between 80 and 100 individual measurements were taken for each fan setting.

3.1.2. Results and Data Reduction

The Scanivalve appended all samples into a spreadsheet. Each sample consisted of an identifier, the pressure at each of the 16 ports in psi, and the temperature of each transducer. A MATLAB script (located in Appendix B.5) was written, to extract and manipulate the data of interest. Table 1 contains the mean dynamic pressure and standard deviation at each tunnel speed. The table also includes the percent error, according to Equation 33, taking the mean pitot dynamic pressure as the true value.

Figure 19 is a graph of the discrepancy between the probe and the inlet pressures for each individual sample represented as a percent error relative to the pitot probe pressure. The two sources of dynamic pressure are almost equivalent, with the inlet slightly under-reporting for the range of interest. The dynamic pressure range of interest for this thesis was between 150 and

1400 Pa. At dynamic pressures below this range, sensor noise and other errors became a significant portion of the signal. At dynamic pressures higher than this range, the magnetically suspended models could not be controlled, and so there are no data points to compare.

$$Percent\ Error = \frac{Experimental\ Value - True\ Value}{True\ Value} * 100\% \quad (33)$$

Table 1: Comparison of dynamic pressures derived from pitot probe and inlet differential.

Pitot Probe		Inlet Differential		Mean Pressure
Mean Q (Pa)	StDev (Pa)	Mean Q (Pa)	StDev (Pa)	Discrepancy (Pa)
0.133	0.138	0.241	0.165	0.108
37.189	0.198	36.276	0.200	-0.914
170.706	0.668	165.684	0.579	-5.022
410.994	1.516	402.574	1.731	-8.421
755.212	3.496	751.325	3.829	-3.888
1208.561	5.314	1204.821	5.297	-3.740
1756.946	6.345	1755.204	6.656	-1.743
2403.900	10.758	2408.142	11.144	4.241

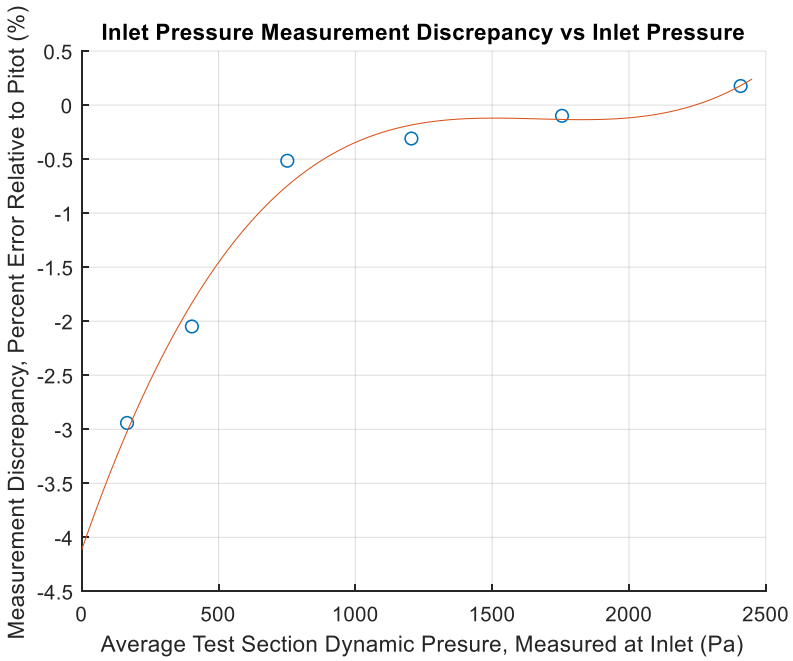

Figure 19: Discrepancy between pressure measurements over range of dynamic pressures.

A calibration constant or equation was necessary to reduce the systematic error at lower dynamic pressures. A scaling constant k was determined in accordance with the methodology presented in Section 1.2.4. This was functionally equivalent to a linear regression with a zero y-intercept. It was apparent that a constant scale factor simply shifted the error to different locations.

For this thesis, a linear regression with non-zero offset was chosen, in order to prevent adding any non-existent behavior between the data points. To focus the linearization on the area of interest, only data points between 150 and 1800 Pa were used. Unless otherwise stated, all of the pressure data in this thesis were corrected according to the regression shown in Equation (34), where P_1-P_3 is the raw pressure data. Figure 20 shows the chosen linear regression as compared to raw experimental data. Figure 21 shows the new error distribution after the data has been corrected. All data points within the range of interest fell between +/- 1.5% error. When averaged, the random error was removed, and the systematic error fell between +/-1% error. After correction, the root mean square error over the range of interest was 1.6647 Pa.

$$q_{interpolated} = 0.9970(P_1 - P_3) + 7.0697 \quad (34)$$

Table 2: Comparison of error generated by linear regression.

	Mean Tunnel Dynamic Pressure (Pa)						
Tunnel Dynamic Pressure (from pitot)	37.19	170.71	410.99	755.21	1208.56	1756.95	2403.90
	Mean Percent Error (%)						
Uncorrected Data	-2.45492	-2.94151	-2.04890	-0.51489	-0.30942	-0.09923	0.17641
Linear Regression	16.26782	0.91354	-0.61784	0.12761	-0.01869	0.00830	0.17483

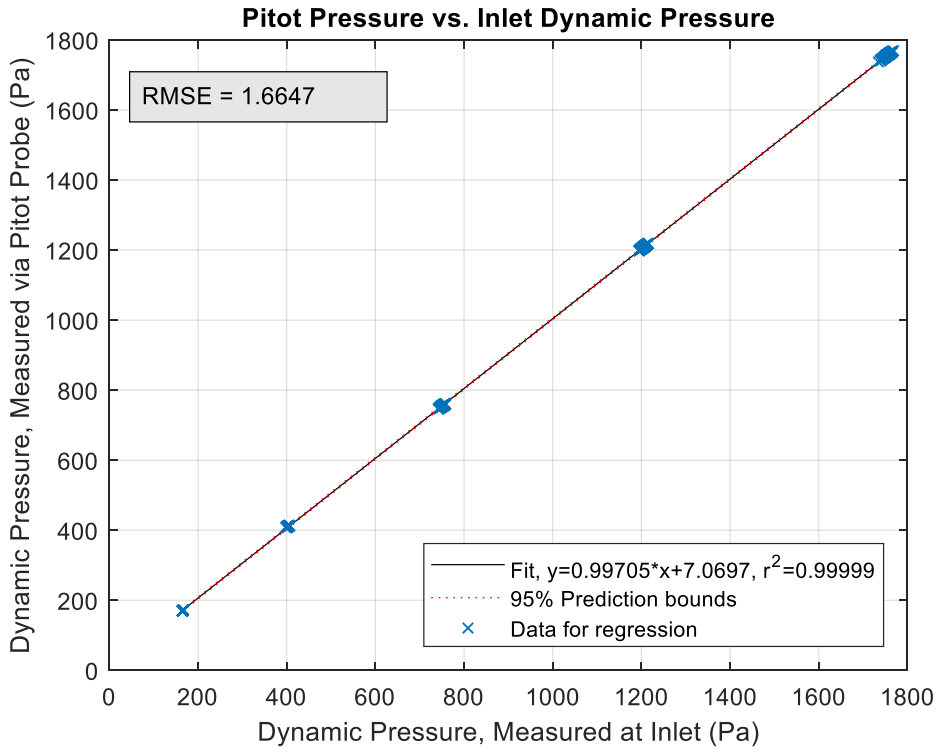

Figure 20: Pressure correction compared to experimental values.

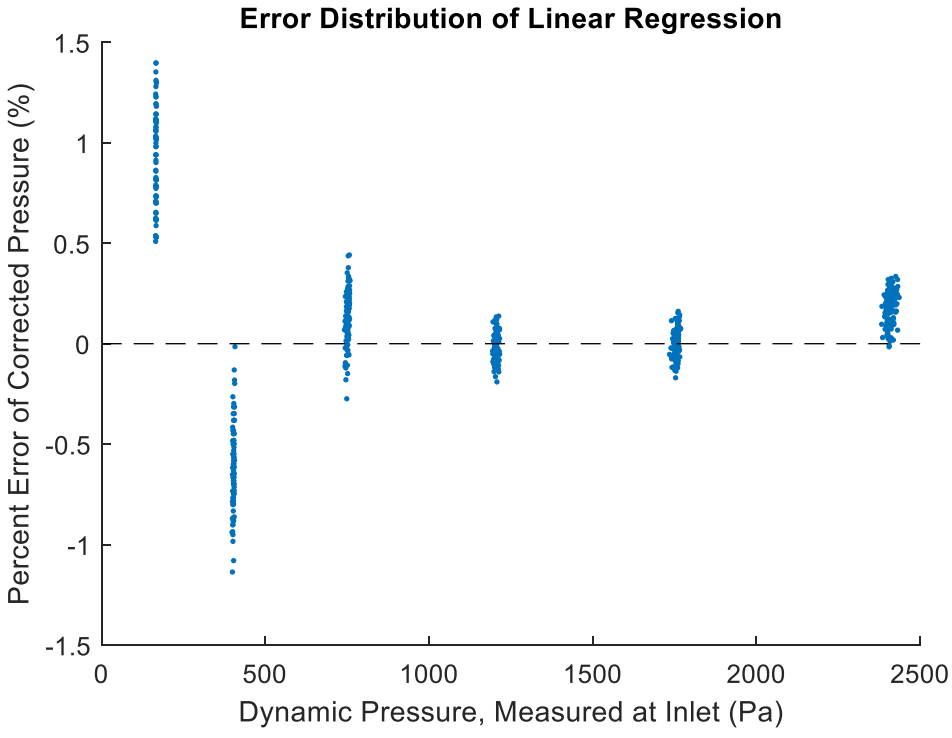

Figure 21: Error distribution of pressure correction.

3.2. MS-100 Balance and Software Tests

3.2.1. Methodology

Prior to performing any measurements, it was necessary to determine the electrical zeros of the balance setup. The electrical zeroes are, theoretically, the output voltages of the strain gauges under zero load in zero gravity. In practice, the electrical zeroes are the average of two measurements chosen to simulate these conditions. One measurement is recorded with gravity acting along the positive axial direction, the other is recorded with gravity acting along the negative axial direction. The electrical zeroes measured in this manner are specific to the test setup; the values will be different if a different DAQ, with different null offsets, is used. In order to compare the measured values to reference values, the electrical zeroes of the balance must be separated from the offsets of the DAQ. As such, an additional zero measurement was recorded with the balance installed, but unpowered and unloaded. Three measurements were taken and averaged for each configuration.

In order to verify that the MS-100 and the reduction software would be able to produce the correct loading conditions, a check loads test was performed. The balance was secured in three different orientations: gravity acting along the negative direction of the axial channel, gravity acting along the positive direction of the normal channel, and gravity acting along the positive direction of the side channel. The three loading configurations allowed for calibration of axial force, normal force, side force, pitching moment, and yawing moment. In addition, with gravity acting along the positive normal channel, an 80 mm moment arm was used to apply an offset load, which caused a known rolling moment.

In each orientation, the balance was zeroed, and a data point was recorded at zero load. Twenty samples were recorded and averaged by the “Balance Controller” VI at each data point.

Using a mass and hanger set, item number ME-8979, six different masses were suspended by string at the balance dowel pin hole. Due to moment arm flexure, only three different masses were used to test the roll channel. The models were not expected to produce any appreciable rolling moment, so the three loading cases were sufficient for software verification. The true mass of the hanger and each brass cylinder were recorded with a separate scale to account for any manufacturing defects.

3.2.2. Results and Data Reduction

Electrical Zeroes

In order to confirm the validity of the wiring and of the calculated zeroes, the zero of the balance was isolated from the zero of the DAQ. The null offset of the DAQ was subtracted from the powered measurements prior to normalization. Across all channels, the offset was approximately 0.266 mV. The measurements were then normalized and averaged. Table 3 compares the calculated electrical zeroes to reference measurements [20]. The reference measurements were normalized, assuming a nominal 5 V source voltage. The calculated values largely agree with the reference values; the balance was wired correctly and was in working order. Any error in these electrical zeroes was captured by the balance and software calibration. The combined electrical zeroes of the MS-100 and DAQ were determined by normalizing the powered measurements without removing the null-offset of the DAQ. These values are shown in Table 4 and were utilized in this thesis to tare the signal voltage prior to balance reduction.

Table 3: Comparison of electrical zeroes to reference values.

Component	Source of Electrical Zeroes		
	Experimental Values	2016 Inspection	1998 Inspection
Normal (mV/V)	2.46425E-01	2.45200E-01	2.42000E-01
Axial (mV/V)	-9.73701E-02	-9.84000E-02	-8.66000E-02
Pitch (mV/V)	3.20008E-01	3.17800E-01	3.25000E-01
Roll (mV/V)	1.79755E-01	1.80600E-01	1.81200E-01
Side (mV/V)	3.70508E-01	3.69800E-01	3.75200E-01
Yaw (mV/V)	-1.61501E-01	-1.60200E-01	-1.60200E-01

Table 4: Combined electrical zeroes of DAQ and MS-100.

Normal (mV/V)	Axial (mV/V)	Pitch (mV/V)	Roll (mV/V)	Side (mV/V)	Yaw (mV/V)
0.299301512	-0.044560128	0.373019414	0.232742971	0.423863518	-0.108458815

Axial Channel

During this test, the balance was oriented so that gravity would act forward along the axial channel. The tare reading, in mV/V, was input into balance reduction software to convert it into forces and moments. The samples were normalized by the source voltage and were averaged. The mean signal and the tare were input into the balance reduction software. The combined magnitude of the calculated forces was compared to the magnitude of the known load, rather than to the force along the axial channel, in order to account for any errors in balance orientation. This comparison is shown in Table 5. Error is within +/-0.0072 N for the considered loading range.

Table 5: Axial channel check loads.

Mass (g)	Applied Force (N)	Measured Force (N)	Load error (N)
0.00	0.000E+00	2.906E-03	2.906E-03
4.96	4.864E-02	4.619E-02	-2.448E-03
55.17	5.410E-01	5.374E-01	-3.612E-03
105.24	1.032E+00	1.029E+00	-2.851E-03
155.36	1.524E+00	1.524E+00	3.456E-04
255.54	2.506E+00	2.505E+00	-5.226E-04
355.73	3.489E+00	3.496E+00	7.158E-03

Normal Force and Pitching Moment Channels

During this test, the balance was oriented so that gravity acted along the positive lift axis. The tare reading, in mV/V, was input into balance reduction software to convert it into forces and moments. The samples were normalized by the source voltage and were averaged. The mean signal and the tare were input into the balance reduction software. The combined magnitude of the calculated forces was compared to the magnitude of the known applied load, rather than to the force along the lift channel, in order to account for any errors in balance orientation. The measured force and applied force are compared in Table 6. The value of the applied force was simply the weight of the mass added. The error was within +/- 0.012 N for the considered loading range.

Table 6: Normal channel check loads.

Mass (g)	Applied Force (N)	Measured Force (N)	Load Error (N)
0.00	0.000E+00	5.034E-03	4.930E-03
4.96	4.864E-02	5.075E-02	2.397E-03
55.17	5.410E-01	5.420E-01	1.184E-03
105.24	1.032E+00	1.035E+00	2.781E-03
155.36	1.524E+00	1.532E+00	9.185E-03
255.54	2.506E+00	2.515E+00	9.333E-03
355.73	3.489E+00	3.500E+00	1.172E-02

Two comparisons were necessary for the pitching moment channel. The first was performed without a moment center correction, in order to ensure that the sensor measurement was correctly measuring the applied load. The measured pitching moment was compared to the theoretically applied pitching moment, as calculated by Equation 35. These values are shown in Table 7 The error was within +/- 0.00046 Nm for the considered loading range.

The second comparison was necessary because, during aerodynamic testing, the lift generated by the model would not act through the balance's moment center and would influence the pitching moment value. Therefore, it was necessary to perform a moment transfer correction and to remove the effect of lift on the pitching moment measurement. To ensure proper moment transfer, the methodology was verified during calibration. In this check loads test, the distance between the MS-100 moment center and the location of the applied load was 41.76 mm. The moment caused by the applied load was removed from the measurement according to Equation (36). The corrected pitching moment is also shown in Table 7. After correction, the measured moment was functionally zero, confirming the validity of the correction.

$$M_{applied} = mass * 0.0417576 * g \tag{35}$$

$$M = M_{measured} - Lift_{measured} * 0.0417576 \tag{36}$$

Table 7: Pitching moment channel check loads.

Mass (g)	Applied Moment (Nm)	Measured Moment (Nm)	Load Error (Nm)	Corrected Moment (Nm)
0.00	0.000E+00	-1.496E-05	-1.496E-05	1.733E-04
4.96	2.031E-03	2.156E-03	1.249E-04	6.766E-05
55.17	2.259E-02	2.268E-02	8.777E-05	8.977E-05
105.24	4.310E-02	4.323E-02	1.340E-04	7.823E-05
155.36	6.362E-02	6.402E-02	3.997E-04	7.830E-05
255.54	1.046E-01	1.051E-01	4.558E-04	1.844E-04
355.73	1.457E-01	1.461E-01	4.278E-04	-1.651E-06

Side Force and Yawing Moment Channels

During this test, the balance was oriented so that gravity would act along the positive side axis. The tare reading, in mV/V, was input into balance reduction software to convert it into forces and moments. The samples were normalized by the source voltage and were averaged. The mean signal and the tare were input into the balance reduction software. The combined magnitude of the calculated forces was compared to the magnitude of the known applied load, rather than to the force along the side channel, in order to account for any errors in balance orientation. The value of the applied force was simply the weight of the mass added. The measured force and the applied force are compared in Table 8. The error was within +/- 0.01 N for the considered loading range.

Table 8: Side channel check loads.

Mass (g)	Applied Force (N)	Measured Force (N)	Load Error (N)
0.00	0.000E+00	2.449E-03	2.449E-03
4.96	4.864E-02	5.192E-02	3.281E-03
55.17	5.410E-01	5.416E-01	5.553E-04
105.24	1.032E+00	1.036E+00	4.415E-03
155.36	1.524E+00	1.528E+00	4.059E-03
255.54	2.506E+00	2.513E+00	7.378E-03
355.73	3.489E+00	3.499E+00	1.006E-02

Just as with the pitching moment channel, the yawing moment channel also required two separate verifications. The first examined the measured value, and the second confirmed the validity of the moment transfer correction. Table 9 compares the measured moment to the known moment, which was calculated according to Equation 37. The error was within +/- 0.00026 Nm for the considered loading range.

$$M_{applied} = mass * 0.0417576 * g \quad (37)$$

As with the pitch channel, the MS-100 also reported the yawing moment as calculated around its moment center. It was necessary to perform a moment transfer correction and remove the effect of side force on the yawing moment measurement during aerodynamic tests due to model placement. To ensure proper moment transfer, the methodology was verified during calibration. In this check loads test, the distance between the MS-100 moment center and the location of the applied load was 41.76 mm. The moment caused by the applied load was removed from the measurement, according to Equation 38. The corrected pitching moment is also shown in Table 9. After correction, the measured moment was functionally zero, confirming the validity of the correction.

$$M = M_{measured} - Side_{measured} * 0.0417576 \quad (38)$$

Table 9: Yawing moment channel check loads.

Mass (g)	Applied Moment (Nm)	Measured Moment (Nm)	Load Error (Nm)	Corrected Moment (Nm)
0.00	0.000E+00	3.702E-05	3.70E-05	-9.909E-05
4.96	2.031E-03	2.094E-03	6.29E-05	-1.173E-04
55.17	2.259E-02	2.254E-02	-5.22E-05	-1.042E-04
105.24	4.310E-02	4.321E-02	1.14E-04	-8.177E-05
155.36	6.362E-02	6.370E-02	7.97E-05	-7.822E-05
255.54	1.046E-01	1.049E-01	2.56E-04	-4.531E-05
355.73	1.457E-01	1.459E-01	2.28E-04	-1.395E-04

Rolling Moment Channel

During this test, the balance was oriented so that gravity would be acting along the positive side axis. The load was applied to induce a negative rolling moment. The tare reading, in mV/V, was input into balance reduction software in order to convert it into forces and moments.

The samples were normalized by the source voltage and were averaged. The mean signal and the tare were input into the balance reduction software. To verify the loading condition, both side force and rolling moment were examined.

The combined magnitude of all of the measured forces was compared to the magnitude of the known applied load, rather than to the force along the side channel, in order to account for any errors in balance orientation. The value of the known applied force was simply the weight of the mass added. The measured force and applied force are compared in Table 10. The error was within +/- 0.0023 N for the considered loading range.

Table 10: Applied load verification during rolling moment channel check load.

Mass (g)	Applied Force (N)	Measured Force (N)	Load Error (N)
0.00	0.000E+00	1.574E-03	1.574E-03
4.96	4.864E-02	5.000E-02	1.364E-03
55.17	5.410E-01	5.433E-01	2.264E-03
105.24	1.032E+00	1.033E+00	1.399E-03

In this test, the load was applied with a moment arm of 80mm. Table 11 compares the measured moment to the applied moment, which was calculated according to Equation 39. The error was within +/- 0.001 Nm. The measurement error on this channel was higher than that of prior moment channels. This was most probably due to an error in moment arm measurement. Regardless of the source, the higher error was acceptable because the tested models were axially symmetric and produced negligible rolling moment.

$$Mapplied = mass * 0.08 * g \tag{39}$$

Table 11: Rolling moment channel check load.

Mass (g)	Applied Moment (Nm)	Measured Moment (Nm)	Percent error (%)
0.00	0.000E+00	6.911E-05	6.911E-05
4.96	-3.892E-03	-3.622E-03	2.697E-04
55.17	-4.329E-02	-4.111E-02	2.181E-03
105.24	-8.257E-02	-8.157E-02	1.001E-03

Sensor Uncertainty

The test loading results showed that the balance and the software were configured properly. The balance and the software recovered the test load with low error, and there was no unexpected coupling. However, the performed tests did not constitute a full balance calibration and, therefore, did not fully capture sensor uncertainty. The 1985 MS-100 calibration file has a stated 0.5% full scale error range on all channels. The absolute be the full-scale error multiplied by the full-scale output. Table 12 shows the absolute uncertainty present on each channel.

Table 12: MS-100 measurement uncertainty on each channel, 1985 calibration.

Normal (N)	Axial (N)	Pitch (Nm)	Roll (Nm)	Yaw (Nm)	Side (N)
+/- 3.34E-01	+/-1.11E-01	+/-8.48E-03	+/-5.65E-03	+/-5.65E-03	+/-1.11E-01

During later uncertainty analysis, as discussed in Section 4.5.1, it was found that these uncertainties caused extremely large error bars. The MS-100 was re-calibrated by NASA. Figure 22 shows the balance as configured for one combination of loads. The new calibration produced significantly smaller error bars. The check loads were calculated with the 1985 calibration, while aerodynamic data used the new calibration. A comparison of the two calibration shows that they produced forces and moments that were within 0.5% of each other. Table 13 shows the new uncertainty ranges.

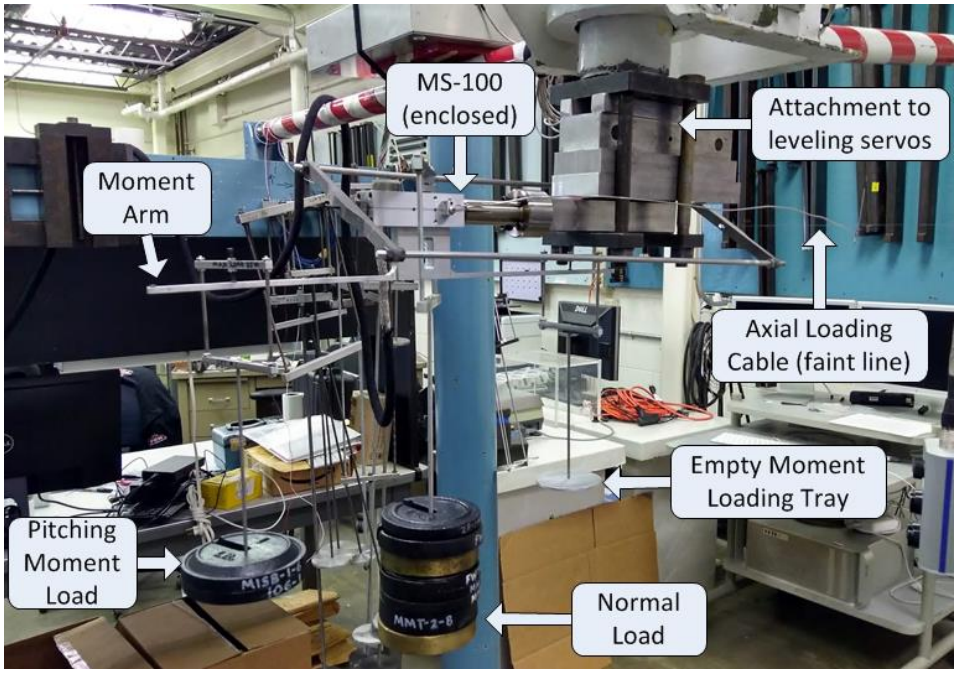

Figure 22: Calibration Setup for Combined Normal, Axial, and Pitch loading.

Table 13: MS-100 measurement uncertainty on each channel, 2019 calibration.

Normal (N)	Axial (N)	Pitch (Nm)	Roll (Nm)	Yaw (Nm)	Side (N)
+/- 2.67E-02	+/-2.56E-02	+/-1.95E-03	+/-1.47E-03	+/-6.22E-04	+/-2.89E-02

3.3. Magnetic Balance Force Calibration

3.3.1. Methodology

To ensure that the MSBS was functioning properly during the aerodynamic tests, it was necessary to recalculate the calibration constants that correlate coil current and generated force. These take the form of Newtons/Amp scaling constants. The values determined from a previous calibration are shown in Table 14.

Table 14: Reference calibration constants.

k_d (N/A)	k_s (N/A)	k_l (N/A)
0.037889	0.028653	0.028653

To correlate the recorded magnetic currents to the applied magnetic forces, several known loads were applied to the suspended magnetic core. To apply drag and side forces, a string was tied to the magnetic element. A pulley was used to suspend the PLASCO hanger and masses from the string. To apply lift forces, different masses of plastic were attached to the element prior to suspension. Eight different drag forces, seven different side forces, and three different lift forces were applied.

For the drag and side force calibration tests, the magnet was inserted into the test section resting on the launch platform. The string was threaded over the pulley and the hanger was added. The magnet was then suspended and the launch platform was removed. The pulley stand and the magnet were maneuvered to ensure that the string would be as level as possible and would not be in contact with the test section. Masses were then added to the hanger, and the controller was allowed to reach a steady state before data collection. The magnetic currents were recorded at 1kHz for 10 seconds for each applied load. Figure 23 is a picture of the pulley configuration during the drag loading test. Figure 24 is a picture of the suspended permanent magnet under applied load during the drag loading test.

For the lift tests, the plastic mass was attached to the magnet prior to insertion into the test section. The magnet and mass were suspended. The magnetic currents were allowed to reach a steady state, and then were recorded at 1kHz for 10 seconds. The launch platform was reinserted into the test section, and the magnet and mass were dropped. The magnet was then removed from the test section, and the attached mass was changed.

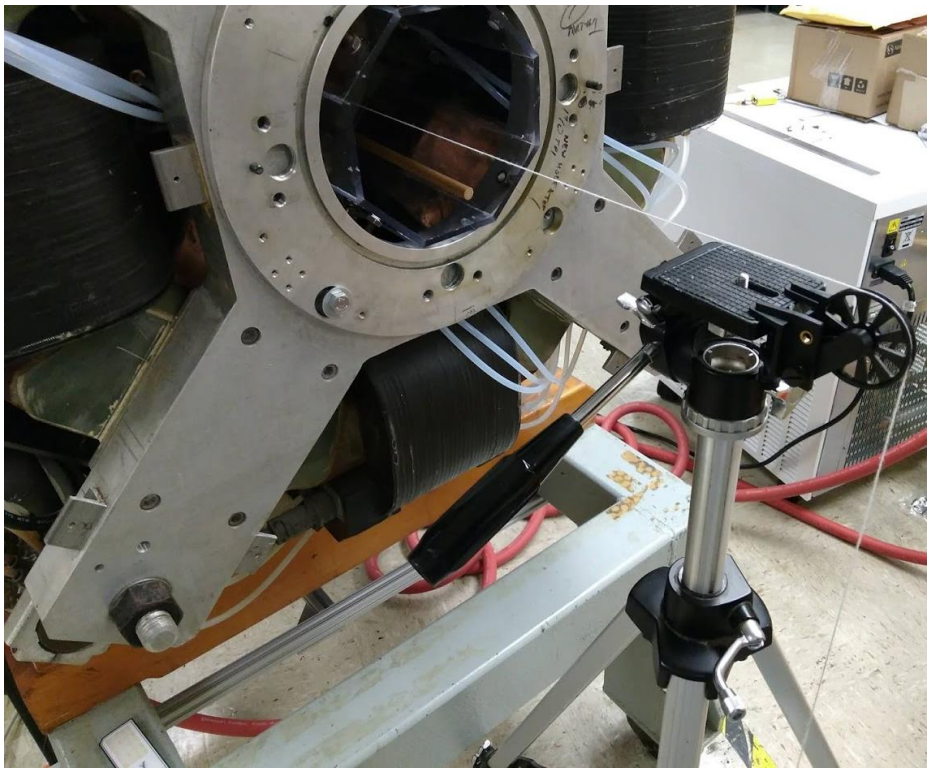

Figure 23:Pulley configuration during drag loading test.

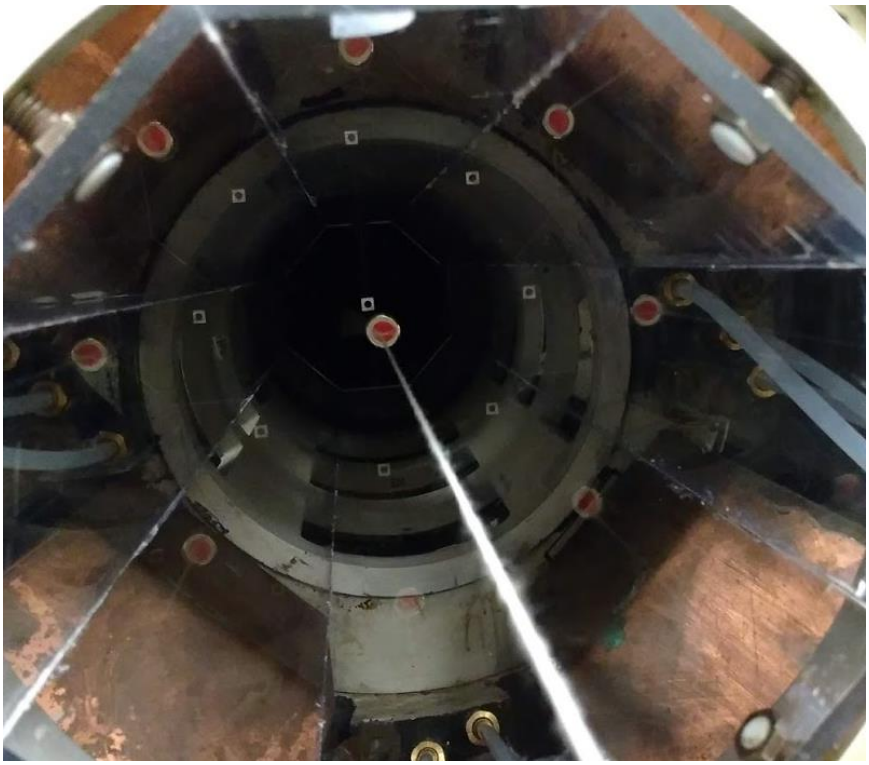

Figure 24:Permanent magnet core under applied load during drag loading test.

3.3.2. Results and Data Reduction

In accordance with reference documents presented in Section 1.2.3, it was assumed that each component was largely decoupled, and that generated force was linearly related to coil current. Any off-axis response during the loading tests was therefore assumed to be an error in loading directionality (pulley misalignment). The 5g loading case was taken to be the zero point for the drag and side loading tests. For the lift loading test, the bare magnet suspension case (40.85g) was taken to be the zero point. The lift coils were assumed to be equivalent to the side coils due to symmetry. The lift loading test was used as confirmation of this assumption.

The alignment imperfection was estimated for the drag loading test, in order to determine the best data reduction method. There was no measurable misalignment in the drag-side plane. There was some misalignment in the drag-lift plane. The misalignment angle was estimated via Equation (40), using the reference calibration constants as shown in Table 14. The pulley was misaligned in the drag-lift plane by approximately 0.8°; however, the effect on the drag loading calculations was neglected, due to small angle assumptions.

$$\gamma = \tan^{-1}\left(\frac{k_l L_{current}}{k_d D_{current}}\right) \tag{40}$$

With negligible misalignment, the drag calibration constant could be determined directly via a linear regression between applied force and drag current. Four data points were used to generate the fit. Three data points were used to check the fit. The calculated k_d value was 0.03792 N/A, and the drag force would be calculated from the drag current via Equation (41). Figure 25 is a comparison of the drag force as calculated via Equation (41) to the known experimental loading data. Table 15 shows the values determined from Equation (41) and compares them to the experimental data. The error was within +/- 0.00365 N for the considered loading range. The three data points with stated upper and lower prediction bounds were used to

check the drag force fit. The data points fall within the 95% prediction interval of the fit. The root mean square error of the fit was 0.0023 N. This was taken to be the systematic error.

$$Drag = 0.03792 * D_{current} \tag{41}$$

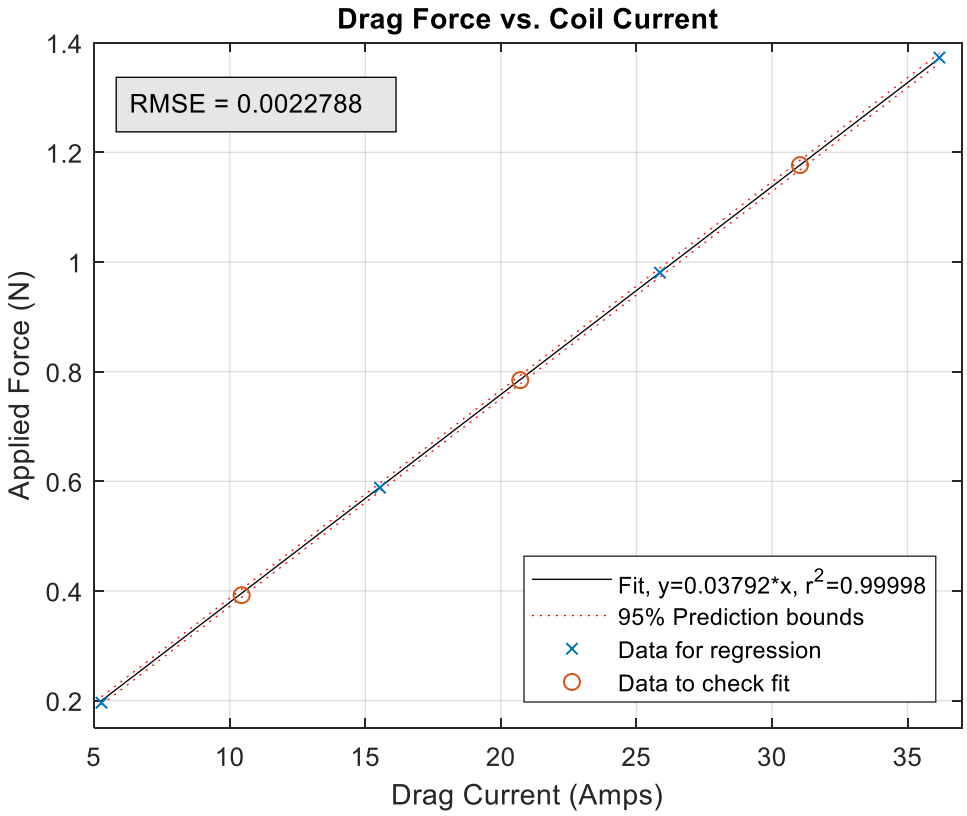

Figure 25: Comparison of drag force regression to experimental data.

Table 15: Comparison of measured load to known load for the drag force loading test.

Applied Drag Force (N)	Measured Drag Force (N)	Load Error (N)	Lower Prediction Bound (N)	Upper Prediction Bound (N
0.19613	0.19978	0.00365		
0.39226	0.39590	0.00364	0.388473	0.403325
0.58839	0.58933	0.00094		
0.78452	0.78546	0.00094	0.777554	0.793383
0.98065	0.98091	0.00026		
1.17678	1.17674	-0.00004	1.168083	1.185419
1.37291	1.37176	-0.00115		

The alignment imperfection was determined for the side loading test. The pulley was misaligned in the side-lift plane by approximately 0.82°, and the effect on side loading was neglected due to small angle assumptions. The misalignment in the drag-side plane was variable, from about 0.8 to 3.7°, depending on the loading condition. This misalignment also fell within the range of acceptable small angle approximations and was neglected.

The side calibration constant could be determined directly via a linear regression between applied force and side current. The calculated k_s value was 0.028904 N/A, and side force would be calculated from side current via Equation (42). Table 17 shows the values determined from Equation (42) and compares them to the experimental data. Figure 26 is a comparison of the side force as calculated via Equation (42) to the known experimental loading data. The error was within +/- 0.0141 N for the considered loading range. This higher error was acceptable because side force was not examined in the magnetically suspended tests. The root mean square error of the fit was 0.00447 N. The three data points with upper and lower prediction bounds were used to check the side force fit. The data points fit fall within the 95% prediction interval of the fit.

$$Side = 0.028904 * S_{current} \quad (42)$$

Table 17: Comparison of calculated load to known load for the side force loading test.

Applied Side Force (N)	Measured Side Force (N)	Load Error (N)	Lower Prediction Bound (N)	Upper Prediction Bound
0.19613	0.19364	-0.00249		
0.39226	0.38789	-0.00437	0.36762	0.40814
0.58839	0.58363	-0.00476		
0.78452	0.78148	-0.00304	0.75830	0.80463
0.98065	0.98398	0.00333		
1.17678	1.19088	0.01410	1.16333	1.21840

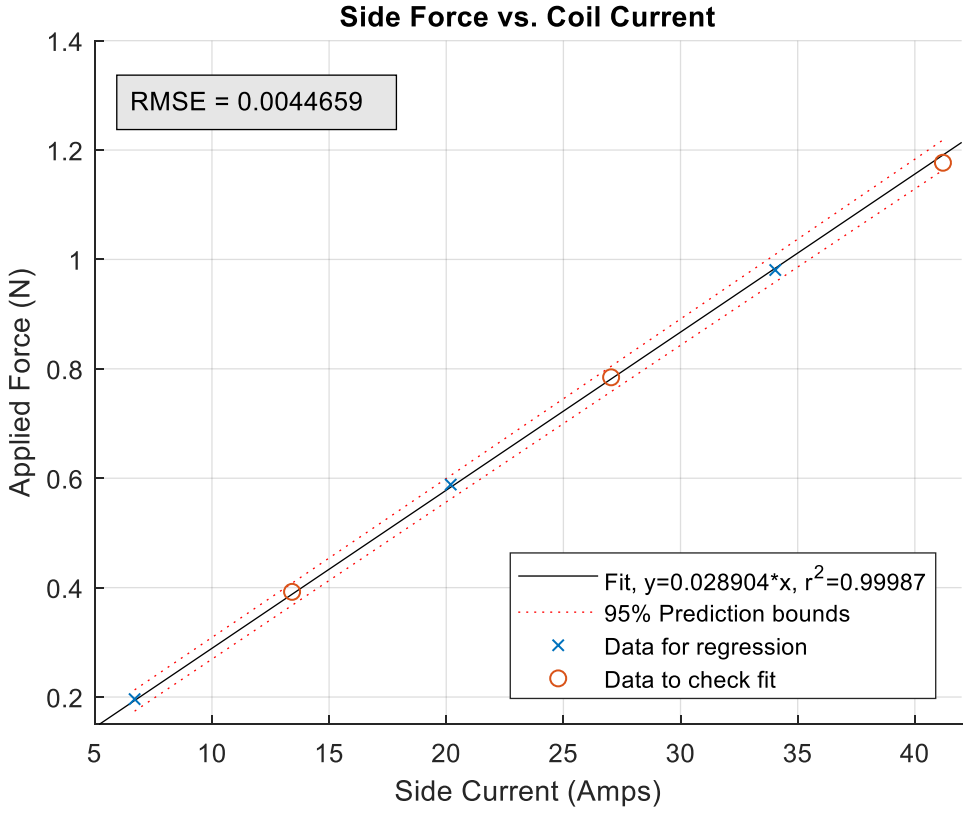

Figure 26: Comparison of side force regression to experimental data.

For the lift loading test, the misalignment of applied loads would theoretically be due to the misalignment of the MSBS to world coordinates. There was no measurable misalignment in the lift-side plane. The misalignment in the lift-drag plane varied between 0 and 5.8°, with an average misalignment of 3.08°. This higher variability was likely due to how the test was performed; each lift data point was a separate suspension, whereas the drag and side tests were performed with a single continuous suspension across the measurements. When the model was removed and reinserted during the lift tests, it was likely suspended at slightly different locations with slightly different interactions.

The lift calibration constant, $k_{l,}$ was assumed to be 0.028904 N/A. Lift force would be calculated from the lift current via Equation (43). Figure 27 is a comparison of the lift force as calculated via Equation (43) to the known experimental loading data. Table 16 shows the values determined from Equation (43) and compares them to the experimental data. The error was within +/- 0.027 N for the considered loading range. The root mean squared error of the fit was 0.0096 N. The majority of points fell within the 95% prediction interval of the fit. The largest load was not within the prediction interval. This is an acceptable fit because the lift current during aerodynamic testing did not exceed 14 amps and because the lift force was not examined during the magnetically suspended tests. Further lift coil characterization should be performed with more granular application of force.

$$Lift = 0.028904 * L_{current} \tag{43}$$

Table 16: Comparison of calculated load to known load for the lift loading test.

Applied Lift Force (N)	Measured Lift Force (N)	Load Error (N)	Lower Prediction Bound (N)	Upper Prediction Bound (N)
0.10777	0.10887	0.00110	0.08957	0.12817
0.10866	0.11038	0.00172	0.09107	0.12968
0.10895	0.10937	0.00042	0.09007	0.12867
0.10934	0.10968	0.00033	0.09037	0.12898
0.10797	0.10782	-0.00015	0.08852	0.12711
0.10562	0.10625	0.00064	0.08696	0.12555
0.10611	0.10659	0.00048	0.08729	0.12588
0.09532	0.09240	-0.00292	0.07313	0.11168
0.08914	0.08848	-0.00066	0.06921	0.10775
0.17662	0.17953	0.00292	0.16009	0.19897
0.36068	0.37952	0.01884	0.35930	0.39973
0.53642	0.56339	0.02697	0.54202	0.58474

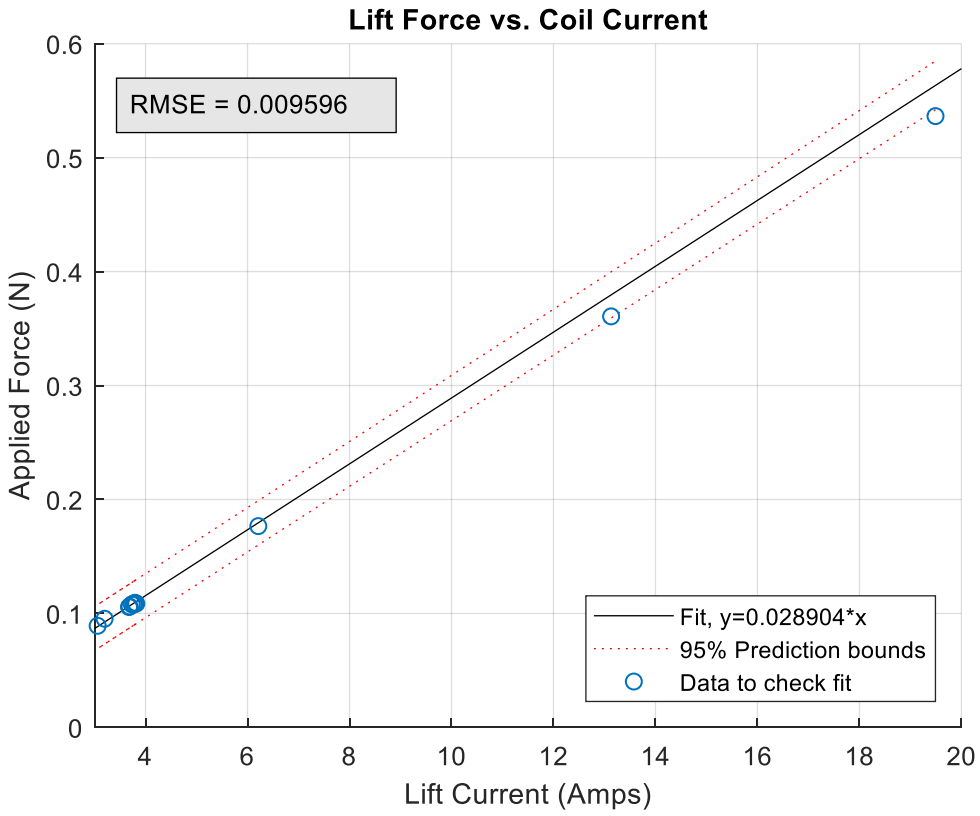

Figure 27: Comparison of lift force regression to experimental data.

To verify the assumptions of linear and decoupled magnetic forces, a final comparison was made. The magnitude of the applied load was compared to the combined magnitude of the three calculated magnetic forces for each loading condition, as calculated via Equation (44). This was to ensure that these assumptions were not adversely affecting the total magnitude of measured force. This comparison is shown in Table 17.

$$|F| = \sqrt{D^2 + L^2 + S^2} \tag{44}$$

Table 17: Comparison of magnetic force magnitude to the magnitude of applied load.

	Magnetic Force Magnitude (N)	Applied Load (N)	Load Error (N)
Drag Loading Test	0.199713	0.19613	0.003583
	0.395746	0.39226	0.003486
	0.58915	0.58839	0.00076
	0.785214	0.78452	0.000694
	0.98059	0.98065	-6E-05
	1.176331	1.17678	-0.00045
	1.371298	1.37291	-0.00161
Side Loading Test	0.192974	0.19613	-0.00316
	0.386617	0.39226	-0.00564
	0.581886	0.58839	-0.0065
	0.779416	0.78452	-0.0051
	0.981836	0.98065	0.001186
	1.189198	1.17678	0.012418
Lift Loading Test	0.085169	0.089141	-0.00397
	0.088871	0.095319	-0.00645
	0.102021	0.105616	-0.0036
	0.102354	0.106106	-0.00375
	0.104645	0.107773	-0.00313
	0.103558	0.10797	-0.00441
	0.105963	0.108656	-0.00269
	0.105023	0.10895	-0.00393
	0.105309	0.109342	-0.00403
	0.172769	0.176615	-0.00385
	0.366069	0.360683	0.005386
	0.543544	0.536416	0.007128

Finally, the determined calibration constants were compared to the reference constants as a ratio of Netwons/Amp. This is shown in Table 18. The experimental calibration and the reference calibration placed primary importance on the drag constant; the repeatability of calibration supports its validity. The side constant largely remained the same; any discrepancy here likely resulted from loading misalignment. The lift constant showed the largest change between the two calibrations. The reference calibration assumed symmetry between the lift and side coils and did not perform a separate test on the lift channel, so this change was not unexpected.

Table 18: Comparison to experimental calibration constants to reference constants.

	k_d (N/A)	k_s (N/A)	k_l (N/A)
Reference Values	0.037889	0.028653	0.028653
Experimental Values	0.037920	0.028904	0.028904

CHAPTER 4.
AERODYNAMIC TESTS

4.1. Sting Supported Tests

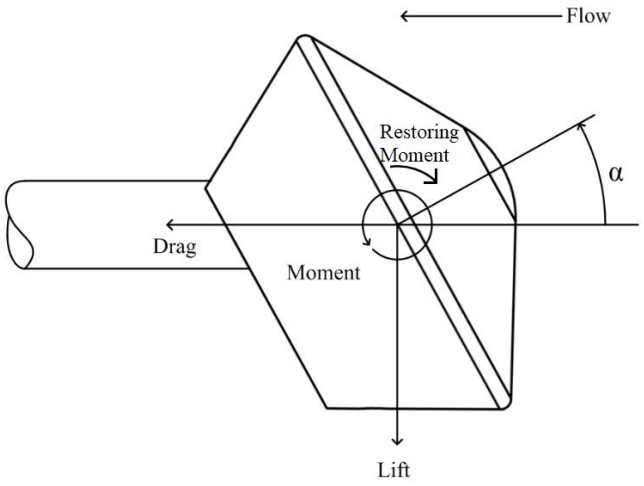

Figure 28: Top-view diagram of positive sign convention used during sting supported tests.

4.1.1. Methodology

Figure 28 is a top view of the experimental configuration during sting supported tests. The models were yawed, rather than pitched, relative to the balance. The sign convention was therefore taken from that of the axial force and the side force channels. The moment convention was chosen to correspond to the standard coefficient of moment sign convention used in reference documents (negative moment representing a restoring moment).

The diffuser was removed from the wind tunnel in order to access the wind tunnel extension. The MS-100 was installed onto the sting and was held in place with the keyway set screws and push on/push off set screws. The sting was then inserted into the vertical support strut and was secured in place with a nut. The vertical support strut was inserted into the extension and secured. The MS-100 signal and power wires were threaded through a hole in one of the

diffuser access doors, and the diffuser was reinstalled. The balance was connected to the NI-DAQ and to the power brick. The inlet was opened in order to access the test section. A model was attached to the MS-100 and was secured with a dowel pin. The inlet was closed and clamped in place to ensure a complete seal. Figure 29 and Figure 30 show the mounting configuration of the 45° model.

The “Balance Controller” LabVIEW VI was used to interface with the balance. The LabVIEW VI had inbuilt balance reduction capabilities, but it was only used to record raw data and to convert the tare voltages into mV/V. A tare was taken before each trial. Each trial began with a zero point and progressed through seven wind tunnel fan speed settings. At each data point, the tunnel was allowed to reach a steady state velocity before data collection. Twenty samples were recorded at each data point. Three trials were completed for each model. Ambient air density was calculated at the time of testing using Equation (45). It was assumed that the conditioned air was dry and that it behaved ideally.

$$\rho = \frac{P_a}{R_a T_a} \tag{45}$$

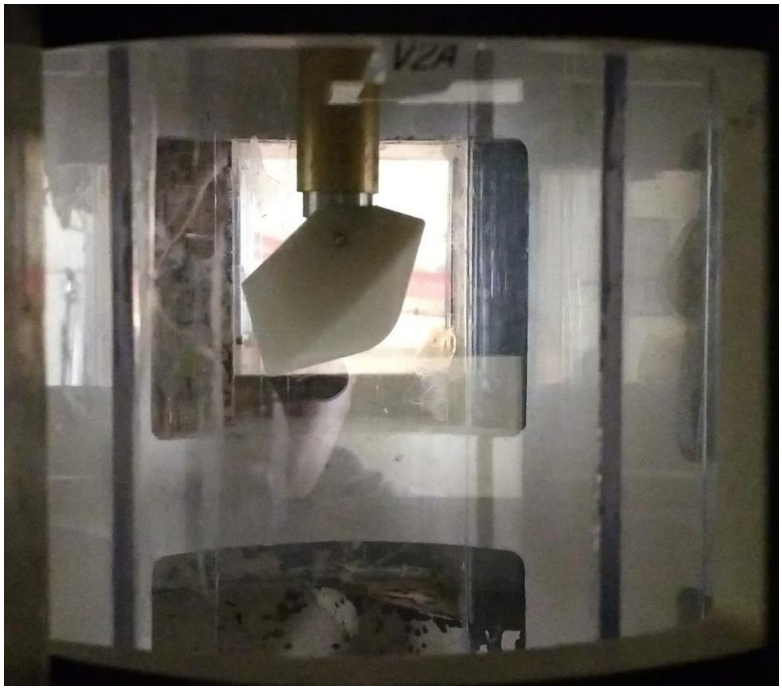

Figure 29: Top view of the 45° sting supported model (Flow is directed upwards in picture).

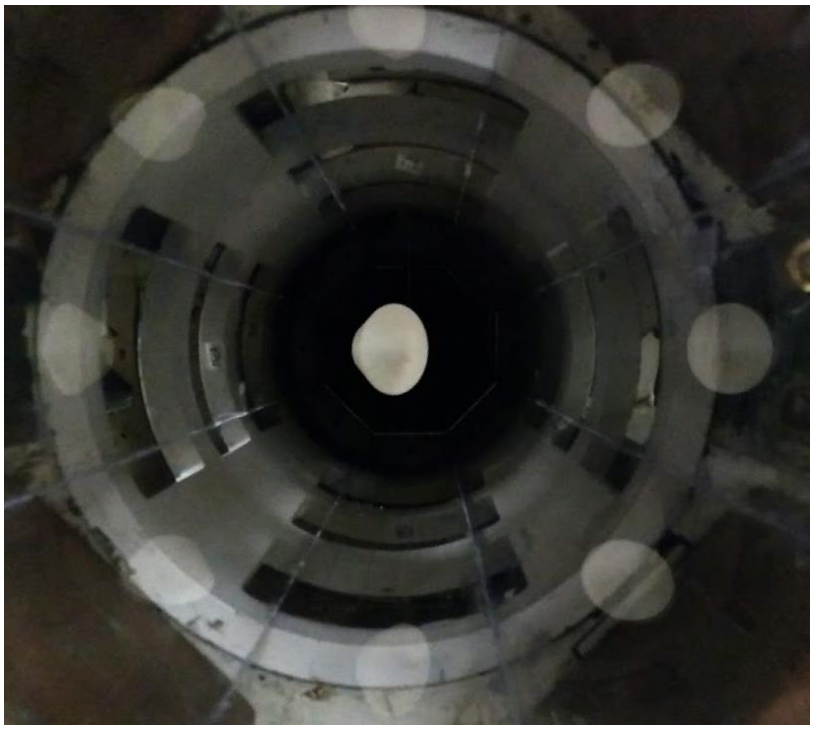

Figure 30: Front view of the 45° sting supported model.

4.1.2. Results and Data Reduction

The output of the "Balance Controller" VI contained the measured dynamic pressure, the tare for each trial, and the raw voltages for each sample taken at each data point. Internally, the VI converted the tare voltages into mV/V values, according to Equation (46). Then, each measurement was converted into mV/V, according to Equation (47).

$$Tare_{\left(\frac{mV}{V}\right)} = \frac{(Tare_{(V)} * 1000\frac{mV}{V})}{Source\ Voltage} - Electrical\ Zeros \tag{46}$$

$$Sample_{\left(\frac{mV}{V}\right)} = \frac{(Sample_{(V)} * 1000\frac{mV}{V})}{Source\ Voltage} - Electrical\ Zeros \tag{47}$$

MATLAB functions and scripts were created to sort through the raw data. These scripts are located in Appendix B.5. First, the normalized tare values were input into the balance reduction functions. The balance reduction functions performed according to the algorithm in Section 1.2.1. The calibration constants and sensitivity constants were originally created in English units and therefore, the algorithm output the tare value for each channel in lbs. or in-lbs. The tare was converted into N and N-m.

The normalized measurements then were input into the same balance reduction software to determine the force or the moment acting on each channel. These outputs were converted into N and N-m, and the tare was subtracted. The dynamic pressure was corrected according to Equation (34). Wall interference corrections were applied according to Section 1.2.4. In general, these corrections reduced the measured aerodynamic coefficients by 3-4%. The moment center was transferred to the model's geometric center in the same manner as in Section 3.3.2. At this stage, the measured forces and moments were known for each of the 20 samples taken at each data point. The Reynolds number was then calculated for each data point, according to Equation

(48), with the velocity calculated using Equation (49). The 20 samples were then averaged, and the standard deviation was determined.

$$Re = \frac{\rho * u * L_{model}}{\mu} \tag{48}$$

$$u = \sqrt{\frac{2q_{test}}{\rho}} \tag{49}$$

In the following figures, only data points taken at a dynamic pressure of 150 Pa or greater were used, due to the high uncertainty at very low dynamic pressures. All of the trendlines were second order and were created with MATLAB's polyfit function. Figure 31 shows the mean coefficient of drag values plotted versus the associated Reynolds number with selected 2σ error bars. The repeated trials were relatively consistent. As angle of attack increased the measured coefficent of drag decreases. The rate of change of CD per degree increased at larger angles of attack. As wind tunnel dynamic pressure increased, the measured CD also increased. The trendlines suggest that CD may then decrease at dynamic pressures above the range tested. Figure 32 shows the fitted CD and CL values for each mounting angle at a Reynolds number of 120,000 with 2σ error bars. The coefficent of lift values were not corrected in any manner beyond the use of the blockage corrected dynamic pressure and are shown purely as a point of comparison. The general trend remained the same; drag coefficent decreased at a rate that increased at larger angles of attack. Figure 32 also compares experimental CD value to reference values taken at a Reynolds number of around 900,000. The reference axial and normal coeffients were transformed into experimental coordinates and are shown in Table 61 [21]. The experimental data and reference data cannot generally be directly compared due to the large Reynolds number discrepancy; however, the behavior of experimental data closely matches that of reference data.

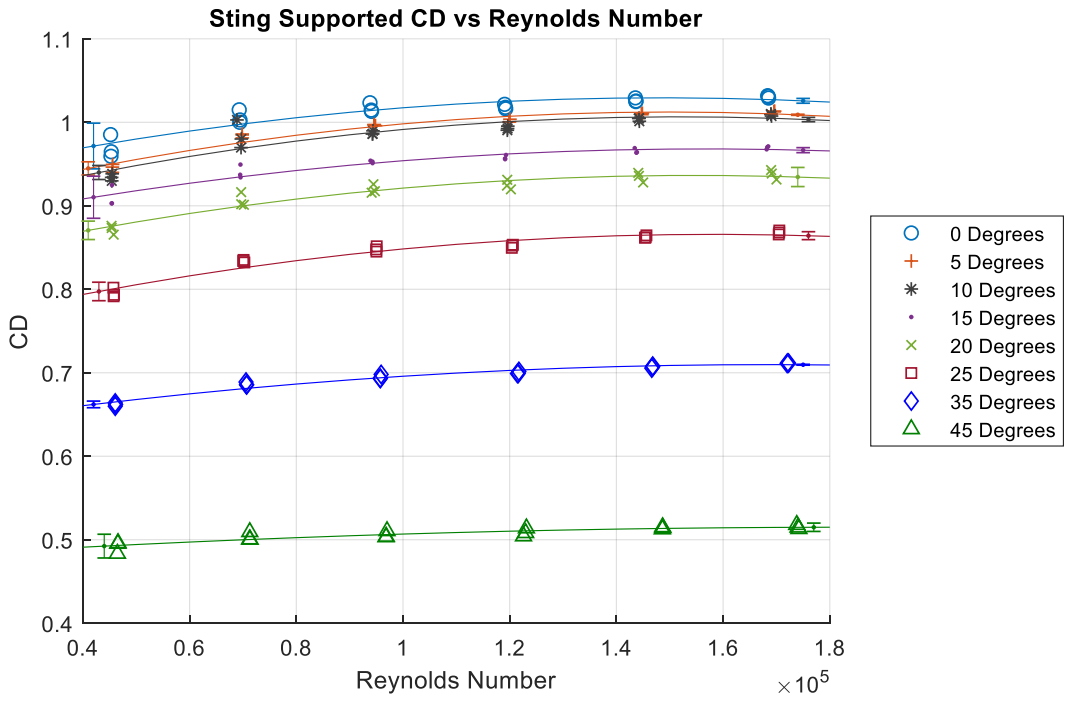

Figure 31: Comparison of drag coefficients for sting supported models at different angles of attack.

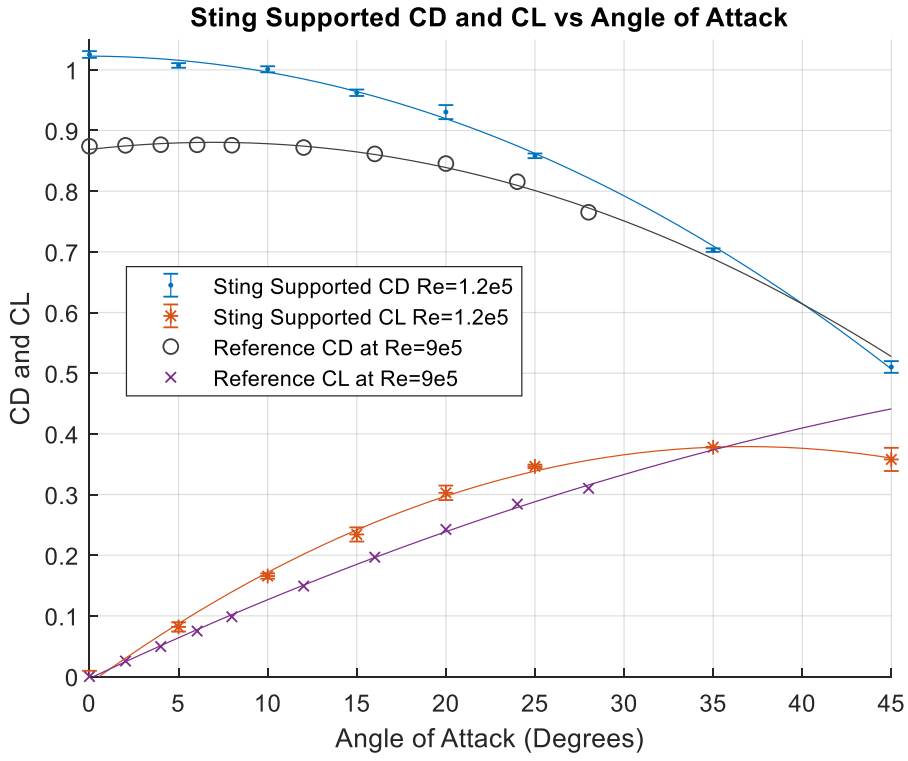

Figure 32: Comparison of CD and CL for sting supported models to reference data.

To further ensure that the embedded moment center transfer correction functioned properly, the sign and magnitude of moment was examined. Moment was negative and therefore restorative in nature. Conventionally, the coefficient of moment is determined using the cross-sectional area, S_{model}, and the diameter, L_{model}, for re-entry capsules. For each angle of attack, the coefficient of moment was averaged across the data points that were taken at Reynolds numbers higher than 100,000. These values were compared to the reference data in Figure 33. The experimental moment center was transferred to the reference moment center. Both sources of data show the restorative moment across the range of angles of attack. The reference data was taken at a Reynolds number of 900,000 and is not directly comparable to experimental data; however, both data sources are similar in trend and magnitude.

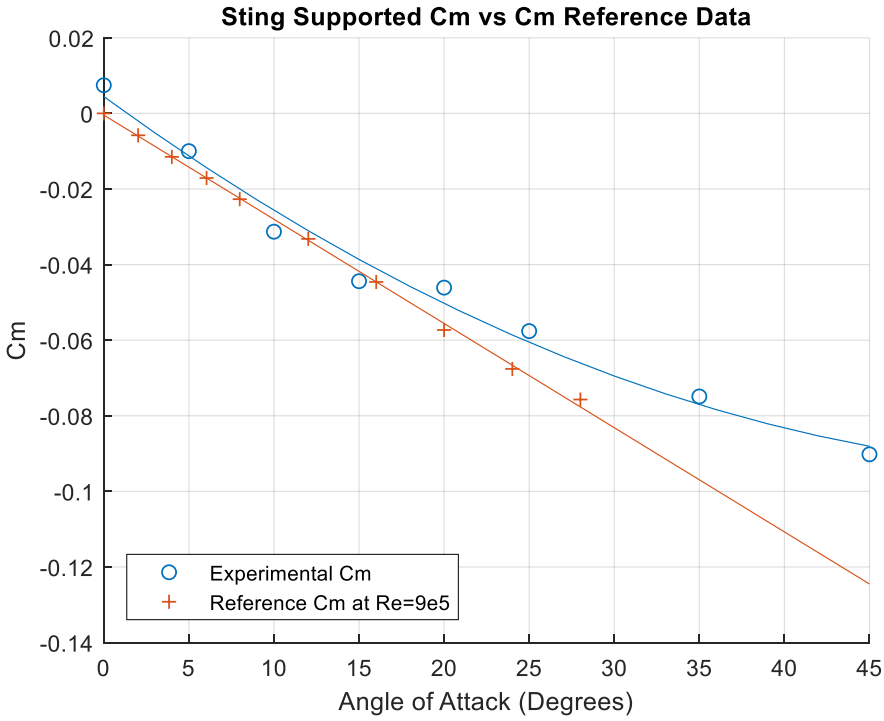

Figure 33: Comparison of experimental Cm to reference Cm data.

4.2. Dummy Sting Tests

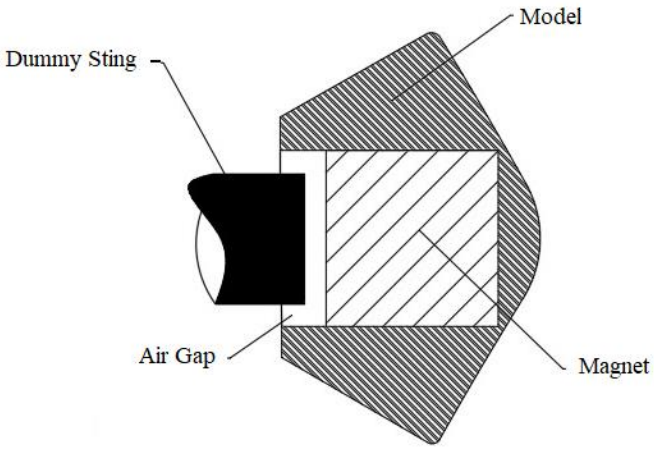

Figure 34: Diagram of dummy sting test configuration.

4.2.1. Methodology

Figure 34 shows a conceptual representation of how the models interacted with the dummy sting during testing. All of the models had an open back cavity that would be docked with the dummy sting. Prior to any dummy sting tests, a depth marker was drawn onto the dummy sting to indicate when the model was resting against the sting; if the marker was visible, the model was not in contact with the sting.

Before each test, the EPS was powered and left to reach a steady state, and then was dialed to produce the cleanest signal. The three position channels were zeroed, with nothing in the test section. The DaniSense system was powered before application of any coil currents. The Speedgoat was powered and tested to ensure communication between the controller PC, the Speedgoat, and the “Wind Tunnel Controller” VI. The Magna-Power DC supply was adjusted to 275 Volts. A model was inserted into the test section with the launch platform and was positioned at the desired axial zero location. The x-channel of the EPS was then zeroed at this

location. The master TDK-Lambda supply was set to 10 amps, which was matched by the slave, for a combined 20 amps of magnetization current. The Performance Control amplifiers were initialized, and the controller was commanded to levitate the model.

Using top view and side view cameras, the model was docked onto the tip of the dummy sting by inserting voltage offsets into states read by the controller. The model was positioned so that the tip of the dummy sting was inside the back cavity, the depth marker was visible, and the model was able to roll freely. Figure 35 is a picture of the 0° model while it was docked on the dummy sting. Figure 36 shows a typical side view from the Edgertronic camera that was used during docking and testing to ensure that the depth marker was visible.

The tunnel was then sealed and the Mensor pressure transducer was zeroed. A zero point was taken, and then the tunnel was stepped through several dynamic pressures. When increasing fan speed, the models drifted back onto the sting. During large jumps in dynamic pressure, the models drifted into contact with the sting. At each test point, data collection was delayed until the tunnel reached a steady state dynamic pressure and the error integrator pulled the model back into its desired location. Data was then taken at 1kHz for 10s. A separate trial was completed with the 0-degree dummy sting model, but with the dummy sting removed from the wind tunnel, to ensure that the addition of the back cavity was not having a significant effect on the aerodynamic data. Ambient air density was calculated at the time of testing, via Equation (45).

When using the second dummy sting to measure cavity pressure, pressures were recorded by the Scanivalve. After the tunnel and the model had reached desired conditions, the Speedgoat and the Scanivalve data collection were started simultaneously. At least 50 samples were recorded by the Scanivalve at each data point.

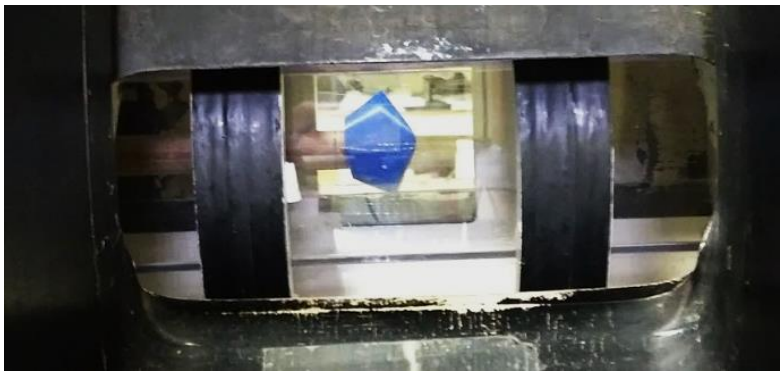

Figure 35: Picture of dummy sting experimental configuration with 0° model.

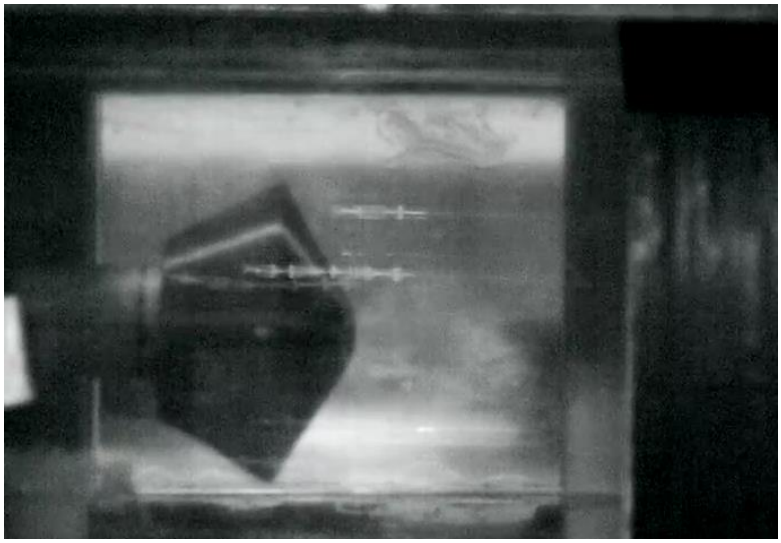

Figure 36: Typical high-speed camera view during dummy sting testing.

4.2.2. Results and Data Reduction

Original Dummy Sting

The output from the Speedgoat consisted of all the raw data collected over the test period. This included coil currents, model position, and dynamic pressure samples collected at 1kHz over the entire test period. The initial reduction was performed by the Speedgoat itself. Each data

collection point was stored separately as an event, and consisted of start and stop time indices and the average of all values of interest over that time period. The mean coil currents were converted into forces with the calibration constants that were determined in Section 3.2. The raw dynamic pressure was calibrated by Equation (34) and then was corrected for wall interference, as described in Section 1.2.4. The Reynolds number was calculated using Equations (48) and (49).

Figure 37 shows the coefficient of drag values plotted versus the associated Reynolds number for all models tested with the dummy sting with selected 2σ error bars. The dispersion between measurements increases as the angle of attack increases. As expected, CD decreased at an increasing rate as the angle of attack increased. A consequence of increasing the angle of attack was that the model had greater dynamic behavior in the lift-side plane. As a result, the high angle of attack models could not be reliably suspended at the desired location at the end of the dummy sting at larger dynamic pressures. Figure 38 shows the fitted CD and CL values for each mounting angle at a Reynolds number of 120,000 with 2σ error bars compared to reference data.

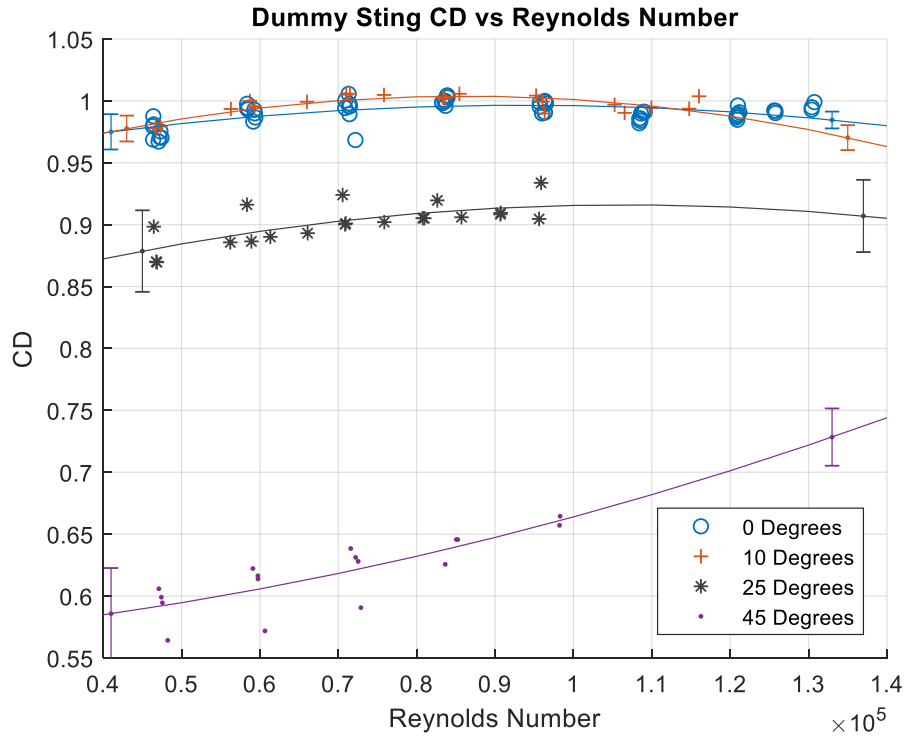

Figure 37: Comparison of drag coefficients of different models tested with the dummy sting.

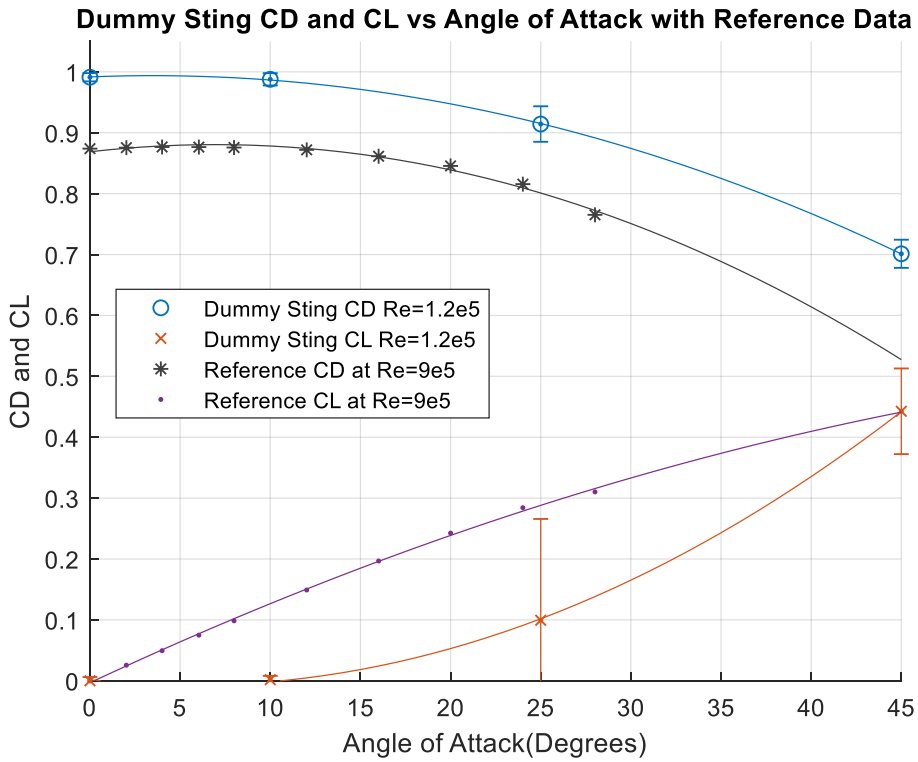

Figure 38: Mean CD and CL compared between models at different angles of attack.

Dummy Sting with Pressure Tap

Unfortunately, the output of the Mensor pressure transducer was not recorded during the repeated trials 6-8 of the zero angle of attack model. However, the test section static pressure, as referenced to atmospheric pressure, was recorded. Therefore, the differential pressure between the test section static tap and atmospheric pressure was used to determine dynamic pressure. This required a separate calibration in the same manner as Section 0.

Following the same assumptions and selection criteria as the inlet differential regression, Equation (50) is the linear regression that was best for the single tap measurement. Table 19 compares the corrected inlet measurements to the corrected single tap measurements. The two methods of determining test section dynamic pressure produce similar levels of error; therefore, the use of this data source is acceptable. The RMSE of the single tap measurements was marginally lower than that of the inlet measurements, +/- 1.29 Pa vs. 1.665 Pa. The measurements that were recorded with this dummy sting were reduced in the same manner as the original dummy sting and were included in Figure 37 and Figure 38.

$$q_{interpolated} = 0.97597(q_{raw}) + 3.8385 \quad (50)$$

Table 19: Comparison of inlet differential pressure calibration to the calibration using the single static tap.

Pitot Q (Pa)	Inlet Q (Pa)	Single Tap Q (Pa)	Inlet Error (Pa)	Single Tap Error (Pa)
37.19	43.24	40.98	5.902	3.786
170.71	172.26	171.46	1.514	0.753
410.99	408.44	408.75	-2.487	-2.244
755.21	756.14	756.79	0.959	1.577
1208.56	1208.28	1208.81	-0.225	0.245
1756.95	1757.01	1756.53	0.146	-0.420
2403.90	2407.99	2405.85	4.210	1.950

4.3. Magnetically Suspended Tests

4.3.1. Methodology

As with the dummy sting tests, the process began with the powering and zeroing of the EPS. The functionality of the Speedgoat, the DaniSense system, the controller PC, and the "Wind Tunnel Controller" VI was verified. A model was inserted into the test section with the launch platform and was positioned at the desired zero location, and the axial EPS channel was zeroed. The Magna-Power DC supply was set to 275 Volts. The TDK-Lambda master supply was dialed to 10 amps, for a combined 20 amps of magnetization current. Finally, the Performance Control amplifiers were enabled, and the model was levitated. Figure 39 is a frontal view of the 45° model while it was magnetically suspended, prior to testing. Figure 40 is a side view of the same model during aerodynamic testing.

After taking a zero point, the tunnel was swept through a range of dynamic pressures. Data collection was delayed until the tunnel reached a steady state dynamic pressure. The tunnel and MSBS states were then recorded at 1kHz for 10 seconds. Ambient air density was calculated at the time of testing, using Equation (45).

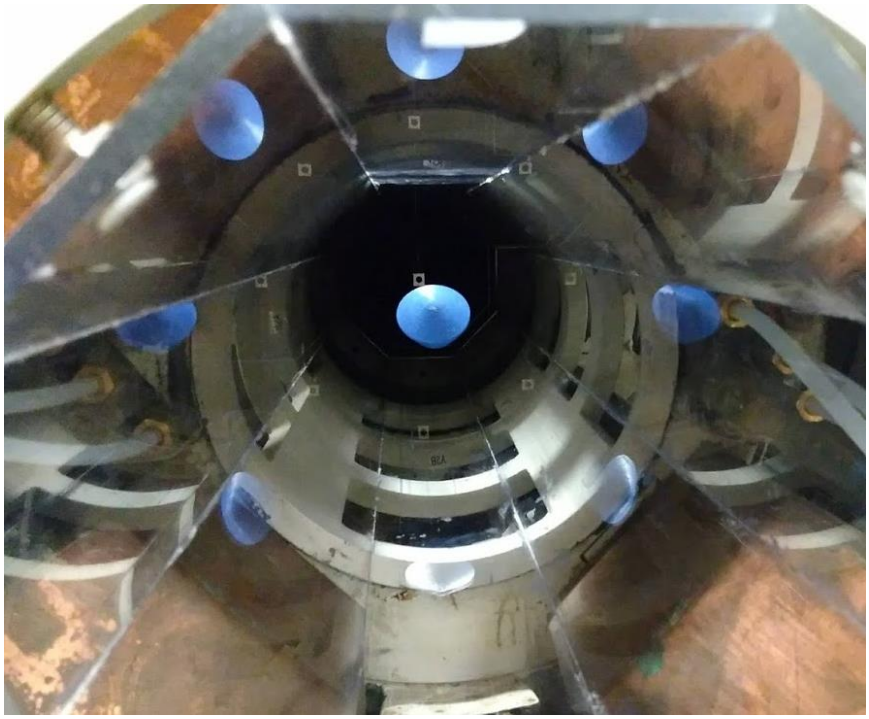

Figure 39: Front view of the 45° model during suspension before sealing the inlet.

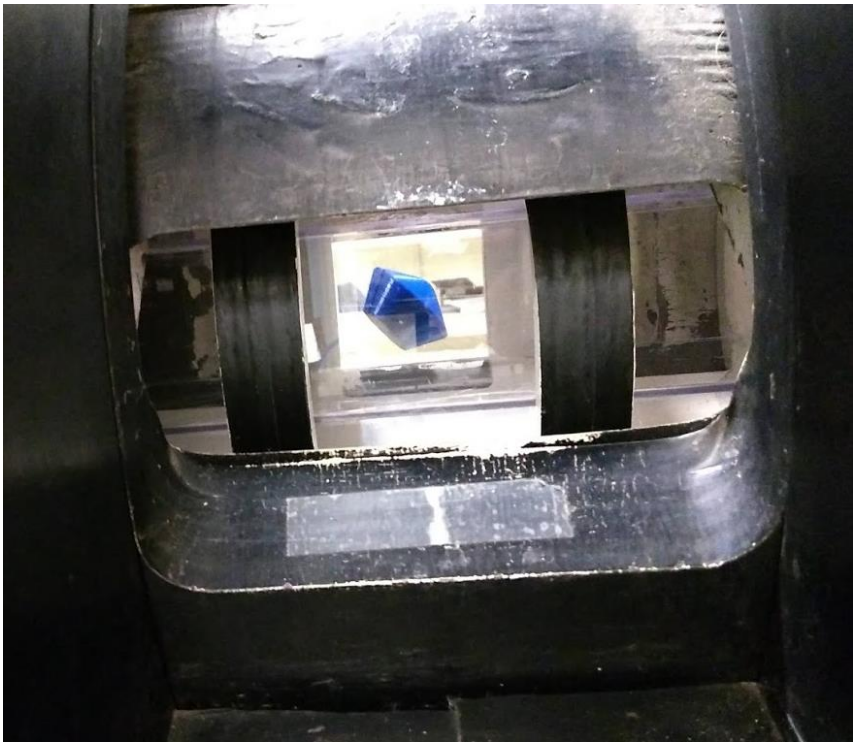

Figure 40: Side view of the 45° model during testing.

4.3.2. Results and Data Reduction

The output from the Speedgoat was the mean dynamic pressure and coil currents for each of the data collection points. The coil currents were multiplied by the respective calibration constant to produce mean forces. The dynamic pressure was calibrated according to Section 0 and then wall interference corrections were applied, as described in Section 1.2.4. It was not possible to recover side and lift forces due to the oscillatory nature of the angled models. The Reynolds number was calculated using Equations (48) and (49).

Figure 41 is a graph of the coefficient of the drag values plotted versus the associated Reynolds number for all of the free-flying models tested with selected 2σ error bars. The concavity of the fitted curves changed across the different angles of attack. This could be due to differing trends at different angles of attack or, more simply, to an effect of noise that could be removed with further data collection. The repeated trials for the high angle of attack models were less consistent than the dummy sting or the sting supported tests. This was likely due to the wider freedom of motion available during these tests. As was the case in the dummy sting tests, as the angle of attack increased, the dynamic behavior and dispersion between the repeated trials increased.

Figure 42 compares the inteference-free drag results with the reference data from prior Stardust testing that was presented in 4.1.2. The large difference in Reynolds number generally precluded direct comparison. Figure 43 shows the fitted CD and CL values for each mounting angle at a Reynolds number of 120,000 with 2σ error bars. Experimental and reference data had similar response behavior to angle of attack. Further comparisons to reference data are made in Section 4.5.

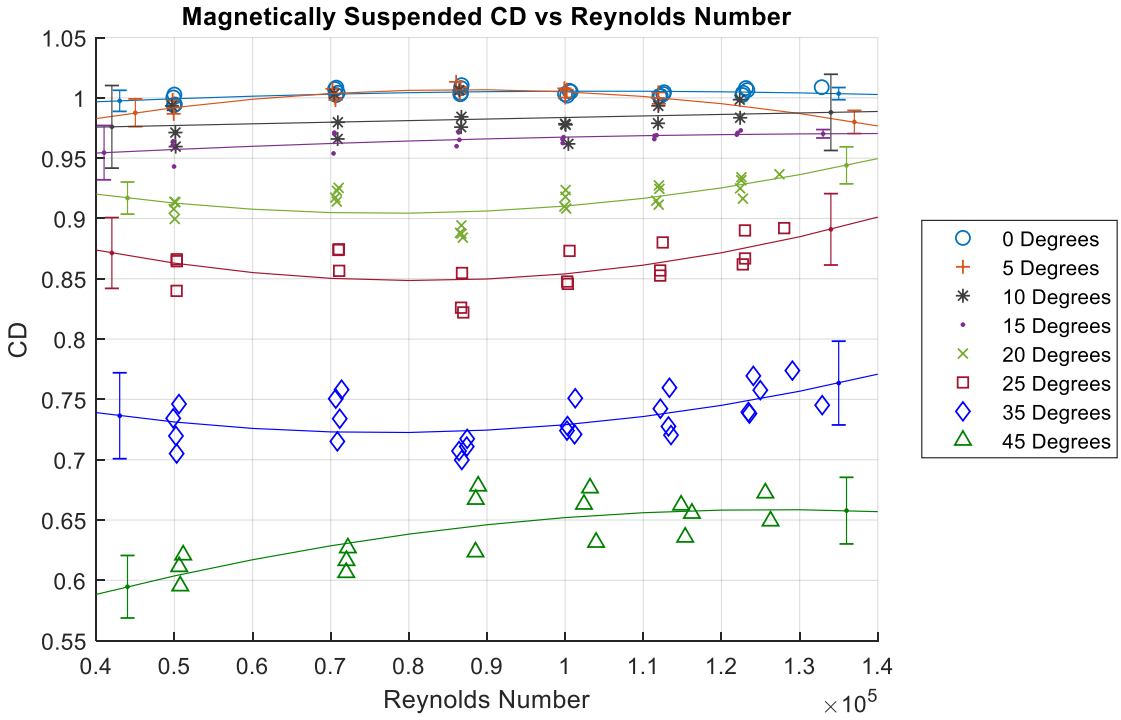

Figure 41: Graph of CD vs angle of attack over a range of Reynolds numbers.

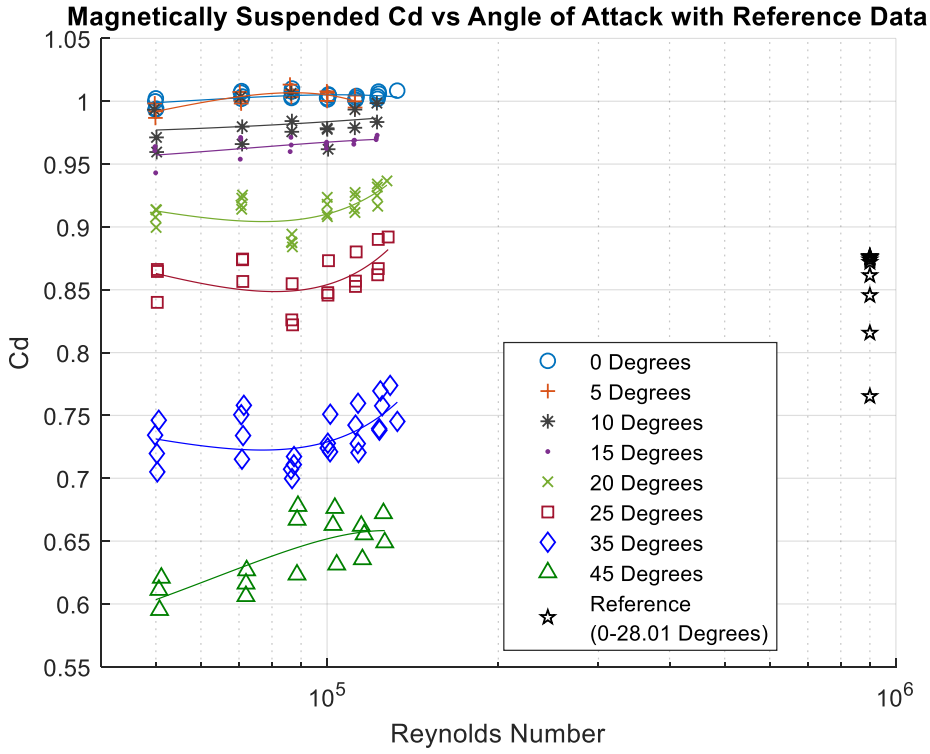

Figure 42: Free flying drag data compared to reference drag data.

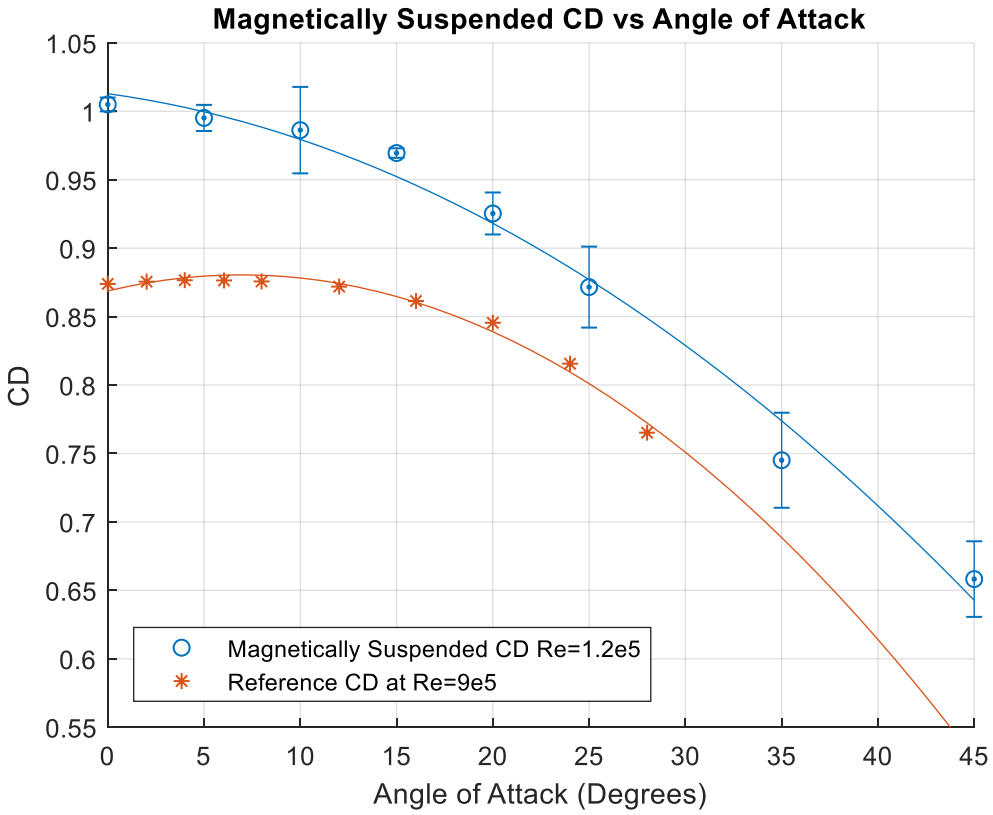

Figure 43: Average free-flying CD at angle of attack compared to reference data.

4.4. Cavity Pressure

The cavity pressure was measured during the second set of dummy sting tests. The output was a differential pressure measured relative to test section static pressure. A coefficient of cavity pressure was generated according to Equations (51) and (52). The calculated coefficients were rather consistent for each angle of attack and are shown in Table 20. Cavity pressure data corresponding to dynamic pressures of 150 Pa or greater was used to generate this table. The cavity pressure coefficients were significantly higher in magnitude than base pressure coefficient

reference data for other bodies of revolution [13, 22]. Table 21 shows the sting supported data that was corrected according to Equations (53)-(57).

These equations were created under the assumption that the cavity pressure added a component of drag to the dummy sting tests that was not present in the sting supported tests. The area where the cavity pressure would act was instead in physical contact with the sting. Some of the discrepancies between the sting and the dummy sting tests would be reduced by adding this component of drag to the sting supported data. A single comparison was completed for mean CD values at a Reynolds number of approximately 70,000. A clear trend was not established; the correction appeared to be too large at small angles of attack and too small at high angles of attack.

$$\Delta Drag = (p_{cav} - p_{\infty})S_{sting} \tag{51}$$

$$Cp_{cav} = \frac{(p_{cav} - p_{\infty})}{q_{cav}} \tag{52}$$

$$\Delta Drag = Cp_{cav}q_{test}S_{sting} \tag{53}$$

$$Drag_{cav} = Drag - \Delta Drag \tag{54}$$

$$Cd_{cav} = \frac{Drag - \Delta Drag}{q_{test}S_{model}} \tag{55}$$

$$Cd_{cav} = Cd - \frac{Cp_{cav}q_{test}S_{sting}}{q_{test}S_{model}} \tag{56}$$

$$Cd_{cav} = Cd - Cp_{cav}\frac{S_{sting}}{S_{model}} \tag{57}$$

Table 20: Coefficient of pressure for the back cavity of the models used with the dummy sting.

AoA (degrees)	Mean Cp_{cav}	Cp_{cav} Standard Deviation
0	-0.6264	0.0131
10	-0.6517	0.0114
25	-0.6755	0.0350
45	-0.5415	0.0268

Table 21: Comparison of corrected sting supported drag data to other support methods.

AoA (degrees)	Sting CD	Sting Cd_{cav}	Dummy Sting CD	Magnetically Suspended CD
0	1.006	1.071	1.000	1.005
10	0.984	1.052	1.011	0.983
25	0.834	0.904	0.918	0.868
45	0.503	0.560	0.625	0.621

4.5. Comparisons Between Support Methods

A full range of general uncertainty bounds is not provided in this section, in order to allow for trend analysis. Some figures have error bars that encompass two standard deviations from the mean. A general uncertainty analysis is presented in Section 4.5.1.

Figure 44 is a comparison of the various support methods at an angle of attack of zero degrees. The dummy sting test showed a reduced drag when compared to the magnetically suspended test. The sting supported test began as the lowest drag case, but it rapidly increased in drag coefficient as dynamic pressure increased. Figure 45 shows the same comparison at 10 degrees. The sting supported data followed a similar trend, starting with less drag and then overtaking the other tests at higher dynamic pressures. At this angle, the dummy sting test exhibited increased drag over the magnetically suspended tests. The magnetically suspended data was relatively noisy when compared to the other support methods. Figure 46 shows the 25-

degree support method comparison. The dummy sting test showed a slightly higher coefficient of drag than the magnetically suspended test, at this angle. Unlike the previous two angles, the sting supported data remained the least drag case over the entire range of dynamic pressures. Figure 47 shows the 45-degree support method comparison. The magnetically suspended and dummy sting coefficients of drag were roughly equivalent at this angle. The sting supported coefficient of drag was significantly lower than the other support methods at this angle.

Figure 48 attempts to combine all of the tests into one comparison. The data points were taken from the CD versus Reynolds number trendlines at a Reynolds number of 120,000. This range was chosen because roughly represented the overlap between the different support methods at the highest possible dynamic pressure. The sting supported coefficients of drag were generally lower than the other methods. The dummy sting and the magnetically suspended coefficients of drag alternated in ranking over different angles of attack.

Figure 49 compares the previously averaged drag data to the Stardust reference data presented in Section 4.1.2. Direct magnitude comparison was not possible, due to the significant difference in Reynolds number; however, the experimental and reference data follow the same general trend and begin to resemble each other at higher angles of attack.

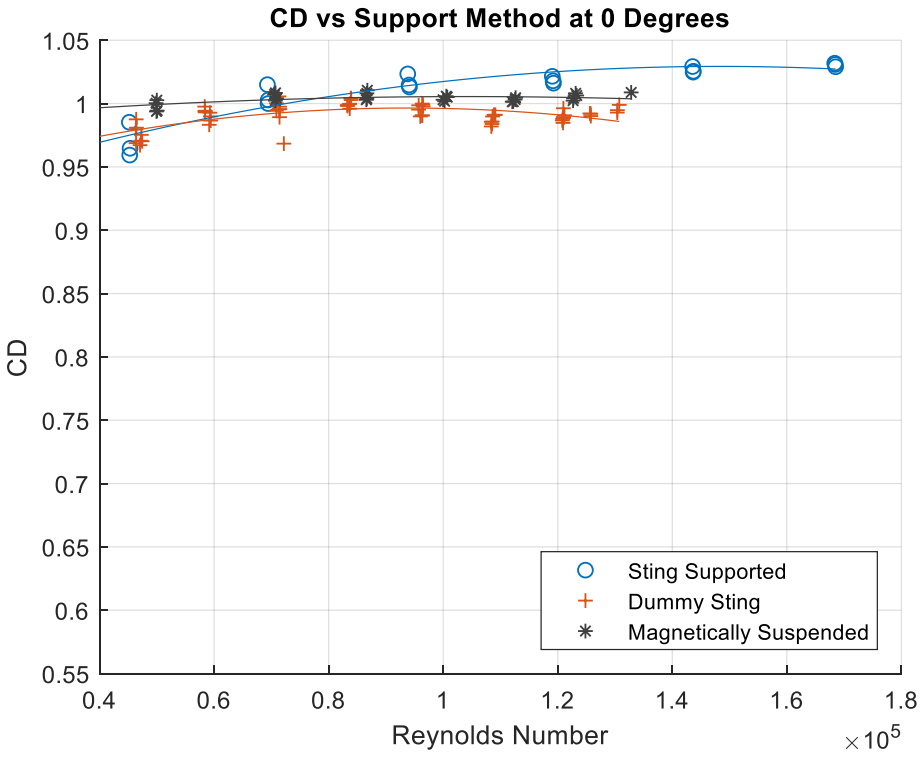

Figure 44: CD comparison between support methods for 0° models.

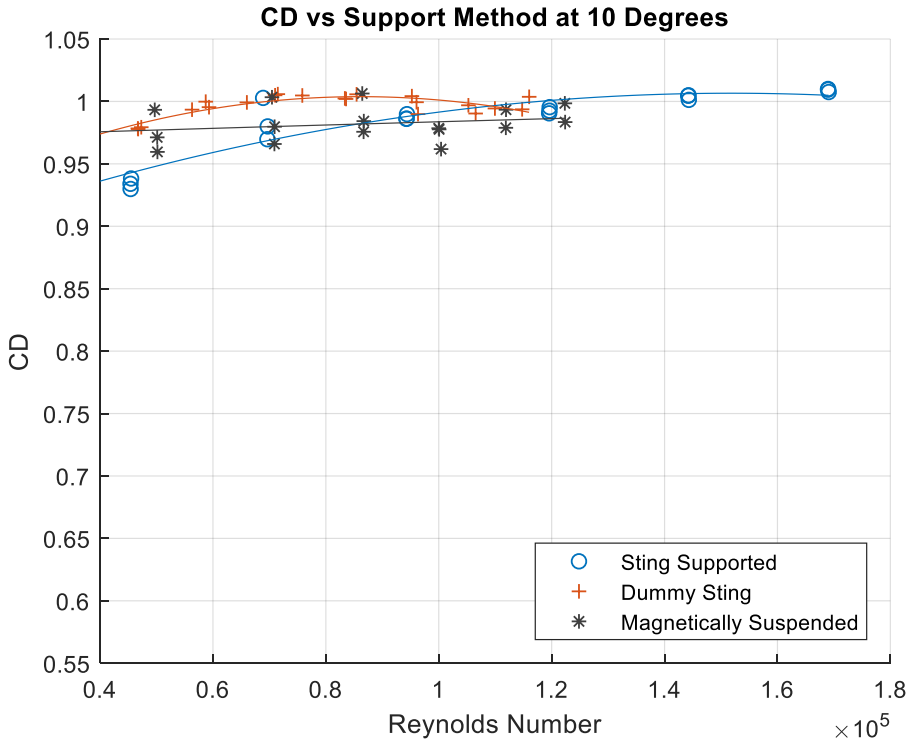

Figure 45: CD comparison between support methods for 10° models.

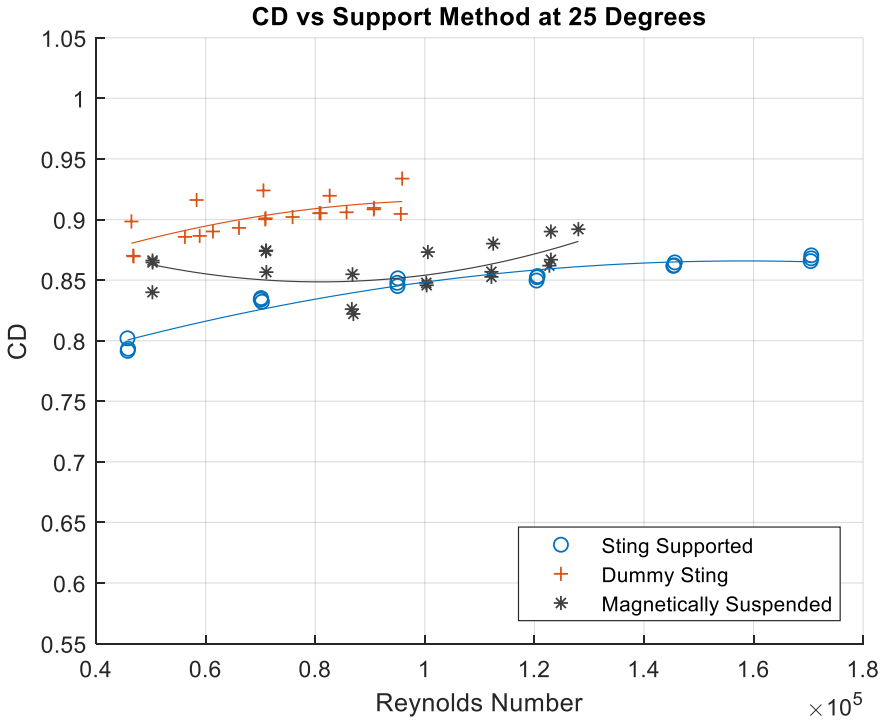

Figure 46: CD comparison between support methods for 25° models.

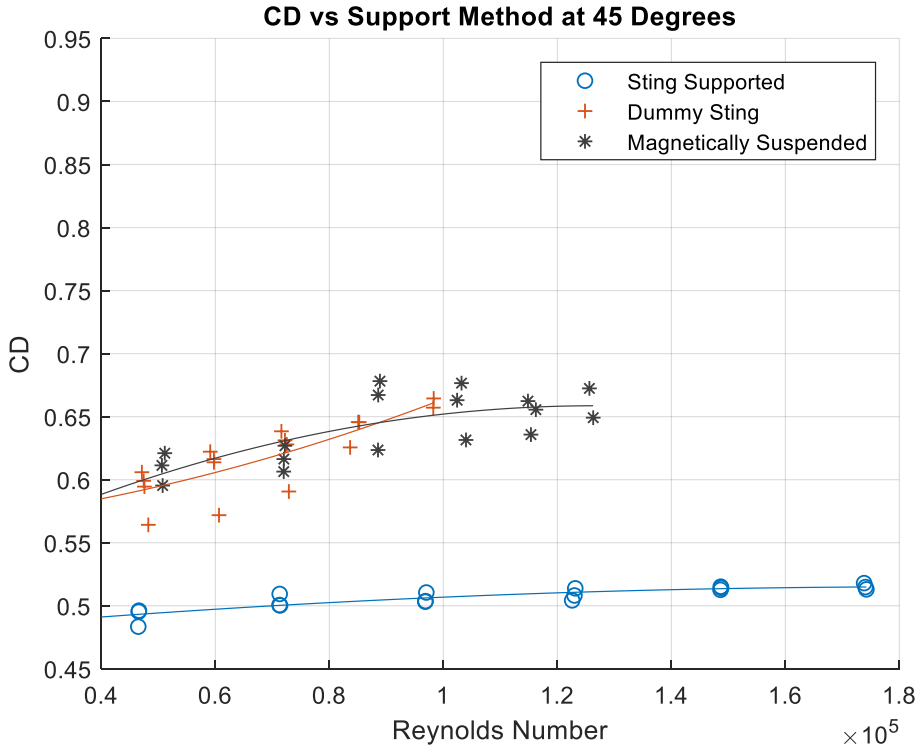

Figure 47: CD comparison between support methods for 45° models.

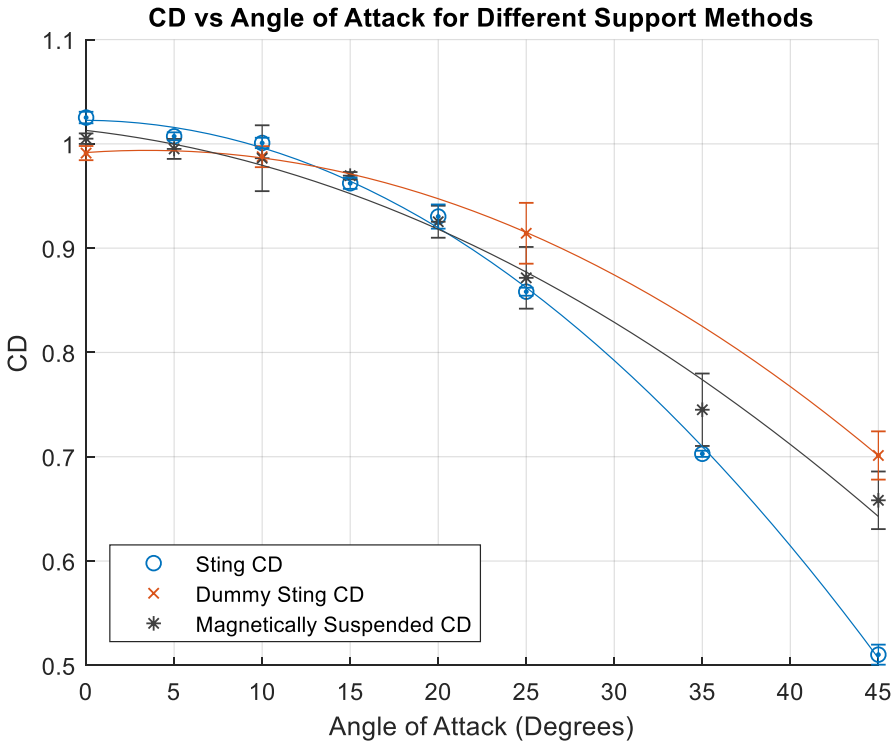

Figure 48: Comparison of average CD between support methods at Re=120,000.

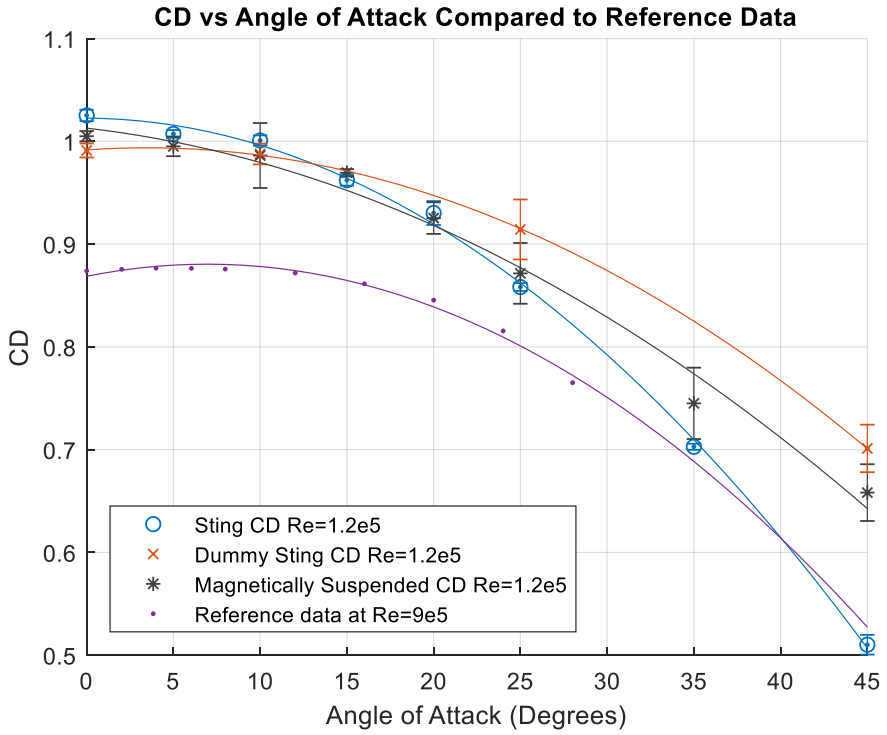

Figure 49: Comparison of average CD between support methods to reference data.

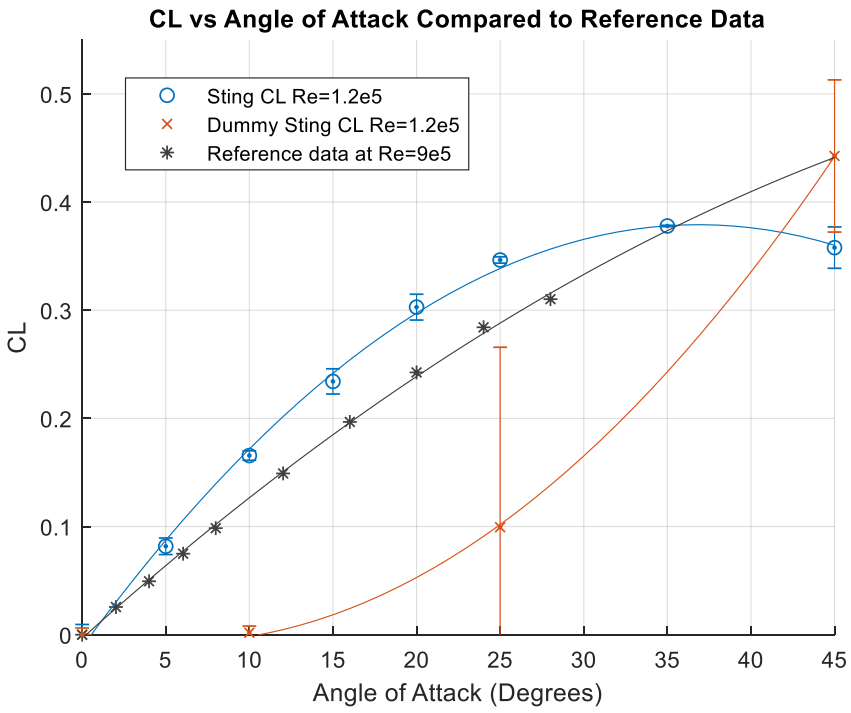

Figure 50: Comparison of average CL between support methods to reference data.

4.5.1. Print Height

As mentioned in Section 2.9.4, the sting supported and magnetically suspended models were printed with different layer heights. This caused a difference in surface roughness. Two additional sting supported models were tested, in order to examine this effect. Data was reduced in the same manner as the other sting supported tests. Figure 51 is a direct comparison between the three surfaces at an angle of attack of zero degrees with 2σ error bars. The 0.127 mm layer height model was the surface finish used in the sting supported tests. The 0.200 mm layer height model approximated the surface finish of the magnetically suspended models. The 0.033 mm layer height model was a comparatively smooth model used as a point of comparison. It appeared that the 0.127 mm layer height model was at a local minimum; both increasing and

decreasing surface roughness increased the coefficient of drag. There was an approximate 1% decrease in the drag coefficients of the sting supported models, relative to the magnetically supported models, due to the difference in surface roughness. As seen from the error bars, the 0.127 mm layer height and 0.200 mm layer height CD values lay within mutual uncertainty and represent a negligible difference. Furthermore, as will be discussed in Section 4.6, the sensor uncertainty of the MS-100 strain gage force balance was an order of magnitude larger than these 2σ error bars and as such all data falls well within overall mutual uncertainty. Figure 52 shows this data as compared to the other support methods. The difference in surface roughness was not large enough to alter the overall trends between support methods.

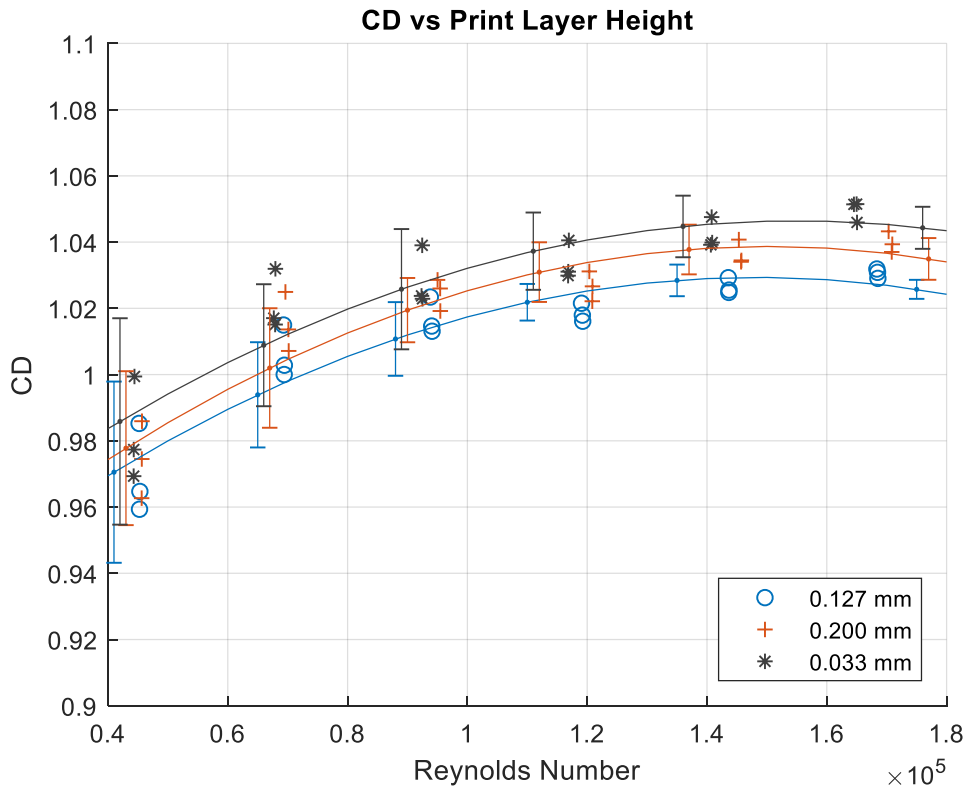

Figure 51: Comparison of the effect caused by different 3D print layer heights for 0° models.

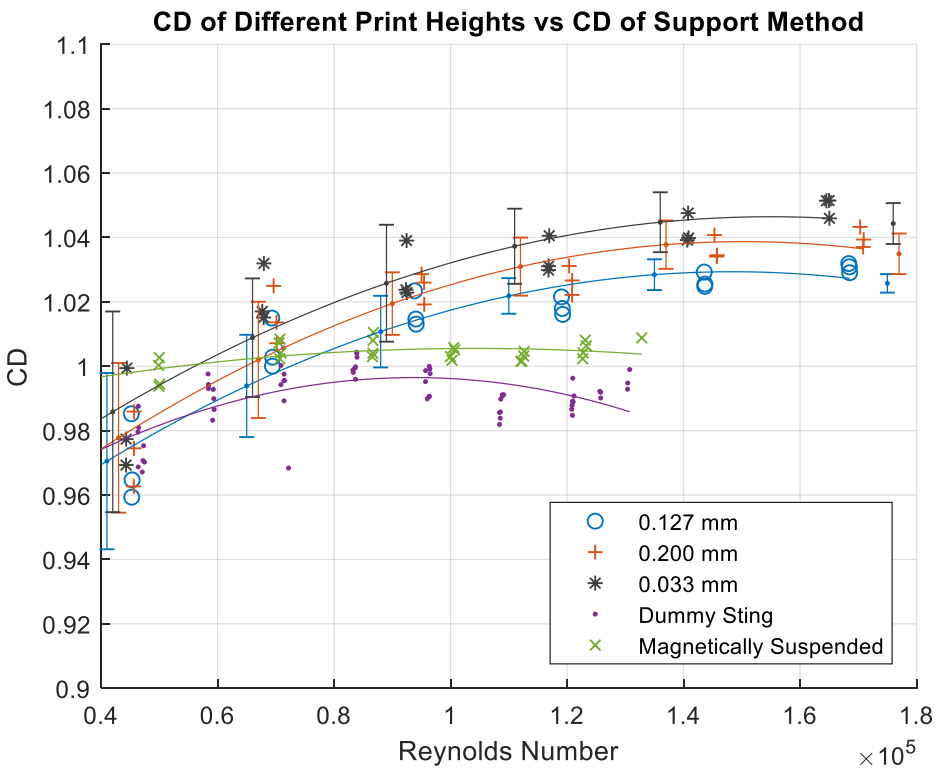

Figure 52: The effect of sting supported model 3d print layer height compared to other support methods for 0° models.

4.5.2. Model Alterations

A significant modification to the geometry of the Stardust capsule was made, in order to accommodate the usage of the dummy sting. It was noted that two variables were changing between the free flying and dummy sting tests: both a back cavity and a dummy sting were added. In order to examine the effects of this alteration, the zero-degree dummy sting model was tested with the dummy sting entirely removed from the test section (referred to as the back cavity test). The data was taken and was reduced in the same manner as the other magnetically supported or free flying tests. Figure 53 compares this data to that taken during the free flying

and dummy sting tests with selected 2σ error bars. When compared to the magnetically suspended model without the back cavity, the addition of a back cavity slightly increased drag.

The difference in the zero-degree drag coefficient between the dummy sting and the magnetically suspended tests was roughly 1%. Comparison of the dummy sting and back cavity tests showed that the sting interference effect could, instead be as high as 3%. There is some uncertainty overlap, and as will be presented in Section 4.6, the expanded uncertainty of MSBS measurements overwhelms this CD discrepancy. It is possible that the effect of the back cavity increases as angle of attack increases. As such, further efforts should be made into adapting the model for use with the dummy sting with a less significant alteration in overall geometry.

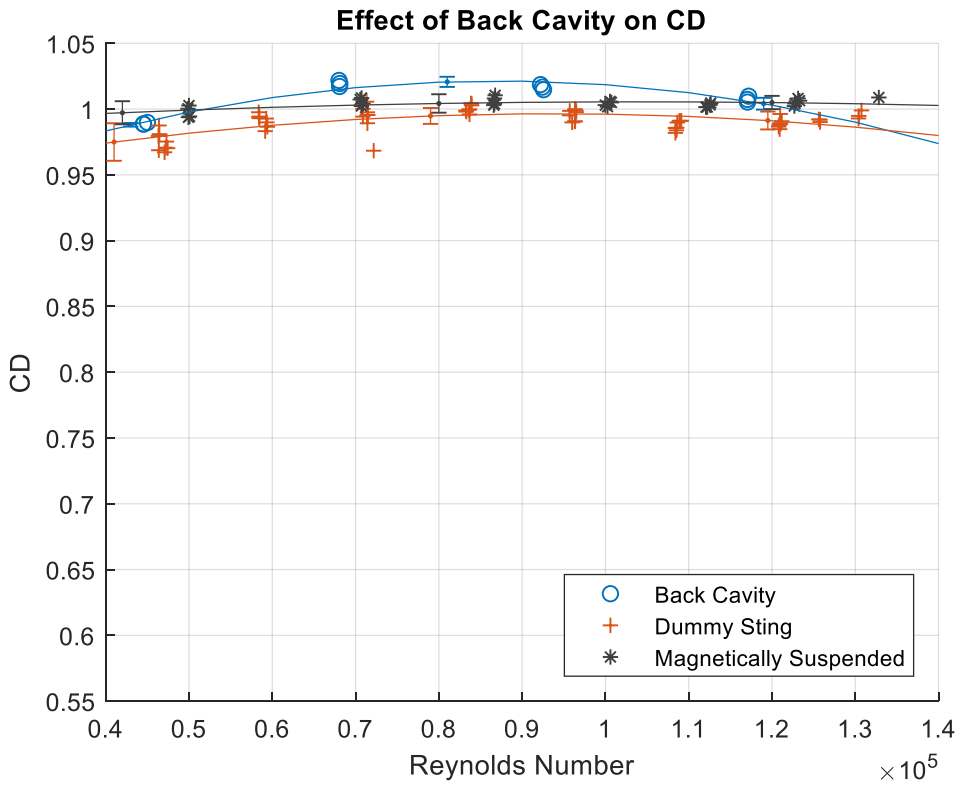

Figure 53: Examination of the effect of model alterations for 0° models.

4.6. Combined Uncertainty Analysis

A general uncertainty analysis is presented in this section and a selection of graphs are reproduced with these error bars. As previously mentioned, a full characterization of the MSBS and of accompanying instruments was not attempted because this level of examination was sufficient areas that were in need of improvement and because the final configuration of the system was not fixed.

The Taylor Series Method with large-sample assumption was used to create a combined uncertainty with a 95% level of confidence [23]. Equation (58) is the large-sample expanded uncertainty approximation for a single measurement. It was used to combine the calibration error with stated sensor uncertainty, and with an estimated random uncertainty from the standard deviation of the mean. Equation (59) is the primary relationship governing uncertainty of a value that was calculated from multiple measurements. In this equation, f is the function being examined, X is the set of variables that may be uncertain, and U is the set of corresponding expanded uncertainties for each variable as calculated from Equation (58).

$$U_i = 2\sqrt{{s_x}^2 + \sum_{k=1}^{M} {b_k}^2} \tag{58}$$

$$U_{95} = \left[\sum_{i=1}^{J} \left(\frac{\partial f}{\partial X_i}\right)^2 {U_i}^2\right]^{\frac{1}{2}} \tag{59}$$

Equation (60) is the uncertainty of the coefficient of drag and was computed by inserting Equation (32), the coefficient of drag, into Equation (59) and simplifying. The uncertainty of the area of the model was disregarded as negligible.

$$U_{cd} = 2\left[\frac{{q_{test}}^2 {U_D}^2 + Drag^2 {U_q}^2}{{S_{model}}^2 {q_{test}}^4}\right]^{\frac{1}{2}} \tag{60}$$

$$U_{re} = \left[\frac{{L_{model}}^2 \rho({T_a}^2 {U_q}^2 + {q_{test}}^2 {U_{Ta}}^2)}{2 * q_{test} * \mu^2 * {T_a}^2}\right]^{\frac{1}{2}} \tag{61}$$

Equation (61) is the uncertainty of the calculated Reynolds Number. It depends on uncertainties in test section dynamic pressure and ambient temperature. The uncertainty of the characteristic length was disregarded as negligible. Any uncertainties in atmospheric pressure were unknown and were not considered in this analysis. Table 22 is a summary of the required systematic uncertainty parameters required to add error bars to the coefficient of drag comparisons. In this thesis, the impact of the standard deviation of the mean was generally negligible when compared to systematic uncertainty due to the large number of samples that were averaged. This may not be fully representative of the behavior of the system and may not accurately capture the variation between repeated trials [23]. In addition, the data taken at 1 kHz may not represent truly independent measurements. As such, a further investigation into the comprehensive uncertainty of these systems should be performed once the final configuration of the MSBS is determined.

Table 22: Systematic uncertainty source summary.

Parameter	Systematic Uncertainty
Test Section Dynamic Pressure	+/- 1.665 Pa
Drag (Magnetically Supported Tests)	+/- 0.0023 N
Drag (Sting Supported Tests)	+/- 0.0256 N
Ambient Temperature	+/- 2.7°C

Figure 54 through Figure 58 are representations of the uncertainties present in the coefficient of drag data for the different support methods. The trendlines are the same second order polynomial fits as shown in previous sections. The uncertainties were calculated for each of the zero-degree data points and were interpolated using the same methodology as the trendlines. The interpolated coefficient of drag and uncertainty was calculated over a range of Reynolds numbers and was graphed for each support method.

Predominantly, the uncertainty in the sting supported drag measurements increased significantly at lower dynamic pressure. This effect has two compounding causes. First, the uncertainty for force balances was provided as a percentage of the full-scale load and, therefore, was constant in magnitude. Second, despite the new calibration over a smaller loading range, the full-scale load was approximately triple the magnitude of the maximum loading conditions experienced in this thesis. These factors combined to cause the uncertainty to overwhelm the lighter loads and may not be a realistic representation of the range of possible drag coefficients. As was shown in Section 413.2, the check loads were recovered with higher precision than might have been expected with these stated uncertainties.

The uncertainty ranges overlapped until higher Reynolds numbers, which interfered with the acute analysis of trends between support methods. This result remained similar for all angles of attack. The data gathered from the different support methods should be compared with these uncertainties in mind. The previously examined alternation of higher average CD between the free flying and dummy sting tests may be explained by the uncertainty overlap.

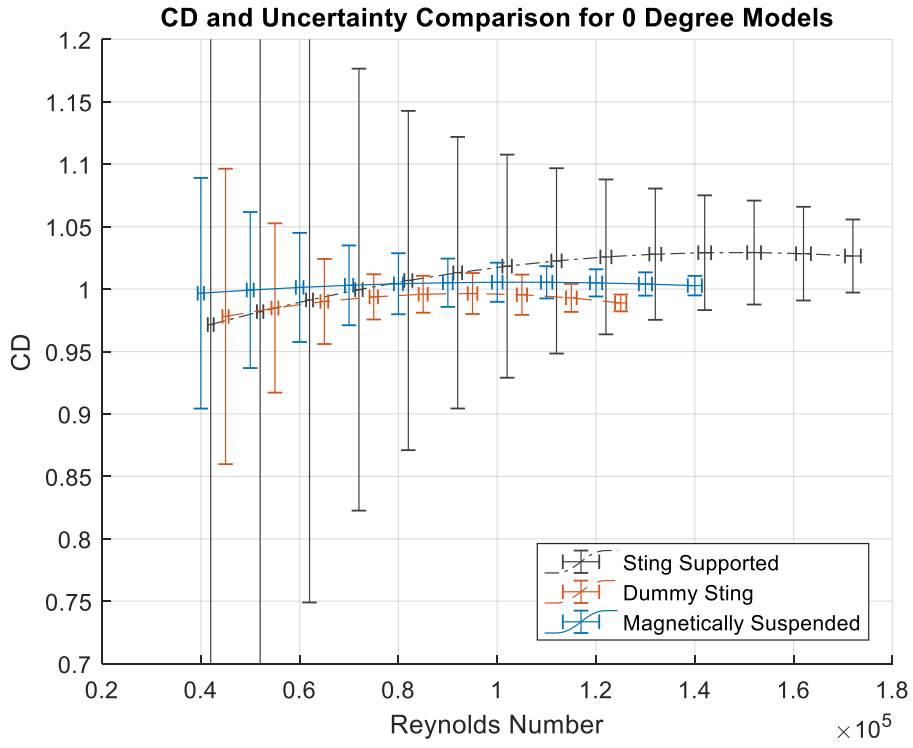

Figure 54: Comparison of CD and Uncertainties for all Support Methods for 0 Degree Models.

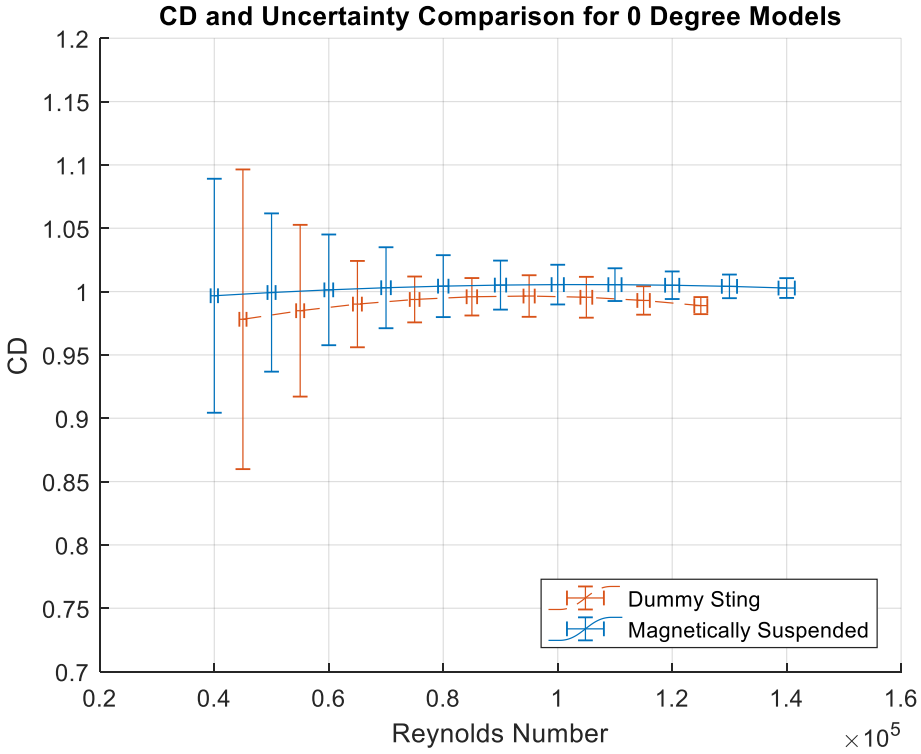

Figure 55: Dummy Sting and Free Flying CD and Uncertainties for 0 Degree Models.

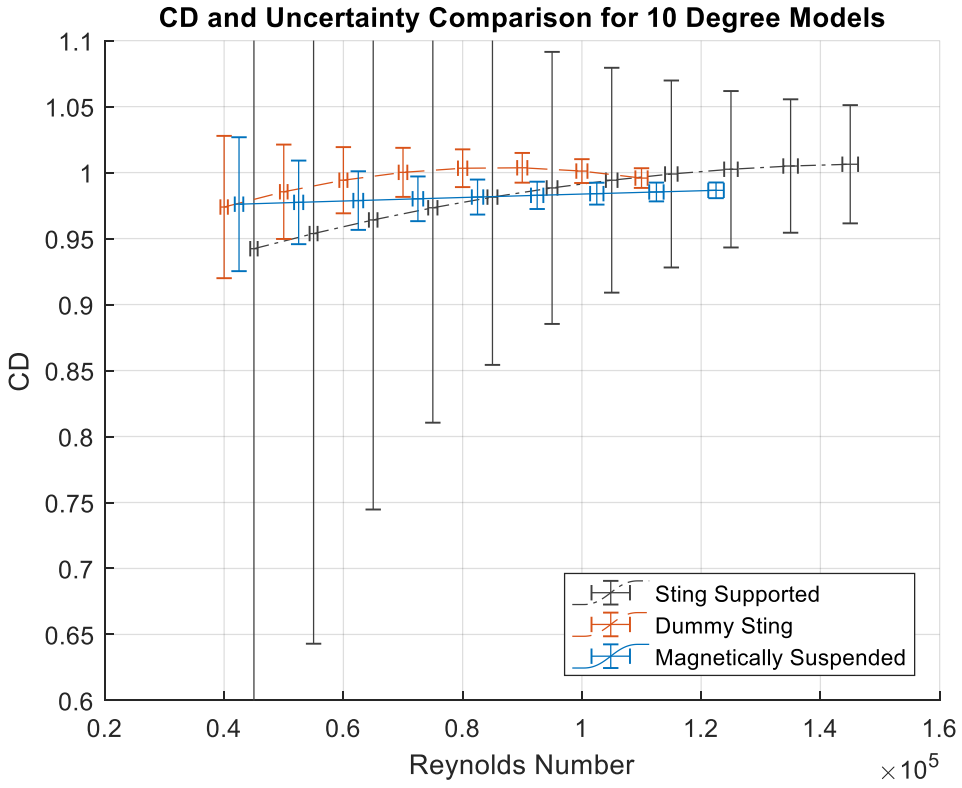

Figure 56: Comparison of CD and Uncertainties for 10 Degree Models.

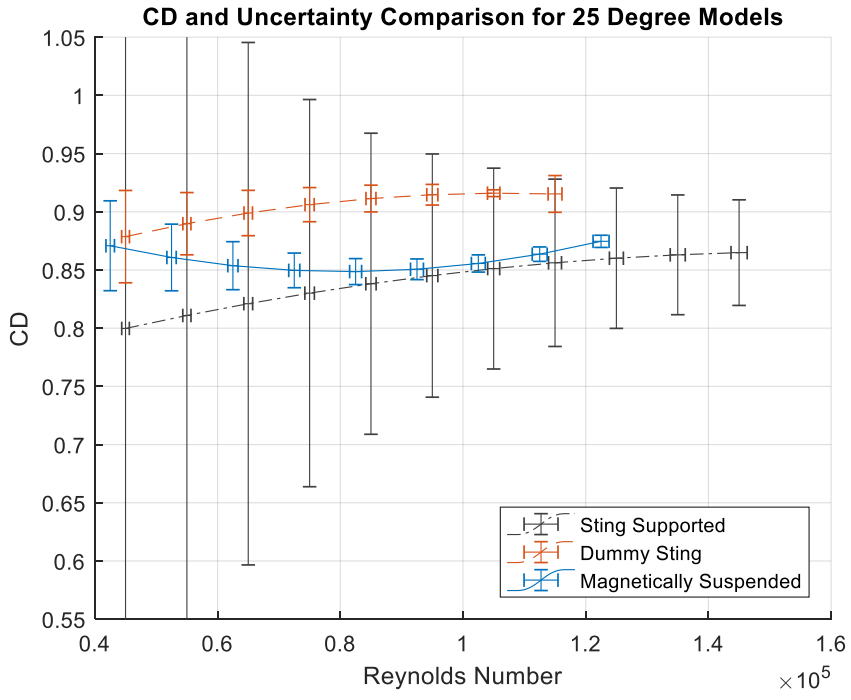

Figure 57: Comparison of CD and Uncertainties for 25 Degree Models.

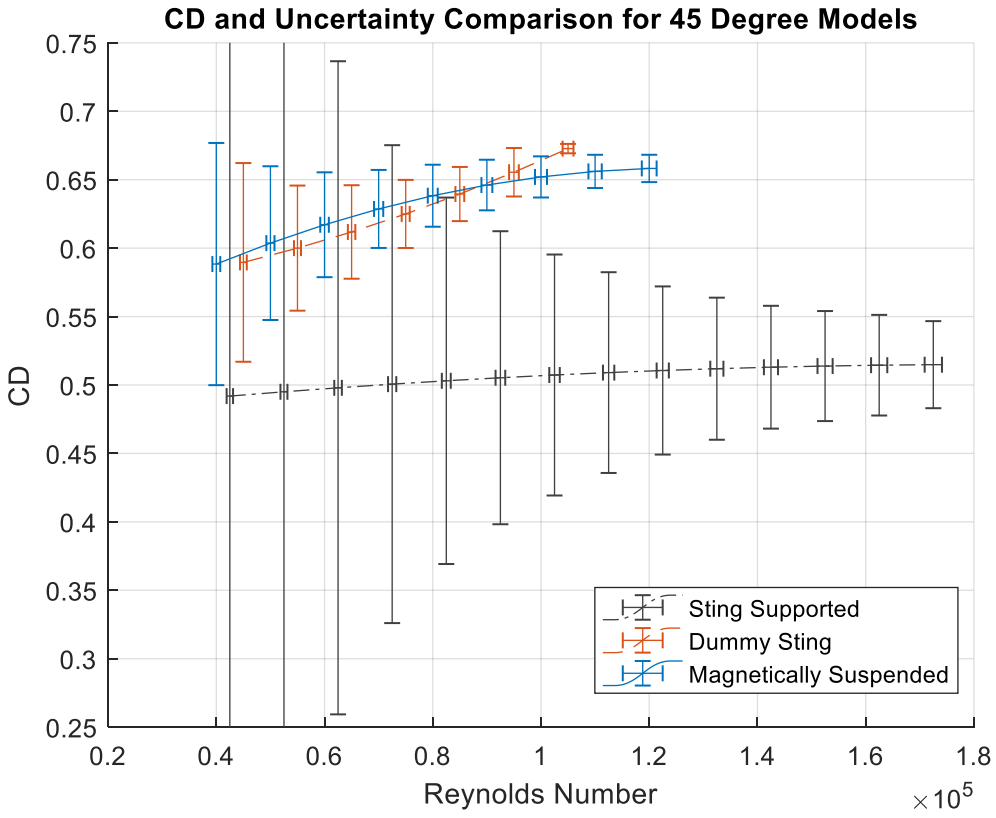

Figure 58: Comparison of CD and Uncertainties for 45 Degree Models.

CHAPTER 5.
DISCUSSION

Based on reference data, it was expected that the different support methods would generate results that could be clearly differentiated from one another. It was expected that the interference-free magnetically suspended tests would exhibit the highest drag coefficients and that the sting supported tests would exhibit the lowest drag coefficients. The dummy sting tests were expected to exhibit drag coefficients that were slightly higher than the sting supported tests. The results shown in the previous section show that the trends are less clearly defined.

As was shown in Figure 48, the angled dummy sting CD values were larger than the free-flying CD values. At 0° the dummy sting caused a reduction in drag compared to the free-flying test. The dummy sting seemed to affect the models in different ways as angle of attack changed. This may have been due to the addition of the back cavity. As was shown in Figure 53, the back cavity caused an increase drag coefficient versus the unaltered model. When the 0° back cavity model was interfered with by the dummy sting, the drag coefficient was lower than that of the unaltered model. At higher angles of attack, it is possible that the effect of the back cavity on CD outpaces the reduction in CD caused by support interference, which would result in the recorded behavior.

The sting supported tests produced results that were largely as expected. Based on reference data and on previous literature, support interference was likely to reduce the coefficient of drag. Discrepancies between sting supported and the magnetically suspended tests increased with increasing angle of attack. This is a behavior which matches known phenomena; the effect of support interference increases in magnitude as more of the support is exposed to airflow [8]. The 0° test case was an outlier; the sting supported models exhibited higher drag than the other

models. Isolated error, such as improper installation, is not likely to be the cause, due to the consistent results shown in Section 4.5.1. Figure 52 contains drag data for three different sting supported models that were tested on three separate days. These models consistently had higher drag coefficients than models with other support methods. It is possible that an uncorrected interference effect exists for this experimental setup that is localized to extremely low angles of attack. Further repeated trials with other models mounted at angles of attack between 0°-5° would help to diagnose this interference.

At low angles of attack, the drag data recovered from each test configuration very closely match one another. In general, the results from a particular support method are within the uncertainty range of the other two support methods. The presence of the sting in the model wake did not significantly affect the airflow around the model for these angles of attack. This is the desired result when designing a sting support apparatus for an experimental configuration.

The reference Stardust aerodynamic data was taken at a much higher Reynolds number than was possible with this wind tunnel. Despite this, the behavior of the experimental data broadly matched the reference data. Presumably, the discrepancies between the experimental and the reference data were predominantly caused by Reynolds number differences. This conclusion, when combined with the minimal differences between the support methods, confirms that the MSBS data can be compared to other data taken at similar test conditions in other wind tunnels.

CHAPTER 6.
CONCLUSIONS

The primary goal of this thesis was to validate the 6-inch MIT/NASA/ODU MSBS as a reliable source of aerodynamic data. This objective was met via force calibration and aerodynamic measurements. The force calibration showed that the MSBS and data collection systems could recover known forces with relatively low uncertainty at high relative Reynolds numbers. The aerodynamic measurements showed good repeatability at moderate angles of attack, not only between tests completed consecutively, but also between tests completed on different days. This verifies that the entire experimental procedure is repeatable and that the MSBS and support equipment will remain consistent despite multiple power cycles and changing ambient conditions.

The secondary goal of this thesis was to compare the MSBS to other support methods, in order to quantify any potential differences between MSBS and traditionally collected reference data. This objective was met by performing multiple aerodynamic tests with different support methods. These tests showed that the MSBS data was not significantly different from data collected with traditional support methods at low angles of attack for the chosen model geometry. In general, the presence of sting in the wake reduced the coefficient of drag, with the effect increasing as the angle of attack increased. There was no clear trend differentiating the dummy sting and the free-flying tests. The agreement between sting supported and free-flying tests further validates the MSBS force recovery methodology.

The tertiary goal of this thesis was to generate support interference free drag data for the Stardust capsule geometry, in order to provide reference data for future NASA testing. This objective was met by performing multiple magnetically suspended tests with the Stardust

geometry at a wide range of angles of attack. The aerodynamic data followed the same trends as the reference data, albeit with a magnitude shift caused by large Reynolds number discrepancies. This data can be used as a reference for further research with the MSBS.

CHAPTER 7.
FUTURE WORK

In this thesis, magnetic cores were used because their high pitch and yaw stiffness allowed for the steady orientation of models relative to the free stream. Unfortunately, the models were free to roll about the axis of magnetization, and this interfered with the recovery of certain aerodynamic forces. The core assumption was that, while the model was stationary, the magnetic forces had to be equal to the aerodynamic forces. Since the free-flying models were oscillating along the lift and side axes, lift and side forces could not be separated from controller inputs. Further attempts should be made to address this problem. A significant mass imbalance might prevent the rolling of a pitched model and might allow for simple static force recovery. Instead, if the model can be prevented from translating, the lift and side forces could be recovered by examining the magnitude and the phase of the coil currents. This may be accomplished by increasing the axial current produced by the MSBS or by increasing controller stiffness.

The model is mounted at an angle of attack relative to the magnetization axis of the core, which creates a misalignment between the model's and magnet's roll axes. As the magnetic core rotates around its magnetization axis, the model slews in orientation, and the direction of the lift vector changes. The MSBS is equipped with saddle coils, which allow for pitch and yaw control of suspended elements. If these saddle coils were activated, the model would no longer need to be mounted at an angle relative to the core. Instead, the model and core would both be pitched relative to the free stream. The model's roll axis and the core's roll axis would then be aligned, and the direction of the lift vector would be constant, regardless of rolling behavior. This would result in true static behavior and would allow for simple extraction of aerodynamic forces.

With the components used and the results presented in this thesis, two distinct projects may be pursued. The first project would expand upon the MSBS force calibration; the second project would examine support interference on dynamic behavior.

In earlier sections, it was determined that the relationship between coil current and applied force was overwhelmingly linear and decoupled. This linear relationship was then used to determine aerodynamic forces acting on the suspended model. A future project should examine the effect of nonlinearities, coupling, and position on magnetic force. To this end, the sting and the MS-100 balance may be attached to a 3-axis traverse. A magnet would be attached to the MS-100, and an automated program would position the magnet, sweep through extensive combinations of currents, and record the loads applied by each combination. With sufficiently diverse positioning and current combinations, a predictive model could be created that would rival the complexity of a traditional force balance calibration. With this expanded relationship, aerodynamic forces could be recovered with higher accuracy.

The ongoing refurbishment of the MSBS is driven by the desire to examine the dynamic behavior of re-entry capsules. With minimal additional components, the sting supported tests can be expanded to recover 1D dynamic behavior, such as aerodynamic pitch dampening. A 3D printed hinge attached to the MS-100 would allow models to pitch freely, while simultaneously recovering aerodynamic forces. Motion capture software would record the pitch history of the model during the test, and the full behavior of the model could be examined. Data recovered from this test could be compared with the current ongoing testing of the 1D dynamic behavior of free flying models. The dummy sting could also be used in these free-flying tests, in order to examine the effect of the sting support on dynamic behavior.

REFERENCES

[1] Somer, Simon C., Short, Barbara J., and Compton, Dale L., "Free-Flight Measurements of Static and Dynamic Stability of Models of the Project Mercury Re-entry Capsule at Mach Numbers 3 and 9.5," NASA TM X-373, 1960.

[2] Schoenenberger, M., Hathaway, W., Yates, L., and Desai, P., "Ballistic Range Testing of the Mars Exploration Rover Entry Capsule," AIAA Paper 2005-55, 43rd AIAA Aerospace Sciences Meeting and Exhibit, Reno, Nevada, January 2005.

[3] Malcolm, G., "Stability and Drag Characteristics at Mach Numbers of 10 and 26 of a Proposed Slender Atmospheric Probe," NASA TN D-3917, 1967.

[4] Stephens, T., "Design, Construction, and Evaluation of a Magnetic Suspension and Balance System for Wind Tunnels," NASA CR-66903, 1969.

[5] Vlajinac, M., "Design, Construction and Evaluation of a Subsonic Wind Tunnel," MS Thesis, Massachusetts Institute of Technology, 1970.

[6] Britcher, C., and Schoenenberger, M., "Feasibility of Dynamic Stability Measurements of Planetary Entry Capsules Using MSBS," 12th International Conference on Flow Dynamics, Sendai, Japan, 27-29 October 2015.

[7] Schoenenberger, M., Cox, D. E., Schott, T., Mackenzie, A., Ramirez, O., Britcher, C., Neill, C., Weinmann, M., and Johnson, D., "Preliminary Aerodynamic Measurements from a Magnetic Suspension and Balance System in a Low-Speed Wind Tunnel," AIAA Paper 2018-3323, 2018 Applied Aerodynamics Conference, Atlanta, Georgia, June 2018.

[8] Barlow, J. B., Rae, W. H., Jr., and Pope, A., *Low-Speed Wind Tunnel Testing*, 3rd ed., Wiley, New York, 1999.

[9] Smith, D., "An Efficient Algorithm Using Matrix Methods to Solve Wind-Tunnel Fore-Balance Equations," NASA TN D-6860, 1972.

[10] Eckert, D., "Correction of Support Influences on Measurements with Sting Mounted Wind Tunnel Models," *Wall Interference, Support Interference, and Flow Field Measurements*, AGARD-CP-535, 73rd Fluid Dynamics Panel Symposium, Brussels, Belgium, 4-7 October 1993.

[11] Loving, D. L., and Luoma, A. A., "Sting-Support Interference on Longitudinal Aerodynamic Characteristics of Cargo-type Airplane Models at Mach 0.70 to 0.84," NASA TN D-4021, 1967.

[12] Mackay, M., "A Review of Sting Support Interference and Some Related Issues for the Marine Dynamic Test Facility (MDTF)," Defense Research Establishment Atlantic, DREA Report 93/107, 1993.

[13] Britcher, C. P., Alcorn, C. W., and Kilgore, W. A., "Subsonic Sting Interference on the Aerodynamic Characteristics of a Family of Slanted-Base Ogive-Cylinders," NASA Contractor Report 4299, June 1990.

[14] Moon, C. F., and Chang, P., "Magnetically Levitated Vehicles," *Superconducting Levitation*, 1st ed., Wiley, New York, 1994, pp. 26-31.

[15] Crain, C. D., Brown, M. D., and Cortner, A. H., "Design and Initial Calibration of a Magnetic Suspension System for Wind Tunnel Models," Arnold Engineering Development Center, AEDC-TR-65-187, September 1965.

[16] Dress, D. A., "Drag Measurements on a Laminar Flow Body of Revolution in Langley's 13" Magnetic Suspension and Balance System," MS Thesis, George Washington University, April 1988.

[17] Judd, M., Vlajinac, M., and Covert, E. E., “Sting-Free Drag Measurements on Ellipsoidal Cylinders at Transitional Reynolds Numbers,” *Journal of Fluid Mechanics,* Vol. 48, part 2, 1971, pp. 353-364.

[18] Kuzin, A.V., Shapovalov, G.K., and Prohorov, N.I., "Force Measurements in Magnetic Suspension and Balance System", NASA CP-3336, pp. 493-503, 1996.

[19] Vlajinac, M., “Construction and Initial Operation of a Subsonic Wind-Tunnel,” Massachusetts Institute of Technology, AR Memo 914, May 1967, not published.

[20] Roth, M., “MS-100 Balance Report,” May 2016, not published.

[21] Mitcheltree, R. A., Wilmoth, R. G., Cheatwood, F. M., Brauckmann, G. J., and Greene, F. A., "Aerodynamics of Stardust Sample Return Capsule", Journal of Spacecraft and Rockets, Vol. 36, No. 3, 1999, pp. 429-435.

[22] Marko, W. J., "Static Aerodynamic Characteristics of Three Blunted Sixty-Degree Half-Angle Cones at Mach Numbers from 0.60 to 1.30," JPL-TR-32-1298, July 1968.

[23] Coleman, H.W., Steele, W. G., *Experimentation, Validation, and Uncertainty Analysis for Engineers*, 3rd ed., Wiley, New York, 2009.

APPENDIX A. SYSTEM DOCUMENTATION

A.1 Strain Gage Coefficients

3-20-1985 Calibration

Table 23: Sensitivity constants.

Normal (lb/mV/V)	Axial (lb/mV/V)	Pitch (in-lb/mV/V)	Roll (in-lb/mV/V)	Yaw (in-lb/mV/V)	Side (lb/mV/V)
10.8313	5.0257	15.6478	8.6521	11.0390	7.7994

Table 24: First order interaction coefficients; so-called 6x6 matrix. Equivalent to C_1 transpose. (For use with English units)

	MS-100 Component					
	Normal	Axial	Pitch	Roll	Yaw	Side
Effect of N	1.00E+00	5.37E-03	-1.89E-02	7.27E-04	-2.00E-03	8.00E-03
Effect of A	0.00E+00	1.00E+00	2.13E-03	0.00E+00	0.00E+00	0.00E+00
Effect of P	0.00E+00	-1.33E-03	1.00E+00	4.64E-03	6.34E-03	-1.63E-03
Effect of R	-8.65E-02	9.86E-03	-8.89E-02	1.00E+00	-3.28E-02	1.11E-02
Effect of Y	-3.30E-03	-1.00E-02	-1.05E-02	-2.32E-02	1.00E+00	4.37E-03
Effect of S	-2.25E-02	-1.25E-02	3.53E-03	1.79E-02	-2.81E-03	1.00E+00

Table 25: Second order interaction coefficient matrix; so-called 21x6 matrix. Equivalent to C_2 transpose. (For use with English units)

	MS-100 Component					
	Normal	Axial	Pitch	Roll	Yaw	Side
Effect of N*N	-3.66E-05	-1.78E-04	0.00E+00	0.00E+00	-2.41E-05	-2.25E-05
Effect of N*A	4.04E-04	6.24E-04	-2.02E-04	0.00E+00	0.00E+00	0.00E+00
Effect of N*P	0.00E+00	1.95E-04	-5.77E-05	0.00E+00	0.00E+00	0.00E+00
Effect of N*R	0.00E+00	0.00E+00	0.00E+00	-5.20E-05	2.07E-04	7.48E-04
Effect of N*Y	0.00E+00	-2.37E-05	-6.37E-05	-5.94E-05	-3.79E-05	-3.84E-05
Effect of N*S	0.00E+00	0.00E+00	0.00E+00	0.00E+00	0.00E+00	0.00E+00
Effect of A*A	0.00E+00	0.00E+00	0.00E+00	0.00E+00	0.00E+00	0.00E+00
Effect of A*P	-2.04E-04	0.00E+00	0.00E+00	0.00E+00	0.00E+00	0.00E+00
Effect of A*R	0.00E+00	0.00E+00	0.00E+00	0.00E+00	0.00E+00	1.05E-04
Effect of A*Y	0.00E+00	0.00E+00	0.00E+00	0.00E+00	1.27E-04	-2.91E-04
Effect of A*S	0.00E+00	0.00E+00	0.00E+00	0.00E+00	-2.60E-04	2.21E-04

Effect of P*P	0.00E+00	6.30E-05	0.00E+00	0.00E+00	0.00E+00	0.00E+00
Effect of P*R	0.00E+00	0.00E+00	0.00E+00	0.00E+00	5.57E-04	4.38E-04
Effect of P*Y	0.00E+00	0.00E+00	0.00E+00	0.00E+00	-3.94E-05	-2.54E-05
Effect of P*S	0.00E+00	0.00E+00	0.00E+00	1.01E-04	0.00E+00	4.02E-05
Effect of R*R	0.00E+00	5.28E-04	0.00E+00	0.00E+00	0.00E+00	0.00E+00
Effect of R*Y	-4.43E-04	-7.78E-04	-4.39E-04	0.00E+00	0.00E+00	0.00E+00
Effect of R*S	-6.23E-04	0.00E+00	-1.80E-04	-1.33E-04	1.07E-04	0.00E+00
Effect of Y*Y	0.00E+00	-6.81E-05	0.00E+00	0.00E+00	0.00E+00	-2.58E-05
Effect of Y*S	0.00E+00	3.06E-04	0.00E+00	0.00E+00	-1.24E-04	0.00E+00
Effect of S*S	0.00E+00	-1.58E-04	0.00E+00	0.00E+00	0.00E+00	0.00E+00

3-20-2019 Calibration

Table 26: Sensitivity constants.

Normal (lb/mV/V)	Axial (lb/mV/V)	Pitch (in-lb/mV/V)	Roll (in-lb/mV/V)	Yaw (in-lb/mV/V)	Side (lb/mV/V)
10.8236	4.9985	15.6383	8.5597	11.008	7.7849

Table 27: First order interaction coefficients; so-called 6x6 matrix. Equivalent to C_1 transpose. (English units)

	MS-100 Component					
	N	A	P	R	Y	S
Effect of N	1	6.12E-03	-2.09E-02	1.95E-03	-2.11E-03	1.06E-02
Effect of A	-4.45E-04	1	-1.40E-03	2.60E-05	1.69E-03	3.34E-05
Effect of P	5.46E-04	-1.29E-03	1	4.06E-03	8.90E-03	-1.43E-03
Effect of R	-8.73E-02	9.84E-03	-8.95E-02	1.00E+00	-3.31E-02	1.15E-02
Effect of Y	-3.05E-03	-9.88E-03	-1.32E-02	-2.25E-02	1.00E+00	4.34E-03
Effect of S	-2.52E-02	-1.24E-02	3.26E-03	1.59E-02	-4.56E-03	1.00E+00

Table 28: Second order interaction coefficient matrix; so-called 21x6 matrix. Equivalent to C_2 transpose. (English units)

	MS-100 Component					
	N	A	P	R	Y	S
Effect of N*N	2.60E-05	-1.97E-04	-2.66E-05	-3.80E-05	4.25E-06	-3.37E-05
Effect of N*A	2.97E-04	7.72E-04	2.48E-04	-9.72E-05	1.84E-05	-7.29E-05
Effect of N*P	1.91E-05	1.68E-04	-4.43E-06	-3.77E-05	-4.89E-06	-2.22E-05
Effect of N*R	5.11E-06	5.52E-06	-2.42E-04	-1.52E-05	2.25E-04	7.35E-04

Effect of N*Y	0.00E+00	0.00E+00	0.00E+00	0.00E+00	0.00E+00	0.00E+00
Effect of N*S	0.00E+00	0.00E+00	0.00E+00	0.00E+00	0.00E+00	0.00E+00
Effect of A*A	-1.31E-04	-3.21E-04	-3.74E-04	2.08E-05	-2.38E-04	-6.46E-05
Effect of A*P	0.00E+00	0.00E+00	0.00E+00	0.00E+00	0.00E+00	0.00E+00
Effect of A*R	0.00E+00	0.00E+00	0.00E+00	0.00E+00	0.00E+00	0.00E+00
Effect of A*Y	0.00E+00	0.00E+00	0.00E+00	0.00E+00	0.00E+00	0.00E+00
Effect of A*S	0.00E+00	0.00E+00	0.00E+00	0.00E+00	0.00E+00	0.00E+00
Effect of P*P	4.61E-06	5.47E-05	2.46E-06	-4.84E-05	-9.92E-06	-2.75E-06
Effect of P*R	-3.15E-05	-1.06E-05	3.10E-06	-2.75E-05	7.10E-04	4.56E-04
Effect of P*Y	0.00E+00	0.00E+00	0.00E+00	0.00E+00	0.00E+00	0.00E+00
Effect of P*S	0.00E+00	0.00E+00	0.00E+00	0.00E+00	0.00E+00	0.00E+00
Effect of R*R	-9.31E-05	5.38E-04	-2.01E-04	-9.07E-06	2.08E-05	3.86E-06
Effect of R*Y	-4.79E-05	-7.84E-04	-5.97E-04	4.76E-05	-1.78E-05	-1.24E-05
Effect of R*S	0.00E+00	0.00E+00	0.00E+00	0.00E+00	0.00E+00	0.00E+00
Effect of Y*Y	2.67E-05	-4.90E-05	2.93E-05	3.06E-05	3.91E-05	1.82E-05
Effect of Y*S	0.00E+00	0.00E+00	0.00E+00	0.00E+00	0.00E+00	0
Effect of S*S	2.09E-06	-1.77E-04	5.53E-05	-7.13E-06	-4.15E-04	5.84E-05

A.2 Strain Gauge Drawing

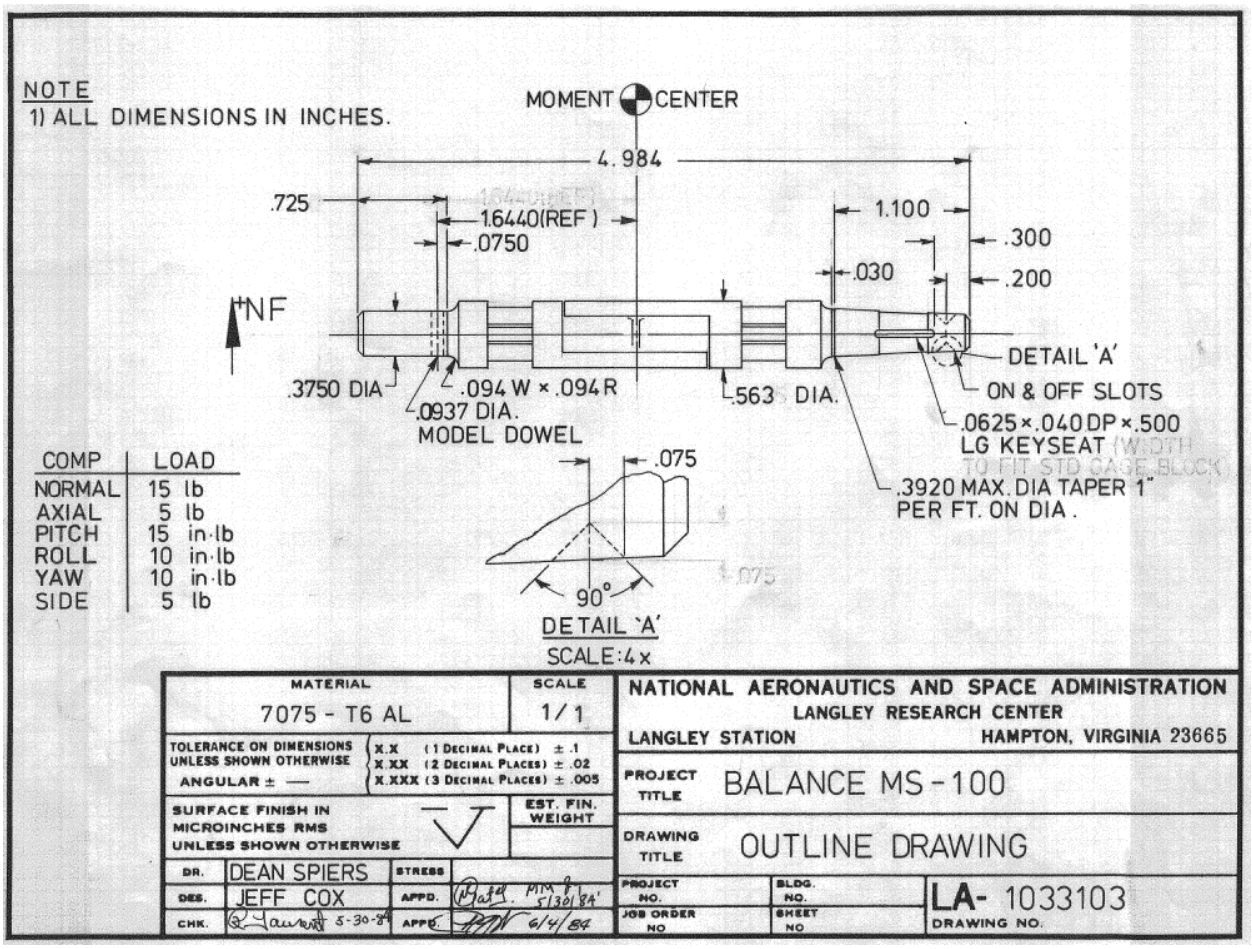

A.3 Sting Drawings

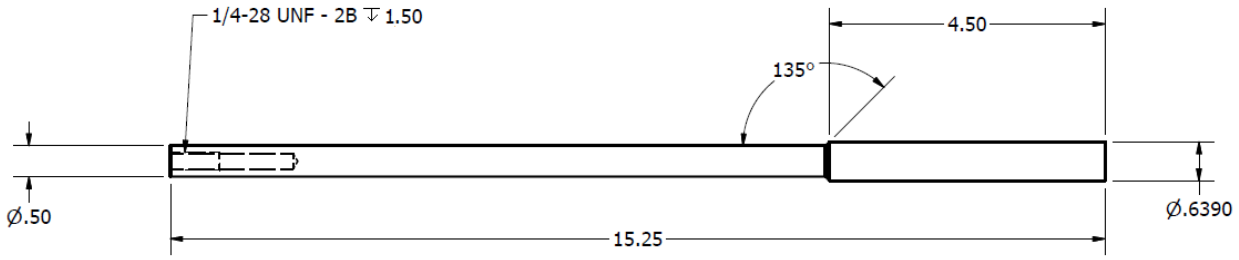

Figure 59: Dummy sting drawing. Measurements in inches.

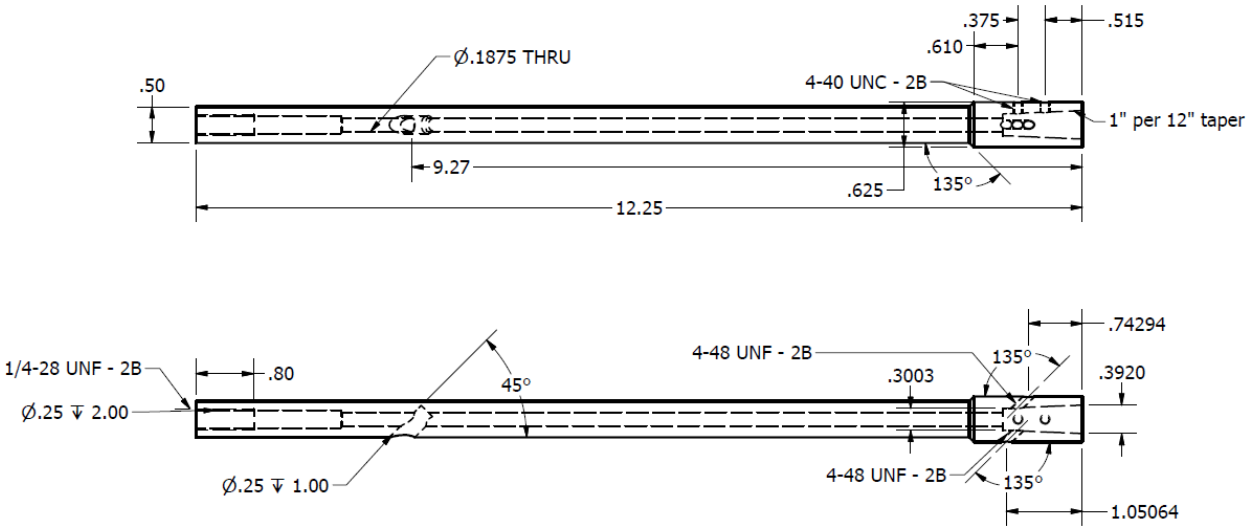

Figure 60: Aluminum sting drawing. Measurements in inches.

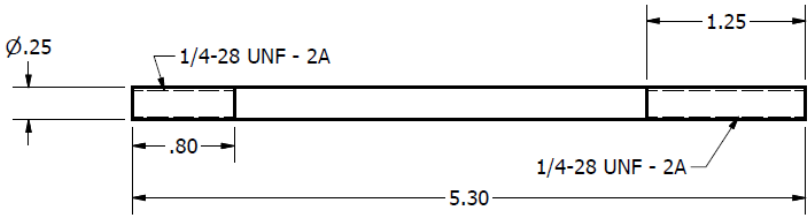

Figure 61: Threaded rod drawing. Measurements in inches. Screws into rear of sting or dummy sting.

A.4 Wind Tunnel Test Section Extension Drawings

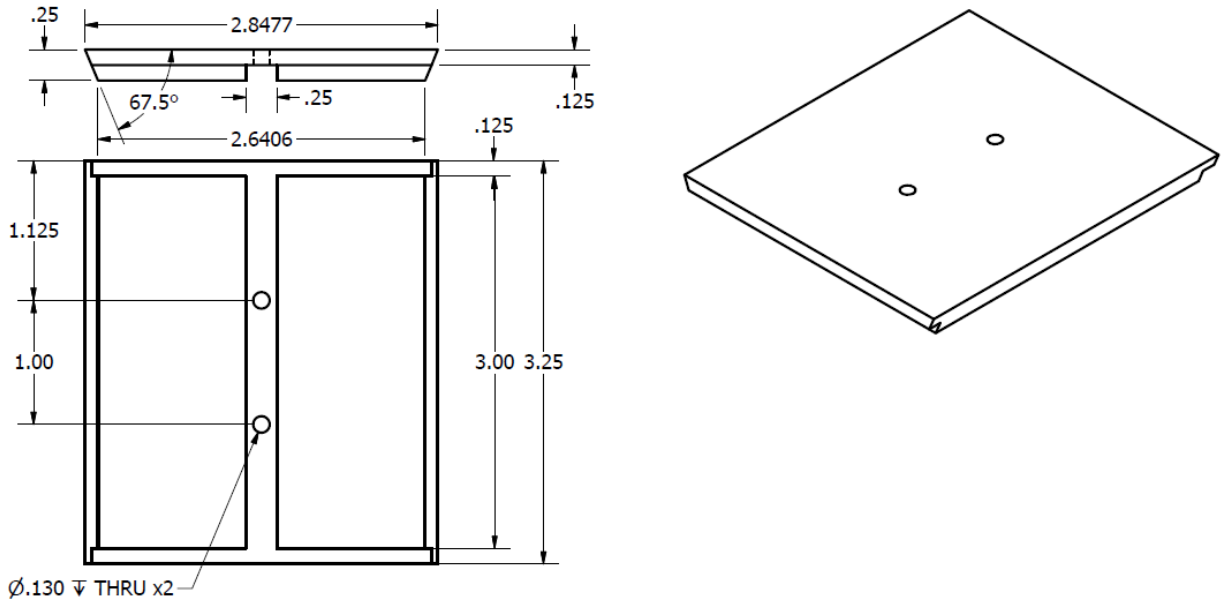

Figure 62: Wind tunnel extension slideway drawing. Two were manufactured and form the top and bottom of the extension with a guideway for the support strut. Measurements in inches.

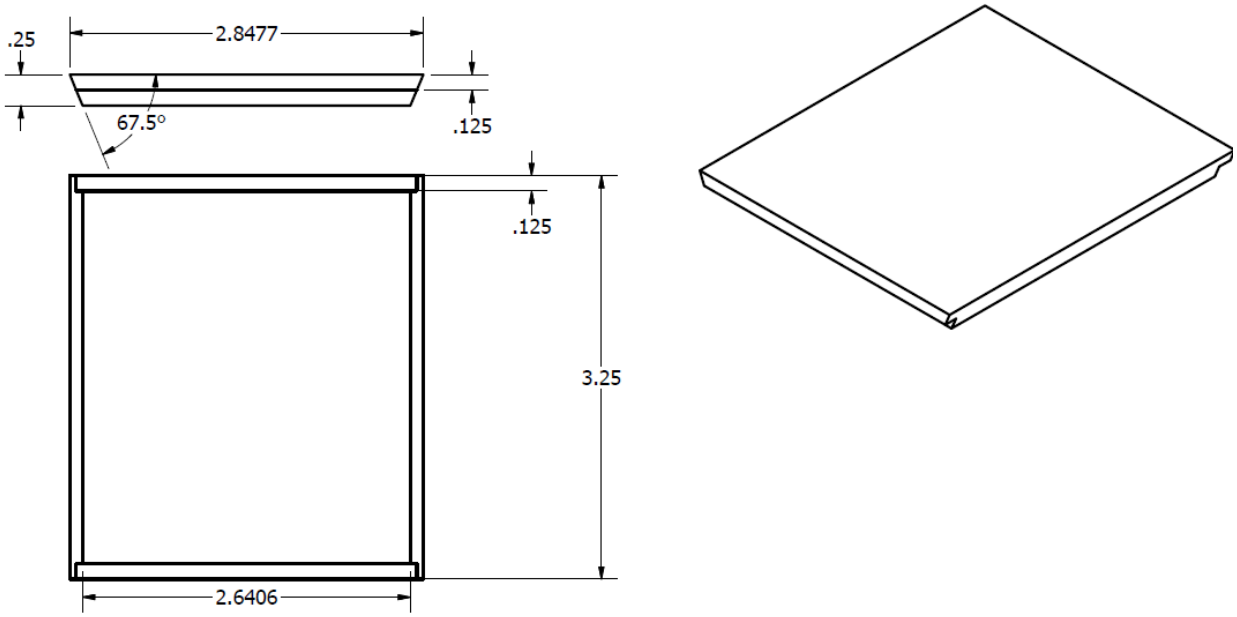

Figure 63: Wind tunnel extension panel drawing. The six manufactured complete the octagonal extension. Measurements in inches.

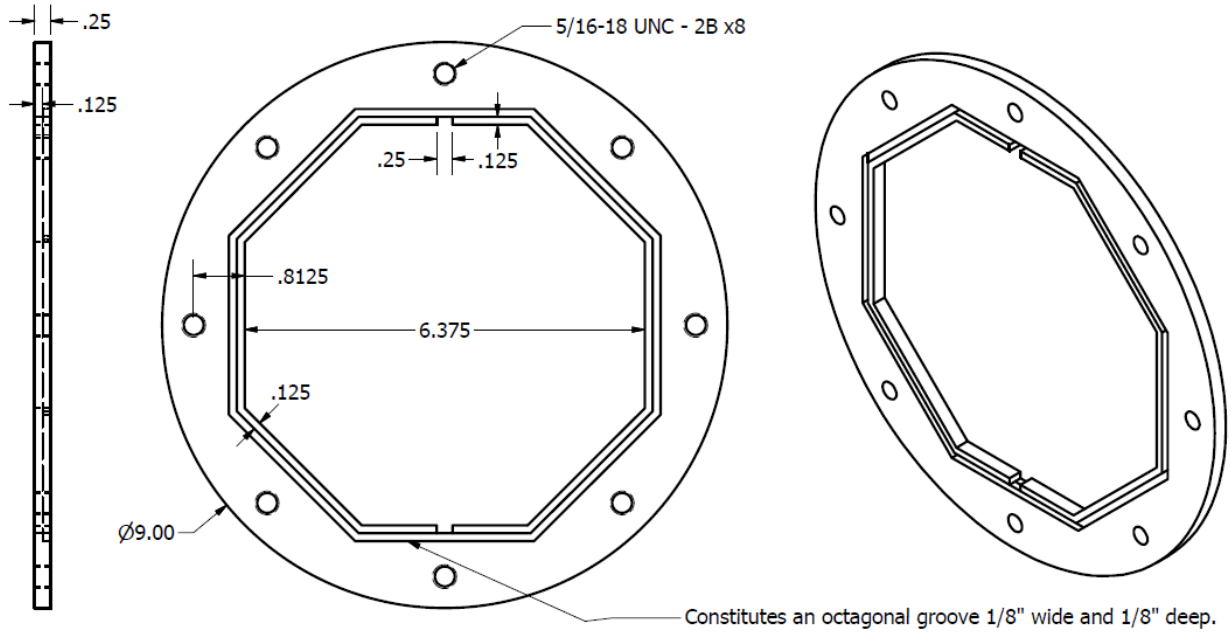

Figure 64: Wind tunnel extension flange plates. Interior is a regular octagon. One flange manufactured with threads, the other was manufactured with 5/16" thru holes. Measurements in inches.

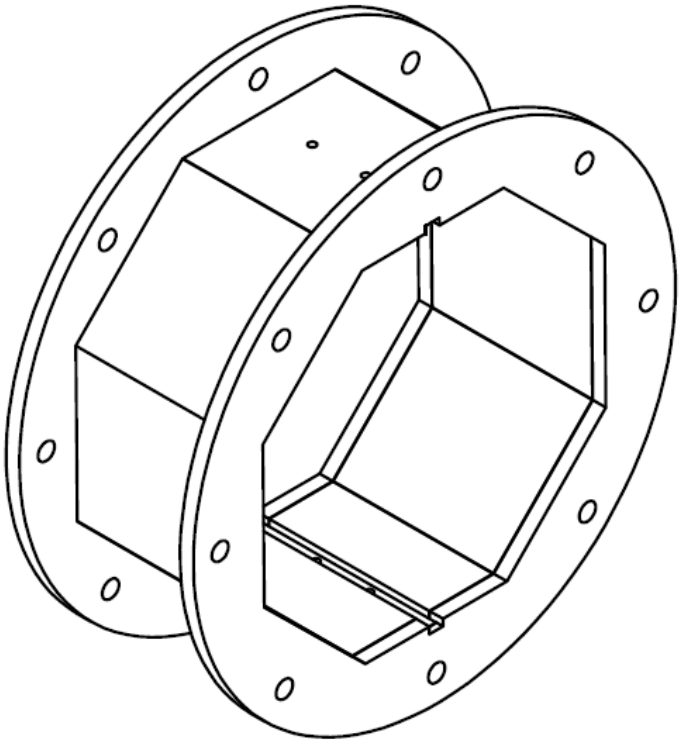

Figure 65: Diagram of wind tunnel test section extension assembly. The edges of each panel slot into the octagonal groove in the extensions to ensure proper fit.

A.5 Vertical Support Strut Drawing

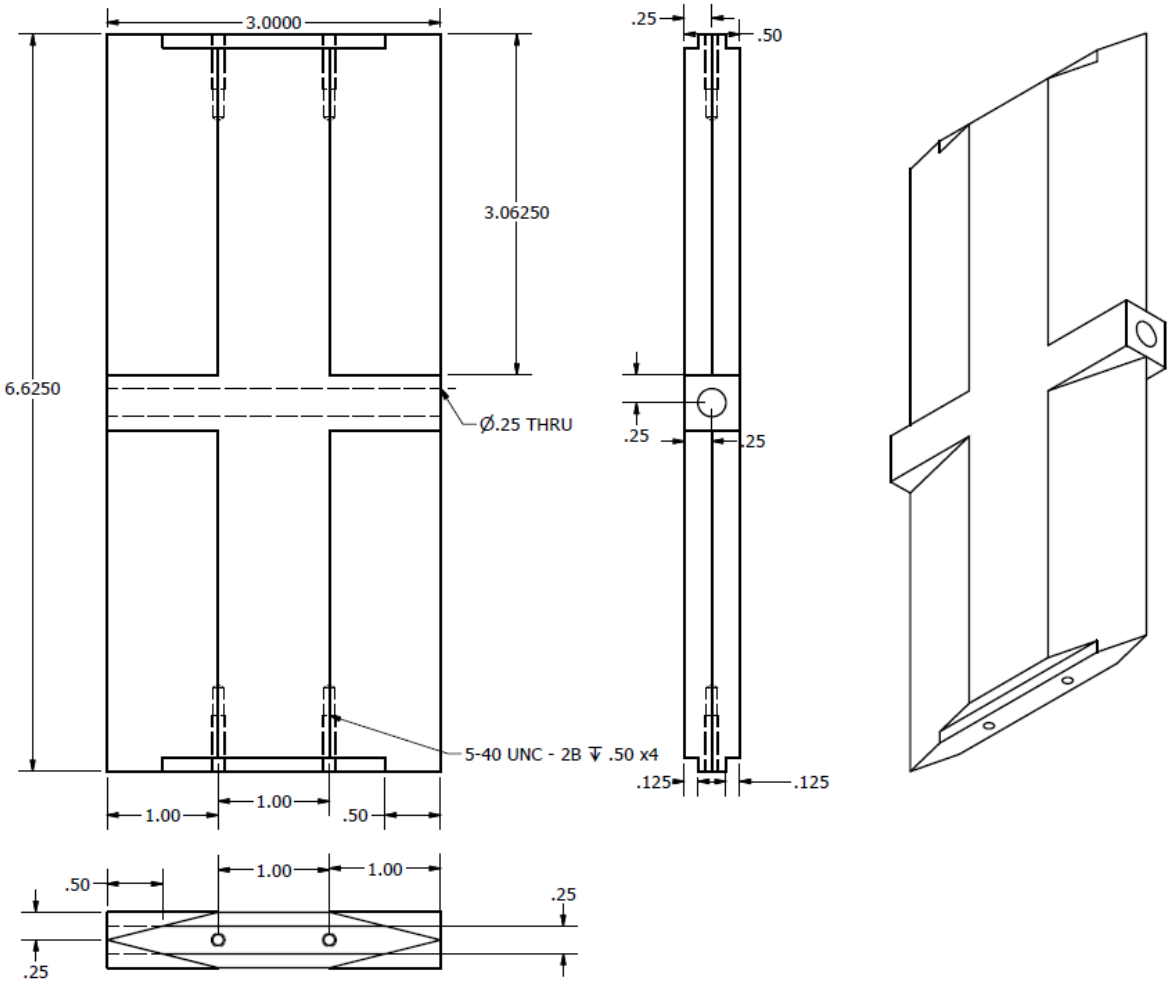

Figure 66: Vertical sting support strut. Dimensions in inches.

A.6 Model Characteristics

Table 29: Sting supported model diameters.

Angle of Attack (deg)	Diameter (mm)
0	44.39
0 Rough surface	44.25
0 Smooth surface	44.1
5	44.47
10	44.48
15	44.47
20	44.39
25	44.44
35	44.45
45	44.45

Table 30: Diameter and mass of models for use with dummy sting.

Angle of Attack (deg)	Diameter (mm)	Mass (g)
0	44.38	9.72
10	44.48	9.8
25	44.44	9.47
45	44.44	9.09

Table 31: Magnetically suspended model diameters and masses.

Angle of Attack (deg)	Diameter (mm)	Mass (g)
0	44.42	10.99
5	44.41	11.08
10	44.41	11.11
15	44.42	11.15
20	44.44	11.09
25	44.43	11.01
35	44.46	10.77
45	44.45	10.82

A.7 Sting Supported Model Drawings

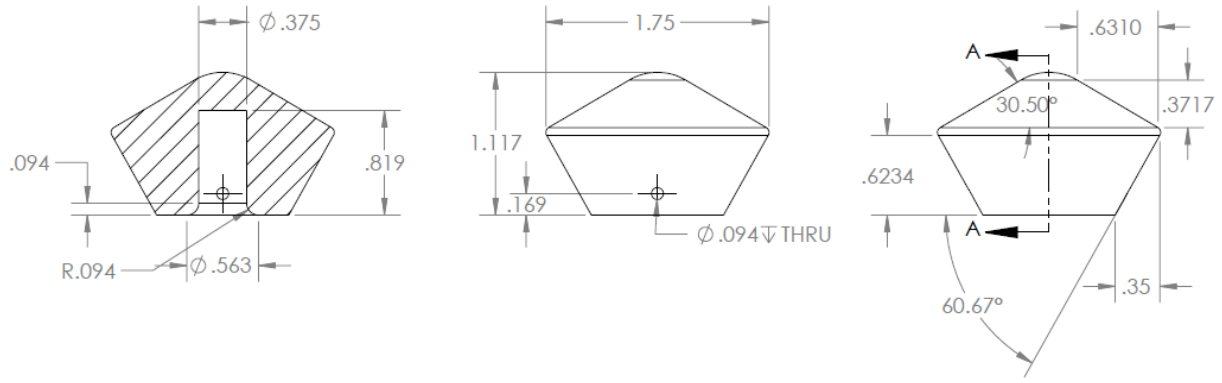

Figure 67: Drawing of 0° sting supported model. Dimensions in inches.

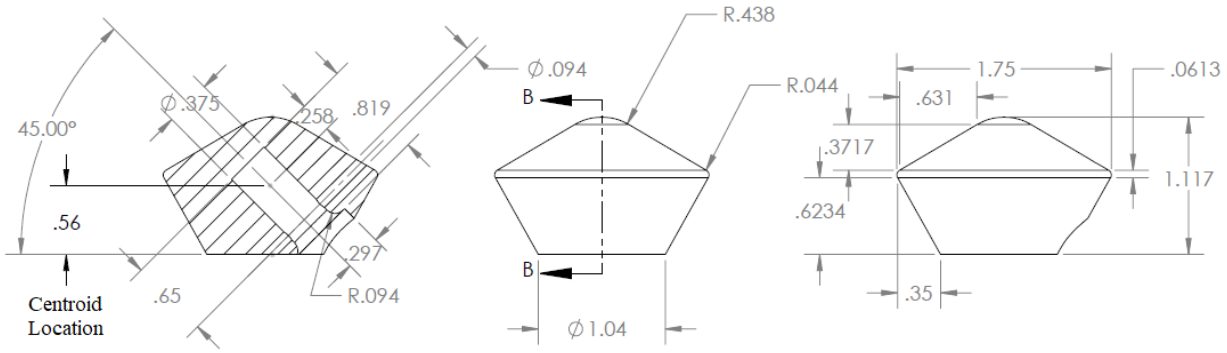

Figure 68: Drawing of 45° model for use with sting and MS-100 balance. Dimensions in inches. Same external geometry as the 0° model. The sting attachment point and dowel pin holes were rotated about the model centroid by 45°. Models at other orientations have the attachment point rotated about the centroid by the desired angle.

A.8 Drawings of Magnetically Suspended Models with Back Cavity

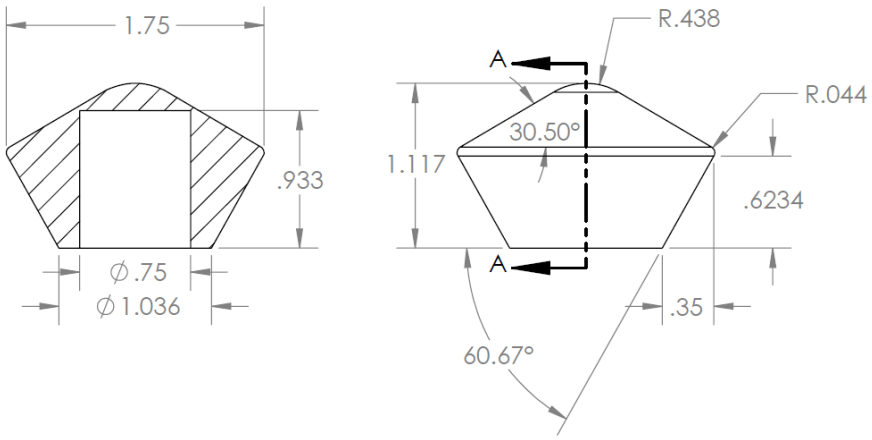

Figure 69: Drawing of 0° model for use with dummy sting. Dimensions in inches.

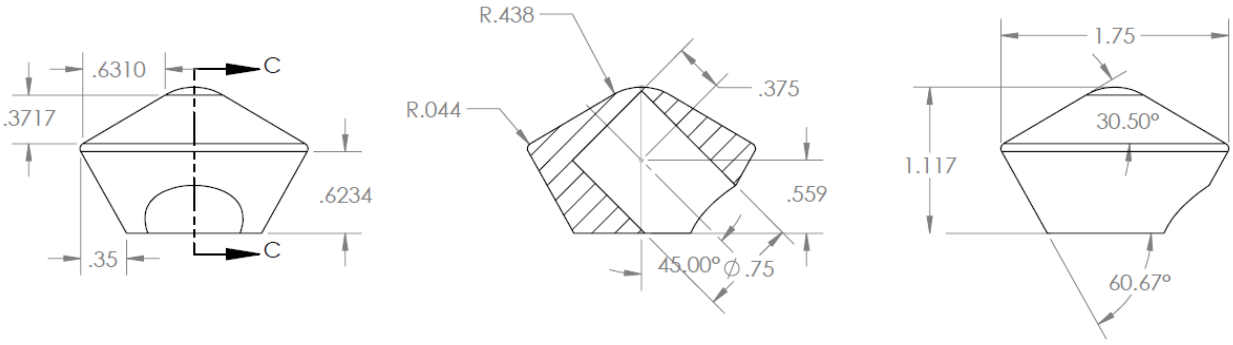

Figure 70: Drawing of 45° model for use with dummy sting. Dimensions in inches. Same external geometry as the 0° model; the internal cavity was rotated about the model centroid by 45°. Models at other orientations have a cavity rotated about the centroid by the desired angle.

A.9 Magnetically Suspended Model Drawings

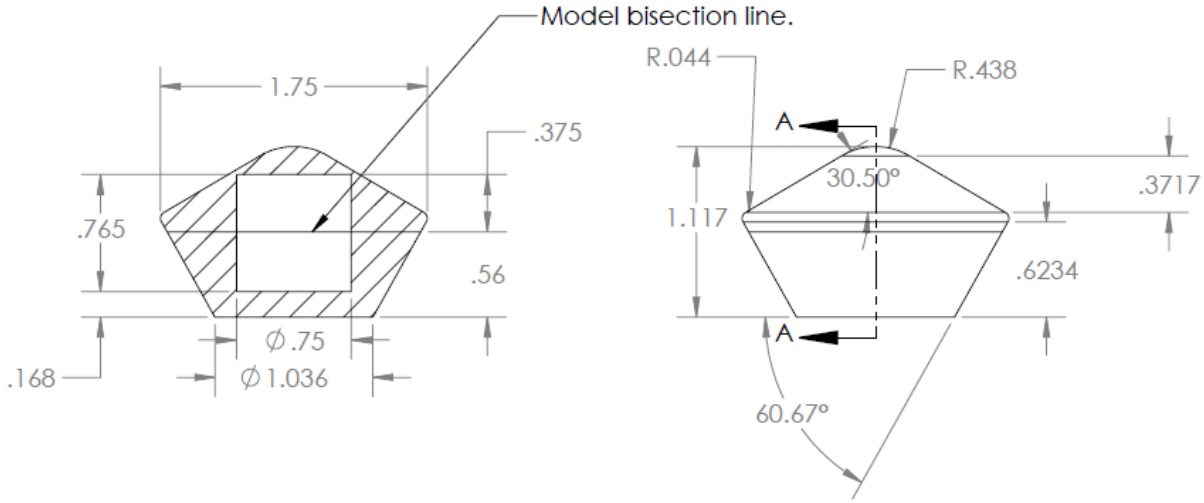

Figure 71: Drawing of 0° magnetically suspended model. Dimensions in inches. Model is bisected at the geometric center (denoted by horizontal line).

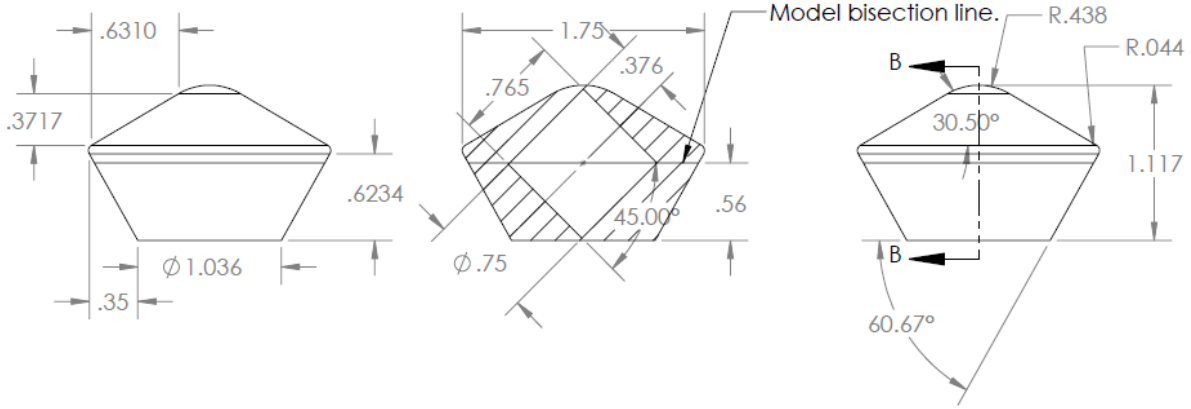

Figure 72: Drawing of 45° magnetically suspended model. Same external geometry as the 45° model. Bisected at geometric center. Dimensions in inches. The center cavity is rotated about the model centroid by 45°. Other models at other orientations have internal cavities rotated by the desired angle.

APPENDIX B. EXPERIMENTAL DATA

B.1 Electrical Zeroes

Table 32: Measurements used to determine MS-100 electrical zeroes.

		Repeated Measurement (values in volts)		
	Component	1	2	3
Gravity acting along positive axial direction. (MS-100 pointing up)	Normal	1.50578E-03	1.50632E-03	1.50612E-03
	Axial	-1.92318E-04	-1.91485E-04	-1.91129E-04
	Pitch	1.87632E-03	1.87672E-03	1.87738E-03
	Roll	1.17074E-03	1.17112E-03	1.17106E-03
	Side	2.13246E-03	2.13176E-03	2.13175E-03
	Yaw	-5.45225E-04	-5.44980E-04	-5.46023E-04
	Source	5.03003E+00	5.03024E+00	5.03011E+00
	Component	1	2	2
Gravity acting along negative axial direction (MS-100 pointing down)	Normal	1.50473E-03	1.50518E-03	1.50510E-03
	Axial	-2.56856E-04	-2.56742E-04	-2.56341E-04
	Pitch	1.87576E-03	1.87597E-03	1.87597E-03
	Roll	1.17020E-03	1.17051E-03	1.17079E-03
	Side	2.13207E-03	2.13313E-03	2.13147E-03
	Yaw	-5.45734E-04	-5.44647E-04	-5.46792E-04
	Source	5.03028E+00	5.03035E+00	5.03005E+00
	Component	1	2	3
Null-offset bias of NiDAQ. (MS-100 unpowered)	Normal	2.65190E-04	2.66130E-04	2.66610E-04
	Axial	2.65170E-04	2.66080E-04	2.65680E-04
	Pitch	2.65780E-04	2.67220E-04	2.66970E-04
	Roll	2.65580E-04	2.67160E-04	2.66880E-04
	Side	2.68570E-04	2.68060E-04	2.68540E-04
	Yaw	2.66950E-04	2.66420E-04	2.67060E-04
	Source	4.42600E-05	4.36800E-05	4.38100E-05

B.2 MS-100 Test Loads

Table 33: Raw voltages from MS-100 Test Loads

Loading Condition	Load Voltages						
Loading Condition	Normal	Axial	Pitch	Roll	Yaw	Side	Source
Positive Normal	1.49160E-03	-1.71030E-04	1.92036E-03	1.17295E-03	2.14666E-03	-5.47490E-04	5.00995
0g	1.49721E-03	-1.70700E-04	1.92638E-03	1.17339E-03	2.14704E-03	-5.47300E-04	5.00986
4.96g	1.54816E-03	-1.71720E-04	1.98376E-03	1.17360E-03	2.14932E-03	-5.45210E-04	5.00956
55.17g	1.59941E-03	-1.73560E-04	2.04142E-03	1.17415E-03	2.15189E-03	-5.42950E-04	5.00985
105.24g	1.65100E-03	-1.74240E-04	2.09947E-03	1.17523E-03	2.15370E-03	-5.41430E-04	5.00951
155.36g	1.75310E-03	-1.77030E-04	2.21465E-03	1.17558E-03	2.15805E-03	-5.37410E-04	5.00950
255.54g	1.85554E-03	-1.78700E-04	2.32941E-03	1.17599E-03	2.16338E-03	-5.32750E-04	5.00981
355.73g	Normal	Axial	Pitch	Roll	Yaw	Side	Source
Positive Side	1.47656E-03	-1.70820E-04	1.90882E-03	1.17301E-03	2.16411E-03	-5.26950E-04	5.00980
0g	1.47622E-03	-1.71500E-04	1.90854E-03	1.17236E-03	2.17221E-03	-5.19690E-04	5.00943
4.96g	1.47291E-03	-1.76300E-04	1.90596E-03	1.16917E-03	2.25404E-03	-4.48540E-04	5.00905
55.17g	1.46981E-03	-1.81080E-04	1.90370E-03	1.16478E-03	2.33700E-03	-3.76690E-04	5.00910
105.24g	1.46650E-03	-1.86020E-04	1.90058E-03	1.15961E-03	2.41932E-03	-3.05420E-04	5.00929
155.36g	1.46016E-03	-1.95710E-04	1.89568E-03	1.15161E-03	2.58444E-03	-1.62290E-04	5.00928
255.54g	1.45364E-03	-2.05230E-04	1.89019E-03	1.14399E-03	2.74895E-03	-1.92500E-05	5.00932
355.73g	Normal	Axial	Pitch	Roll	Yaw	Side	Source
Negative Roll 0.08m offset	1.47835E-03	-1.71530E-04	1.91017E-03	1.17160E-03	2.16481E-03	-5.25950E-04	5.00939
0g	1.48022E-03	-1.72060E-04	1.91191E-03	1.15256E-03	2.17402E-03	-5.19160E-04	5.00944
4.96g	1.49557E-03	-1.79710E-04	1.92673E-03	9.59070E-04	2.26579E-03	-4.49880E-04	5.00925
55.17g	1.50528E-03	-1.88680E-04	1.93588E-03	7.50440E-04	2.35291E-03	-3.80990E-04	5.00925
105.24g	Normal	Axial	Pitch	Roll	Yaw	Side	Source
Negative Axial	1.47690E-03	-2.02750E-04	1.90867E-03	1.17219E-03	2.14703E-03	-5.47570E-04	5.00925
0g	1.47780E-03	-2.12940E-04	1.90939E-03	1.17307E-03	2.14751E-03	-5.47090E-04	5.00946
4.96g	1.47753E-03	-3.23080E-04	1.90912E-03	1.17267E-03	2.14653E-03	-5.46850E-04	5.00915
55.17g	1.47773E-03	-4.33300E-04	1.90827E-03	1.17337E-03	2.14853E-03	-5.46400E-04	5.00915
105.24g	1.47747E-03	-5.44140E-04	1.90660E-03	1.17277E-03	2.14759E-03	-5.46040E-04	5.00914
155.36g	1.47770E-03	-7.64150E-04	1.90287E-03	1.17312E-03	2.15104E-03	-5.45130E-04	5.00925
255.54g	1.47741E-03	-9.85920E-04	1.90373E-03	1.17311E-03	2.14855E-03	-5.44030E-04	5.00887

Table 34: Tare values for MS-100 test loads.

Loading Condition	**Tare Values (mV/V)**					
Positive Normal	Normal	Axial	Pitch	Roll	Yaw	Side
0g	-1.49855E-03	1.05609E-02	1.02938E-02	1.45535E-03	4.59559E-03	-8.53240E-04
4.96g	-1.49855E-03	1.05609E-02	1.02938E-02	1.45535E-03	4.59559E-03	-8.53240E-04
55.17g	-1.49855E-03	1.05609E-02	1.02938E-02	1.45535E-03	4.59559E-03	-8.53240E-04
105.24g	-1.49855E-03	1.05609E-02	1.02938E-02	1.45535E-03	4.59559E-03	-8.53240E-04
155.36g	-1.49855E-03	1.05609E-02	1.02938E-02	1.45535E-03	4.59559E-03	-8.53240E-04
255.54g	-1.49855E-03	1.05609E-02	1.02938E-02	1.45535E-03	4.59559E-03	-8.53240E-04
355.73g	-1.49855E-03	1.05609E-02	1.02938E-02	1.45535E-03	4.59559E-03	-8.53240E-04
Positive Side	Normal	Axial	Pitch	Roll	Yaw	Side
0g	-4.55664E-03	1.04560E-02	8.06079E-03	1.39973E-03	8.08287E-03	3.25220E-03
4.96g	-4.55664E-03	1.04560E-02	8.06079E-03	1.39973E-03	8.08287E-03	3.25220E-03
55.17g	-4.55664E-03	1.04560E-02	8.06079E-03	1.39973E-03	8.08287E-03	3.25220E-03
105.24g	-4.55664E-03	1.04560E-02	8.06079E-03	1.39973E-03	8.08287E-03	3.25220E-03
155.36g	-4.55664E-03	1.04560E-02	8.06079E-03	1.39973E-03	8.08287E-03	3.25220E-03
255.54g	-4.55664E-03	1.04560E-02	8.06079E-03	1.39973E-03	8.08287E-03	3.25220E-03
355.73g	-4.55664E-03	1.04560E-02	8.06079E-03	1.39973E-03	8.08287E-03	3.25220E-03
Negative Roll 0.08m offset	Normal	Axial	Pitch	Roll	Yaw	Side
0g	-4.18409E-03	1.03139E-02	8.28411E-03	1.10631E-03	8.34779E-03	3.47117E-03
4.96g	-4.18409E-03	1.03139E-02	8.28411E-03	1.10631E-03	8.34779E-03	3.47117E-03
55.17g	-4.18409E-03	1.03139E-02	8.28411E-03	1.10631E-03	8.34779E-03	3.47117E-03
105.24g	-4.18409E-03	1.03139E-02	8.28411E-03	1.10631E-03	8.34779E-03	3.47117E-03
Negative Axial	Normal	Axial	Pitch	Roll	Yaw	Side
0g	-4.40527E-03	4.13548E-03	8.07390E-03	1.26229E-03	4.79050E-03	-7.88300E-04
4.96g	-4.40527E-03	4.13548E-03	8.07390E-03	1.26229E-03	4.79050E-03	-7.88300E-04
55.17g	-4.40527E-03	4.13548E-03	8.07390E-03	1.26229E-03	4.79050E-03	-7.88300E-04
105.24g	-4.40527E-03	4.13548E-03	8.07390E-03	1.26229E-03	4.79050E-03	-7.88300E-04
155.36g	-4.40527E-03	4.13548E-03	8.07390E-03	1.26229E-03	4.79050E-03	-7.88300E-04
255.54g	-4.40527E-03	4.13548E-03	8.07390E-03	1.26229E-03	4.79050E-03	-7.88300E-04
355.73g	-4.40527E-03	4.13548E-03	8.07390E-03	1.26229E-03	4.79050E-03	-7.88300E-04

Table 35: MS-100 test loading outputs with moment center transfer.

Loading Condition	Calculated Loads (N and Nm as appropriate)					
Positive Normal	Normal	Axial	Pitch	Roll	Yaw	Side
0g	-3.61342E-03	-2.15607E-03	1.73297E-04	-3.22097E-05	-1.28671E-04	2.56972E-03
4.96g	5.09126E-02	-8.64270E-04	6.76591E-05	4.86354E-05	-6.98376E-05	3.46530E-03
55.17g	5.41967E-01	-6.73440E-03	8.97734E-05	5.12738E-06	-5.90000E-05	1.50286E-02
105.24g	1.03432E+00	-1.62028E-02	7.82323E-05	3.21143E-07	-1.04438E-04	2.81895E-02
155.36g	1.53219E+00	-2.08126E-02	7.83022E-05	1.26284E-04	-3.28011E-05	3.56886E-02
255.54g	2.51439E+00	-3.60758E-02	1.84395E-04	-4.09056E-06	-1.02564E-04	5.82164E-02
355.73g	3.49889E+00	-4.63040E-02	-1.65138E-06	-1.33616E-04	-1.52860E-04	8.53563E-02
Positive Side	Normal	Axial	Pitch	Roll	Yaw	Side
0g	-2.41421E-04	1.05295E-03	-6.35425E-05	4.16123E-05	-9.90871E-05	2.19836E-03
4.96g	-1.37096E-03	-5.69224E-04	-5.65303E-05	-4.32355E-05	-1.17261E-04	5.19011E-02
55.17g	-1.96594E-02	-7.69535E-03	-2.10530E-05	-3.94485E-04	-1.04233E-04	5.41177E-01
105.24g	-3.78484E-02	-1.44386E-02	4.55257E-05	-9.96633E-04	-8.17746E-05	1.03568E+00
155.36g	-5.91239E-02	-2.19574E-02	-9.90657E-05	-1.75824E-03	-7.82211E-05	1.52632E+00
255.54g	-9.61805E-02	-3.63422E-02	-4.67349E-05	-2.80754E-03	-4.53146E-05	2.51127E+00
355.73g	-1.34906E-01	-5.01482E-02	-1.35291E-04	-3.78687E-03	-1.39468E-04	3.49562E+00
Negative Roll 0.08m offset	Normal	Axial	Pitch	Roll	Yaw	Side
0g	2.38891E-04	9.37084E-04	5.44609E-05	6.91124E-05	-1.71456E-04	1.24232E-03
4.96g	6.86401E-03	1.43723E-03	7.82419E-05	-3.62208E-03	-1.84957E-05	4.95107E-02
55.17g	4.09312E-02	-4.23301E-03	7.74260E-04	-4.11068E-02	1.09526E-03	5.41737E-01
105.24g	9.36017E-03	-1.59554E-02	1.86514E-03	-8.15732E-02	9.72786E-04	1.03328E+00
Negative Axial	Normal	Axial	Pitch	Roll	Yaw	Side
0g	-2.77852E-03	-2.89771E-04	3.87847E-05	4.06304E-05	-6.09951E-05	-8.01934E-04
4.96g	5.91549E-03	-4.57424E-02	-7.67747E-05	2.02226E-04	-9.91543E-05	2.53984E-03
55.17g	3.94961E-03	-5.37391E-01	-3.08608E-05	1.32980E-04	-3.74524E-04	4.03976E-03
105.24g	6.48480E-03	-1.02916E+00	-3.90709E-04	2.81024E-04	8.25192E-06	6.96145E-03
155.36g	3.60007E-03	-1.52387E+00	-8.46597E-04	1.60417E-04	-3.32113E-04	9.52162E-03
255.54g	6.01323E-03	-2.50541E+00	-2.20761E-03	2.46724E-04	2.73135E-04	1.56015E-02
355.73g	4.32617E-03	-3.49560E+00	-1.73734E-03	2.43231E-04	-6.20616E-04	2.30679E-02

B.3 MSBS Test Loads

Table 36: Test loads used to calibrate the MSBS coil coefficients.

Loading Condition	Applied Mass (g)	Applied Force (N)	Drag (amps)	Lift (amps)	Side (amps
Drag Loading	4.96	0.0490325	-1.0670052	-13.897547	-0.036787837
	25	0.2451625	-6.3354432	-13.977238	-0.015746707
	45	0.4412925	-11.507279	-13.982649	-0.040593539
	65	0.6374225	-16.608428	-14.18072	-0.02990115
	85	0.8335525	-21.780626	-14.260626	-0.031827146
	105	1.0296825	-26.934833	-14.320782	-0.041669033
	125	1.2258125	-32.099146	-14.31002	0.03130119
	145	1.4219425	-37.242236	-14.41722	-0.025987204
Side Loading	4.96	0.0490325	0.18914156	-13.946021	1.616696295
	25	0.2451625	0.2561685	-14.023205	8.316283803
	45	0.4412925	0.4204692	-14.11819	15.03664803
	65	0.6374225	0.69067717	-14.221147	21.80885594
	85	0.8335525	1.05618005	-14.325881	28.65362856
	105	1.0296825	1.52944736	-14.440636	35.65976479
	125	1.2258125	2.22376357	-14.540021	42.81805099
Lift Loading	51.84	0.50836896	0.2762	-17.6513	-0.0496
	51.93	0.509251545	0.156	-17.7034	-0.0324
	51.96	0.50954574	0.0963	-17.6686	-0.0445
	52	0.509938	0.1075	-17.6792	-0.0429
	51.86	0.50856509	0.2243	-17.6149	-0.0445
	51.62	0.50621153	0.1401	-17.5608	-0.0487
	51.67	0.506701855	0.1893	-17.5724	-0.0486
	50.57	0.495914705	0.2827	-17.0816	-0.0355
	49.94	0.48973661	0.298	-16.9459	-0.0533
	40.85	0.400595525	0.14690752	-13.88468	0.056138593
	58.86	0.57721059	0.4679	-20.096	-0.0694
	77.63	0.761278595	1.11157424	-27.015016	0.101800809
	95.55	0.937011075	1.60528774	-33.376409	-0.124503488

B.4 Sting Supported Data

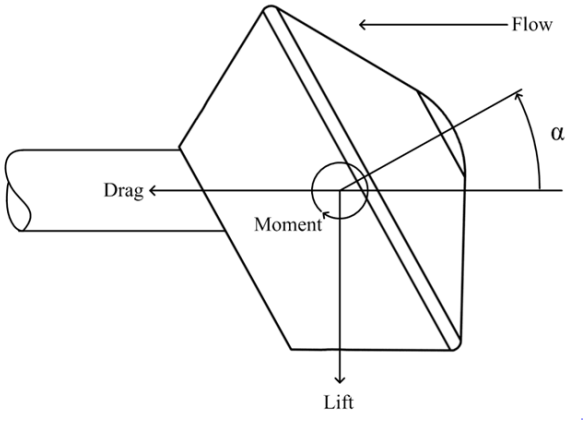

Figure 73: Sign convention for raw data. Taken from the balance convention for Side Force and Yawing Moment.

Table 37: Experimental data for sting supported 0° model. Air density was 1.9591 kg/m^3 for all tests.

Mean Values							
Q (Pa)	Re	Drag (N)	Lift (N)	Pitching (Nm)	C_D	C_L	C_M
7.874E+00	1.044E+04	-4.826E-04	1.481E-03	-4.872E-05	-4.181E-02	1.216E-01	-8.976E-02
7.956E+00	1.049E+04	3.323E-03	5.604E-03	-2.347E-04	2.678E-01	4.543E-01	-4.278E-01
1.047E+01	1.203E+04	-2.422E-05	1.051E-03	-1.592E-04	-2.261E-03	6.492E-02	-2.212E-01
3.804E+01	2.294E+04	4.990E-02	3.771E-03	-1.955E-04	8.476E-01	6.399E-02	-7.465E-02
3.824E+01	2.300E+04	4.596E-02	2.081E-03	-1.260E-04	7.764E-01	3.521E-02	-4.809E-02
3.828E+01	2.301E+04	4.787E-02	2.021E-03	-7.766E-05	8.080E-01	3.414E-02	-2.947E-02
1.477E+02	4.519E+04	2.252E-01	7.152E-03	-3.918E-04	9.853E-01	3.129E-02	-3.862E-02
1.481E+02	4.526E+04	2.199E-01	1.201E-03	-1.349E-04	9.593E-01	5.241E-03	-1.325E-02
1.485E+02	4.532E+04	2.217E-01	2.779E-03	-2.285E-04	9.647E-01	1.208E-02	-2.240E-02
3.473E+02	6.930E+04	5.455E-01	1.180E-02	-6.759E-04	1.015E+00	2.194E-02	-2.831E-02
3.484E+02	6.942E+04	5.392E-01	-2.303E-03	-9.664E-05	1.000E+00	-4.294E-03	-4.014E-03
3.487E+02	6.945E+04	5.412E-01	-2.907E-03	-3.181E-04	1.003E+00	-5.390E-03	-1.329E-02
6.363E+02	9.381E+04	1.008E+00	-1.927E-03	-3.761E-05	1.023E+00	-1.955E-03	-8.414E-04
6.395E+02	9.404E+04	1.004E+00	2.501E-03	-3.433E-04	1.015E+00	2.517E-03	-7.810E-03
6.403E+02	9.410E+04	1.004E+00	-7.680E-03	-3.173E-04	1.013E+00	-7.737E-03	-7.231E-03
1.025E+03	1.191E+05	1.620E+00	1.091E-02	-1.070E-03	1.022E+00	6.898E-03	-1.521E-02
1.027E+03	1.192E+05	1.618E+00	-2.051E-03	-6.088E-04	1.018E+00	-1.286E-03	-8.636E-03
1.028E+03	1.193E+05	1.617E+00	-8.989E-03	-2.221E-04	1.016E+00	-5.650E-03	-3.139E-03
1.490E+03	1.436E+05	2.374E+00	4.480E-03	4.704E-05	1.029E+00	1.925E-03	4.750E-04
1.492E+03	1.436E+05	2.366E+00	-1.984E-02	-4.596E-04	1.025E+00	-8.594E-03	-4.487E-03
1.493E+03	1.437E+05	2.369E+00	-4.653E-03	-8.692E-04	1.026E+00	-1.995E-03	-8.482E-03

2.049E+03	1.684E+05	3.273E+00	1.282E-02	-1.091E-03	1.032E+00	4.071E-03	-7.771E-03
2.052E+03	1.685E+05	3.274E+00	2.982E-03	-1.721E-03	1.031E+00	9.246E-04	-1.220E-02
2.053E+03	1.685E+05	3.270E+00	-1.946E-02	-8.386E-04	1.029E+00	-6.111E-03	-5.977E-03
			Standard Deviation				
Q (Pa)	Re	Drag (N)	Lift (N)	Pitching (Nm)	C_D	C_L	C_M
7.821E-02	5.191E+01	3.176E-03	3.928E-03	1.979E-04	2.627E-01	3.220E-01	3.664E-01
8.145E-02	5.369E+01	2.922E-03	6.329E-03	2.226E-04	2.345E-01	5.139E-01	4.069E-01
5.836E-02	3.351E+01	2.721E-03	3.299E-03	2.084E-04	1.674E-01	2.040E-01	2.896E-01
1.057E-01	3.187E+01	2.714E-03	6.157E-03	3.247E-04	4.517E-02	1.046E-01	1.242E-01
1.408E-01	4.234E+01	3.691E-03	5.893E-03	2.369E-04	6.022E-02	9.932E-02	9.009E-02
1.050E-01	3.157E+01	2.366E-03	6.685E-03	2.685E-04	3.843E-02	1.129E-01	1.022E-01
3.734E-01	5.714E+01	3.115E-03	5.417E-03	3.115E-04	1.338E-02	2.375E-02	3.071E-02
4.402E-01	6.725E+01	3.188E-03	8.068E-03	3.670E-04	1.472E-02	3.518E-02	3.607E-02
4.064E-01	6.201E+01	3.325E-03	5.597E-03	2.657E-04	1.423E-02	2.435E-02	2.601E-02
1.252E+00	1.249E+02	3.071E-03	9.647E-03	5.441E-04	6.760E-03	1.793E-02	2.278E-02
1.088E+00	1.084E+02	6.138E-03	1.369E-02	7.814E-04	9.911E-03	2.536E-02	3.263E-02
1.097E+00	1.093E+02	6.931E-03	8.030E-03	5.975E-04	1.204E-02	1.490E-02	2.495E-02
2.985E+00	2.202E+02	8.580E-03	1.505E-02	8.007E-04	1.013E-02	1.527E-02	1.834E-02
3.035E+00	2.232E+02	6.793E-03	1.629E-02	1.167E-03	7.830E-03	1.645E-02	2.653E-02
2.678E+00	1.968E+02	8.673E-03	1.509E-02	1.162E-03	7.705E-03	1.520E-02	2.641E-02
2.664E+00	1.547E+02	1.123E-02	2.273E-02	1.296E-03	7.393E-03	1.432E-02	1.843E-02
3.294E+00	1.911E+02	1.483E-02	2.203E-02	1.653E-03	7.999E-03	1.387E-02	2.345E-02
3.476E+00	2.015E+02	1.190E-02	2.032E-02	9.731E-04	7.410E-03	1.277E-02	1.377E-02
5.196E+00	2.502E+02	1.701E-02	3.282E-02	1.917E-03	8.306E-03	1.423E-02	1.874E-02
5.012E+00	2.413E+02	1.737E-02	2.714E-02	1.941E-03	8.402E-03	1.175E-02	1.893E-02
5.799E+00	2.793E+02	1.385E-02	3.363E-02	2.094E-03	5.752E-03	1.457E-02	2.041E-02
9.743E+00	4.000E+02	1.752E-02	3.853E-02	2.744E-03	6.394E-03	1.214E-02	1.946E-02
5.993E+00	2.461E+02	1.659E-02	4.186E-02	2.846E-03	6.492E-03	1.315E-02	2.017E-02
7.869E+00	3.230E+02	2.369E-02	4.490E-02	3.027E-03	7.668E-03	1.411E-02	2.143E-02

Table 38: Experimental data for sting supported 0° model with smooth surface. Air density was 1.2035 kg/m^3 for all tests.

			Mean Values				
Q (Pa)	Re	Drag (N)	Lift (N)	Pitching (Nm)	C_D	C_L	C_M
7.831E+00	1.037E+04	-2.537E-03	3.361E-03	-3.409E-04	-2.134E-01	2.812E-01	-6.462E-01
7.834E+00	1.037E+04	-2.117E-03	-4.148E-03	4.044E-05	-1.787E-01	-3.468E-01	7.630E-02
7.864E+00	1.039E+04	-1.177E-03	-1.480E-03	-5.620E-05	-9.926E-02	-1.226E-01	-1.062E-01
7.958E+00	1.045E+04	2.550E-03	5.236E-03	-1.764E-04	2.073E-01	4.330E-01	-3.317E-01
3.672E+01	2.246E+04	4.211E-02	5.158E-03	-4.735E-04	7.508E-01	9.203E-02	-1.914E-01

3.686E+01	2.250E+04	4.384E-02	5.350E-04	-8.903E-05	7.785E-01	9.591E-03	-3.602E-02
3.690E+01	2.251E+04	4.874E-02	3.203E-03	3.480E-06	8.646E-01	5.682E-02	1.475E-03
1.428E+02	4.429E+04	2.114E-01	5.099E-03	-3.473E-04	9.693E-01	2.338E-02	-3.610E-02
1.429E+02	4.430E+04	2.133E-01	-8.993E-04	-1.083E-04	9.774E-01	-4.124E-03	-1.123E-02
1.436E+02	4.442E+04	2.193E-01	5.158E-03	-1.306E-04	9.994E-01	2.350E-02	-1.344E-02
3.335E+02	6.768E+04	5.181E-01	6.233E-03	-4.153E-04	1.017E+00	1.224E-02	-1.847E-02
3.357E+02	6.791E+04	5.205E-01	-6.014E-03	-8.964E-05	1.015E+00	-1.170E-02	-4.039E-03
3.361E+02	6.795E+04	5.298E-01	1.732E-03	-2.977E-04	1.032E+00	3.351E-03	-1.313E-02
6.208E+02	9.234E+04	9.708E-01	-6.673E-03	-1.035E-04	1.024E+00	-6.968E-03	-2.646E-03
6.223E+02	9.246E+04	9.876E-01	2.862E-03	-4.116E-04	1.039E+00	3.017E-03	-9.786E-03
6.229E+02	9.250E+04	9.732E-01	-1.518E-02	1.715E-04	1.023E+00	-1.599E-02	4.158E-03
9.933E+02	1.168E+05	1.563E+00	-1.020E-02	4.344E-04	1.030E+00	-6.712E-03	6.468E-03
9.938E+02	1.168E+05	1.565E+00	-8.777E-03	6.401E-05	1.031E+00	-5.789E-03	9.800E-04
9.955E+02	1.169E+05	1.582E+00	3.003E-03	-2.301E-04	1.041E+00	1.970E-03	-3.410E-03
1.440E+03	1.406E+05	2.286E+00	-1.207E-02	7.823E-04	1.039E+00	-5.479E-03	8.055E-03
1.443E+03	1.408E+05	2.309E+00	-1.962E-03	-4.715E-04	1.048E+00	-8.928E-04	-4.832E-03
1.445E+03	1.409E+05	2.294E+00	-1.429E-02	9.624E-04	1.040E+00	-6.476E-03	9.878E-03
1.971E+03	1.645E+05	3.165E+00	-1.681E-02	2.621E-04	1.051E+00	-5.573E-03	1.951E-03
1.981E+03	1.650E+05	3.182E+00	-9.318E-03	8.183E-04	1.051E+00	-3.079E-03	6.145E-03

Standard Deviation

Q (Pa)	Re	Drag (N)	Lift (N)	Pitching (Nm)	C_D	C_L	C_M
6.327E-02	4.196E+01	2.454E-03	4.063E-03	2.044E-04	2.083E-01	3.391E-01	3.869E-01
6.836E-02	4.522E+01	2.944E-03	4.371E-03	1.811E-04	2.473E-01	3.645E-01	3.422E-01
6.181E-02	4.082E+01	2.383E-03	4.732E-03	2.027E-04	1.990E-01	3.935E-01	3.814E-01
9.628E-02	6.332E+01	2.975E-03	5.148E-03	2.141E-04	2.426E-01	4.267E-01	4.021E-01
1.478E-01	4.521E+01	3.301E-03	7.381E-03	4.383E-04	5.679E-02	1.316E-01	1.772E-01
7.136E-02	2.178E+01	2.722E-03	6.274E-03	3.988E-04	4.785E-02	1.114E-01	1.607E-01
1.238E-01	3.776E+01	2.906E-03	6.232E-03	4.196E-04	4.997E-02	1.106E-01	1.688E-01
2.375E-01	3.685E+01	3.680E-03	8.891E-03	6.133E-04	1.650E-02	4.077E-02	6.374E-02
1.075E-01	1.666E+01	4.375E-03	1.214E-02	8.309E-04	1.931E-02	5.563E-02	8.633E-02
3.936E-01	6.088E+01	4.042E-03	1.594E-02	1.147E-03	1.785E-02	7.264E-02	1.185E-01
9.904E-01	1.005E+02	6.153E-03	1.075E-02	1.174E-03	1.046E-02	2.110E-02	5.234E-02
1.464E+00	1.481E+02	5.796E-03	1.449E-02	1.172E-03	1.291E-02	2.824E-02	5.185E-02
1.091E+00	1.102E+02	6.340E-03	1.115E-02	8.621E-04	1.175E-02	2.172E-02	3.808E-02
2.838E+00	2.110E+02	9.454E-03	3.920E-02	3.309E-03	9.556E-03	4.137E-02	7.912E-02
3.657E+00	2.717E+02	1.101E-02	2.699E-02	2.211E-03	1.091E-02	2.842E-02	5.280E-02
3.576E+00	2.657E+02	9.012E-03	3.271E-02	2.930E-03	1.096E-02	3.437E-02	6.977E-02
1.899E+00	1.116E+02	1.287E-02	2.740E-02	2.569E-03	8.381E-03	1.807E-02	3.843E-02
3.087E+00	1.815E+02	9.954E-03	4.424E-02	3.441E-03	6.926E-03	2.913E-02	5.141E-02
2.881E+00	1.691E+02	1.478E-02	3.413E-02	3.409E-03	1.066E-02	2.243E-02	5.082E-02
4.323E+00	2.112E+02	1.322E-02	4.524E-02	4.237E-03	5.548E-03	2.059E-02	4.368E-02

4.563E+00	2.227E+02	1.788E-02	3.548E-02	2.924E-03	8.169E-03	1.608E-02	3.003E-02
5.318E+00	2.592E+02	1.596E-02	3.839E-02	3.045E-03	6.972E-03	1.741E-02	3.130E-02
5.494E+00	2.294E+02	1.654E-02	4.740E-02	3.302E-03	6.432E-03	1.573E-02	2.486E-02
6.048E+00	2.519E+02	2.345E-02	4.966E-02	5.066E-03	8.186E-03	1.642E-02	3.800E-02

Table 39: Experimental data for sting supported 0° model with rough surface. Air density was 1.2175 kg/m^3 for all tests.

Mean Values							
Q (Pa)	Re	Drag (N)	Lift (N)	Pitching (Nm)	C_D	C_L	C_M
7.910E+00	1.052E+04	-1.266E-04	3.421E-04	-1.763E-04	-1.248E-02	2.703E-02	-3.267E-01
7.922E+00	1.053E+04	1.539E-03	8.706E-04	-1.540E-04	1.248E-01	7.291E-02	-2.875E-01
7.952E+00	1.055E+04	3.092E-03	2.386E-03	-1.748E-04	2.507E-01	1.951E-01	-3.231E-01
3.731E+01	2.285E+04	4.536E-02	3.201E-03	-1.913E-04	7.903E-01	5.604E-02	-7.555E-02
3.738E+01	2.287E+04	4.707E-02	5.924E-04	-1.813E-05	8.188E-01	1.029E-02	-7.083E-03
3.760E+01	2.294E+04	4.729E-02	4.200E-03	-2.577E-04	8.178E-01	7.255E-02	-1.008E-01
1.488E+02	4.562E+04	2.202E-01	-7.689E-04	-1.508E-04	9.627E-01	-3.354E-03	-1.491E-02
1.489E+02	4.564E+04	2.232E-01	-1.525E-03	-5.569E-05	9.745E-01	-6.655E-03	-5.523E-03
1.491E+02	4.567E+04	2.261E-01	3.568E-03	-3.091E-04	9.859E-01	1.559E-02	-3.044E-02
3.464E+02	6.962E+04	5.461E-01	4.328E-03	-4.170E-04	1.025E+00	8.154E-03	-1.772E-02
3.514E+02	7.012E+04	5.477E-01	2.785E-03	-2.122E-04	1.014E+00	5.139E-03	-8.860E-03
3.519E+02	7.017E+04	5.450E-01	-1.791E-04	-1.356E-04	1.007E+00	-3.264E-04	-5.683E-03
6.453E+02	9.502E+04	1.021E+00	5.316E-03	-5.916E-04	1.029E+00	5.352E-03	-1.348E-02
6.512E+02	9.545E+04	1.028E+00	-2.691E-04	6.748E-05	1.026E+00	-2.777E-04	1.535E-03
6.516E+02	9.548E+04	1.021E+00	3.551E-03	-3.362E-04	1.019E+00	3.556E-03	-7.569E-03
1.035E+03	1.204E+05	1.642E+00	2.397E-03	-1.226E-04	1.031E+00	1.511E-03	-1.759E-03
1.044E+03	1.209E+05	1.641E+00	1.029E-02	-6.198E-04	1.022E+00	6.402E-03	-8.736E-03
1.044E+03	1.209E+05	1.649E+00	2.181E-03	-2.181E-04	1.027E+00	1.350E-03	-3.071E-03
1.509E+03	1.453E+05	2.416E+00	-9.474E-03	-7.120E-05	1.041E+00	-4.099E-03	-6.789E-04
1.517E+03	1.457E+05	2.413E+00	-2.156E-02	-2.123E-04	1.034E+00	-9.259E-03	-2.043E-03
1.518E+03	1.457E+05	2.415E+00	3.676E-03	1.030E-05	1.034E+00	1.580E-03	1.033E-04
2.073E+03	1.703E+05	3.326E+00	-1.458E-02	7.650E-04	1.043E+00	-4.567E-03	5.414E-03
2.086E+03	1.708E+05	3.327E+00	-6.869E-03	2.463E-04	1.037E+00	-2.145E-03	1.736E-03
2.088E+03	1.709E+05	3.338E+00	-9.612E-03	-3.670E-05	1.039E+00	-2.986E-03	-2.695E-04
Standard Deviation							
Q (Pa)	Re	Drag (N)	Lift (N)	Pitching (Nm)	C_D	C_L	C_M
7.764E-02	5.159E+01	3.056E-03	3.221E-03	1.472E-04	2.504E-01	2.648E-01	2.727E-01
7.806E-02	5.201E+01	2.480E-03	5.360E-03	2.284E-04	2.050E-01	4.404E-01	4.250E-01
7.299E-02	4.848E+01	3.029E-03	5.237E-03	1.921E-04	2.470E-01	4.287E-01	3.547E-01
1.318E-01	4.036E+01	3.239E-03	7.975E-03	3.983E-04	5.411E-02	1.392E-01	1.568E-01

1.357E-01	4.152E+01	3.171E-03	8.329E-03	4.412E-04	5.310E-02	1.452E-01	1.736E-01
8.454E-02	2.578E+01	3.339E-03	6.313E-03	2.837E-04	5.602E-02	1.092E-01	1.109E-01
3.989E-01	6.118E+01	4.035E-03	5.441E-03	4.121E-04	1.680E-02	2.377E-02	4.067E-02
3.675E-01	5.634E+01	3.768E-03	7.312E-03	3.149E-04	1.488E-02	3.197E-02	3.103E-02
5.014E-01	7.681E+01	3.437E-03	6.076E-03	3.063E-04	1.546E-02	2.655E-02	3.016E-02
1.433E+00	1.439E+02	6.803E-03	1.364E-02	5.714E-04	1.302E-02	2.561E-02	2.426E-02
1.380E+00	1.376E+02	7.353E-03	9.702E-03	5.999E-04	1.292E-02	1.796E-02	2.506E-02
1.309E+00	1.305E+02	6.421E-03	9.128E-03	5.451E-04	1.141E-02	1.689E-02	2.277E-02
3.667E+00	2.701E+02	5.938E-03	1.308E-02	7.421E-04	6.460E-03	1.323E-02	1.690E-02
3.064E+00	2.244E+02	8.522E-03	1.604E-02	9.907E-04	7.861E-03	1.602E-02	2.234E-02
3.056E+00	2.241E+02	7.633E-03	1.448E-02	1.070E-03	6.681E-03	1.449E-02	2.416E-02
3.510E+00	2.040E+02	9.790E-03	2.187E-02	1.307E-03	4.281E-03	1.372E-02	1.855E-02
3.123E+00	1.808E+02	1.033E-02	2.147E-02	1.651E-03	6.176E-03	1.337E-02	2.324E-02
3.609E+00	2.089E+02	1.093E-02	2.231E-02	1.334E-03	6.631E-03	1.388E-02	1.878E-02
4.042E+00	1.945E+02	1.478E-02	2.907E-02	1.972E-03	6.374E-03	1.252E-02	1.919E-02
3.997E+00	1.920E+02	2.154E-02	2.996E-02	2.116E-03	1.017E-02	1.285E-02	2.049E-02
3.569E+00	1.713E+02	2.027E-02	2.717E-02	1.867E-03	9.168E-03	1.165E-02	1.808E-02
7.008E+00	2.879E+02	2.056E-02	3.597E-02	2.449E-03	7.251E-03	1.127E-02	1.735E-02
7.716E+00	3.158E+02	2.888E-02	3.272E-02	2.717E-03	1.071E-02	1.021E-02	1.916E-02
6.499E+00	2.659E+02	2.483E-02	3.895E-02	2.511E-03	8.213E-03	1.213E-02	1.766E-02

Table 40: Experimental data for sting supported 5° model. Air density was 1.19591 kg/m^3 for all tests.

Mean Values							
Q (Pa)	Re	Drag (N)	Lift (N)	Pitching (Nm)	C_D	C_L	C_M
7.843E+00	1.043E+04	-2.480E-03	-9.569E-04	-7.120E-05	-2.058E-01	-7.868E-02	-1.316E-01
7.903E+00	1.047E+04	1.044E-03	2.133E-03	-1.540E-04	8.310E-02	1.741E-01	-2.822E-01
7.925E+00	1.049E+04	3.750E-05	-9.723E-04	-1.149E-04	1.963E-03	-7.881E-02	-2.100E-01
3.832E+01	2.306E+04	4.691E-02	4.377E-03	9.480E-06	7.882E-01	7.367E-02	3.534E-03
3.847E+01	2.311E+04	4.630E-02	7.449E-03	-1.930E-04	7.748E-01	1.246E-01	-7.275E-02
3.849E+01	2.311E+04	4.561E-02	3.002E-03	-7.640E-05	7.628E-01	5.026E-02	-2.884E-02
1.493E+02	4.553E+04	2.180E-01	1.691E-02	-4.610E-05	9.400E-01	7.288E-02	-4.469E-03
1.493E+02	4.553E+04	2.195E-01	1.875E-02	4.280E-05	9.464E-01	8.083E-02	4.166E-03
1.496E+02	4.557E+04	2.210E-01	2.045E-02	1.123E-04	9.496E-01	8.799E-02	1.086E-02
3.516E+02	6.986E+04	5.378E-01	4.709E-02	4.600E-05	9.849E-01	8.621E-02	1.920E-03
3.516E+02	6.986E+04	5.384E-01	4.137E-02	2.152E-04	9.860E-01	7.580E-02	8.812E-03
3.517E+02	6.987E+04	5.360E-01	4.153E-02	2.708E-04	9.813E-01	7.602E-02	1.116E-02
6.441E+02	9.455E+04	9.972E-01	8.113E-02	2.510E-04	9.969E-01	8.108E-02	5.651E-03
6.446E+02	9.459E+04	9.985E-01	8.179E-02	4.030E-04	9.974E-01	8.168E-02	9.098E-03

6.480E+02	9.484E+04	1.002E+00	8.599E-02	3.174E-04	9.960E-01	8.545E-02	7.090E-03
1.035E+03	1.199E+05	1.608E+00	1.350E-01	4.328E-04	1.000E+00	8.398E-02	6.042E-03
1.037E+03	1.200E+05	1.612E+00	1.264E-01	1.025E-03	1.001E+00	7.845E-02	1.430E-02
1.038E+03	1.200E+05	1.618E+00	1.384E-01	-4.580E-05	1.004E+00	8.581E-02	-6.422E-04
1.508E+03	1.447E+05	2.366E+00	1.944E-01	6.639E-04	1.010E+00	8.300E-02	6.390E-03
1.510E+03	1.448E+05	2.367E+00	1.899E-01	1.230E-04	1.009E+00	8.096E-02	1.186E-03
1.512E+03	1.449E+05	2.374E+00	1.781E-01	9.090E-04	1.011E+00	7.583E-02	8.714E-03
2.071E+03	1.695E+05	3.258E+00	2.568E-01	1.050E-03	1.013E+00	7.984E-02	7.354E-03
2.072E+03	1.696E+05	3.259E+00	2.522E-01	1.860E-03	1.013E+00	7.836E-02	1.301E-02
2.074E+03	1.697E+05	3.264E+00	2.760E-01	-3.170E-04	1.013E+00	8.569E-02	-2.200E-03

Standard Deviation

Q (Pa)	Re	Drag (N)	Lift (N)	Pitching (Nm)	C_D	C_L	C_M
7.433E-02	4.938E+01	3.068E-03	4.035E-03	1.853E-04	2.532E-01	3.299E-01	3.420E-01
7.419E-02	4.914E+01	3.099E-03	5.538E-03	1.950E-04	2.520E-01	4.502E-01	3.575E-01
6.170E-02	4.087E+01	2.297E-03	4.815E-03	2.218E-04	1.871E-01	3.910E-01	4.054E-01
1.303E-01	3.923E+01	2.516E-03	7.118E-03	2.408E-04	4.088E-02	1.198E-01	9.109E-02
1.242E-01	3.733E+01	3.379E-03	5.995E-03	2.992E-04	5.476E-02	1.001E-01	1.125E-01
1.076E-01	3.232E+01	3.407E-03	6.001E-03	2.642E-04	5.519E-02	1.006E-01	9.945E-02
3.756E-01	5.727E+01	3.351E-03	6.103E-03	3.661E-04	1.387E-02	2.626E-02	3.547E-02
3.904E-01	5.950E+01	3.418E-03	9.001E-03	3.234E-04	1.512E-02	3.878E-02	3.137E-02
4.479E-01	6.822E+01	4.933E-03	7.213E-03	3.515E-04	2.041E-02	3.107E-02	3.404E-02
1.619E+00	1.608E+02	5.489E-03	1.261E-02	7.189E-04	9.799E-03	2.303E-02	2.966E-02
1.373E+00	1.364E+02	4.585E-03	1.132E-02	7.291E-04	9.428E-03	2.093E-02	3.003E-02
8.638E-01	8.581E+01	4.655E-03	1.004E-02	6.512E-04	7.844E-03	1.832E-02	2.681E-02
2.850E+00	2.093E+02	7.288E-03	1.461E-02	9.040E-04	7.385E-03	1.452E-02	2.029E-02
3.509E+00	2.574E+02	9.626E-03	1.372E-02	1.112E-03	1.079E-02	1.361E-02	2.510E-02
2.489E+00	1.824E+02	9.299E-03	1.748E-02	1.152E-03	8.975E-03	1.745E-02	2.576E-02
3.243E+00	1.878E+02	1.128E-02	2.065E-02	1.412E-03	6.718E-03	1.295E-02	1.976E-02
3.603E+00	2.085E+02	1.357E-02	2.061E-02	1.513E-03	8.878E-03	1.278E-02	2.110E-02
2.297E+00	1.328E+02	1.376E-02	2.220E-02	1.721E-03	8.932E-03	1.378E-02	2.401E-02
5.298E+00	2.542E+02	1.454E-02	3.332E-02	2.670E-03	6.203E-03	1.421E-02	2.563E-02
3.728E+00	1.788E+02	1.498E-02	3.189E-02	2.288E-03	7.146E-03	1.357E-02	2.191E-02
4.045E+00	1.937E+02	1.585E-02	3.384E-02	1.959E-03	6.844E-03	1.444E-02	1.877E-02
4.985E+00	2.042E+02	2.388E-02	3.950E-02	2.737E-03	7.528E-03	1.218E-02	1.915E-02
7.216E+00	2.954E+02	2.232E-02	3.379E-02	1.933E-03	6.489E-03	1.045E-02	1.354E-02
6.306E+00	2.581E+02	1.637E-02	4.337E-02	2.826E-03	5.461E-03	1.347E-02	1.973E-02

Table 41: Experimental data for sting supported 10° model. Air density was 1.19591 kg/m^3 for all tests.

Mean Values							
Q (Pa)	Re	Drag (N)	Lift (N)	Pitching (Nm)	C_D	C_L	C_M
7.875E+00	1.046E+04	-1.586E-03	1.365E-03	-1.454E-04	-1.325E-01	1.119E-01	-2.678E-01
7.897E+00	1.047E+04	4.649E-04	3.818E-03	-1.142E-04	3.628E-02	3.115E-01	-2.096E-01
7.903E+00	1.048E+04	1.266E-04	9.454E-04	-8.560E-05	8.209E-03	7.579E-02	-1.564E-01
7.918E+00	1.052E+04	2.222E-03	4.767E-03	-1.630E-04	1.796E-01	3.883E-01	-2.978E-01
3.816E+01	2.302E+04	4.534E-02	1.110E-02	-1.763E-04	7.645E-01	1.872E-01	-6.678E-02
3.823E+01	2.304E+04	4.590E-02	7.919E-03	-1.483E-05	7.726E-01	1.334E-01	-5.714E-03
3.830E+01	2.306E+04	4.710E-02	9.460E-03	9.802E-05	7.914E-01	1.590E-01	3.712E-02
1.484E+02	4.539E+04	2.154E-01	3.677E-02	4.343E-05	9.340E-01	1.595E-01	4.270E-03
1.485E+02	4.541E+04	2.146E-01	3.977E-02	-2.142E-04	9.299E-01	1.724E-01	-2.089E-02
1.491E+02	4.550E+04	2.173E-01	3.508E-02	2.243E-04	9.383E-01	1.515E-01	2.175E-02
3.396E+02	6.889E+04	5.292E-01	9.245E-02	2.077E-04	1.003E+00	1.752E-01	8.820E-03
3.493E+02	6.964E+04	5.263E-01	8.987E-02	4.035E-05	9.697E-01	1.656E-01	1.660E-03
3.498E+02	6.969E+04	5.327E-01	8.591E-02	4.363E-04	9.800E-01	1.581E-01	1.806E-02
6.401E+02	9.428E+04	9.807E-01	1.648E-01	6.258E-04	9.860E-01	1.657E-01	1.413E-02
6.404E+02	9.430E+04	9.814E-01	1.659E-01	6.899E-04	9.863E-01	1.667E-01	1.554E-02
6.414E+02	9.437E+04	9.864E-01	1.593E-01	8.642E-04	9.898E-01	1.599E-01	1.946E-02
1.029E+03	1.196E+05	1.584E+00	2.697E-01	1.208E-03	9.905E-01	1.686E-01	1.700E-02
1.030E+03	1.196E+05	1.589E+00	2.639E-01	1.660E-03	9.926E-01	1.648E-01	2.332E-02
1.031E+03	1.196E+05	1.595E+00	2.702E-01	1.340E-03	9.954E-01	1.687E-01	1.881E-02
1.497E+03	1.442E+05	2.337E+00	3.717E-01	3.377E-03	1.005E+00	1.598E-01	3.263E-02
1.499E+03	1.443E+05	2.340E+00	3.805E-01	2.922E-03	1.005E+00	1.634E-01	2.821E-02
1.499E+03	1.443E+05	2.333E+00	3.817E-01	3.089E-03	1.001E+00	1.638E-01	2.980E-02
2.056E+03	1.690E+05	3.225E+00	5.280E-01	2.533E-03	1.009E+00	1.653E-01	1.780E-02
2.056E+03	1.690E+05	3.227E+00	5.436E-01	2.952E-03	1.010E+00	1.702E-01	2.077E-02
Standard Deviation							
Q (Pa)	Re	Drag (N)	Lift (N)	Pitching (Nm)	C_D	C_L	C_M
9.040E-02	5.994E+01	3.432E-03	4.565E-03	2.177E-04	2.814E-01	3.724E-01	3.999E-01
7.610E-02	5.036E+01	2.446E-03	4.178E-03	2.042E-04	1.975E-01	3.406E-01	3.755E-01
7.945E-02	5.268E+01	2.941E-03	4.549E-03	1.883E-04	2.397E-01	3.690E-01	3.447E-01
6.334E-02	4.203E+01	2.205E-03	3.541E-03	2.079E-04	1.779E-01	2.887E-01	3.795E-01
1.275E-01	3.845E+01	3.456E-03	6.195E-03	3.052E-04	5.643E-02	1.044E-01	1.158E-01
1.027E-01	3.095E+01	2.618E-03	1.084E-02	4.079E-04	4.294E-02	1.827E-01	1.545E-01
1.186E-01	3.571E+01	3.638E-03	7.702E-03	3.298E-04	5.932E-02	1.294E-01	1.246E-01
7.139E-01	1.091E+02	3.847E-03	7.758E-03	4.559E-04	1.454E-02	3.343E-02	4.449E-02
3.542E-01	5.416E+01	3.456E-03	7.838E-03	4.046E-04	1.452E-02	3.414E-02	3.943E-02
4.076E-01	6.221E+01	2.746E-03	9.698E-03	4.732E-04	1.193E-02	4.192E-02	4.591E-02
1.075E+00	1.091E+02	6.430E-03	1.632E-02	8.202E-04	1.291E-02	3.088E-02	3.489E-02

1.248E+00	1.243E+02	4.927E-03	1.167E-02	8.239E-04	8.413E-03	2.140E-02	3.412E-02
1.019E+00	1.015E+02	4.919E-03	1.404E-02	6.820E-04	9.180E-03	2.576E-02	2.821E-02
2.754E+00	2.029E+02	5.924E-03	1.862E-02	1.259E-03	5.043E-03	1.887E-02	2.844E-02
3.274E+00	2.412E+02	6.224E-03	1.973E-02	1.439E-03	6.923E-03	2.017E-02	3.247E-02
2.829E+00	2.080E+02	6.683E-03	1.832E-02	1.025E-03	7.380E-03	1.877E-02	2.309E-02
3.273E+00	1.900E+02	1.309E-02	3.311E-02	2.302E-03	7.538E-03	2.053E-02	3.238E-02
3.567E+00	2.070E+02	1.182E-02	2.561E-02	1.411E-03	7.697E-03	1.599E-02	1.983E-02
3.025E+00	1.755E+02	1.119E-02	2.869E-02	1.517E-03	7.036E-03	1.773E-02	2.126E-02
3.261E+00	1.570E+02	1.014E-02	4.599E-02	2.734E-03	4.898E-03	1.979E-02	2.645E-02
2.540E+00	1.223E+02	1.335E-02	2.773E-02	2.595E-03	6.192E-03	1.196E-02	2.507E-02
3.612E+00	1.738E+02	1.677E-02	3.555E-02	2.821E-03	6.726E-03	1.517E-02	2.722E-02
7.799E+00	3.205E+02	1.808E-02	4.834E-02	2.614E-03	6.862E-03	1.554E-02	1.836E-02
5.683E+00	2.333E+02	1.960E-02	5.833E-02	4.155E-03	6.645E-03	1.828E-02	2.922E-02

Table 42: Experimental data for sting supported 15° model. Air density was 1.19591 kg/m^3 for all tests. This model was incorrectly mounted at -15°, and so the raw data exhibits a sign reversal.

Mean Values

Q (Pa)	Re	Drag (N)	Lift (N)	Pitching (Nm)	C_D	C_L	C_M
7.897E+00	1.047E+04	1.853E-04	-5.831E-04	7.986E-05	1.297E-02	-4.749E-02	1.469E-01
7.927E+00	1.049E+04	8.075E-04	2.672E-03	-1.421E-04	6.378E-02	2.159E-01	-2.589E-01
7.977E+00	1.052E+04	3.487E-03	4.059E-03	-7.536E-05	2.799E-01	3.290E-01	-1.380E-01
3.820E+01	2.303E+04	4.448E-02	-9.401E-03	-1.824E-04	7.495E-01	-1.584E-01	-6.920E-02
3.825E+01	2.304E+04	4.315E-02	-1.029E-02	-1.149E-04	7.262E-01	-1.733E-01	-4.339E-02
3.842E+01	2.309E+04	4.940E-02	-6.725E-03	-1.364E-04	8.279E-01	-1.127E-01	-5.137E-02
1.485E+02	4.540E+04	2.082E-01	-5.127E-02	-3.884E-04	9.028E-01	-2.223E-01	-3.784E-02
1.488E+02	4.544E+04	2.087E-01	-4.912E-02	-3.500E-04	9.031E-01	-2.126E-01	-3.407E-02
1.488E+02	4.545E+04	2.138E-01	-4.798E-02	-2.854E-04	9.248E-01	-2.075E-01	-2.776E-02
3.478E+02	6.948E+04	5.063E-01	-1.195E-01	-9.481E-04	9.372E-01	-2.211E-01	-3.945E-02
3.483E+02	6.953E+04	5.136E-01	-1.187E-01	-1.083E-03	9.494E-01	-2.194E-01	-4.501E-02
3.485E+02	6.955E+04	5.055E-01	-1.172E-01	-8.620E-04	9.341E-01	-2.166E-01	-3.580E-02
6.353E+02	9.391E+04	9.414E-01	-2.313E-01	-1.410E-03	9.540E-01	-2.344E-01	-3.211E-02
6.404E+02	9.428E+04	9.477E-01	-2.202E-01	-1.661E-03	9.529E-01	-2.214E-01	-3.752E-02
6.406E+02	9.430E+04	9.463E-01	-2.282E-01	-1.669E-03	9.511E-01	-2.294E-01	-3.770E-02
1.022E+03	1.191E+05	1.519E+00	-3.789E-01	-2.564E-03	9.567E-01	-2.386E-01	-3.632E-02
1.023E+03	1.191E+05	1.518E+00	-3.624E-01	-2.763E-03	9.558E-01	-2.282E-01	-3.906E-02
1.025E+03	1.193E+05	1.530E+00	-3.792E-01	-2.069E-03	9.608E-01	-2.380E-01	-2.921E-02
1.482E+03	1.434E+05	2.231E+00	-5.511E-01	-3.242E-03	9.691E-01	-2.394E-01	-3.164E-02
1.489E+03	1.437E+05	2.228E+00	-5.607E-01	-2.932E-03	9.635E-01	-2.425E-01	-2.851E-02

1.491E+03	1.438E+05	2.232E+00	-5.433E-01	-3.295E-03	9.642E-01	-2.347E-01	-3.199E-02
2.037E+03	1.682E+05	3.062E+00	-7.520E-01	-5.254E-03	9.676E-01	-2.377E-01	-3.733E-02
2.040E+03	1.683E+05	3.075E+00	-7.577E-01	-3.985E-03	9.702E-01	-2.391E-01	-2.828E-02
2.044E+03	1.685E+05	3.084E+00	-7.568E-01	-4.895E-03	9.712E-01	-2.383E-01	-3.466E-02
Standard Deviation							
Q (Pa)	Re	Drag (N)	Lift (N)	Pitching (Nm)	C_D	C_L	C_M
7.875E-02	5.214E+01	3.094E-03	4.601E-03	1.518E-04	2.513E-01	3.759E-01	2.802E-01
7.669E-02	5.068E+01	2.770E-03	3.646E-03	1.368E-04	2.233E-01	2.962E-01	2.498E-01
7.239E-02	4.779E+01	2.651E-03	4.777E-03	2.059E-04	2.121E-01	3.890E-01	3.751E-01
1.169E-01	3.524E+01	3.383E-03	5.532E-03	2.911E-04	5.567E-02	9.334E-02	1.103E-01
1.081E-01	3.254E+01	2.622E-03	4.780E-03	2.586E-04	4.266E-02	8.037E-02	9.774E-02
1.112E-01	3.343E+01	3.162E-03	5.149E-03	2.181E-04	5.175E-02	8.628E-02	8.218E-02
5.025E-01	7.681E+01	2.819E-03	7.234E-03	3.967E-04	1.232E-02	3.163E-02	3.867E-02
6.111E-01	9.331E+01	3.972E-03	8.647E-03	4.965E-04	1.636E-02	3.750E-02	4.833E-02
4.494E-01	6.860E+01	4.272E-03	6.815E-03	3.842E-04	1.751E-02	2.958E-02	3.737E-02
1.181E+00	1.179E+02	6.251E-03	9.789E-03	5.275E-04	1.175E-02	1.835E-02	2.192E-02
1.258E+00	1.255E+02	5.731E-03	1.156E-02	6.795E-04	1.158E-02	2.164E-02	2.831E-02
1.822E+00	1.818E+02	6.924E-03	8.948E-03	5.683E-04	1.275E-02	1.680E-02	2.360E-02
3.883E+00	2.870E+02	9.266E-03	1.888E-02	1.379E-03	9.046E-03	1.902E-02	3.140E-02
3.999E+00	2.947E+02	9.140E-03	2.255E-02	1.058E-03	9.033E-03	2.275E-02	2.390E-02
3.323E+00	2.446E+02	1.212E-02	1.910E-02	1.118E-03	1.326E-02	1.927E-02	2.522E-02
3.118E+00	1.817E+02	9.852E-03	2.664E-02	1.628E-03	5.430E-03	1.658E-02	2.306E-02
4.774E+00	2.783E+02	1.277E-02	2.117E-02	1.745E-03	5.602E-03	1.372E-02	2.461E-02
3.920E+00	2.279E+02	1.089E-02	2.456E-02	1.485E-03	7.834E-03	1.535E-02	2.093E-02
6.376E+00	3.085E+02	1.957E-02	3.138E-02	2.162E-03	8.454E-03	1.390E-02	2.111E-02
4.748E+00	2.292E+02	1.907E-02	2.232E-02	1.415E-03	8.372E-03	9.549E-03	1.374E-02
4.756E+00	2.294E+02	1.538E-02	2.925E-02	2.398E-03	5.799E-03	1.277E-02	2.329E-02
9.580E+00	3.953E+02	1.944E-02	2.648E-02	1.919E-03	5.551E-03	8.270E-03	1.359E-02
9.137E+00	3.765E+02	1.938E-02	3.578E-02	3.130E-03	6.936E-03	1.119E-02	2.223E-02
8.091E+00	3.334E+02	1.923E-02	3.900E-02	2.485E-03	7.042E-03	1.246E-02	1.758E-02

Table 43: Experimental data for sting supported 20° model. Air density was 1.19591 kg/m^3 for most tests.

Mean Values							
Q (Pa)	Re	Drag (N)	Lift (N)	Pitching (Nm)	C_D	C_L	C_M
7.879E+00	1.044E+04	-8.301E-04	-4.567E-03	1.754E-05	-7.003E-02	-3.751E-01	3.257E-02
7.885E+00	1.044E+04	-4.444E-04	1.959E-03	-8.433E-05	-3.879E-02	1.604E-01	-1.560E-01
7.910E+00	1.046E+04	2.845E-05	2.156E-03	-2.039E-04	-9.297E-04	1.770E-01	-3.760E-01
3.839E+01	2.304E+04	4.215E-02	1.644E-02	-1.581E-04	7.092E-01	2.767E-01	-5.987E-02

3.850E+01	2.307E+04	4.428E-02	1.639E-02	-1.098E-05	7.431E-01	2.751E-01	-4.200E-03
3.890E+01	2.319E+04	4.394E-02	1.025E-02	9.974E-05	7.299E-01	1.703E-01	3.729E-02
1.488E+02	4.537E+04	2.018E-01	6.768E-02	2.729E-04	8.760E-01	2.938E-01	2.670E-02
1.491E+02	4.540E+04	2.015E-01	6.355E-02	3.707E-04	8.735E-01	2.755E-01	3.618E-02
1.515E+02	4.577E+04	2.029E-01	6.421E-02	2.837E-04	8.654E-01	2.739E-01	2.727E-02
3.509E+02	6.967E+04	4.977E-01	1.630E-01	5.264E-04	9.164E-01	3.001E-01	2.184E-02
3.511E+02	6.968E+04	4.900E-01	1.612E-01	5.845E-04	9.019E-01	2.968E-01	2.424E-02
3.560E+02	7.017E+04	4.966E-01	1.561E-01	8.385E-04	9.012E-01	2.833E-01	3.429E-02
6.407E+02	9.413E+04	9.079E-01	2.956E-01	1.522E-03	9.156E-01	2.981E-01	3.460E-02
6.452E+02	9.446E+04	9.244E-01	2.974E-01	1.614E-03	9.259E-01	2.978E-01	3.650E-02
6.489E+02	9.473E+04	9.213E-01	2.883E-01	1.741E-03	9.175E-01	2.871E-01	3.911E-02
1.032E+03	1.195E+05	1.477E+00	4.875E-01	2.087E-03	9.242E-01	3.051E-01	2.943E-02
1.033E+03	1.195E+05	1.489E+00	4.953E-01	1.991E-03	9.312E-01	3.097E-01	2.804E-02
1.045E+03	1.202E+05	1.487E+00	4.818E-01	2.194E-03	9.197E-01	2.979E-01	3.054E-02
1.501E+03	1.441E+05	2.183E+00	7.210E-01	3.456E-03	9.395E-01	3.103E-01	3.348E-02
1.504E+03	1.442E+05	2.178E+00	7.119E-01	3.532E-03	9.358E-01	3.059E-01	3.419E-02
1.520E+03	1.450E+05	2.184E+00	7.097E-01	3.528E-03	9.280E-01	3.016E-01	3.377E-02
2.065E+03	1.690E+05	3.013E+00	9.860E-01	5.077E-03	9.428E-01	3.085E-01	3.577E-02
2.068E+03	1.691E+05	3.004E+00	1.018E+00	4.407E-03	9.386E-01	3.182E-01	3.103E-02
2.090E+03	1.700E+05	3.012E+00	9.897E-01	4.220E-03	9.315E-01	3.060E-01	2.938E-02

Standard Deviation

Q (Pa)	Re	Drag (N)	Lift (N)	Pitching (Nm)	C_D	C_L	C_M
7.159E-02	4.743E+01	2.949E-03	4.610E-03	2.234E-04	2.427E-01	3.798E-01	4.136E-01
8.065E-02	5.352E+01	3.156E-03	3.487E-03	1.277E-04	2.614E-01	2.854E-01	2.357E-01
9.485E-02	6.274E+01	3.585E-03	3.917E-03	1.901E-04	2.940E-01	3.178E-01	3.485E-01
1.154E-01	3.458E+01	3.863E-03	4.898E-03	2.612E-04	6.364E-02	8.200E-02	9.886E-02
1.293E-01	3.877E+01	2.521E-03	3.548E-03	2.168E-04	4.075E-02	5.963E-02	8.195E-02
1.093E-01	3.258E+01	2.965E-03	5.472E-03	2.168E-04	4.878E-02	9.096E-02	8.107E-02
5.234E-01	7.982E+01	3.666E-03	5.942E-03	3.657E-04	1.474E-02	2.559E-02	3.580E-02
5.374E-01	8.190E+01	3.658E-03	6.414E-03	4.485E-04	1.465E-02	2.767E-02	4.379E-02
3.264E-01	4.930E+01	3.271E-03	8.088E-03	3.839E-04	1.361E-02	3.456E-02	3.689E-02
1.303E+00	1.294E+02	5.867E-03	9.356E-03	6.133E-04	1.040E-02	1.713E-02	2.546E-02
1.328E+00	1.318E+02	4.648E-03	1.133E-02	5.678E-04	9.014E-03	2.101E-02	2.354E-02
1.103E+00	1.088E+02	3.722E-03	1.098E-02	6.778E-04	7.602E-03	1.995E-02	2.772E-02
4.533E+00	3.329E+02	5.359E-03	1.663E-02	1.270E-03	5.694E-03	1.678E-02	2.883E-02
3.504E+00	2.562E+02	6.132E-03	2.061E-02	1.336E-03	8.990E-03	2.010E-02	3.022E-02
3.903E+00	2.850E+02	7.474E-03	1.255E-02	8.512E-04	8.360E-03	1.214E-02	1.921E-02
3.079E+00	1.782E+02	8.943E-03	2.498E-02	1.716E-03	5.781E-03	1.576E-02	2.419E-02
3.127E+00	1.808E+02	9.768E-03	2.431E-02	1.279E-03	5.830E-03	1.519E-02	1.803E-02
3.168E+00	1.822E+02	9.945E-03	2.789E-02	1.693E-03	6.027E-03	1.727E-02	2.351E-02
6.975E+00	3.343E+02	1.192E-02	3.233E-02	2.034E-03	5.207E-03	1.439E-02	1.966E-02

4.620E+00	2.216E+02	1.081E-02	3.596E-02	2.217E-03	5.673E-03	1.551E-02	2.148E-02
4.138E+00	1.973E+02	1.135E-02	2.889E-02	1.778E-03	3.655E-03	1.215E-02	1.701E-02
9.686E+00	3.963E+02	1.696E-02	4.694E-02	2.299E-03	5.525E-03	1.482E-02	1.615E-02
5.770E+00	2.360E+02	1.956E-02	3.964E-02	2.542E-03	6.458E-03	1.237E-02	1.790E-02
6.997E+00	2.846E+02	1.815E-02	2.875E-02	1.867E-03	6.704E-03	9.025E-03	1.296E-02

Table 44: Experimental data for sting supported 25° model. Air density was 1.19591 kg/m^3 for most tests.

Mean Values

Q (Pa)	Re	Drag (N)	Lift (N)	Pitching (Nm)	C_D	C_L	C_M
7.870E+00	1.044E+04	-1.803E-03	2.196E-03	-1.468E-04	-1.491E-01	1.803E-01	-2.713E-01
7.894E+00	1.046E+04	-7.732E-05	1.252E-04	-1.728E-05	-8.420E-03	1.043E-02	-3.222E-02
7.915E+00	1.047E+04	-1.106E-04	3.709E-04	-6.826E-05	-1.085E-02	3.176E-02	-1.266E-01
3.877E+01	2.318E+04	4.020E-02	1.597E-02	-2.429E-05	6.685E-01	2.657E-01	-9.120E-03
3.880E+01	2.319E+04	3.940E-02	1.615E-02	4.114E-06	6.546E-01	2.684E-01	1.575E-03
3.887E+01	2.321E+04	3.959E-02	1.564E-02	-3.964E-05	6.566E-01	2.595E-01	-1.492E-02
1.508E+02	4.572E+04	1.876E-01	7.528E-02	2.840E-04	8.019E-01	3.218E-01	2.732E-02
1.511E+02	4.576E+04	1.855E-01	7.453E-02	3.066E-04	7.916E-01	3.181E-01	2.947E-02
1.516E+02	4.584E+04	1.865E-01	7.290E-02	4.204E-04	7.933E-01	3.101E-01	4.023E-02
3.540E+02	7.005E+04	4.578E-01	1.854E-01	8.051E-04	8.338E-01	3.377E-01	3.298E-02
3.547E+02	7.012E+04	4.595E-01	1.830E-01	9.986E-04	8.352E-01	3.327E-01	4.088E-02
3.562E+02	7.027E+04	4.597E-01	1.837E-01	8.502E-04	8.321E-01	3.325E-01	3.462E-02
6.507E+02	9.497E+04	8.557E-01	3.464E-01	1.692E-03	8.478E-01	3.432E-01	3.774E-02
6.514E+02	9.503E+04	8.539E-01	3.406E-01	1.715E-03	8.451E-01	3.371E-01	3.820E-02
6.520E+02	9.507E+04	8.612E-01	3.472E-01	1.629E-03	8.515E-01	3.433E-01	3.623E-02
1.046E+03	1.204E+05	1.378E+00	5.550E-01	2.720E-03	8.496E-01	3.422E-01	3.773E-02
1.047E+03	1.205E+05	1.384E+00	5.596E-01	2.968E-03	8.523E-01	3.445E-01	4.114E-02
1.049E+03	1.206E+05	1.389E+00	5.613E-01	2.837E-03	8.533E-01	3.449E-01	3.923E-02
1.524E+03	1.454E+05	2.037E+00	8.188E-01	3.980E-03	8.618E-01	3.464E-01	3.787E-02
1.527E+03	1.455E+05	2.042E+00	8.374E-01	3.567E-03	8.622E-01	3.535E-01	3.390E-02
1.530E+03	1.456E+05	2.052E+00	8.213E-01	4.909E-03	8.646E-01	3.461E-01	4.657E-02
2.095E+03	1.704E+05	2.813E+00	1.133E+00	6.422E-03	8.657E-01	3.488E-01	4.445E-02
2.098E+03	1.705E+05	2.824E+00	1.126E+00	6.453E-03	8.680E-01	3.462E-01	4.462E-02
2.098E+03	1.705E+05	2.833E+00	1.155E+00	6.513E-03	8.704E-01	3.549E-01	4.504E-02

Standard Deviation

Q (Pa)	Re	Drag (N)	Lift (N)	Pitching (Nm)	C_D	C_L	C_M
7.362E-02	4.881E+01	2.075E-03	3.800E-03	1.832E-04	1.704E-01	3.125E-01	3.386E-01
8.327E-02	5.524E+01	2.685E-03	4.232E-03	1.972E-04	2.199E-01	3.461E-01	3.626E-01
7.081E-02	4.687E+01	2.790E-03	5.978E-03	2.722E-04	2.277E-01	4.877E-01	4.986E-01

9.387E-02	2.805E+01	2.763E-03	5.892E-03	2.217E-04	4.499E-02	9.811E-02	8.298E-02
1.070E-01	3.197E+01	3.672E-03	7.188E-03	2.974E-04	5.996E-02	1.193E-01	1.112E-01
1.480E-01	4.417E+01	2.431E-03	4.985E-03	2.674E-04	3.947E-02	8.303E-02	9.993E-02
4.322E-01	6.554E+01	3.081E-03	5.719E-03	3.530E-04	1.301E-02	2.413E-02	3.395E-02
4.652E-01	7.049E+01	3.166E-03	5.516E-03	2.491E-04	1.369E-02	2.315E-02	2.396E-02
4.636E-01	7.010E+01	3.825E-03	6.262E-03	2.362E-04	1.642E-02	2.680E-02	2.259E-02
1.922E+00	1.901E+02	5.894E-03	8.931E-03	5.941E-04	1.020E-02	1.642E-02	2.423E-02
2.315E+00	2.287E+02	4.058E-03	9.264E-03	5.178E-04	7.678E-03	1.686E-02	2.121E-02
1.747E+00	1.723E+02	5.080E-03	8.077E-03	5.415E-04	7.019E-03	1.494E-02	2.204E-02
4.369E+00	3.189E+02	1.140E-02	1.394E-02	7.302E-04	1.054E-02	1.384E-02	1.633E-02
4.256E+00	3.104E+02	8.358E-03	1.420E-02	5.195E-04	8.894E-03	1.407E-02	1.160E-02
3.305E+00	2.411E+02	5.566E-03	1.051E-02	8.006E-04	7.465E-03	1.093E-02	1.776E-02
3.802E+00	2.188E+02	1.156E-02	1.991E-02	1.078E-03	7.420E-03	1.249E-02	1.492E-02
4.211E+00	2.423E+02	7.451E-03	1.773E-02	1.258E-03	5.654E-03	1.101E-02	1.751E-02
3.716E+00	2.135E+02	9.668E-03	1.854E-02	7.633E-04	7.192E-03	1.149E-02	1.056E-02
6.653E+00	3.171E+02	1.156E-02	2.383E-02	1.685E-03	6.049E-03	1.040E-02	1.601E-02
3.398E+00	1.619E+02	8.882E-03	2.138E-02	1.402E-03	3.977E-03	8.811E-03	1.335E-02
5.130E+00	2.441E+02	1.354E-02	3.064E-02	2.158E-03	6.195E-03	1.265E-02	2.052E-02
6.128E+00	2.491E+02	1.283E-02	2.929E-02	1.645E-03	4.407E-03	9.471E-03	1.133E-02
5.946E+00	2.417E+02	1.716E-02	3.458E-02	2.370E-03	5.205E-03	1.088E-02	1.638E-02
8.243E+00	3.349E+02	1.586E-02	3.339E-02	2.242E-03	4.785E-03	1.015E-02	1.555E-02

Table 45: Experimental data for sting supported 35° model. Air density was 1.19591 kg/m^3 for most tests.

Mean Values							
Q (Pa)	Re	Drag (N)	Lift (N)	Pitching (Nm)	C_D	C_L	C_M
7.893E+00	1.046E+04	-2.263E-04	5.685E-04	-1.210E-04	-2.232E-02	4.583E-02	-2.239E-01
7.900E+00	1.047E+04	4.822E-04	1.433E-03	-1.249E-04	3.765E-02	1.176E-01	-2.303E-01
7.941E+00	1.049E+04	1.159E-03	-2.910E-04	-1.343E-04	9.265E-02	-2.296E-02	-2.448E-01
3.917E+01	2.331E+04	3.421E-02	1.797E-02	-1.721E-05	5.628E-01	2.955E-01	-6.250E-03
3.918E+01	2.331E+04	3.315E-02	1.870E-02	4.786E-06	5.451E-01	3.076E-01	1.757E-03
3.928E+01	2.334E+04	3.443E-02	2.177E-02	-1.845E-05	5.648E-01	3.572E-01	-6.763E-03
1.530E+02	4.606E+04	1.576E-01	8.646E-02	4.256E-04	6.639E-01	3.642E-01	4.031E-02
1.530E+02	4.606E+04	1.567E-01	8.458E-02	4.665E-04	6.599E-01	3.562E-01	4.419E-02
1.535E+02	4.614E+04	1.577E-01	8.536E-02	4.304E-04	6.620E-01	3.584E-01	4.066E-02
3.592E+02	7.057E+04	3.839E-01	2.044E-01	1.234E-03	6.889E-01	3.668E-01	4.979E-02
3.600E+02	7.066E+04	3.830E-01	2.073E-01	1.233E-03	6.856E-01	3.711E-01	4.962E-02
3.605E+02	7.071E+04	3.835E-01	2.071E-01	1.322E-03	6.856E-01	3.702E-01	5.318E-02
6.606E+02	9.571E+04	7.107E-01	3.797E-01	2.434E-03	6.933E-01	3.704E-01	5.340E-02

6.614E+02	9.577E+04	7.115E-01	3.833E-01	2.284E-03	6.932E-01	3.735E-01	5.008E-02
6.632E+02	9.590E+04	7.183E-01	3.869E-01	2.605E-03	6.980E-01	3.760E-01	5.695E-02
1.064E+03	1.215E+05	1.154E+00	6.208E-01	3.832E-03	6.991E-01	3.761E-01	5.222E-02
1.066E+03	1.216E+05	1.157E+00	6.233E-01	4.195E-03	6.992E-01	3.767E-01	5.702E-02
1.068E+03	1.217E+05	1.163E+00	6.243E-01	4.464E-03	7.017E-01	3.766E-01	6.058E-02
1.550E+03	1.466E+05	1.698E+00	9.130E-01	6.048E-03	7.056E-01	3.795E-01	5.654E-02
1.554E+03	1.468E+05	1.705E+00	9.275E-01	5.906E-03	7.071E-01	3.847E-01	5.510E-02
1.554E+03	1.468E+05	1.708E+00	9.236E-01	6.269E-03	7.080E-01	3.829E-01	5.848E-02
2.133E+03	1.720E+05	2.354E+00	1.269E+00	8.422E-03	7.112E-01	3.832E-01	5.723E-02
2.137E+03	1.721E+05	2.360E+00	1.280E+00	7.964E-03	7.117E-01	3.859E-01	5.404E-02
2.140E+03	1.723E+05	2.363E+00	1.277E+00	8.301E-03	7.116E-01	3.845E-01	5.623E-02

Standard Deviation

Q (Pa)	Re	Drag (N)	Lift (N)	Pitching (Nm)	C_D	C_L	C_M
1.011E-01	6.711E+01	4.087E-03	4.515E-03	2.065E-04	3.357E-01	3.680E-01	3.808E-01
6.958E-02	4.613E+01	2.791E-03	4.123E-03	1.367E-04	2.278E-01	3.362E-01	2.529E-01
7.580E-02	5.004E+01	2.164E-03	4.491E-03	1.852E-04	1.745E-01	3.622E-01	3.365E-01
1.428E-01	4.251E+01	3.383E-03	5.059E-03	2.386E-04	5.433E-02	8.295E-02	8.834E-02
1.119E-01	3.330E+01	2.835E-03	5.910E-03	2.151E-04	4.541E-02	9.730E-02	7.974E-02
1.126E-01	3.346E+01	2.632E-03	4.359E-03	1.578E-04	4.223E-02	7.141E-02	5.826E-02
7.216E-01	1.087E+02	2.321E-03	5.150E-03	2.307E-04	1.061E-02	2.222E-02	2.184E-02
6.155E-01	9.266E+01	3.079E-03	5.953E-03	2.324E-04	1.223E-02	2.486E-02	2.201E-02
6.196E-01	9.306E+01	3.133E-03	5.938E-03	2.768E-04	1.346E-02	2.494E-02	2.614E-02
1.832E+00	1.799E+02	4.413E-03	7.876E-03	3.815E-04	7.777E-03	1.438E-02	1.538E-02
2.048E+00	2.011E+02	3.893E-03	5.284E-03	3.214E-04	7.279E-03	9.315E-03	1.291E-02
1.634E+00	1.602E+02	3.417E-03	9.023E-03	4.112E-04	7.351E-03	1.595E-02	1.656E-02
3.585E+00	2.600E+02	4.323E-03	1.132E-02	5.488E-04	4.370E-03	1.155E-02	1.195E-02
4.830E+00	3.496E+02	6.597E-03	8.886E-03	5.945E-04	8.304E-03	8.892E-03	1.307E-02
3.017E+00	2.180E+02	3.479E-03	1.217E-02	6.823E-04	4.438E-03	1.146E-02	1.496E-02
3.555E+00	2.030E+02	6.471E-03	1.337E-02	6.990E-04	4.424E-03	8.439E-03	9.467E-03
3.248E+00	1.852E+02	9.381E-03	2.026E-02	8.439E-04	4.554E-03	1.235E-02	1.143E-02
3.245E+00	1.849E+02	6.621E-03	1.515E-02	5.586E-04	4.002E-03	9.329E-03	7.546E-03
4.859E+00	2.298E+02	1.137E-02	2.455E-02	1.020E-03	4.832E-03	1.080E-02	9.428E-03
3.872E+00	1.828E+02	1.130E-02	2.127E-02	1.222E-03	4.180E-03	9.234E-03	1.133E-02
4.098E+00	1.935E+02	1.072E-02	2.456E-02	1.282E-03	4.663E-03	1.005E-02	1.200E-02
8.442E+00	3.401E+02	1.031E-02	2.505E-02	1.272E-03	3.956E-03	7.935E-03	8.599E-03
5.535E+00	2.228E+02	1.724E-02	2.987E-02	1.523E-03	5.424E-03	8.836E-03	1.033E-02
6.409E+00	2.581E+02	1.445E-02	2.280E-02	1.807E-03	4.258E-03	6.427E-03	1.224E-02

Table 46: Experimental data for sting supported 45° model. Air density was 1.19591 kg/m^3 for most tests.

Mean Values

Q (Pa)	Re	Drag (N)	Lift (N)	Pitching (Nm)	C_D	C_L	C_M
7.878E+00	1.045E+04	-1.145E-03	-1.138E-04	-6.526E-05	-9.737E-02	-9.120E-03	-1.193E-01
7.910E+00	1.047E+04	1.039E-03	2.415E-03	-1.298E-04	8.272E-02	1.972E-01	-2.378E-01
7.912E+00	1.047E+04	8.337E-04	-1.566E-03	-3.203E-05	6.555E-02	-1.283E-01	-5.828E-02
3.967E+01	2.345E+04	2.495E-02	1.489E-02	1.674E-04	4.053E-01	2.418E-01	6.117E-02
3.978E+01	2.349E+04	2.616E-02	1.416E-02	1.135E-04	4.238E-01	2.295E-01	4.130E-02
3.991E+01	2.353E+04	2.788E-02	1.789E-02	9.909E-05	4.501E-01	2.889E-01	3.587E-02
1.557E+02	4.647E+04	1.168E-01	7.981E-02	6.991E-04	4.834E-01	3.302E-01	6.508E-02
1.562E+02	4.654E+04	1.201E-01	8.422E-02	6.466E-04	4.953E-01	3.474E-01	6.001E-02
1.565E+02	4.659E+04	1.205E-01	8.115E-02	8.477E-04	4.961E-01	3.341E-01	7.849E-02
3.660E+02	7.125E+04	2.843E-01	1.996E-01	1.761E-03	5.006E-01	3.515E-01	6.973E-02
3.664E+02	7.128E+04	2.896E-01	2.030E-01	1.886E-03	5.094E-01	3.571E-01	7.463E-02
3.670E+02	7.134E+04	2.849E-01	2.011E-01	1.776E-03	5.003E-01	3.531E-01	7.016E-02
6.759E+02	9.682E+04	5.278E-01	3.629E-01	3.508E-03	5.032E-01	3.460E-01	7.524E-02
6.766E+02	9.686E+04	5.288E-01	3.706E-01	3.058E-03	5.037E-01	3.530E-01	6.554E-02
6.786E+02	9.701E+04	5.375E-01	3.675E-01	3.446E-03	5.105E-01	3.491E-01	7.358E-02
1.084E+03	1.226E+05	8.480E-01	5.867E-01	5.498E-03	5.043E-01	3.489E-01	7.358E-02
1.091E+03	1.230E+05	8.601E-01	5.999E-01	5.403E-03	5.081E-01	3.544E-01	7.182E-02
1.093E+03	1.231E+05	8.718E-01	6.235E-01	5.235E-03	5.138E-01	3.675E-01	6.941E-02
1.593E+03	1.486E+05	1.267E+00	8.922E-01	8.676E-03	5.126E-01	3.610E-01	7.897E-02
1.593E+03	1.487E+05	1.274E+00	8.932E-01	8.628E-03	5.151E-01	3.613E-01	7.850E-02
1.595E+03	1.487E+05	1.272E+00	9.095E-01	8.214E-03	5.141E-01	3.675E-01	7.466E-02
2.178E+03	1.738E+05	1.751E+00	1.225E+00	1.135E-02	5.179E-01	3.623E-01	7.556E-02
2.184E+03	1.740E+05	1.745E+00	1.230E+00	1.118E-02	5.148E-01	3.628E-01	7.424E-02
2.188E+03	1.742E+05	1.742E+00	1.223E+00	1.110E-02	5.130E-01	3.602E-01	7.356E-02

Standard Deviation

Q (Pa)	Re	Drag (N)	Lift (N)	Pitching (Nm)	C_D	C_L	C_M
1.039E-01	6.871E+01	3.836E-03	4.826E-03	2.380E-04	3.125E-01	3.918E-01	4.356E-01
7.829E-02	5.185E+01	2.873E-03	4.909E-03	2.441E-04	2.338E-01	4.002E-01	4.476E-01
8.464E-02	5.610E+01	3.056E-03	4.077E-03	1.908E-04	2.486E-01	3.320E-01	3.506E-01
8.058E-02	2.383E+01	3.204E-03	6.269E-03	2.343E-04	5.153E-02	1.018E-01	8.570E-02
1.227E-01	3.624E+01	2.833E-03	4.268E-03	1.570E-04	4.527E-02	6.958E-02	5.723E-02
1.269E-01	3.741E+01	2.606E-03	5.722E-03	2.296E-04	4.141E-02	9.286E-02	8.337E-02
5.298E-01	7.906E+01	2.849E-03	4.531E-03	2.604E-04	1.191E-02	1.881E-02	2.423E-02
8.206E-01	1.223E+02	2.246E-03	6.226E-03	2.518E-04	9.555E-03	2.562E-02	2.339E-02
7.084E-01	1.054E+02	3.672E-03	6.349E-03	2.685E-04	1.398E-02	2.652E-02	2.483E-02
1.726E+00	1.680E+02	3.454E-03	8.387E-03	4.447E-04	6.219E-03	1.530E-02	1.757E-02
1.896E+00	1.844E+02	3.481E-03	6.957E-03	3.138E-04	6.200E-03	1.268E-02	1.239E-02

1.614E+00	1.570E+02	4.058E-03	5.918E-03	3.031E-04	6.403E-03	1.043E-02	1.196E-02
2.701E+00	1.935E+02	4.720E-03	1.312E-02	6.532E-04	4.295E-03	1.252E-02	1.409E-02
5.588E+00	4.005E+02	4.503E-03	1.189E-02	4.260E-04	5.307E-03	1.189E-02	9.182E-03
5.809E+00	4.154E+02	5.942E-03	1.506E-02	4.973E-04	5.786E-03	1.493E-02	1.030E-02
6.913E+00	3.910E+02	9.102E-03	1.955E-02	7.745E-04	4.770E-03	1.106E-02	1.059E-02
4.654E+00	2.625E+02	5.991E-03	1.725E-02	4.578E-04	3.702E-03	1.080E-02	6.044E-03
3.883E+00	2.187E+02	7.803E-03	1.770E-02	8.687E-04	4.118E-03	1.007E-02	1.153E-02
6.717E+00	3.132E+02	1.117E-02	2.084E-02	9.750E-04	5.699E-03	9.103E-03	8.765E-03
5.615E+00	2.620E+02	8.010E-03	2.214E-02	7.685E-04	3.764E-03	9.623E-03	6.941E-03
6.538E+00	3.049E+02	9.207E-03	1.554E-02	8.697E-04	3.951E-03	6.537E-03	7.891E-03
9.268E+00	3.698E+02	1.418E-02	2.488E-02	9.102E-04	4.370E-03	6.911E-03	6.082E-03
1.378E+01	5.490E+02	1.318E-02	3.082E-02	1.080E-03	3.578E-03	8.937E-03	7.172E-03
8.186E+00	3.260E+02	1.343E-02	3.330E-02	1.328E-03	3.736E-03	9.739E-03	8.764E-03

B.5 Dummy Sting Data

Table 47: Experimental data for 0° back cavity model with dummy sting. Mean values over each data event.

Q raw (Pa)	Drag (amps)	Lift (amps)	Side (amps)	Diameter (m)	Model Area (m^2)	Air Density (kg/m^3)
-1.744E-02	3.403E-01	-1.706E+01	-4.685E-02	4.438E-02	1.547E-03	1.206E+00
-1.478E-03	2.804E-01	-1.708E+01	-5.107E-02	4.438E-02	1.547E-03	1.206E+00
5.796E-03	2.827E-01	-1.708E+01	-3.545E-02	4.438E-02	1.547E-03	1.206E+00
1.732E-02	2.615E-01	-1.713E+01	-4.738E-02	4.438E-02	1.547E-03	1.206E+00
7.734E+00	6.339E-01	-1.705E+01	-4.910E-02	4.438E-02	1.547E-03	1.206E+00
7.818E+00	6.549E-01	-1.706E+01	-4.505E-02	4.438E-02	1.547E-03	1.206E+00
7.897E+00	5.968E-01	-1.711E+01	-4.469E-02	4.438E-02	1.547E-03	1.206E+00
3.389E+01	1.734E+00	-1.704E+01	-2.796E-02	4.438E-02	1.547E-03	1.206E+00
3.390E+01	1.831E+00	-1.695E+01	-6.055E-02	4.438E-02	1.547E-03	1.206E+00
3.391E+01	1.785E+00	-1.695E+01	-3.017E-02	4.438E-02	1.547E-03	1.206E+00
3.403E+01	1.777E+00	-1.698E+01	-2.738E-02	4.438E-02	1.547E-03	1.206E+00
7.920E+01	3.784E+00	-1.675E+01	6.578E-03	4.438E-02	1.547E-03	1.206E+00
7.972E+01	3.787E+00	-1.681E+01	-3.832E-03	4.438E-02	1.547E-03	1.206E+00
7.983E+01	3.756E+00	-1.691E+01	-9.488E-03	4.438E-02	1.547E-03	1.206E+00
7.999E+01	3.812E+00	-1.681E+01	2.890E-03	4.438E-02	1.547E-03	1.206E+00
1.428E+02	6.609E+00	-1.649E+01	7.086E-02	4.438E-02	1.547E-03	1.206E+00
1.437E+02	6.590E+00	-1.672E+01	4.337E-02	4.438E-02	1.547E-03	1.206E+00
1.443E+02	6.665E+00	-1.661E+01	4.196E-02	4.438E-02	1.547E-03	1.206E+00
1.452E+02	6.671E+00	-1.661E+01	7.386E-02	4.438E-02	1.547E-03	1.206E+00

2.296E+02	1.041E+01	-1.610E+01	1.993E-01	4.438E-02	1.547E-03	1.206E+00
2.305E+02	1.049E+01	-1.620E+01	1.134E-01	4.438E-02	1.547E-03	1.206E+00
2.311E+02	1.046E+01	-1.652E+01	1.133E-01	4.438E-02	1.547E-03	1.206E+00
2.316E+02	1.047E+01	-1.632E+01	1.288E-01	4.438E-02	1.547E-03	1.206E+00
3.367E+02	1.525E+01	-1.607E+01	2.320E-01	4.438E-02	1.547E-03	1.206E+00
3.374E+02	1.510E+01	-1.627E+01	2.217E-01	4.438E-02	1.547E-03	1.206E+00
3.378E+02	1.523E+01	-1.600E+01	2.987E-01	4.438E-02	1.547E-03	1.206E+00
3.383E+02	1.517E+01	-1.611E+01	2.116E-01	4.438E-02	1.547E-03	1.206E+00
4.663E+02	2.083E+01	-1.570E+01	4.378E-01	4.438E-02	1.547E-03	1.206E+00
4.685E+02	2.094E+01	-1.570E+01	3.308E-01	4.438E-02	1.547E-03	1.206E+00
4.688E+02	2.097E+01	-1.592E+01	3.165E-01	4.438E-02	1.547E-03	1.206E+00
4.691E+02	2.095E+01	-1.567E+01	4.099E-01	4.438E-02	1.547E-03	1.206E+00
6.203E+02	2.723E+01	-1.474E+01	1.656E+00	4.438E-02	1.547E-03	1.206E+00
6.204E+02	2.744E+01	-1.569E+01	4.985E-01	4.438E-02	1.547E-03	1.206E+00
6.218E+02	2.746E+01	-1.540E+01	5.020E-01	4.438E-02	1.547E-03	1.206E+00
6.224E+02	2.747E+01	-1.574E+01	5.550E-01	4.438E-02	1.547E-03	1.206E+00
7.878E+02	3.423E+01	-1.590E+01	8.253E-01	4.438E-02	1.547E-03	1.206E+00
7.947E+02	3.465E+01	-1.501E+01	6.108E-01	4.438E-02	1.547E-03	1.206E+00
7.954E+02	3.469E+01	-1.563E+01	6.069E-01	4.438E-02	1.547E-03	1.206E+00
7.980E+02	3.481E+01	-1.564E+01	7.816E-01	4.438E-02	1.547E-03	1.206E+00
9.808E+02	4.249E+01	-1.523E+01	6.366E-01	4.438E-02	1.547E-03	1.206E+00
9.826E+02	4.296E+01	-1.583E+01	9.768E-01	4.438E-02	1.547E-03	1.206E+00
9.834E+02	4.272E+01	-1.616E+01	1.222E+00	4.438E-02	1.547E-03	1.206E+00
9.859E+02	4.285E+01	-1.605E+01	1.168E+00	4.438E-02	1.547E-03	1.206E+00
1.060E+03	4.616E+01	-1.621E+01	1.394E+00	4.438E-02	1.547E-03	1.206E+00
1.063E+03	4.620E+01	-1.621E+01	1.619E+00	4.438E-02	1.547E-03	1.206E+00
1.063E+03	4.610E+01	-1.598E+01	1.273E+00	4.438E-02	1.547E-03	1.206E+00
1.143E+03	4.974E+01	-1.594E+01	1.462E+00	4.438E-02	1.547E-03	1.206E+00
1.143E+03	4.979E+01	-1.601E+01	1.538E+00	4.438E-02	1.547E-03	1.206E+00
1.149E+03	5.024E+01	-1.581E+01	2.403E-01	4.438E-02	1.547E-03	1.206E+00

Table 48: Experimental data for 0° back cavity model with dummy sting with cavity pressure tap. Mean values over each data event. Air density was 1.2151 kg/m^3 for all tets. Model diameter of 0.04438 m.

Q raw (Pa)	Drag (amps)	Lift (amps)	Side (amps)	Cavity Pressure (Pa)
-2.137E-01	3.595E-01	-1.707E+01	-4.552E-02	-7.249E-02
-1.205E-01	3.960E-01	-1.709E+01	-3.761E-02	1.970E-02
3.159E-02	3.712E-01	-1.713E+01	-3.605E-02	-6.128E-02
1.026E-01	3.289E-01	-1.713E+01	-4.026E-02	1.000E-01
6.674E+00	6.725E-01	-1.707E+01	-3.894E-02	-4.518E+00

6.919E+00	6.815E-01	-1.707E+01	-3.334E-02	-4.653E+00
6.966E+00	6.528E-01	-1.710E+01	-4.282E-02	-4.716E+00
6.967E+00	6.205E-01	-1.712E+01	-4.192E-02	-4.658E+00
3.213E+01	1.737E+00	-1.700E+01	-1.732E-02	-2.132E+01
3.235E+01	1.745E+00	-1.700E+01	-2.625E-02	-2.144E+01
3.239E+01	1.708E+00	-1.706E+01	-3.379E-02	-2.186E+01
3.256E+01	1.677E+00	-1.703E+01	-5.617E-02	-2.162E+01
7.717E+01	3.623E+00	-1.699E+01	-2.039E-03	-5.220E+01
7.751E+01	3.605E+00	-1.692E+01	-3.277E-02	-5.200E+01
7.758E+01	3.666E+00	-1.680E+01	2.407E-02	-5.119E+01
7.777E+01	3.657E+00	-1.666E+01	1.198E-01	-5.122E+01
1.433E+02	6.478E+00	-1.692E+01	1.835E-02	-9.696E+01
1.436E+02	6.409E+00	-1.568E+01	5.871E-01	-9.458E+01
1.437E+02	6.569E+00	-1.686E+01	1.776E-02	-9.762E+01
1.440E+02	6.473E+00	-1.685E+01	-1.465E-03	-9.679E+01
2.295E+02	1.026E+01	-1.670E+01	7.725E-02	-1.566E+02
2.301E+02	1.021E+01	-1.687E+01	4.419E-01	-1.559E+02
2.301E+02	1.023E+01	-1.683E+01	7.770E-02	-1.570E+02
2.301E+02	1.018E+01	-1.661E+01	1.105E-01	-1.536E+02
3.404E+02	1.499E+01	-1.649E+01	2.031E-01	-2.282E+02
3.405E+02	1.484E+01	-1.577E+01	2.742E-01	-2.246E+02
3.458E+02	1.503E+01	-1.670E+01	1.895E-01	-2.348E+02
3.536E+02	1.501E+01	-1.657E+01	2.035E-01	-2.397E+02
4.711E+02	2.050E+01	-1.625E+01	3.751E-01	-3.109E+02
4.716E+02	2.044E+01	-1.609E+01	3.465E-01	-3.086E+02
4.749E+02	2.064E+01	-1.637E+01	3.732E-01	-3.133E+02
4.760E+02	2.062E+01	-1.659E+01	3.070E-01	-3.175E+02
6.239E+02	2.687E+01	-1.583E+01	5.912E-01	-4.036E+02
6.240E+02	2.690E+01	-1.638E+01	4.414E-01	-4.084E+02
6.280E+02	2.685E+01	-1.619E+01	5.255E-01	-4.043E+02
6.327E+02	2.709E+01	-1.659E+01	4.632E-01	-4.132E+02
8.020E+02	3.391E+01	-1.617E+01	6.453E-01	-5.073E+02
8.039E+02	3.402E+01	-1.602E+01	7.367E-01	-5.077E+02
8.043E+02	3.411E+01	-1.663E+01	7.282E-01	-5.174E+02
8.050E+02	3.424E+01	-1.623E+01	6.132E-01	-5.141E+02
9.968E+02	4.219E+01	-1.694E+01	1.082E+00	-6.432E+02
9.989E+02	4.218E+01	-1.622E+01	8.614E-01	-6.294E+02
9.992E+02	4.243E+01	-1.653E+01	1.017E+00	-6.395E+02
1.000E+03	4.239E+01	-1.628E+01	7.123E-01	-6.349E+02

Table 49: Experimental data for 10° back cavity model with dummy sting. Mean values over each data event.

Q raw (Pa)	Drag (amps)	Lift (amps)	Side (amps)	Diameter (m)	Model Area (m^2)	Air Density (kg/m^3)
-6.993E-03	3.412E-01	-1.712E+01	-6.759E-02	4.438E-02	1.547E-03	1.218E+00
-6.712E-03	3.187E-01	-1.718E+01	-5.439E-02	4.438E-02	1.547E-03	1.218E+00
6.500E-03	2.892E-01	-1.716E+01	-3.955E-02	4.438E-02	1.547E-03	1.206E+00
2.851E+00	3.861E-01	-1.713E+01	-5.506E-02	4.438E-02	1.547E-03	1.211E+00
7.840E+00	6.188E-01	-1.720E+01	-7.917E-02	4.438E-02	1.547E-03	1.206E+00
9.509E+00	6.815E-01	-1.719E+01	-3.929E-02	4.438E-02	1.547E-03	1.211E+00
3.294E+01	1.767E+00	-1.733E+01	-1.423E-01	4.438E-02	1.547E-03	1.218E+00
3.315E+01	1.802E+00	-1.726E+01	-1.584E-01	4.438E-02	1.547E-03	1.218E+00
3.374E+01	1.744E+00	-1.734E+01	-1.379E-02	4.438E-02	1.547E-03	1.211E+00
3.382E+01	1.752E+00	-1.733E+01	-2.066E-01	4.438E-02	1.547E-03	1.206E+00
7.628E+01	3.712E+00	-1.742E+01	-2.498E-01	4.438E-02	1.547E-03	1.218E+00
7.725E+01	3.674E+00	-1.757E+01	3.061E-03	4.438E-02	1.547E-03	1.211E+00
7.838E+01	3.775E+00	-1.756E+01	-2.528E-01	4.438E-02	1.547E-03	1.218E+00
7.924E+01	3.750E+00	-1.756E+01	-3.945E-01	4.438E-02	1.547E-03	1.206E+00
1.407E+02	6.526E+00	-1.759E+01	-4.016E-01	4.438E-02	1.547E-03	1.218E+00
1.411E+02	6.523E+00	-1.785E+01	-2.193E-02	4.438E-02	1.547E-03	1.211E+00
1.425E+02	6.543E+00	-1.792E+01	-6.114E-01	4.438E-02	1.547E-03	1.206E+00
1.445E+02	6.670E+00	-1.789E+01	-4.281E-01	4.438E-02	1.547E-03	1.218E+00
2.097E+02	9.503E+00	-1.827E+01	-8.180E-01	4.438E-02	1.547E-03	1.206E+00
2.240E+02	9.986E+00	-1.804E+01	9.727E-02	4.438E-02	1.547E-03	1.211E+00
2.264E+02	1.033E+01	-1.788E+01	-5.431E-01	4.438E-02	1.547E-03	1.218E+00
2.311E+02	1.047E+01	-1.825E+01	-7.135E-01	4.438E-02	1.547E-03	1.218E+00
2.908E+02	1.303E+01	-1.871E+01	-1.085E+00	4.438E-02	1.547E-03	1.206E+00
3.297E+02	1.477E+01	-1.714E+01	-1.097E+00	4.438E-02	1.547E-03	1.211E+00
3.343E+02	1.503E+01	-1.811E+01	-4.631E-01	4.438E-02	1.547E-03	1.218E+00
3.389E+02	1.522E+01	-1.867E+01	-1.241E+00	4.438E-02	1.547E-03	1.218E+00
3.860E+02	1.720E+01	-1.923E+01	-1.295E+00	4.438E-02	1.547E-03	1.206E+00
4.636E+02	2.051E+01	-1.908E+01	-1.646E+00	4.438E-02	1.547E-03	1.218E+00
4.660E+02	2.063E+01	-1.780E+01	-7.029E-01	4.438E-02	1.547E-03	1.218E+00
4.920E+02	2.178E+01	-1.977E+01	-1.449E+00	4.438E-02	1.547E-03	1.206E+00
6.130E+02	2.695E+01	-2.014E+01	-2.074E+00	4.438E-02	1.547E-03	1.206E+00
6.179E+02	2.705E+01	-1.936E+01	-2.381E+00	4.438E-02	1.547E-03	1.218E+00
6.216E+02	2.696E+01	-1.687E+01	-9.930E-01	4.438E-02	1.547E-03	1.218E+00
7.505E+02	3.261E+01	-2.066E+01	-2.668E+00	4.438E-02	1.547E-03	1.206E+00
7.618E+02	3.292E+01	-1.667E+01	-1.481E+00	4.438E-02	1.547E-03	1.218E+00
8.197E+02	3.547E+01	-2.069E+01	-3.059E+00	4.438E-02	1.547E-03	1.206E+00
8.939E+02	3.860E+01	-2.010E+01	-3.889E+00	4.438E-02	1.547E-03	1.206E+00

9.044E+02	3.950E+01	-2.090E+01	-2.986E+00	4.438E-02	1.547E-03	1.218E+00
-6.993E-03	3.412E-01	-1.712E+01	-6.759E-02	4.438E-02	1.547E-03	1.218E+00
-6.712E-03	3.187E-01	-1.718E+01	-5.439E-02	4.438E-02	1.547E-03	1.218E+00
6.500E-03	2.892E-01	-1.716E+01	-3.955E-02	4.438E-02	1.547E-03	1.206E+00
2.851E+00	3.861E-01	-1.713E+01	-5.506E-02	4.438E-02	1.547E-03	1.211E+00
7.840E+00	6.188E-01	-1.720E+01	-7.917E-02	4.438E-02	1.547E-03	1.206E+00
9.509E+00	6.815E-01	-1.719E+01	-3.929E-02	4.438E-02	1.547E-03	1.211E+00
3.294E+01	1.767E+00	-1.733E+01	-1.423E-01	4.438E-02	1.547E-03	1.218E+00
3.315E+01	1.802E+00	-1.726E+01	-1.584E-01	4.438E-02	1.547E-03	1.218E+00
3.374E+01	1.744E+00	-1.734E+01	-1.379E-02	4.438E-02	1.547E-03	1.211E+00
3.382E+01	1.752E+00	-1.733E+01	-2.066E-01	4.438E-02	1.547E-03	1.206E+00
7.628E+01	3.712E+00	-1.742E+01	-2.498E-01	4.438E-02	1.547E-03	1.218E+00
7.725E+01	3.674E+00	-1.757E+01	3.061E-03	4.438E-02	1.547E-03	1.211E+00
7.838E+01	3.775E+00	-1.756E+01	-2.528E-01	4.438E-02	1.547E-03	1.218E+00
7.924E+01	3.750E+00	-1.756E+01	-3.945E-01	4.438E-02	1.547E-03	1.206E+00
1.407E+02	6.526E+00	-1.759E+01	-4.016E-01	4.438E-02	1.547E-03	1.218E+00
1.411E+02	6.523E+00	-1.785E+01	-2.193E-02	4.438E-02	1.547E-03	1.211E+00
1.425E+02	6.543E+00	-1.792E+01	-6.114E-01	4.438E-02	1.547E-03	1.206E+00
1.445E+02	6.670E+00	-1.789E+01	-4.281E-01	4.438E-02	1.547E-03	1.218E+00
2.097E+02	9.503E+00	-1.827E+01	-8.180E-01	4.438E-02	1.547E-03	1.206E+00
2.240E+02	9.986E+00	-1.804E+01	9.727E-02	4.438E-02	1.547E-03	1.211E+00
2.264E+02	1.033E+01	-1.788E+01	-5.431E-01	4.438E-02	1.547E-03	1.218E+00
2.311E+02	1.047E+01	-1.825E+01	-7.135E-01	4.438E-02	1.547E-03	1.218E+00
2.908E+02	1.303E+01	-1.871E+01	-1.085E+00	4.438E-02	1.547E-03	1.206E+00
3.297E+02	1.477E+01	-1.714E+01	-1.097E+00	4.438E-02	1.547E-03	1.211E+00
3.343E+02	1.503E+01	-1.811E+01	-4.631E-01	4.438E-02	1.547E-03	1.218E+00
3.389E+02	1.522E+01	-1.867E+01	-1.241E+00	4.438E-02	1.547E-03	1.218E+00
3.860E+02	1.720E+01	-1.923E+01	-1.295E+00	4.438E-02	1.547E-03	1.206E+00
4.636E+02	2.051E+01	-1.908E+01	-1.646E+00	4.438E-02	1.547E-03	1.218E+00
4.660E+02	2.063E+01	-1.780E+01	-7.029E-01	4.438E-02	1.547E-03	1.218E+00
4.920E+02	2.178E+01	-1.977E+01	-1.449E+00	4.438E-02	1.547E-03	1.206E+00
6.130E+02	2.695E+01	-2.014E+01	-2.074E+00	4.438E-02	1.547E-03	1.206E+00
6.179E+02	2.705E+01	-1.936E+01	-2.381E+00	4.438E-02	1.547E-03	1.218E+00
6.216E+02	2.696E+01	-1.687E+01	-9.930E-01	4.438E-02	1.547E-03	1.218E+00
7.505E+02	3.261E+01	-2.066E+01	-2.668E+00	4.438E-02	1.547E-03	1.206E+00
7.618E+02	3.292E+01	-1.667E+01	-1.481E+00	4.438E-02	1.547E-03	1.218E+00
8.197E+02	3.547E+01	-2.069E+01	-3.059E+00	4.438E-02	1.547E-03	1.206E+00
8.939E+02	3.860E+01	-2.010E+01	-3.889E+00	4.438E-02	1.547E-03	1.206E+00
9.044E+02	3.950E+01	-2.090E+01	-2.986E+00	4.438E-02	1.547E-03	1.218E+00

Table 50: Experimental data for 25° back cavity model with dummy sting. Mean values over each data event.

Q raw (Pa)	Drag (amps)	Lift (amps)	Side (amps)	Diameter (m)	Model Area (m^2)	Air Density (kg/m^3)
-2.341E-02	3.965E-01	-1.710E+01	-4.418E-02	4.444E-02	1.551E-03	1.211E+00
-2.298E-02	2.823E-01	-1.707E+01	5.498E-02	4.444E-02	1.551E-03	1.206E+00
-1.897E-02	2.784E-01	-1.701E+01	-4.839E-02	4.444E-02	1.551E-03	1.206E+00
4.938E+00	5.114E-01	-1.713E+01	7.832E-03	4.444E-02	1.551E-03	1.206E+00
6.691E+00	6.693E-01	-1.720E+01	-3.650E-02	4.444E-02	1.551E-03	1.211E+00
2.125E+01	1.149E+00	-1.741E+01	3.993E-02	4.444E-02	1.551E-03	1.206E+00
3.133E+01	1.656E+00	-1.761E+01	-3.988E-02	4.444E-02	1.551E-03	1.211E+00
3.396E+01	1.581E+00	-1.760E+01	-5.104E-02	4.444E-02	1.551E-03	1.206E+00
4.993E+01	2.244E+00	-1.790E+01	1.281E-01	4.444E-02	1.551E-03	1.206E+00
7.552E+01	3.427E+00	-1.832E+01	-1.465E-02	4.444E-02	1.551E-03	1.211E+00
7.859E+01	3.308E+00	-1.839E+01	-1.190E-02	4.444E-02	1.551E-03	1.206E+00
9.054E+01	3.813E+00	-1.859E+01	2.454E-01	4.444E-02	1.551E-03	1.206E+00
1.400E+02	6.044E+00	-1.923E+01	-1.301E-01	4.444E-02	1.551E-03	1.211E+00
1.428E+02	5.850E+00	-1.945E+01	3.111E-01	4.444E-02	1.551E-03	1.206E+00
1.434E+02	5.866E+00	-1.953E+01	1.280E-01	4.444E-02	1.551E-03	1.206E+00
2.093E+02	8.472E+00	-2.058E+01	4.763E-01	4.444E-02	1.551E-03	1.206E+00
2.248E+02	9.484E+00	-2.002E+01	-5.134E-01	4.444E-02	1.551E-03	1.211E+00
2.306E+02	9.281E+00	-2.102E+01	2.319E-01	4.444E-02	1.551E-03	1.206E+00
2.505E+02	1.008E+01	-2.125E+01	6.156E-01	4.444E-02	1.551E-03	1.206E+00
2.919E+02	1.170E+01	-2.195E+01	7.220E-01	4.444E-02	1.551E-03	1.206E+00
3.318E+02	1.380E+01	-2.067E+01	-8.178E-01	4.444E-02	1.551E-03	1.211E+00
3.366E+02	1.351E+01	-2.280E+01	7.149E-01	4.444E-02	1.551E-03	1.206E+00
3.374E+02	1.355E+01	-2.271E+01	8.077E-01	4.444E-02	1.551E-03	1.206E+00
3.868E+02	1.547E+01	-2.348E+01	1.037E+00	4.444E-02	1.551E-03	1.206E+00
4.394E+02	1.757E+01	-2.437E+01	1.347E+00	4.444E-02	1.551E-03	1.206E+00
4.417E+02	1.765E+01	-2.447E+01	1.345E+00	4.444E-02	1.551E-03	1.206E+00
4.580E+02	1.869E+01	-2.094E+01	-1.545E+00	4.444E-02	1.551E-03	1.211E+00
4.958E+02	1.976E+01	-2.535E+01	1.070E+00	4.444E-02	1.551E-03	1.206E+00
5.556E+02	2.214E+01	-2.642E+01	6.825E-01	4.444E-02	1.551E-03	1.206E+00
5.561E+02	2.219E+01	-2.637E+01	1.615E+00	4.444E-02	1.551E-03	1.206E+00
6.164E+02	2.267E+01	-1.634E+01	1.029E-01	4.444E-02	1.551E-03	1.206E+00
6.186E+02	2.449E+01	-2.738E+01	4.933E-01	4.444E-02	1.551E-03	1.206E+00
6.212E+02	2.539E+01	-1.888E+01	2.182E+00	4.444E-02	1.551E-03	1.206E+00
6.231E+02	2.160E+01	-1.914E+01	-4.202E+00	4.444E-02	1.551E-03	1.211E+00

Table 51: Experimental data for 45° back cavity model with dummy sting. Mean values over each data event.

Q raw (Pa)	Drag (amps)	Lift (amps)	Side (amps)	Diameter (m)	Model Area (m^2)	Air Density (kg/m^3)
-5.052E-02	2.980E-01	-1.695E+01	-5.332E-02	4.444E-02	1.551E-03	1.206E+00
-3.359E-02	4.078E-01	-1.697E+01	-5.487E-02	4.444E-02	1.551E-03	1.211E+00
-2.200E-02	3.318E-01	-1.697E+01	-6.405E-02	4.444E-02	1.551E-03	1.218E+00
-7.103E-03	3.197E-01	-1.693E+01	-6.458E-02	4.444E-02	1.551E-03	1.218E+00
6.919E+00	5.853E-01	-1.709E+01	-5.255E-02	4.444E-02	1.551E-03	1.211E+00
8.450E+00	5.072E-01	-1.708E+01	-3.879E-02	4.444E-02	1.551E-03	1.206E+00
3.248E+01	1.269E+00	-1.756E+01	-3.975E-02	4.444E-02	1.551E-03	1.211E+00
3.450E+01	1.243E+00	-1.756E+01	-9.458E-02	4.444E-02	1.551E-03	1.218E+00
3.473E+01	1.243E+00	-1.762E+01	-1.436E-01	4.444E-02	1.551E-03	1.218E+00
3.632E+01	1.214E+00	-1.761E+01	-1.050E-04	4.444E-02	1.551E-03	1.206E+00
7.828E+01	2.440E+00	-1.856E+01	-2.844E-02	4.444E-02	1.551E-03	1.211E+00
7.873E+01	2.415E+00	-1.853E+01	-1.527E-01	4.444E-02	1.551E-03	1.218E+00
7.969E+01	2.425E+00	-1.863E+01	-3.502E-01	4.444E-02	1.551E-03	1.218E+00
8.497E+01	2.398E+00	-1.860E+01	1.021E-01	4.444E-02	1.551E-03	1.206E+00
1.459E+02	4.206E+00	-1.999E+01	-1.412E-01	4.444E-02	1.551E-03	1.211E+00
1.472E+02	4.225E+00	-1.999E+01	-2.261E-01	4.444E-02	1.551E-03	1.218E+00
1.480E+02	4.228E+00	-2.010E+01	-5.073E-01	4.444E-02	1.551E-03	1.218E+00
1.542E+02	4.139E+00	-2.003E+01	1.702E-01	4.444E-02	1.551E-03	1.206E+00
2.336E+02	6.604E+00	-2.194E+01	-4.373E-01	4.444E-02	1.551E-03	1.211E+00
2.375E+02	6.694E+00	-2.200E+01	-3.868E-01	4.444E-02	1.551E-03	1.218E+00
2.377E+02	6.683E+00	-2.206E+01	-1.353E+00	4.444E-02	1.551E-03	1.218E+00
2.478E+02	6.451E+00	-2.188E+01	-3.817E-01	4.444E-02	1.551E-03	1.206E+00
3.457E+02	9.779E+00	-2.415E+01	-3.788E-01	4.444E-02	1.551E-03	1.211E+00
3.502E+02	9.872E+00	-2.455E+01	-2.330E+00	4.444E-02	1.551E-03	1.218E+00
3.534E+02	9.895E+00	-2.457E+01	-5.546E-01	4.444E-02	1.551E-03	1.218E+00
3.609E+02	9.479E+00	-2.400E+01	-1.008E+00	4.444E-02	1.551E-03	1.206E+00
4.643E+02	1.036E+01	-1.892E+01	1.224E+00	4.444E-02	1.551E-03	1.206E+00
4.749E+02	1.298E+01	-2.690E+01	-8.236E-01	4.444E-02	1.551E-03	1.211E+00
4.883E+02	1.386E+01	-2.740E+01	-1.690E+00	4.444E-02	1.551E-03	1.218E+00
4.905E+02	1.393E+01	-2.722E+01	-4.956E+00	4.444E-02	1.551E-03	1.218E+00
6.533E+02	1.870E+01	-3.093E+01	-1.948E+00	4.444E-02	1.551E-03	1.218E+00
6.541E+02	1.894E+01	-3.275E+01	-5.978E+00	4.444E-02	1.551E-03	1.218E+00

Table 52: Experimental data for 0° back cavity model without dummy sting. Mean values over each data event.

Q raw (Pa)	Drag (amps)	Lift (amps)	Side (amps)	Diameter (m)	Model Area (m^2)	Air Density (kg/m^3)
-5.052E-02	2.980E-01	-1.695E+01	-5.332E-02	4.444E-02	1.551E-03	1.206E+00
-3.359E-02	4.078E-01	-1.697E+01	-5.487E-02	4.444E-02	1.551E-03	1.211E+00
-2.200E-02	3.318E-01	-1.697E+01	-6.405E-02	4.444E-02	1.551E-03	1.218E+00
-7.103E-03	3.197E-01	-1.693E+01	-6.458E-02	4.444E-02	1.551E-03	1.218E+00
6.919E+00	5.853E-01	-1.709E+01	-5.255E-02	4.444E-02	1.551E-03	1.211E+00
8.450E+00	5.072E-01	-1.708E+01	-3.879E-02	4.444E-02	1.551E-03	1.206E+00
3.248E+01	1.269E+00	-1.756E+01	-3.975E-02	4.444E-02	1.551E-03	1.211E+00
3.450E+01	1.243E+00	-1.756E+01	-9.458E-02	4.444E-02	1.551E-03	1.218E+00
3.473E+01	1.243E+00	-1.762E+01	-1.436E-01	4.444E-02	1.551E-03	1.218E+00
3.632E+01	1.214E+00	-1.761E+01	-1.050E-04	4.444E-02	1.551E-03	1.206E+00
7.828E+01	2.440E+00	-1.856E+01	-2.844E-02	4.444E-02	1.551E-03	1.211E+00
7.873E+01	2.415E+00	-1.853E+01	-1.527E-01	4.444E-02	1.551E-03	1.218E+00
7.969E+01	2.425E+00	-1.863E+01	-3.502E-01	4.444E-02	1.551E-03	1.218E+00
8.497E+01	2.398E+00	-1.860E+01	1.021E-01	4.444E-02	1.551E-03	1.206E+00
1.459E+02	4.206E+00	-1.999E+01	-1.412E-01	4.444E-02	1.551E-03	1.211E+00
1.472E+02	4.225E+00	-1.999E+01	-2.261E-01	4.444E-02	1.551E-03	1.218E+00
1.480E+02	4.228E+00	-2.010E+01	-5.073E-01	4.444E-02	1.551E-03	1.218E+00
1.542E+02	4.139E+00	-2.003E+01	1.702E-01	4.444E-02	1.551E-03	1.206E+00
2.336E+02	6.604E+00	-2.194E+01	-4.373E-01	4.444E-02	1.551E-03	1.211E+00
2.375E+02	6.694E+00	-2.200E+01	-3.868E-01	4.444E-02	1.551E-03	1.218E+00
2.377E+02	6.683E+00	-2.206E+01	-1.353E+00	4.444E-02	1.551E-03	1.218E+00
2.478E+02	6.451E+00	-2.188E+01	-3.817E-01	4.444E-02	1.551E-03	1.206E+00
3.457E+02	9.779E+00	-2.415E+01	-3.788E-01	4.444E-02	1.551E-03	1.211E+00
3.502E+02	9.872E+00	-2.455E+01	-2.330E+00	4.444E-02	1.551E-03	1.218E+00
3.534E+02	9.895E+00	-2.457E+01	-5.546E-01	4.444E-02	1.551E-03	1.218E+00
3.609E+02	9.479E+00	-2.400E+01	-1.008E+00	4.444E-02	1.551E-03	1.206E+00
4.643E+02	1.036E+01	-1.892E+01	1.224E+00	4.444E-02	1.551E-03	1.206E+00
4.749E+02	1.298E+01	-2.690E+01	-8.236E-01	4.444E-02	1.551E-03	1.211E+00
4.883E+02	1.386E+01	-2.740E+01	-1.690E+00	4.444E-02	1.551E-03	1.218E+00
4.905E+02	1.393E+01	-2.722E+01	-4.956E+00	4.444E-02	1.551E-03	1.218E+00
6.533E+02	1.870E+01	-3.093E+01	-1.948E+00	4.444E-02	1.551E-03	1.218E+00
6.541E+02	1.894E+01	-3.275E+01	-5.978E+00	4.444E-02	1.551E-03	1.218E+00

B.6 Magnetically Suspended Data

Table 53: Experimental data for 0° free-flying model. Mean values over each data event Model diameter 0.04442 m..

Q raw (Pa)	Drag (amps)	Lift (amps)	Side (amps)	Air Density (kg/m^3)
-2.416E-02	-2.713E-02	-1.765E+01	-6.604E-02	1.206E+00
-2.404E-02	6.940E-02	-1.766E+01	-3.365E-02	1.206E+00
7.538E-03	2.762E-01	-1.765E+01	-4.959E-02	1.197E+00
1.759E-02	1.543E-01	-1.759E+01	-4.945E-02	1.197E+00
1.622E+02	7.253E+00	-1.753E+01	-2.201E-01	1.206E+00
1.630E+02	7.403E+00	-1.757E+01	1.107E-02	1.206E+00
1.638E+02	7.455E+00	-1.730E+01	7.043E-02	1.197E+00
1.647E+02	7.621E+00	-1.723E+01	4.116E-02	1.197E+00
3.275E+02	1.465E+01	-1.740E+01	-4.320E-01	1.206E+00
3.290E+02	1.483E+01	-1.737E+01	1.261E-01	1.206E+00
3.313E+02	1.492E+01	-1.698E+01	1.817E-01	1.197E+00
3.331E+02	1.515E+01	-1.687E+01	1.624E-01	1.197E+00
4.977E+02	2.213E+01	-1.735E+01	-6.693E-01	1.206E+00
4.987E+02	2.233E+01	-1.714E+01	2.699E-01	1.206E+00
5.004E+02	2.244E+01	-1.658E+01	2.324E-01	1.197E+00
5.014E+02	2.238E+01	-1.671E+01	3.450E-01	1.197E+00
6.708E+02	2.970E+01	-1.651E+01	5.393E-01	1.197E+00
6.735E+02	2.973E+01	-1.723E+01	-8.976E-01	1.206E+00
6.745E+02	2.995E+01	-1.634E+01	4.479E-01	1.197E+00
6.758E+02	2.990E+01	-1.701E+01	3.679E-01	1.206E+00
8.460E+02	3.722E+01	-1.637E+01	7.320E-01	1.197E+00
8.473E+02	3.716E+01	-1.705E+01	-9.633E-01	1.206E+00
8.484E+02	3.745E+01	-1.612E+01	5.740E-01	1.197E+00
8.487E+02	3.737E+01	-1.696E+01	5.392E-01	1.206E+00
1.016E+03	4.461E+01	-1.633E+01	1.012E+00	1.197E+00
1.016E+03	4.470E+01	-1.722E+01	-1.170E+00	1.206E+00
1.018E+03	4.488E+01	-1.623E+01	8.414E-01	1.197E+00
1.019E+03	4.485E+01	-1.727E+01	8.355E-01	1.206E+00
1.184E+03	5.206E+01	-1.719E+01	-1.131E+00	1.206E+00
-2.416E-02	-2.713E-02	-1.765E+01	-6.604E-02	1.206E+00
-2.404E-02	6.940E-02	-1.766E+01	-3.365E-02	1.206E+00
7.538E-03	2.762E-01	-1.765E+01	-4.959E-02	1.197E+00
1.759E-02	1.543E-01	-1.759E+01	-4.945E-02	1.197E+00
1.622E+02	7.253E+00	-1.753E+01	-2.201E-01	1.206E+00
1.630E+02	7.403E+00	-1.757E+01	1.107E-02	1.206E+00
1.638E+02	7.455E+00	-1.730E+01	7.043E-02	1.197E+00

1.647E+02	7.621E+00	-1.723E+01	4.116E-02	1.197E+00
3.275E+02	1.465E+01	-1.740E+01	-4.320E-01	1.206E+00
3.290E+02	1.483E+01	-1.737E+01	1.261E-01	1.206E+00
3.313E+02	1.492E+01	-1.698E+01	1.817E-01	1.197E+00
3.331E+02	1.515E+01	-1.687E+01	1.624E-01	1.197E+00
4.977E+02	2.213E+01	-1.735E+01	-6.693E-01	1.206E+00
4.987E+02	2.233E+01	-1.714E+01	2.699E-01	1.206E+00
5.004E+02	2.244E+01	-1.658E+01	2.324E-01	1.197E+00
5.014E+02	2.238E+01	-1.671E+01	3.450E-01	1.197E+00
6.708E+02	2.970E+01	-1.651E+01	5.393E-01	1.197E+00
6.735E+02	2.973E+01	-1.723E+01	-8.976E-01	1.206E+00
6.745E+02	2.995E+01	-1.634E+01	4.479E-01	1.197E+00
6.758E+02	2.990E+01	-1.701E+01	3.679E-01	1.206E+00

Table 54: Experimental data for 5° free-flying model. Mean values over each data event Model diameter 0.04441 m..

Q raw (Pa)	Drag (amps)	Lift (amps)	Side (amps)	Air Density (kg/m^3)
-5.228E-03	6.346E-02	-1.765E+01	-3.830E-02	1.197E+00
-1.652E-03	1.405E-01	-1.767E+01	-4.393E-02	1.206E+00
5.057E-03	1.560E-01	-1.770E+01	-3.237E-02	1.197E+00
1.617E+02	7.381E+00	-1.749E+01	-5.884E-01	1.206E+00
1.638E+02	7.309E+00	-1.758E+01	-6.216E-02	1.197E+00
1.642E+02	7.459E+00	-1.737E+01	-5.878E-01	1.197E+00
3.246E+02	1.468E+01	-1.757E+01	-1.324E+00	1.206E+00
3.303E+02	1.484E+01	-1.715E+01	-1.345E+00	1.197E+00
3.307E+02	1.474E+01	-1.741E+01	-1.166E-01	1.197E+00
4.906E+02	2.211E+01	-1.767E+01	-2.034E+00	1.206E+00
4.999E+02	2.221E+01	-1.730E+01	-1.586E-01	1.197E+00
5.009E+02	2.247E+01	-1.728E+01	-2.281E+00	1.197E+00
6.650E+02	2.959E+01	-1.716E+01	-2.627E+00	1.206E+00
6.717E+02	2.957E+01	-1.726E+01	-2.281E-01	1.197E+00
6.740E+02	2.996E+01	-1.718E+01	-3.059E+00	1.197E+00
8.381E+02	3.698E+01	-1.733E+01	-3.209E+00	1.206E+00
8.435E+02	3.696E+01	-1.724E+01	-3.151E-01	1.197E+00
8.455E+02	3.695E+01	-1.635E+01	-2.977E+00	1.197E+00
9.984E+02	3.520E+01	-1.811E+01	-3.983E-01	1.206E+00

Table 55: Experimental data for 10° free-flying model. Mean values over each data event Model diameter 0.04441 m..

Q raw (Pa)	Drag (amps)	Lift (amps)	Side (amps)	Air Density (kg/m^3)
-6.286E-03	2.510E-01	-1.767E+01	-4.314E-02	1.206E+00
3.095E-03	9.633E-02	-1.767E+01	-4.449E-02	1.197E+00
6.703E-03	4.495E-02	-1.765E+01	-4.340E-02	1.197E+00
1.611E+02	7.429E+00	-1.795E+01	-1.128E+00	1.206E+00
1.653E+02	7.291E+00	-1.809E+01	-8.359E-01	1.197E+00
1.657E+02	7.164E+00	-1.743E+01	3.976E-01	1.197E+00
3.268E+02	1.483E+01	-1.855E+01	-2.092E+00	1.206E+00
3.337E+02	1.436E+01	-1.760E+01	9.437E-03	1.197E+00
3.338E+02	1.462E+01	-1.878E+01	-2.003E+00	1.197E+00
4.954E+02	2.227E+01	-1.933E+01	-2.775E+00	1.206E+00
5.024E+02	2.166E+01	-1.791E+01	-7.000E-02	1.197E+00
5.026E+02	2.192E+01	-1.953E+01	-3.077E+00	1.197E+00
6.671E+02	2.889E+01	-1.807E+01	-2.365E+00	1.206E+00
6.730E+02	2.891E+01	-1.829E+01	-4.954E-03	1.197E+00
6.781E+02	2.869E+01	-1.956E+01	-2.545E+00	1.197E+00
8.383E+02	3.668E+01	-1.649E+01	1.917E-01	1.206E+00
8.444E+02	3.617E+01	-1.871E+01	8.809E-03	1.197E+00
1.004E+03	4.400E+01	-1.639E+01	3.740E-01	1.206E+00
1.013E+03	4.348E+01	-1.963E+01	1.904E-01	1.206E+00

Table 56: Experimental data for 15° free-flying model. Mean values over each data event Model diameter 0.04442 m..

Q raw (Pa)	Drag (amps)	Lift (amps)	Side (amps)	Air Density (kg/m^3)
-1.312E-02	6.805E-02	-1.767E+01	-4.512E-02	1.206E+00
3.624E-03	1.494E-02	-1.766E+01	-4.032E-02	1.197E+00
7.242E-03	1.075E-01	-1.768E+01	-4.289E-02	1.197E+00
1.622E+02	7.077E+00	-1.902E+01	-1.091E+00	1.206E+00
1.631E+02	7.130E+00	-1.874E+01	-1.133E+00	1.197E+00
1.643E+02	6.954E+00	-1.762E+01	-1.884E-02	1.197E+00
3.271E+02	1.418E+01	-2.030E+01	-2.276E+00	1.206E+00
3.287E+02	1.394E+01	-1.776E+01	-1.862E-02	1.197E+00
3.299E+02	1.432E+01	-2.021E+01	-2.346E+00	1.197E+00
4.949E+02	2.128E+01	-2.157E+01	-3.201E+00	1.206E+00
4.956E+02	2.100E+01	-1.773E+01	-1.057E-01	1.197E+00
4.998E+02	2.138E+01	-2.064E+01	-3.455E+00	1.197E+00

6.645E+02	2.828E+01	-1.792E+01	-1.263E-01	1.206E+00
6.673E+02	2.839E+01	-1.761E+01	-1.300E-01	1.197E+00
6.679E+02	2.822E+01	-1.796E+01	-5.021E-02	1.197E+00
8.355E+02	3.546E+01	-1.831E+01	-1.783E-01	1.206E+00
8.372E+02	3.536E+01	-1.821E+01	-7.951E-02	1.197E+00
8.372E+02	3.556E+01	-1.780E+01	-2.020E-01	1.197E+00
1.006E+03	4.253E+01	-1.894E+01	8.418E-02	1.206E+00
1.007E+03	4.279E+01	-1.878E+01	-1.593E-01	1.206E+00
1.007E+03	4.276E+01	-1.829E+01	-2.954E-01	1.197E+00

Table 57: Experimental data for 20° free-flying model. Mean values over each data event Model diameter 0.04444 m..

Q raw (Pa)	Drag (amps)	Lift (amps)	Side (amps)	Air Density (kg/m^3)
-1.323E-02	-3.604E-02	-1.765E+01	-4.032E-02	1.206E+00
-9.260E-03	9.759E-02	-1.764E+01	-5.157E-02	1.206E+00
6.781E-04	7.391E-02	-1.763E+01	-3.437E-02	1.197E+00
7.255E-03	1.715E-01	-1.764E+01	-4.119E-02	1.197E+00
1.630E+02	6.587E+00	-1.975E+01	-8.976E-01	1.206E+00
1.635E+02	6.785E+00	-1.954E+01	-1.048E+00	1.206E+00
1.651E+02	6.718E+00	-1.860E+01	-1.078E+00	1.197E+00
1.655E+02	6.938E+00	-1.941E+01	-1.487E+00	1.197E+00
3.287E+02	1.334E+01	-2.192E+01	-2.043E+00	1.206E+00
3.306E+02	1.364E+01	-2.159E+01	-2.183E+00	1.206E+00
3.329E+02	1.357E+01	-2.048E+01	-2.885E+00	1.197E+00
3.351E+02	1.393E+01	-2.144E+01	-2.535E+00	1.197E+00
5.003E+02	1.964E+01	-1.889E+01	-9.381E-01	1.206E+00
5.018E+02	1.969E+01	-1.737E+01	3.094E-02	1.197E+00
5.025E+02	1.951E+01	-2.081E+01	-1.993E+00	1.206E+00
5.038E+02	2.000E+01	-1.885E+01	-1.302E+00	1.197E+00
6.682E+02	2.699E+01	-1.807E+01	-1.137E-01	1.206E+00
6.686E+02	2.704E+01	-1.836E+01	-1.124E-01	1.206E+00
6.715E+02	2.694E+01	-1.717E+01	1.668E-01	1.197E+00
6.747E+02	2.692E+01	-1.738E+01	5.922E-02	1.197E+00
8.406E+02	3.402E+01	-1.878E+01	-1.704E-01	1.206E+00
8.417E+02	3.409E+01	-1.851E+01	-1.817E-01	1.206E+00
8.419E+02	3.380E+01	-1.707E+01	2.070E-01	1.197E+00
8.467E+02	3.376E+01	-1.754E+01	1.323E-01	1.197E+00
1.009E+03	4.106E+01	-1.907E+01	-6.702E-02	1.206E+00
1.009E+03	4.104E+01	-1.944E+01	-1.172E-01	1.206E+00
1.013E+03	4.102E+01	-1.726E+01	4.174E-01	1.197E+00

1.020E+03	4.078E+01	-1.776E+01	2.297E-01	1.197E+00
1.091E+03	4.448E+01	-1.992E+01	5.763E-02	1.206E+00

Table 58: Experimental data for 25° free-flying model. Mean values over each data event Model diameter 0.04443 m..

Q raw (Pa)	Drag (amps)	Lift (amps)	Side (amps)	Air Density (kg/m^3)
-1.643E-02	5.211E-03	-1.762E+01	-4.084E-02	1.206E+00
-6.669E-03	2.243E-01	-1.761E+01	-4.454E-02	1.197E+00
-5.336E-04	1.282E-01	-1.760E+01	-4.452E-02	1.197E+00
1.659E+02	6.421E+00	-2.022E+01	-3.929E-02	1.206E+00
1.671E+02	6.389E+00	-1.953E+01	-8.921E-01	1.197E+00
1.671E+02	6.676E+00	-2.017E+01	-9.345E-01	1.197E+00
3.332E+02	1.290E+01	-2.304E+01	2.651E-02	1.206E+00
3.361E+02	1.324E+01	-2.241E+01	-2.097E+00	1.197E+00
3.367E+02	1.289E+01	-2.256E+01	-2.087E+00	1.197E+00
5.021E+02	1.886E+01	-1.747E+01	4.793E-03	1.206E+00
5.049E+02	1.843E+01	-1.804E+01	1.018E-01	1.197E+00
5.083E+02	1.855E+01	-1.783E+01	-8.042E-01	1.197E+00
6.770E+02	2.585E+01	-1.781E+01	-1.918E-01	1.206E+00
6.785E+02	2.535E+01	-1.724E+01	-1.064E-01	1.197E+00
6.796E+02	2.523E+01	-1.803E+01	6.064E-02	1.197E+00
8.500E+02	3.260E+01	-1.792E+01	-1.438E-01	1.206E+00
8.519E+02	3.200E+01	-1.718E+01	-2.100E-01	1.197E+00
8.520E+02	3.175E+01	-1.833E+01	4.067E-02	1.197E+00
1.018E+03	3.943E+01	-1.829E+01	-1.696E-01	1.206E+00
1.022E+03	3.840E+01	-1.879E+01	5.256E-02	1.206E+00
1.027E+03	3.890E+01	-1.718E+01	-7.748E-02	1.197E+00
1.104E+03	4.281E+01	-1.863E+01	-9.884E-02	1.206E+00
-1.643E-02	5.211E-03	-1.762E+01	-4.084E-02	1.206E+00
-6.669E-03	2.243E-01	-1.761E+01	-4.454E-02	1.197E+00
-5.336E-04	1.282E-01	-1.760E+01	-4.452E-02	1.197E+00
1.659E+02	6.421E+00	-2.022E+01	-3.929E-02	1.206E+00
1.671E+02	6.389E+00	-1.953E+01	-8.921E-01	1.197E+00
1.671E+02	6.676E+00	-2.017E+01	-9.345E-01	1.197E+00
3.332E+02	1.290E+01	-2.304E+01	2.651E-02	1.206E+00

Table 59: Experimental data for 35° free-flying model. Mean values over each data event Model diameter 0.04446 m..

Q raw (Pa)	Drag (amps)	Lift (amps)	Side (amps)	Air Density (kg/m^3)
-2.857E-02	-7.694E-02	-1.755E+01	-6.919E-02	1.206E+00
-9.544E-03	1.401E-01	-1.756E+01	-4.868E-02	1.197E+00
-4.651E-03	6.605E-02	-1.752E+01	-3.694E-02	1.197E+00
2.304E-03	5.281E-02	-1.751E+01	-4.509E-02	1.206E+00
1.666E+02	5.520E+00	-2.075E+01	-1.015E-01	1.197E+00
1.666E+02	5.143E+00	-2.075E+01	-8.668E-01	1.206E+00
1.671E+02	5.413E+00	-2.064E+01	-1.545E-01	1.197E+00
1.683E+02	5.643E+00	-2.077E+01	1.197E-01	1.206E+00
3.335E+02	1.043E+01	-2.399E+01	-2.114E+00	1.206E+00
3.374E+02	1.118E+01	-2.425E+01	4.903E-01	1.197E+00
3.381E+02	1.136E+01	-2.404E+01	9.766E-01	1.206E+00
3.386E+02	1.102E+01	-2.429E+01	7.190E-01	1.197E+00
5.078E+02	1.560E+01	-1.857E+01	2.352E-01	1.197E+00
5.093E+02	1.571E+01	-1.903E+01	8.332E-01	1.197E+00
5.114E+02	1.582E+01	-2.658E+01	-2.974E+00	1.206E+00
5.120E+02	1.612E+01	-1.655E+01	-5.024E-01	1.206E+00
6.804E+02	2.151E+01	-1.802E+01	5.034E-01	1.197E+00
6.813E+02	2.173E+01	-1.746E+01	6.035E-01	1.197E+00
6.891E+02	2.155E+01	-1.808E+01	-1.749E-01	1.206E+00
6.894E+02	2.261E+01	-1.750E+01	-1.472E-01	1.206E+00
8.550E+02	2.761E+01	-1.818E+01	8.380E-01	1.197E+00
8.653E+02	2.723E+01	-1.821E+01	-9.848E-02	1.206E+00
8.661E+02	2.862E+01	-1.747E+01	-2.230E-01	1.206E+00
8.769E+02	2.752E+01	-1.975E+01	1.057E-01	1.197E+00
1.033E+03	3.293E+01	-1.846E+01	6.940E-02	1.206E+00
1.038E+03	3.329E+01	-1.802E+01	5.561E-01	1.197E+00
1.040E+03	3.473E+01	-1.737E+01	-3.732E-02	1.206E+00
1.063E+03	3.502E+01	-1.907E+01	-9.286E-02	1.197E+00
1.126E+03	3.780E+01	-1.747E+01	-5.839E-02	1.206E+00
1.195E+03	3.845E+01	-1.867E+01	1.875E-01	1.206E+00

Table 60: Experimental data for 45° free-flying model. Mean values over each data event Model diameter 0.04445 m..

Q raw (Pa)	Drag (amps)	Lift (amps)	Side (amps)	Air Density (kg/m^3)
-1.664E-02	1.893E-01	-1.757E+01	-4.859E-02	1.197E+00
-4.794E-03	2.438E-01	-1.749E+01	-5.530E-02	1.206E+00
3.090E-03	1.248E-01	-1.755E+01	-4.334E-02	1.197E+00
1.707E+02	4.805E+00	-2.118E+01	-8.492E-02	1.197E+00
1.717E+02	4.643E+00	-2.128E+01	-2.038E-02	1.197E+00
1.729E+02	4.993E+00	-2.096E+01	9.335E-02	1.206E+00
3.479E+02	9.807E+00	-2.393E+01	3.719E-01	1.206E+00
3.486E+02	9.387E+00	-2.384E+01	2.028E-01	1.197E+00
3.488E+02	9.610E+00	-2.406E+01	-1.036E-01	1.197E+00
5.299E+02	1.592E+01	-1.978E+01	-6.971E-01	1.206E+00
5.303E+02	1.561E+01	-2.051E+01	4.323E-01	1.197E+00
5.308E+02	1.453E+01	-1.969E+01	-2.768E-01	1.197E+00
7.129E+02	2.062E+01	-1.947E+01	-1.102E-01	1.197E+00
7.235E+02	2.142E+01	-2.112E+01	-1.874E-01	1.197E+00
7.307E+02	2.022E+01	-2.083E+01	-2.911E-01	1.206E+00
8.997E+02	2.586E+01	-1.967E+01	-1.197E-01	1.197E+00
9.090E+02	2.512E+01	-2.054E+01	8.528E-03	1.197E+00
9.155E+02	2.615E+01	-2.119E+01	-2.399E-01	1.206E+00
1.078E+03	3.139E+01	-1.968E+01	-1.007E-01	1.197E+00
1.091E+03	3.070E+01	-2.059E+01	-1.165E-02	1.197E+00

B.7 Reference Data

Table 61: Reference data for Stardust capsule aerodynamics taken at a Reynolds number of 9e5 after transformation into experimental coordinate system.

AoA (degrees)	CD	CL	Cm
0.00	0.8739	0.0000	0.0000
2.02	0.8755	0.0256	-0.0058
4.00	0.8766	0.0494	-0.0115
6.04	0.8764	0.0749	-0.0171
7.99	0.8757	0.0985	-0.0227
12.02	0.8719	0.1491	-0.0332
16.01	0.8614	0.1967	-0.0446
20.00	0.8455	0.2425	-0.0573
24.01	0.8156	0.2842	-0.0676
28.01	0.7652	0.3102	-0.0757

APPENDIX C. COMPUTER CODES

C.1 MATLAB Code

Balance Reduction

```
function output=getStingData(data)
%Separate data from matrix
%Raw voltages
voltageD=data(:,2:8);
%Tare Voltages
tareD=data(:,9:14);
%Characteristic Length
L=data(:,16);
%Air Density
density=data(:,15);
%Calculate Model Area
S=pi().*(L./2).^2;
%Calculate approximate shperical model volume
V=(4/3)*pi().*(L./2).^3;
%Dynamic Pressure
pressureD=data(:,1);
number=length(pressureD);
record=[];

for i=1:1:number
    %Iterate Tare Calculations
    voltageT=tareD(i,:);
    [tare,~,~,~]=gettare(voltageT);
    %Iterate Force and Moment calculations
    voltage=voltageD(i,:);
    [FM,RecordP,RecordFM,RecordE]=calculateFM(voltage,tare);
    record=vertcat(record,FM');
end
%Interpolate pressure using sensor calibration
for i=1:1:number

    pressureD(i)=  pressureD(i)*0.9970+7.697;
    if pressureD(i)<0
        pressureD(i)=0;
    end
end
re=[];
v=[];
%perform wake corrections
for i=1:1:number
    Cdu=record(i,2)/(pressureD(i)*S(i));
    Esolid=0.8*(V(i))/(0.020985)^(3/2);
    Ewake=(Cdu*S(i)/(4*0.020985));
    pressureD(i)=pressureD(i)*(1+Ewake+Esolid)^2;
    %calculate velocity and reynolds number
    v(i)=sqrt(pressureD(i)*2/density(i));
    re(i)=v(i)*L(i)*density(i)/(1.846e-5);
end
```

```
coefficients=[];
%reduce coefficients from forces and moments
for i=1:1:number
    coefficients(i,1)=record(i,1)/(pressureD(i)*S(i));
    coefficients(i,2)=record(i,2)/(pressureD(i)*S(i));
    coefficients(i,3)=record(i,3)/(pressureD(i)*S(i)*L(i));
    coefficients(i,4)=record(i,4)/(pressureD(i)*S(i)*L(i));
    coefficients(i,5)=record(i,5)/(pressureD(i)*S(i)*L(i));
    coefficients(i,6)=record(i,6)/(pressureD(i)*S(i));
end
output=[];
Interim=horzcat(pressureD,re',v',record,coefficients,density,L);

%Take individual samples and reduce to mean values and standard deviaton
while isempty(Interim)==false
    result=[];
    for index=1:1:17
        value=mean(Interim(1:20,index));
        result= horzcat(result,value);
    end
    for index=1:1:15
        value=std(Interim(1:20,index));
        result= horzcat(result,value);
    end
    output=vertcat(output,result);

    Interim(1:21,:)=[];
end

end



function [FM,RecordP,RecordFM,RecordE]=gettare(voltage)
% %Load first order corrections
% C1=[1.00000E+00   0.00000E+00 0.00000E+00 -8.65140E-02    -3.30260E-03    -
2.25000E-02;
% 5.37320E-03   1.00000E+00 -1.33390E-03    9.86480E-03 -1.00000E-02    -
1.25080E-02;
% -1.88620E-02  2.13150E-03 1.00000E+00 -8.89050E-02    -1.05160E-02
3.53270E-03;
% 7.27370E-04   0.00000E+00 4.64280E-03 1.00000E+00 -2.31530E-02    1.79320E-
02;
% -2.00320E-03  0.00000E+00 6.34270E-03 -3.28290E-02    1.00000E+00 -
2.80650E-03;
% 7.99690E-03   0.00000E+00 -1.62600E-03    1.10570E-02 4.36640E-03
1.00000E+00];
% %load second order corrections
% C2=[-3.65640E-05  4.04370E-04 0.00000E+00 0.00000E+00 0.00000E+00
0.00000E+00 0.00000E+00 -2.03650E-04    0.00000E+00 0.00000E+00 0.00000E+00
0.00000E+00 0.00000E+00 0.00000E+00 0.00000E+00 0.00000E+00 -4.43170E-04    -
6.22950E-04    0.00000E+00 0.00000E+00 0.00000E+00;
% -1.77910E-04  6.24210E-04 1.94870E-04 0.00000E+00 -2.37370E-05
0.00000E+00 0.00000E+00 0.00000E+00 0.00000E+00 0.00000E+00 0.00000E+00
6.29900E-05 0.00000E+00 0.00000E+00 0.00000E+00 5.28100E-04 -7.77700E-04
0.00000E+00 -6.80530E-05    3.05800E-04 -1.58380E-04;
```

```
% 0.00000E+00   -2.01570E-04    -5.76680E-05    0.00000E+00 -6.36520E-05
0.00000E+00 0.00000E+00 0.00000E+00 0.00000E+00 0.00000E+00 0.00000E+00
0.00000E+00 0.00000E+00 0.00000E+00 0.00000E+00 0.00000E+00 -4.38540E-04    -
1.80350E-04    0.00000E+00 0.00000E+00 0.00000E+00;
% 0.00000E+00   0.00000E+00 0.00000E+00 -5.20030E-05    -5.94410E-05
0.00000E+00 0.00000E+00 0.00000E+00 0.00000E+00 0.00000E+00 0.00000E+00
0.00000E+00 0.00000E+00 0.00000E+00 1.00700E-04 0.00000E+00 0.00000E+00 -
1.33450E-04    0.00000E+00 0.00000E+00 0.00000E+00;
% -2.41090E-05  0.00000E+00 0.00000E+00 2.07110E-04 -3.79190E-05
0.00000E+00 0.00000E+00 0.00000E+00 0.00000E+00 1.27230E-04 -2.60450E-04
0.00000E+00 5.56750E-04 -3.94160E-05    0.00000E+00 0.00000E+00 0.00000E+00
1.06650E-04 0.00000E+00 -1.24420E-04    0.00000E+00;
% -2.24910E-05  0.00000E+00 0.00000E+00 7.47910E-04 -3.84240E-05
0.00000E+00 0.00000E+00 0.00000E+00 1.04700E-04 -2.90560E-04    2.21030E-04
0.00000E+00 4.37960E-04 -2.53810E-05    4.01870E-05 0.00000E+00 0.00000E+00
0.00000E+00 -2.57760E-05    0.00000E+00 0.00000E+00];
%
% %distribute 6 sensitivity constants to matrix diagonal
% sensconst=zeros(6,6);
% values=[1.08313E+01   5.02570E+00 1.56478E+01 8.65210E+00 1.10390E+01
7.79940E+00];
%% 2019 Cal
%Load first order corrections
C1=[1   -4.45E-04   5.46E-04    -8.73E-02   -3.05E-03   -2.52E-02;
6.12E-03    1   -1.29E-03   9.84E-03    -9.88E-03   -1.24E-02;
-2.09E-02   -1.40E-03   1   -8.95E-02   -1.32E-02   3.26E-03;
1.95E-03    2.60E-05    4.06E-03    1.00E+00    -2.25E-02   1.59E-02;
-2.11E-03   1.69E-03    8.90E-03    -3.31E-02   1.00E+00    -4.56E-03;
1.06E-02    3.34E-05    -1.43E-03   1.15E-02    4.34E-03    1.00E+00];

%load second order corrections
C2=[2.6005E-05  2.9707E-04  1.9142E-05  5.1063E-06  0.0000E+00  0.0000E+00  -
1.3123E-04 0.0000E+00  0.0000E+00  0.0000E+00  0.0000E+00  4.6104E-06  -
3.1474E-05 0.0000E+00  0.0000E+00  -9.3050E-05 -4.7859E-05 0.0000E+00
2.6676E-05  0.0000E+00  2.0903E-06;
-1.9734E-04 7.7198E-04  1.6778E-04  5.5213E-06  0.0000E+00  0.0000E+00  -
3.2050E-04 0.0000E+00  0.0000E+00  0.0000E+00  0.0000E+00  5.4682E-05  -
1.0550E-05 0.0000E+00  0.0000E+00  5.3799E-04  -7.8428E-04 0.0000E+00  -
4.8960E-05 0.0000E+00  -1.7673E-04;
-2.6594E-05 2.4841E-04  -4.4250E-06 -2.4201E-04 0.0000E+00  0.0000E+00  -
3.7442E-04 0.0000E+00  0.0000E+00  0.0000E+00  0.0000E+00  2.4607E-06
3.0966E-06  0.0000E+00  0.0000E+00  -2.0145E-04 -5.9736E-04 0.0000E+00
2.9309E-05  0.0000E+00  5.5321E-05;
-3.8006E-05 -9.7212E-05 -3.7711E-05 -1.5249E-05 0.0000E+00  0.0000E+00
2.0817E-05  0.0000E+00  0.0000E+00  0.0000E+00  0.0000E+00  -4.8378E-05 -
2.7542E-05 0.0000E+00  0.0000E+00  -9.0661E-06 4.7574E-05  0.0000E+00
3.0645E-05  0.0000E+00  -7.1282E-06;
4.2497E-06  1.8412E-05  -4.8851E-06 2.2512E-04  0.0000E+00  0.0000E+00  -
2.3816E-04 0.0000E+00  0.0000E+00  0.0000E+00  0.0000E+00  -9.9170E-06
7.0985E-04  0.0000E+00  0.0000E+00  2.0821E-05  -1.7784E-05 0.0000E+00
3.9098E-05  0.0000E+00  -4.1455E-04;
-3.3726E-05 -7.2914E-05 -2.2198E-05 7.3488E-04  0.0000E+00  0.0000E+00  -
6.4633E-05 0.0000E+00  0.0000E+00  0.0000E+00  0.0000E+00  -2.7455E-06
4.5591E-04  0.0000E+00  0.0000E+00  3.8618E-06  -1.2416E-05 0.0000E+00
1.8160E-05  0.0000E+00  5.8363E-05];
```

```
%load electrical zeroes
eleczero=[0.2993    -0.0446 0.3730  0.2327  0.4239  -0.1085];
%distribute 6 sensitivity constants to matrix diagonal
sensconst=zeros(6,6);
values=[10.8236 4.9985  15.6383 8.5597  11.008  7.7849];
%%
for x=1:1:6
   sensconst(x,x)= values(x);
end
Fu=sensconst*voltage';
% calculate F1, the first order correction
F1=C1\Fu;
%Calculate the first approximation of the second order matrix
Fn=F1(1);
Fa=F1(2);
My=F1(3);
Mx=F1(4);
Mz=F1(5);
Fy=F1(6);
P1=[Fn^2,Fn*Fa,Fn*My,Fn*Mx,Fn*Mz,Fn*Fy,Fa^2,Fa*My,Fa*Mx,Fa*Mz,Fa*Fy,My^2,My*M
x,My*Mz,My*Fy,Mx^2,Mx*Mz,Mx*Fy,Mz^2,Mz*Fy,Fy^2]';

RecordP=P1;
RecordFM=F1;
%Calculate M
M=C1\C2;
%initialize values
check=0;
En=M*P1;
%Record error term
RecordE=En;
runagain=true;
while runagain==true
    %iterate corrected force Fn
   Fi=F1-En;
   %extract new loads
   Fn=Fi(1);
Fa=Fi(2);
My=Fi(3);
Mx=Fi(4);
Mz=Fi(5);
Fy=Fi(6);
%Record new loads
RecordFM=horzcat(RecordFM,Fi);
%Calculate new second order matrix

Pn=[Fn^2,Fn*Fa,Fn*My,Fn*Mx,Fn*Mz,Fn*Fy,Fa^2,Fa*My,Fa*Mx,Fa*Mz,Fa*Fy,My^2,My*M
x,My*Mz,My*Fy,Mx^2,Mx*Mz,Mx*Fy,Mz^2,Mz*Fy,Fy^2]';
%Store old error matrix
Eold=En;
   %Calculate new error matrix
En=M*Pn;
%Record En
RecordE=horzcat(RecordE,En);
%calculate error magnitude
runagain=false;
deltaEn=Eold-En;
```

```
for x=1:1:length(deltaEn)
    if abs(deltaEn(x))>0.000001
        runagain=true;
    end
end
%Record Pn
RecordP=horzcat(RecordP,Pn);

end
%Perform second-order correction with interated error
Fi=F1-En;
%Transform values from imperial to metric.
FM=Fi.*[4.448221615, 4.448221615,
0.112984829,0.112984829,0.112984829,4.448221615]';
end



function [FM,RecordP,RecordFM,RecordE]=calculateFM(voltage,tare)
%% 1985 Cal
% %Load first order corrections
% C1=[1.00000E+00   0.00000E+00 0.00000E+00 -8.65140E-02    -3.30260E-03    -
2.25000E-02;
% 5.37320E-03   1.00000E+00 -1.33390E-03    9.86480E-03 -1.00000E-02    -
1.25080E-02;
% -1.88620E-02  2.13150E-03 1.00000E+00 -8.89050E-02    -1.05160E-02
3.53270E-03;
% 7.27370E-04   0.00000E+00 4.64280E-03 1.00000E+00 -2.31530E-02    1.79320E-
02;
% -2.00320E-03  0.00000E+00 6.34270E-03 -3.28290E-02    1.00000E+00 -
2.80650E-03;
% 7.99690E-03   0.00000E+00 -1.62600E-03    1.10570E-02 4.36640E-03
1.00000E+00];
% %load second order corrections
% C2=[-3.65640E-05  4.04370E-04 0.00000E+00 0.00000E+00 0.00000E+00
0.00000E+00 0.00000E+00 -2.03650E-04    0.00000E+00 0.00000E+00 0.00000E+00
0.00000E+00 0.00000E+00 0.00000E+00 0.00000E+00 0.00000E+00 -4.43170E-04    -
6.22950E-04    0.00000E+00 0.00000E+00 0.00000E+00;
% -1.77910E-04  6.24210E-04 1.94870E-04 0.00000E+00 -2.37370E-05
0.00000E+00 0.00000E+00 0.00000E+00 0.00000E+00 0.00000E+00 0.00000E+00
6.29900E-05 0.00000E+00 0.00000E+00 0.00000E+00 5.28100E-04 -7.77700E-04
0.00000E+00 -6.80530E-05    3.05800E-04 -1.58380E-04;
% 0.00000E+00   -2.01570E-04    -5.76680E-05    0.00000E+00 -6.36520E-05
0.00000E+00 0.00000E+00 0.00000E+00 0.00000E+00 0.00000E+00 0.00000E+00
0.00000E+00 0.00000E+00 0.00000E+00 0.00000E+00 0.00000E+00 -4.38540E-04    -
1.80350E-04    0.00000E+00 0.00000E+00 0.00000E+00;
% 0.00000E+00   0.00000E+00 0.00000E+00 -5.20030E-05    -5.94410E-05
0.00000E+00 0.00000E+00 0.00000E+00 0.00000E+00 0.00000E+00 0.00000E+00
0.00000E+00 0.00000E+00 0.00000E+00 1.00700E-04 0.00000E+00 0.00000E+00 -
1.33450E-04    0.00000E+00 0.00000E+00 0.00000E+00;
% -2.41090E-05  0.00000E+00 0.00000E+00 2.07110E-04 -3.79190E-05
0.00000E+00 0.00000E+00 0.00000E+00 0.00000E+00 1.27230E-04 -2.60450E-04
0.00000E+00 5.56750E-04 -3.94160E-05    0.00000E+00 0.00000E+00 0.00000E+00
1.06650E-04 0.00000E+00 -1.24420E-04    0.00000E+00;
% -2.24910E-05  0.00000E+00 0.00000E+00 7.47910E-04 -3.84240E-05
0.00000E+00 0.00000E+00 0.00000E+00 1.04700E-04 -2.90560E-04    2.21030E-04
```

```
0.00000E+00 4.37960E-04 -2.53810E-05    4.01870E-05 0.00000E+00 0.00000E+00
0.00000E+00 -2.57760E-05    0.00000E+00 0.00000E+00];
% %load electrical zeroes
% eleczero=[0.2993  -0.0446 0.3730  0.2327  0.4239  -0.1085];
% %distribute 6 sensitivity constants to matrix diagonal
% sensconst=zeros(6,6);
% values=[1.08313E+01   5.02570E+00 1.56478E+01 8.65210E+00 1.10390E+01
7.79940E+00];

%% 2019 Cal
%Load first order corrections
C1=[1   -4.45E-04   5.46E-04    -8.73E-02   -3.05E-03   -2.52E-02;
6.12E-03    1   -1.29E-03   9.84E-03    -9.88E-03   -1.24E-02;
-2.09E-02   -1.40E-03   1   -8.95E-02   -1.32E-02   3.26E-03;
1.95E-03    2.60E-05    4.06E-03    1.00E+00    -2.25E-02   1.59E-02;
-2.11E-03   1.69E-03    8.90E-03    -3.31E-02   1.00E+00    -4.56E-03;
1.06E-02    3.34E-05    -1.43E-03   1.15E-02    4.34E-03    1.00E+00];

%load second order corrections
C2=[2.6005E-05  2.9707E-04  1.9142E-05  5.1063E-06  0.0000E+00  0.0000E+00  -
1.3123E-04 0.0000E+00  0.0000E+00  0.0000E+00  0.0000E+00  4.6104E-06  -
3.1474E-05 0.0000E+00  0.0000E+00  -9.3050E-05 -4.7859E-05 0.0000E+00
2.6676E-05  0.0000E+00  2.0903E-06;
-1.9734E-04 7.7198E-04  1.6778E-04  5.5213E-06  0.0000E+00  0.0000E+00  -
3.2050E-04 0.0000E+00  0.0000E+00  0.0000E+00  0.0000E+00  5.4682E-05  -
1.0550E-05 0.0000E+00  0.0000E+00  5.3799E-04  -7.8428E-04 0.0000E+00  -
4.8960E-05 0.0000E+00  -1.7673E-04;
-2.6594E-05 2.4841E-04  -4.4250E-06 -2.4201E-04 0.0000E+00  0.0000E+00  -
3.7442E-04 0.0000E+00  0.0000E+00  0.0000E+00  0.0000E+00  2.4607E-06
3.0966E-06  0.0000E+00  0.0000E+00  -2.0145E-04 -5.9736E-04 0.0000E+00
2.9309E-05  0.0000E+00  5.5321E-05;
-3.8006E-05 -9.7212E-05 -3.7711E-05 -1.5249E-05 0.0000E+00  0.0000E+00
2.0817E-05  0.0000E+00  0.0000E+00  0.0000E+00  0.0000E+00  -4.8378E-05 -
2.7542E-05 0.0000E+00  0.0000E+00  -9.0661E-06 4.7574E-05  0.0000E+00
3.0645E-05  0.0000E+00  -7.1282E-06;
4.2497E-06  1.8412E-05  -4.8851E-06 2.2512E-04  0.0000E+00  0.0000E+00  -
2.3816E-04 0.0000E+00  0.0000E+00  0.0000E+00  0.0000E+00  -9.9170E-06
7.0985E-04  0.0000E+00  0.0000E+00  2.0821E-05  -1.7784E-05 0.0000E+00
3.9098E-05  0.0000E+00  -4.1455E-04;
-3.3726E-05 -7.2914E-05 -2.2198E-05 7.3488E-04  0.0000E+00  0.0000E+00  -
6.4633E-05 0.0000E+00  0.0000E+00  0.0000E+00  0.0000E+00  -2.7455E-06
4.5591E-04  0.0000E+00  0.0000E+00  3.8618E-06  -1.2416E-05 0.0000E+00
1.8160E-05  0.0000E+00  5.8363E-05];

%load electrical zeroes
eleczero=[0.2993    -0.0446 0.3730  0.2327  0.4239  -0.1085];
%distribute 6 sensitivity constants to matrix diagonal
sensconst=zeros(6,6);
values=[10.8236 4.9985  15.6383 8.5597  11.008  7.7849];
%%
for x=1:1:6
   sensconst(x,x)= values(x);
end
%isolate power supply voltage
sourceV=voltage(7);
%convert the 6 voltage channels from V to mV/V
```

```
datapoint=voltage(1:6)*1000/sourceV;
%zero the datapoint
datapoint=datapoint-eleczero;
% calculate uncorrected loads
Fu=sensconst*datapoint';
% calculate F1, the first order correction
F1=C1\Fu;
%Calculate the first approximation of the second order matrix
Fn=F1(1);
Fa=F1(2);
My=F1(3);
Mx=F1(4);
Mz=F1(5);
Fy=F1(6);
P1=[Fn^2,Fn*Fa,Fn*My,Fn*Mx,Fn*Mz,Fn*Fy,Fa^2,Fa*My,Fa*Mx,Fa*Mz,Fa*Fy,My^2,My*M
x,My*Mz,My*Fy,Mx^2,Mx*Mz,Mx*Fy,Mz^2,Mz*Fy,Fy^2]';
%Keep record of loads over each pass
RecordP=P1;
RecordFM=F1;
%Calculate M matrix
M=C1\C2;
%initialize values for loop

En=M*P1;
%Record error term
RecordE=En;
runagain=true;
while runagain==true
    %iterate corrected force Fn
    Fi=F1-En;
    %extract new loads
    Fn=Fi(1);
    Fa=Fi(2);
    My=Fi(3);
    Mx=Fi(4);
    Mz=Fi(5);
    Fy=Fi(6);
%Record new loads
RecordFM=horzcat(RecordFM,Fi);
%Calculate new second order matrix

Pn=[Fn^2,Fn*Fa,Fn*My,Fn*Mx,Fn*Mz,Fn*Fy,Fa^2,Fa*My,Fa*Mx,Fa*Mz,Fa*Fy,My^2,My*M
x,My*Mz,My*Fy,Mx^2,Mx*Mz,Mx*Fy,Mz^2,Mz*Fy,Fy^2]';
   %Store old error matrix
Eold=En;
%Calculate new error matrix
En=M*Pn;
%Record En;
RecordE=horzcat(RecordE,En);
%calculate error magnitude
deltaEn=Eold-En;
for x=1:1:length(deltaEn)
    if abs(deltaEn(x))>0.00000001
        runagain=true;
    else
        runagain=false;
    end
```

```
end
%Record Pn
RecordP=horzcat(RecordP,Pn);

end
Fi=F1-En;
%Convert from lbs and in-lb to N and Nm
FM=Fi.*[4.448221615, 4.448221615,
0.112984829,0.112984829,0.112984829,4.448221615]'-tare;
%Perform moment center transfer to model geometric center
FM(3)=FM(3)-FM(1)*0.0516509;
FM(5)=FM(5)-FM(6)*0.0516509;
end
```

Pressure Calibration

```
%Isolate the pressure data from the raw Scanivalve data
pressuredata=scani;
%Isolate the specific measurements from the pressure data
 pitotstatic=pressuredata(17:17:end);
 pitotstagnation=pressuredata(16:17:end);
 forwardtap=pressuredata(14:17:end);
 backtap=pressuredata(15:17:end);
 %Determine Q by using the two different methods and convert to Pa
 Qprobe=-(pitotstagnation-pitotstatic)*6894.75729;
 Qinlet=-(backtap-forwardtap)*6894.75729;
 %Qinlet=-(backtap)*6894.75729;
% Datapoints for Q<100Pa are removed from the
 %fitted data points to improve accuracy over the area of interest

 zeroindex=Qprobe<30;
 Qprobe(zeroindex)=[];
 Qinlet(zeroindex)=[];
%   zeroindex=Qprobe>2000;
%  Qprobe(zeroindex)=[];
%  Qinlet(zeroindex)=[];

 % Determine polynomial fits for different orders
 [p1,s1]=polyfit(Qinlet,Qprobe,1);
 [p2,s2]=polyfit(Qinlet,Qprobe,2);
 [p3,s3]=polyfit(Qinlet,Qprobe,3);
 [p4,s4]=polyfit(Qinlet,Qprobe,4);
 [p5,s5]=polyfit(Qinlet,Qprobe,5);
 PercError= (Qinlet-Qprobe)./(Qprobe)*100;
 [p6,s6]=polyfit(Qinlet,PercError,3);


 % Direct comparison of pitot probe and inlet dynamic pressures
  figure
 hold on
 scatter(Qinlet(Qinlet>10),(Qinlet(Qinlet>10)-
Qprobe(Qinlet>10))./Qprobe(Qinlet>10)*100,'.')
 index=linspace(0,2450,100);
```

```
 f0 = polyval(p6,index);
 plot(index,f0)
 hold off

% Plot the fits and percent errors
index=linspace(0,2450,100);
f1 = polyval(p1,index);
%T1 = table(Qinlet,Qprobe,f1,((f1-
Qprobe)./Qprobe*100),'VariableNames',{'Qinlet','Qprobe','Fit','FitErrorPercen
t'});
figure
hold on
scatter(Qinlet,Qprobe,'.')
plot(index,f1,'r--')
hold off
figure
scatter(Qinlet(Qinlet>10),((polyval(p1,Qinlet(Qinlet>10))-
Qprobe(Qinlet>10))./Qprobe(Qinlet>10)*100),'.')

f2 = polyval(p2,index);
%T2 = table(Qinlet,Qprobe,f2,((f2-
Qprobe)./Qprobe*100),'VariableNames',{'Qinlet','Qprobe','Fit','FitErrorPercen
t'});
figure
hold on
scatter(Qinlet,Qprobe,'.')
plot(index,f2,'r--')
hold off
figure
scatter(Qinlet(Qinlet>10),((polyval(p2,Qinlet(Qinlet>10))-
Qprobe(Qinlet>10))./Qprobe(Qinlet>10)*100),'.')

f3 = polyval(p3,index);
%T3 = table(Qinlet,Qprobe,f3,((f3-
Qprobe)./Qprobe*100),'VariableNames',{'Qinlet','Qprobe','Fit','FitErrorPercen
t'});
figure
hold on
scatter(Qinlet,Qprobe,'.')
plot(index,f3,'r--')
hold off
figure
scatter(Qinlet(Qinlet>10),((polyval(p3,Qinlet(Qinlet>10))-
Qprobe(Qinlet>10))./Qprobe(Qinlet>10)*100),'.')

f4 = polyval(p4,index);
%T4 = table(Qinlet,Qprobe,f4,((f4-
Qprobe)./Qprobe*100),'VariableNames',{'Qinlet','Qprobe','Fit','FitErrorPercen
t'});
figure
hold on
scatter(Qinlet,Qprobe,'.')
plot(index,f4,'r--')
hold off
figure
```

```
scatter(Qinlet(Qinlet>10),((polyval(p4,Qinlet(Qinlet>10))-
Qprobe(Qinlet>10))./Qprobe(Qinlet>10)*100),'.')

f5 = polyval(p5,index);
%T5 = table(Qinlet,Qprobe,f5,((f5-
Qprobe)./Qprobe*100),'VariableNames',{'Qinlet','Qprobe','Fit','FitErrorPercen
t'});
figure
hold on
scatter(Qinlet,Qprobe,'.')
plot(index,f5,'r--')
hold off
figure
scatter(Qinlet(Qinlet>10),((polyval(p5,Qinlet(Qinlet>10))-
Qprobe(Qinlet>10))./Qprobe(Qinlet>10)*100),'.')

f6 = index-index.*polyval(p6,index);
%T6 = table(Qinlet,Qprobe,f6,((f6-
Qprobe)./Qprobe*100),'VariableNames',{'Qinlet','Qprobe','Fit','FitErrorPercen
t'});
figure
hold on
scatter(Qinlet,Qprobe,'.')
plot(index,f6,'r--')
hold off
figure
scatter(Qinlet(Qinlet>10),(((Qinlet(Qinlet>10)-
polyval(p6,Qinlet(Qinlet>10)).*Qinlet(Qinlet>10))-
Qprobe(Qinlet>10))./Qprobe(Qinlet>10)*100),'.')
%
%Determine the average error magnitude for each pressure range and fit
point0=Qinlet<100;
point1=(Qinlet>100 & Qinlet<300);
point2=(Qinlet>300 & Qinlet<500);
point3=(Qinlet>500 & Qinlet<800);
point4=(Qinlet>1000 & Qinlet<1400);
point5=(Qinlet>1600 & Qinlet<2000);
point6=Qinlet>2000;
e0=(Qinlet-Qprobe)./Qprobe*100;
error0=[mean(abs(e0(point1))),mean(abs(e0(point2))),mean(abs(e0(point3))),mea
n(abs(e0(point4))),mean(abs(e0(point5))),mean(abs(e0(point6)))];

e1=(polyval(p1,Qinlet(Qinlet>10))-Qprobe(Qinlet>10))./Qprobe(Qinlet>10)*100;
error1=[mean(abs(e1(point1))),mean(abs(e1(point2))),mean(abs(e1(point3))),mea
n(abs(e1(point4))),mean(abs(e1(point5))),mean(abs(e1(point6)))];
e2=(polyval(p2,Qinlet(Qinlet>10))-Qprobe(Qinlet>10))./Qprobe(Qinlet>10)*100;
error2=[mean(abs(e2(point1))),mean(abs(e2(point2))),mean(abs(e2(point3))),mea
n(abs(e2(point4))),mean(abs(e2(point5))),mean(abs(e2(point6)))];
e3=(polyval(p3,Qinlet(Qinlet>10))-Qprobe(Qinlet>10))./Qprobe(Qinlet>10)*100;
error3=[mean(abs(e3(point1))),mean(abs(e3(point2))),mean(abs(e3(point3))),mea
n(abs(e3(point4))),mean(abs(e3(point5))),mean(abs(e3(point6)))];
e4=(polyval(p4,Qinlet(Qinlet>10))-Qprobe(Qinlet>10))./Qprobe(Qinlet>10)*100;
error4=[mean(abs(e4(point1))),mean(abs(e4(point2))),mean(abs(e4(point3))),mea
n(abs(e4(point4))),mean(abs(e4(point5))),mean(abs(e4(point6)))];
e5=(polyval(p5,Qinlet(Qinlet>10))-Qprobe(Qinlet>10))./Qprobe(Qinlet>10)*100;
```

```
error5=[mean(abs(e5(point1))),mean(abs(e5(point2))),mean(abs(e5(point3))),mea
n(abs(e5(point4))),mean(abs(e5(point5))),mean(abs(e5(point6)))];
e6=(Qinlet(Qinlet>10)-polyval(p6,Qinlet(Qinlet>10)).*Qinlet(Qinlet>10)-
Qprobe(Qinlet>10))./Qprobe(Qinlet>10)*100;
error6=[mean((e6(point1))),mean((e6(point2))),mean((e6(point3))),mean((e6(poi
nt4))),mean((e6(point5))),mean((e6(point6)))];
```

C.2 LabVIEW Code

Wind Tunnel Controller VI

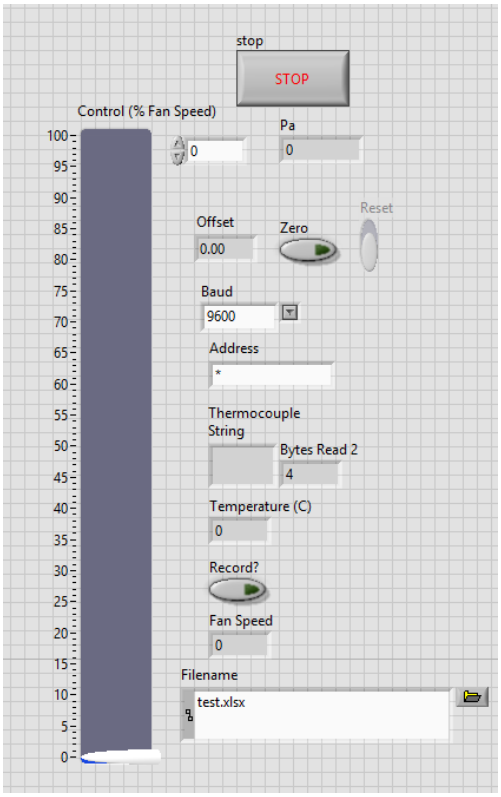

Figure 74: Wind Tunnel Controller VI front panel.

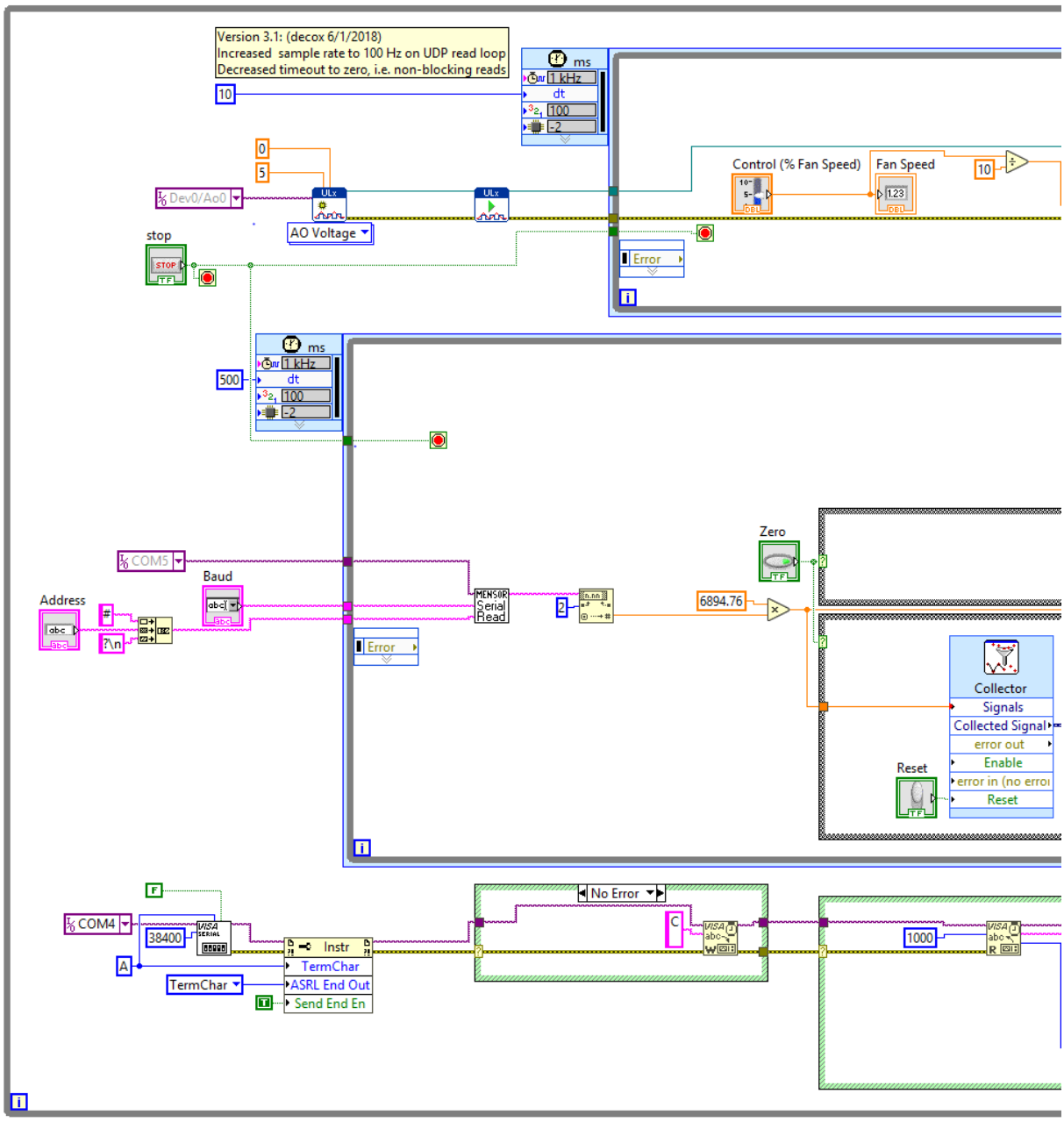

Figure 75: Wind Tunnel Controller VI block diagram.

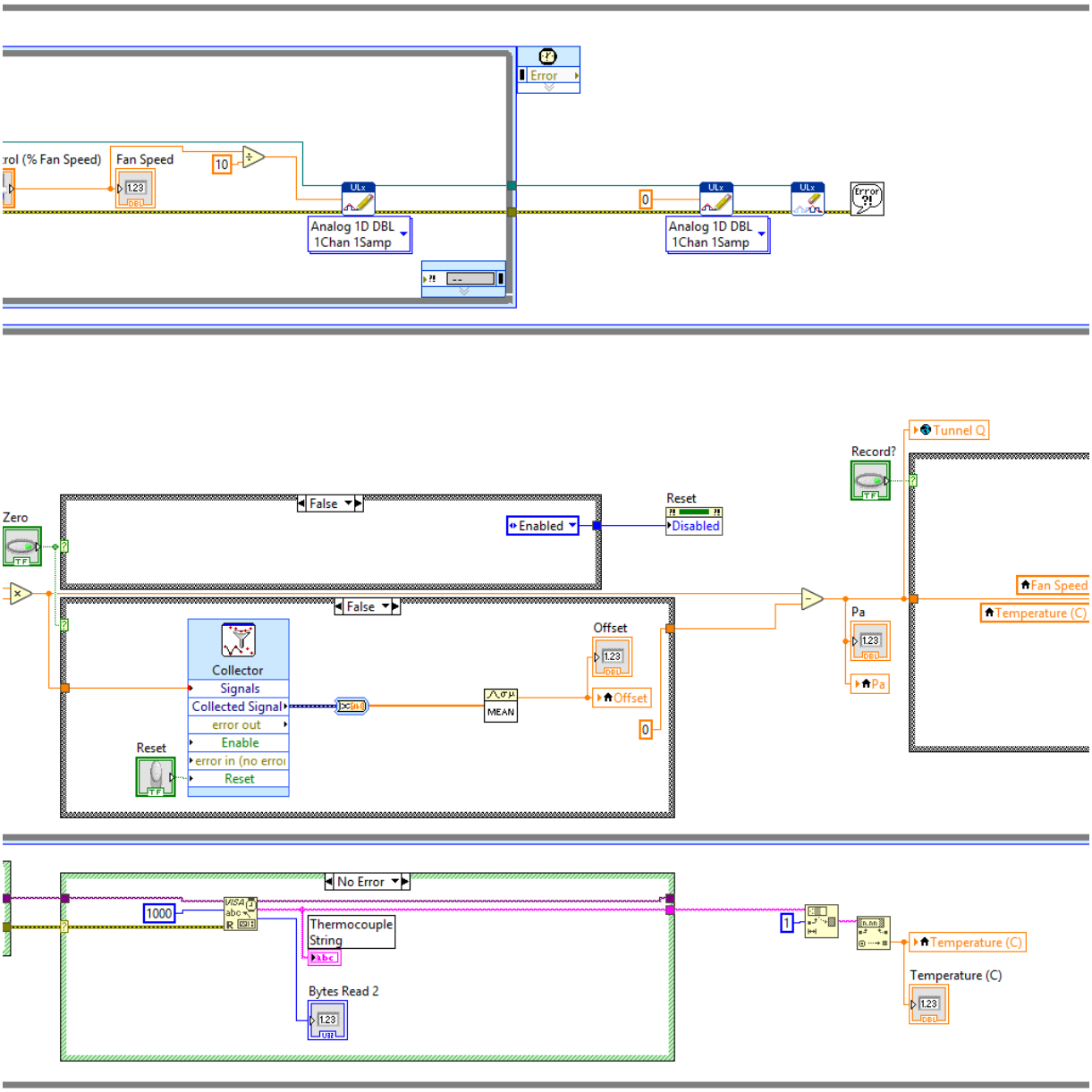

Figure 75 continued.

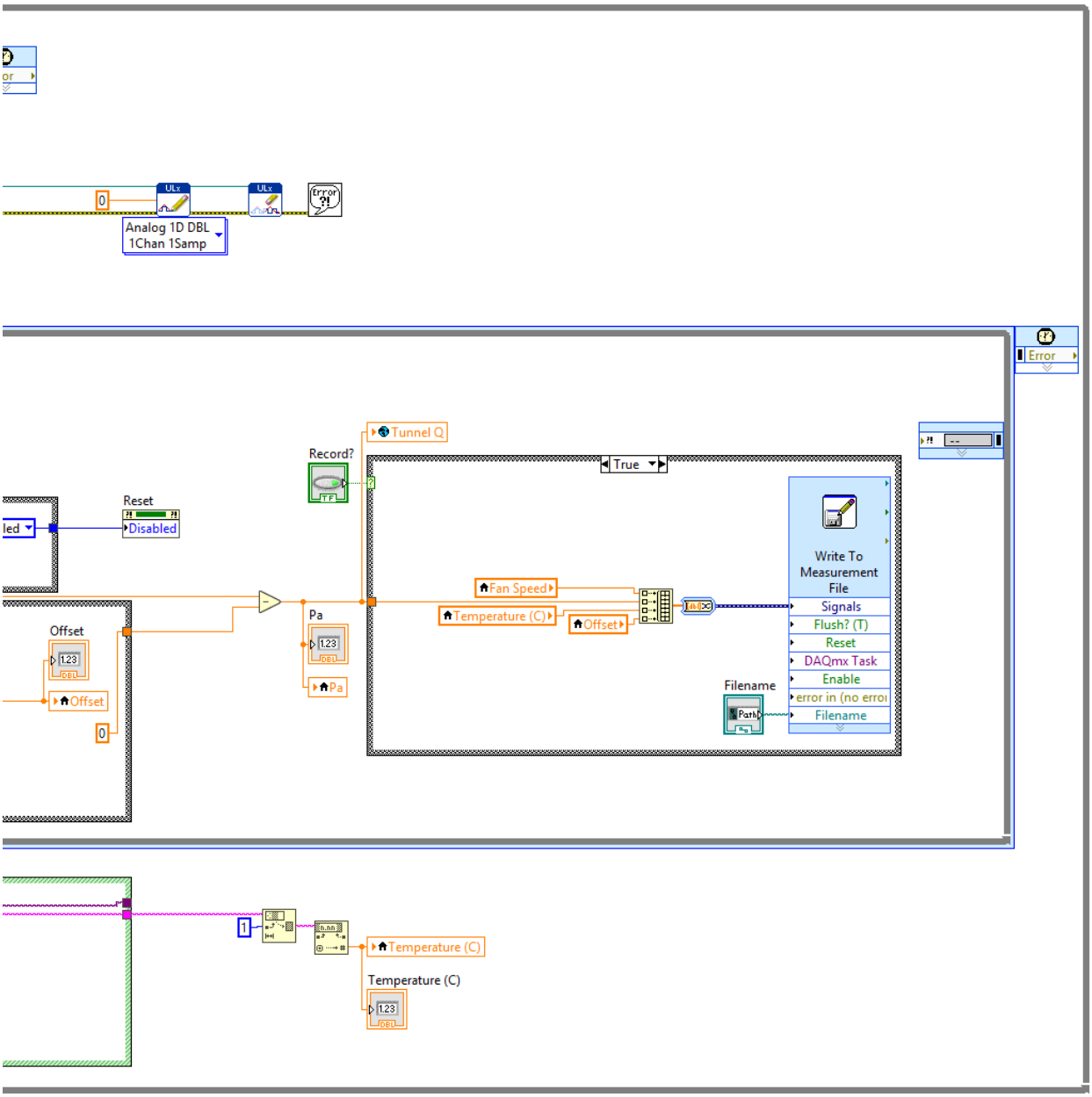

Figure 75 continued.

Balance Controller VI

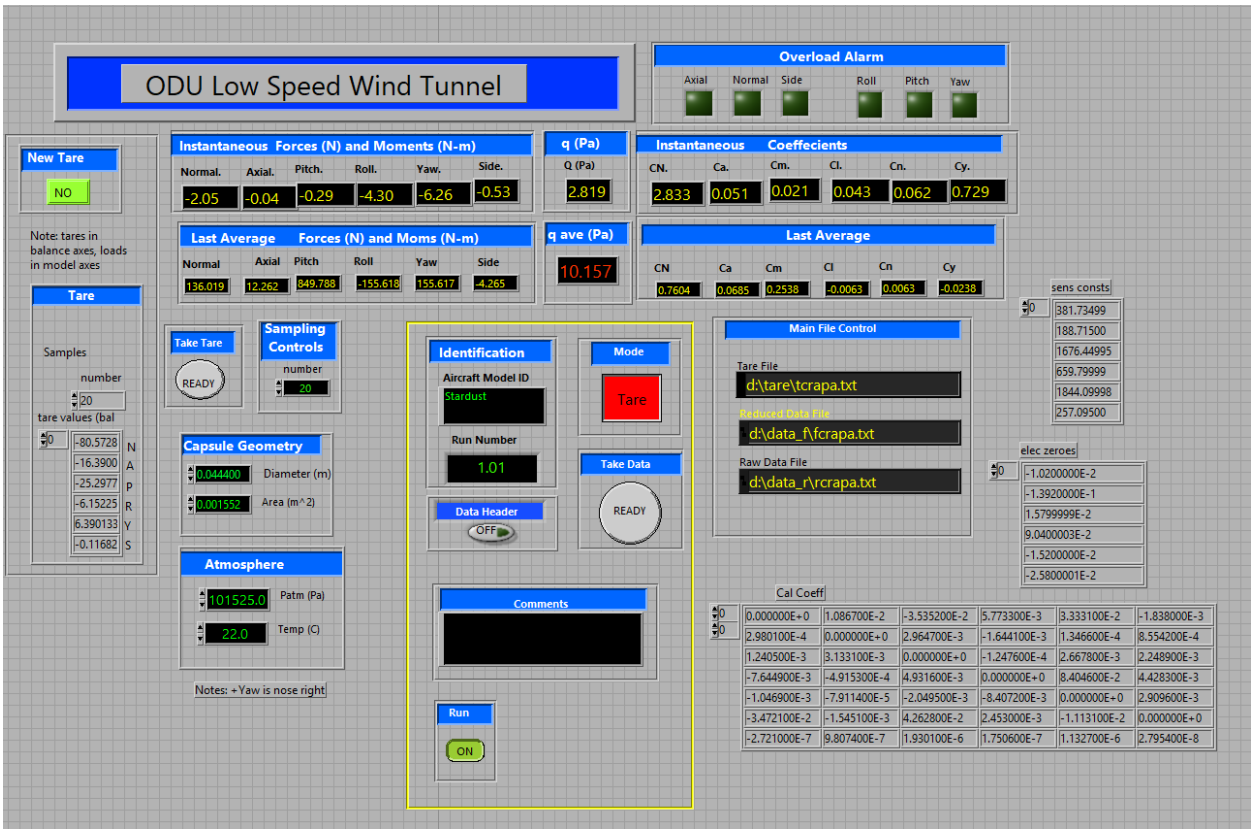

Figure 76: Balance Controller VI front panel. This is a complex VI with multiple sub-VIs. It was used to record the raw output voltages from the MS-100 balance. Other features were not used.

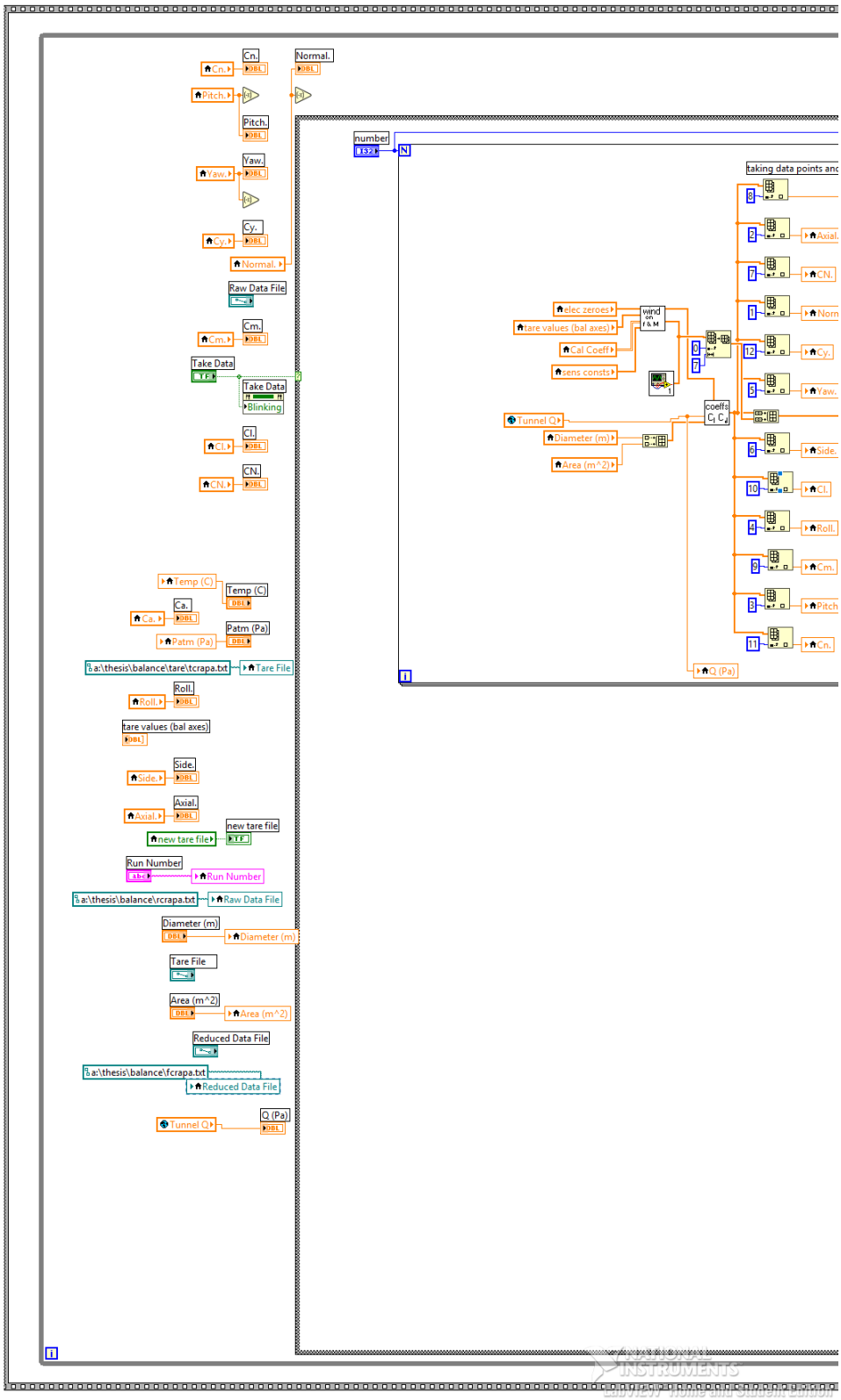

Figure 77: Balance Controller VI block diagram. 'Take Data' configuration.

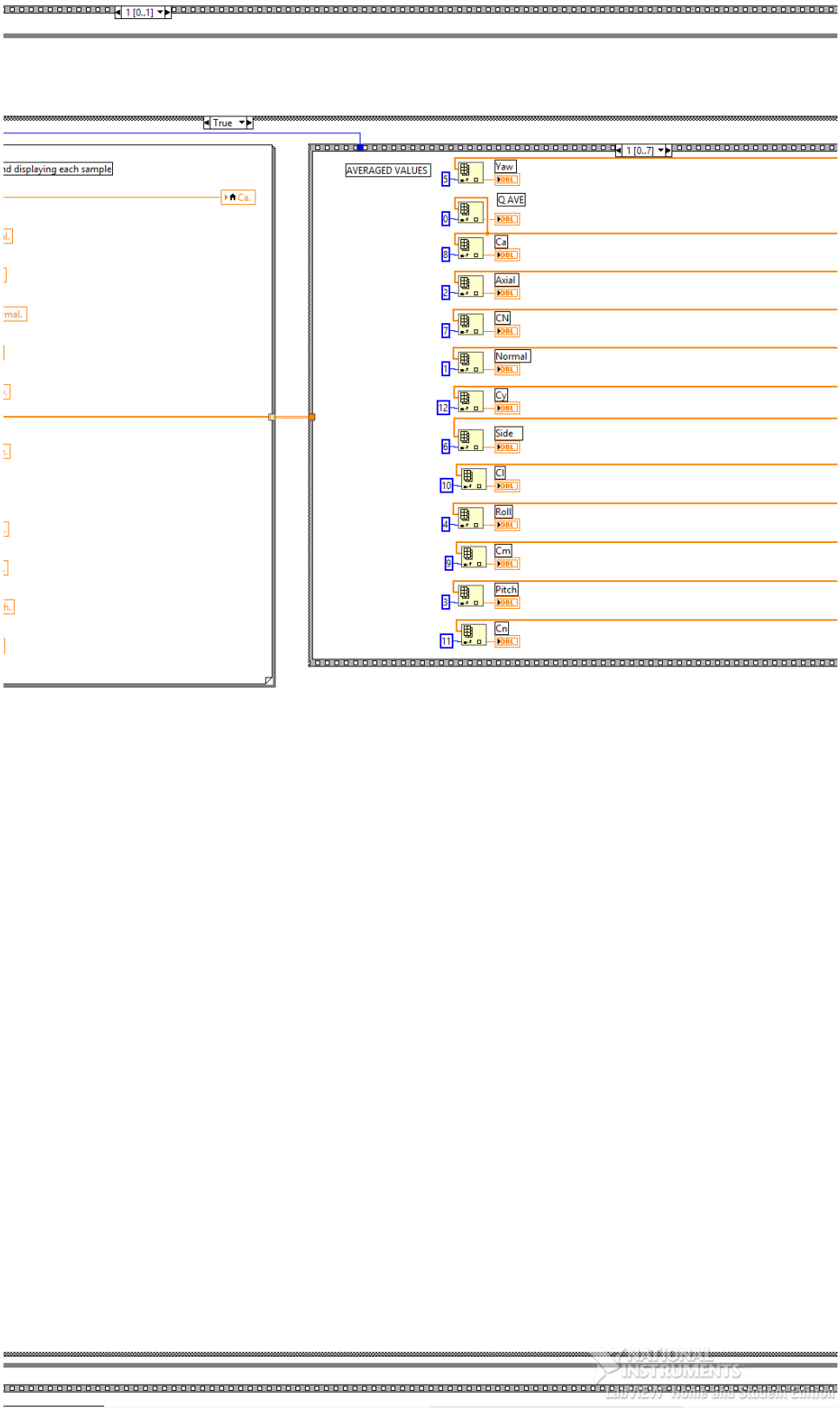

Figure 77 *continued.*

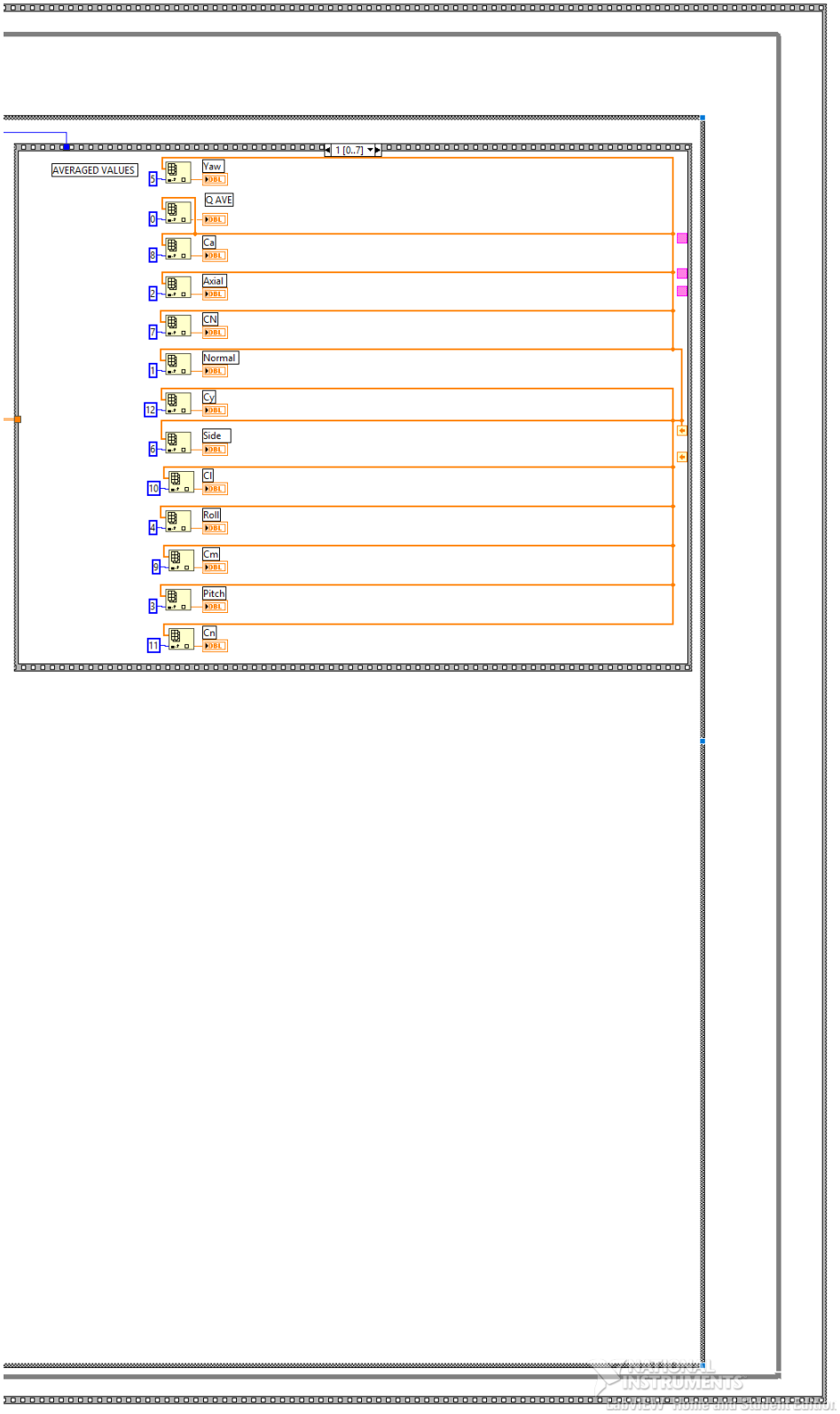

Figure 77 *continued.*

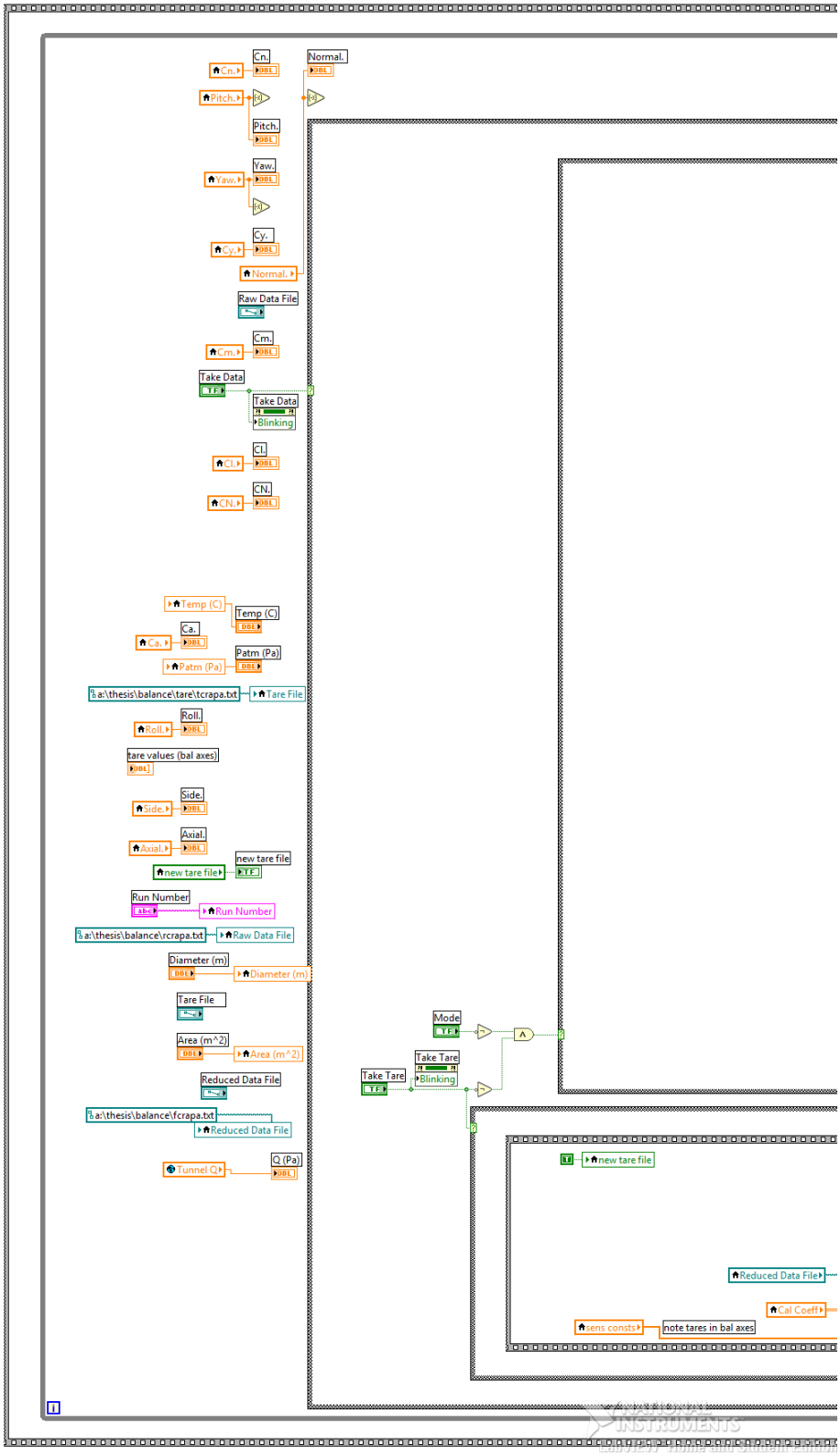

Figure 78: Balance Controller VI block diagram. 'Take Tare' configuration.

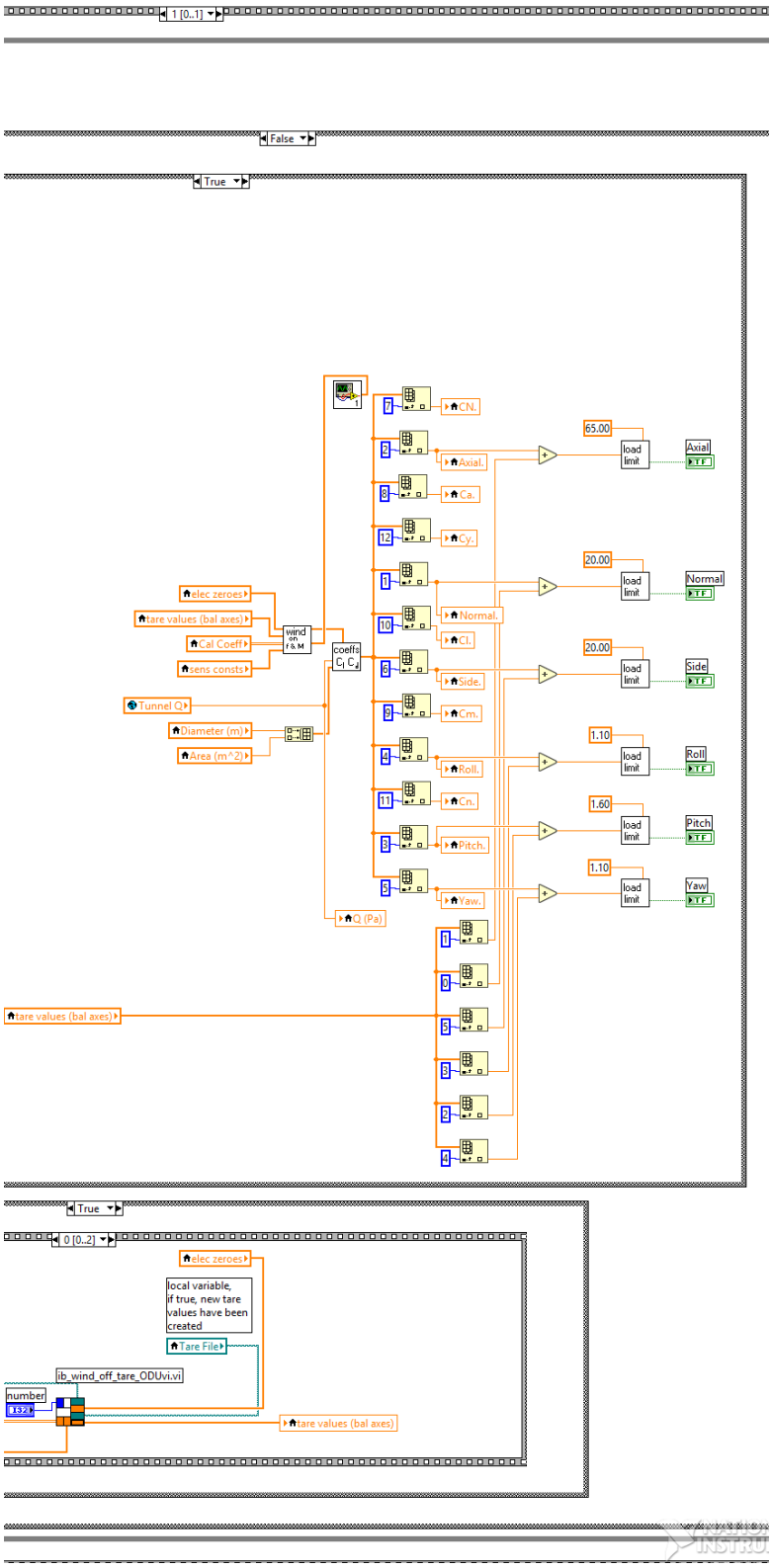

Figure 78 continued.

VITA

Cameron K. Neill

Mechanical & Aerospace Engineering
Old Dominion University
214A Kaufman Hall, Norfolk, VA 23529

Email:
cam.k.neill@gmail.com

Education:

M.S. Aerospace Engineering, Old Dominion University, May 2019
B.S. Aerospace Engineering, Georgia Institute of Technology, May 2016

Academic Employment:

Graduate Research Assistant to Dr. Colin Britcher, Department of Mechanical & Aerospace Engineering, Old Dominion University, June 2016-August 2018

Professional Employment:

Engineering Intern, Newport News Shipbuilding, May-July 2013, 2014, 2015